TRIGGERABLE LIGAND PRESENTATION USING CAGED-RGD

A Dissertation
Presented to
The Academic Faculty

By

Ted Lee

In Partial Fulfillment
Of the Requirements for the Degree
Doctor of Philosophy in Bioengineering

Georgia Institute of Technology

December 2013

TRIGGERABLE LIGAND PRESENTATION USING CAGED-RGD

Approved by:

Andres J. Garcia, Ph.D.
Woodruff School of Mechanical Engineering
Petit Institute for Bioengineering and Bioscience
Georgia Institute of Technology
Atlanta, GA

Thomas Barker, Ph.D.
Wallace H. Coulter Department of Biomedical Engineering
Georgia Institute of Technology
Atlanta, GA

Arancha del Campo, Ph.D.
Max-Planck-Institut für Polymerforschung
Mainz, Germany

Jennifer Curtis, Ph.D.
School of Physics
Georgia Institute of Technology
Atlanta, GA

Cheng Zhu, Ph.D.
Woodruff School of Mechanical Engineering
Petit Institute for Bioengineering and Bioscience
Georgia Institute of Technology
Atlanta, GA

Date Approved: Jun 28th 2013

I did it for the poofy hat!

ACKNOWLEDGEMENTS

There are many people who made this Ph.D. possible. First, I would like to thank my parents and grandparents for supporting me throughout my years of schooling, always encouraging me to strive for the best. Through endless nagging and goading, saying things are good for me, I guess they were right. They never spared a penny on my education and always gave me no excuse to not succeed. If I failed it would be by my own doing gumption and choices.

There are a two of professors that without their support I probably would not have gotten the research opportunities that allowed me to succeed. Marilyn Wolf trusted a young naive version of me to mill aimlessly in the cleanroom for a whole summer, to create an electrowetting biochip that likely would have been an entire Ph.D. thesis. Nevertheless, she believed in the power of setting lofty goals that way even you make it 20% the way there you have learned something. I would also like to thank Ron Weiss, who gave me the first introduction to bacteria and mammalian cell work, synthetic biology, and embedded bacteria culture. So I suppose that was my first experience with biocompatibility – agar counts as a biomaterial right? These two professors during their tenure at Princeton formed the foundation of my academic research endeavors and helped me to succeed.

I have to spend some extra time thanking my Master Thesis advisor Chris Chen for trusting a wildcard with little appreciation for class and grades, but hey, I had microfabrication experience. Without the guidance of Chris Chen I would have never gotten into the cell adhesion and mechanotransduction field. Back then I just thought he was a good professor since he had Nature papers, but I learned that success in

academia was more than just fancy equipment and R01 grants. It was also the art of selling and framing research goals in ways that mattered – trying to actually answer a question for sciences sake just because we were nerds and it was interesting. Then again pretending that everything we did would cure cancer probably helped too.

Andres Garcia, my Ph.D advisor, has been the consummate advisor. Throughout the years, he has taught me so many facets of about science and research, while interspersing volumes of unsolicited life pointers. He has always been a great coach and motivator, which is not always simple when dealing with the laziest person on the planet – me. He has always had confidence in me and trusted me to make informed decisions on my own research while ensuring that our lab always had the best possible equipment and resources to succeed. He always liked to joke that I spent the most money in the lab, which simply was not true; however, I did have expensive tastes when it came to laboratory equipment. When it doubt buy the best – if it's the most expensive it has got to be the best right? At any rate, I am sure Andres wanted to pull all his hair out many times, ranging from my qualification exams, proposal, conference presentations, and my defense. I always knew that the talk was going well if Andres was turning bright red and subtlety shaking his head at me. Regardless, without Andre's motivation and constant whip cracking I probably would have taken 8 years to finish my Ph.D., so thanks for that.

I need to put a special shout out to Kellie Templeman who tirelessly woke up early to join me in my endeavors in the PRL, gossiping about life and lab. Her light-hearted and down to earth attitude was always a welcome departure from the stuffiness of Ph.D. land. Garcia lab people, you guys were pretty cool, at least you put up with my constant shenanigans, but hey, I'd like to think we learned from each other.

I also need to thank my former colleagues and friends, especially the Cyrpess St. happy hour crew for holding it down all these years. The old school crew, David Dumbauld, Kelly Erby, Rich Carpendeo, Sean Coyer, Shetal Shah, Jeremy Lin, Ed Phelps, Vince Fiore, Chris Dosier, and Scraub, good times throughout those stupidly hot Braves tailgates, porch parties, and fancy beer places. Too bad about those new rules they put in at the Viewpoint pool, probably because of us. Alison Douglas, Devon Headen, Amy Cheng, Apoorva Salimath, Efrain Cermeno, Albert Cheng and sometimes Jose Garcia – solid additions to the crew over the years.

There are many other people that have made this undertaking possible, you are not forgotten. Thanks to all.

TABLE OF CONTENTS

LIST OF FIGURES

LIST OF ABBREVIATIONS

ECM	Extracellular Matrix
PEG	Poly(ethylene glycol)
FBCG	Foreign Body Giant Cell
RGD	(Arginine-Glycine-Aspartic Acid) Tri-Peptide
UV	Ultra-Violet
mPADs	Multiple Post Array Deflection Substrate
eGFP	Enhanced Green Fluorescent Protein
FN	Fibronectin
FA	Focal Adhesion
FAK	Focal Adhesion Kinase
SRC	c-SRC Tyrosine Kinase
ROCK	Rho-associated Protein Kinase
MLC	Myosin Light Chain
IgG	Immunoglobulin G
SAM	Self-Assembled Monolayer
PDMS	Poly(dimethylsiloxane)
EG	Ethylene Glycol
Au	Gold (element)
-SH	Thiol Group
VDW	Van der Waals Interactions

-OH	Hydroxyl Group
SI-ATRP	Surface-Initiated Atom-Transfer Radical Polymerization
OEGMA	Oligo(ethylene glycol)methacrylate
YIGSR	(Tyrosine-Isoleucine-Glycine-Serine-Arginine) Oligopeptide
PHSRN	(Proline-Histidine-Serine-Arginine-Asparagine) FN Synergy Site
HUVEC	Human Umbilical Vein Endothelial Cell
BSA	Bovine Serum Albumin
diH_2O	Deionized H_2O
µCP	Microcontact Printing
BCE	Bovine Capillary Endothelial Cell
OEG	Oligoethylene Glycol
SECM	Scanning Electrochemical Microscopy
NPE-TCSP	1-(2-Nitrophenyl)Ethyl-5-Trichloro Silylpentanoate
NVOC	Nitroveratryloxy-Carbonyl
DMNPB	3-(4,5,Dimethoxy-2-Nitrophenyl)-2-Butyl Ester
TEG	Tetraethyleneglycol
LCST	Lower Critical Solution Temperature
Poly(NIPAMM)	Poly(N-Isopropylacrylamide)
PAA	Polyacrylamide
MEFs	Mouse Embryonic Fibroblasts
V_H	Vinculin Head Domain
V_T	Vinculin Tail Domain
T_{12}	Constitutively-Active Full Length Vinculin
FRAP	Fluorescence Recovery After Photobleaching

VEGF	Vascular Endothelial Growth Factor
PEGDA	Poly(Ethylene Glycol) Di-Acrylate
SVA	Succinimidyl Valerate
MALDI	Matrix Assisted Laser Desorption Ionization
MS	Mass Spectroscopy
Acryl	Acrylate
RDG	(Arginine-Aspartic Acid-Glycine) Scrambled Peptide
AM	Acetoxymethyl Ester
GMA	Glycol Methacrylate
CD68	Cluster of Differentiation 68
DAPI	4',6-Diamidino-2-Phenylindole Nuclear Stain
PEG-MAL	4 Arm-Poly(Ethylene Glycol)-Maleimide
VPM	(Valine-Proline-Methionine) Tri-Peptide
MMP2	Matrix Metalloproteinase II
IMR90	Human Caucasian Fetal Lung Fibroblast
DPBS	Dulbecco's Phosphate Buffered Saline
DMEM	Dulbecco's Modified Eagle Media
FBS	Fetal Bovine Serum
TEMED	Tetramethylethylenediamine
APS	Ammonium Persulfate
IACUC	Institutional Animal Care and Use Committee
NIH	National Institutes of Health
TEA	Triethanolamine
PIP2	Phosphatidylinositol 4,5 Biphosphate
CSK	Cytoskeleton

VASP	Vasodilator Stimulated Phosphoprotein
Arp2/3	Actin-Related Protein 2/3
FRET	Fluorescence Resonance Energy Transfer
HT1080	Human Fibrosarcoma Cell Line
NHS	N-Hydroxysuccinimide
Δ9DiI	1,1'-Dioleyl-3,3,3',3'-Tetramethylindocarbocyanine Methanesulfonate
WT	Wild Type
ROI	Region of Interest

SUMMARY

Engineering surfaces for biocompatibility and cell adhesion is an important challenge facing the biotechnology industry. Whether it is developing new tools for discovery or making highly defined materials for clinical applications, the rational design of biomaterial surfaces is of paramount importance. Through the control of chemical and biomolecular moieties on metals, polymers, and hydrogels, cell-material interfaces can be engineered to exhibit specific characteristics. These highly defined surfaces can be used to either decouple the complex interplay between cells and a myriad of extracellular matrix (ECM) components adsorbed onto material surfaces, or prevent unwanted signaling through immobilization of specific biomolecules or chemical chelators. Using model systems such as poly(ethylene glycol) [PEG], that offer a "clean slate background", we are able to investigate specific receptor-ligand interactions and their effects on downstream cell behavior, signaling, and ultimately tissue/organ level responses.

We demonstrated a new method and technology to investigate the role of spatiotemporal ligand presentation in *in vitro* as well as *in vivo* settings. Biomaterial associated inflammation and the foreign body giant response (FBGC) are critical limiters of the performance of implantable biomaterials. Downstream fibrous encapsulation limits the lifetime of all tissue-material interfaces, and leads to premature implant failure and undesirable fibrous tissue formation. Novel caged-compounds that can modulate their presentation of ligands *in situ*, after implantation, offer a novel platform for *in vivo* research. Precise triggering of ligands *in vivo* allowed for new studies into the role of spatiotemporal control in modulating cellular response into implanted constructs. In the context of both biomaterial implant associated inflammation and cell infiltration into

implanted materials, the caged-RGD ligand, in conjunction with PEG-based hydrogels, provided insights into previously unanswerable questions.

We also demonstrated a new research tool that probed the specific relationship between ligand presentation and subsequent cellular events such as focal adhesion formation and cell traction force generation/reinforcement. This work was the first system that provided precise spatiotemporal modulation of ligand presentation *in situ* while also tracking protein localization/activation and traction force generation to a single focal adhesion. This new methodology provided both valuable insights into specific cellular mechanotransduction events and future researchers with new questions and platforms for discovery.

Ultimately, future research into the spatiotemporal presentation of biomolecules will rely heavily on novel caged compounds. Once the caging larger biomolecules and chemicals become more technologically accessible, the applications of this technology are truly overwhelming. Whether it is modulating antigen presentation for immunomodulation or generating novel biochemical assays for single chip diagnostics, the possibilities are truly limited to our collective imagination.

CHAPTER 1

INTRODUCTION AND SPECIFIC AIMS

1.1 INTRODUCTION

Cells rely on time-dependent binding and activation by the ECM to initiate downstream signal transduction. It is unknown whether adhesion to a ligand is required throughout various cell processes, or only during a specified time period ("temporal threshold"). Current approaches to ligand presentation often comprise of static, constant densities of ligands. In contrast, natural cell adhesive interactions with ECMs exhibit spatiotemporal patterns of binding and activation. Therefore, a key to future research in controlling cell-material interactions will be the development of materials that can respond to external stimuli.

The *objective* of this project is to engineer biomaterials that present a UV-labile caged-Arginine-Glycine-Aspartic Acid (RGD) ligand and evaluate the effects on cell activities. RGD is the minimal adhesive sequence of fibronectin. By dynamically modulating adhesive ligand presentation, the effects of temporal control on cell processes can be elucidated. In this caged-peptide, a photo-labile group adjacent to the aspartic acid residue of RGD effectively "masks" a cyclo(RGDfk) peptide. Upon UV irradiation (360 nm), the caging group is released thereby restoring the adhesive activity of the peptide.

1.2 SPECIFIC AIM 1

Examine the role of temporal activation of caged-RGD presenting hydrogels in an *in vivo* subcutaneous inflammation and vasculogenesis model. We have succeeded in producing caged-RGD poly(ethylene glycol)-acrylate conjugates that can be tethered to poly(ethylene glycol) di-acrylate based hydrogels. Using this non-degradable, hydrogel-surface presentation system, we can study the effects of adhesive control on cell types both *in vitro* and *in vivo*. Using a murine subcutaneous implantation model, we evaluated the effects of caged-RGD activation on inflammatory response and vasculogenesis. We hypothesized that the delayed activation of adhesive ligands would attenuate the effects of the acute phase inflammatory response on implant fibrous capsule formation and macrophage activity. Also, we hypothesized that transdermal caged-RGD activation in a PEG-hydrogel would be able to modulate blood vessel infiltration into the implant.

1.3 SPECIFIC AIM 2

Analyze the effects of spatiotemporal presentation of RGD on a multiple post array deflection substrates on cell traction force and focal adhesion assembly. We have demonstrated the utility of using multiple post array deflection substrates (mPADs) in a variety of applications. The optical clarity of the PDMS device allows for high resolution, real-time, live cell microscopy studies. When used in the conjunction with cells containing fluorescently labeled proteins of interest, we can perform real-time studies to decipher the relationships between adhesive ligand presentation and cell traction force. We hypothesized that by tethering caged-RGD ligands to the surface of mPAD substrates and using stable cells lines expressing eGFP-vinculin, we would be able to study the real-time formation of focal adhesion components after confocal microscopy-based UV irradiation of the device.

1.4 SIGNIFICANCE

This thesis presents a *significant* contribution to field of biomaterials research by demonstrating the utility of dynamic, triggerable biomaterials using novel caged-compounds. By having unparalleled spatiotemporal control of RGD ligand presentation, we demonstrated two novel tools for discovery: 1) *in vivo* ligand presentation to probe downstream tissue behavior and cell infiltration to biomaterial implants, and 2) *in vitro* ligand presentation *in situ* using confocal-based live cell microscopy to investigate real-time vinculin recruitment and cell traction force generation. The power of triggerable *in vivo* adhesive ligand presentation was evaluated in both a biomaterial-associated implant inflammation model and an *in vivo* vasculogenesis study. These studies represented the first demonstration of triggerable adhesive ligand presentation *in vivo* and demonstrated the utility of caged-compounds at probing specific receptor-ligand responses on highly defined PEG-based hydrogels. Triggerable *in vitro* ligand presentation, combined with traction force microscopy, demonstrated a new research tool for investigating focal adhesion formation and downstream force generation. Taken in whole, these results provide previously unknown insights into the power of spatiotemporal control of adhesive ligand presentation and created novel new research platforms for future discovery.

CHAPTER 2

The Biological Basics of Engineering Surfaces[1]

2.1 The Extracellular Matrix

2.1.1 Constituents and Functions of the ECM

Before we can investigate how to engineer surfaces for cell adhesion, we must first understand the basics of extracellular matrices, its protein constituents, and the fundamentals of cell adhesion and spreading. This overview presents important knowledge to understand the composition of the ECM and engineer synthetic ECMs to tune cell-fate based processes.

ECMs comprise of a complex, insoluble, three-dimensional mixture of secreted macromolecules, including collagens and non-collagenous proteins, such as elastin and fibronectin, glycosaminoglycans, and proteoglycans, which are present between cells [1]. Provisional fibrin-based networks constitute specialized matrices for wound healing and tissue repair. The ECM's provides structure and order in the extracellular space, which serves to regulate many cellular functions including the establishment, maintenance, and remodeling of differentiated tissues [2]. In particular, ECM components such as fibronectin, laminin, and vitronectin mediate adhesive interactions that support cell anchorage, migration, and tissue organization. These cell-ECM

[1] [1] Adapted from: Lee TT, García AJ. "Biology lessons for engineering surfaces for controlling cell-material adhesion." In: João F. Mano, *Biomimetic Approaches for Biomaterials Development*. Wiley-VCH, 2012, ISBN 978-3-527-32916-8

interaction all serve to activate signaling pathways that direct cell survival, proliferation, and differentiation.

Aside from providing physical use to cells, ECM components can also interact with growth and differentiation factors, chemokines, and other soluble factors that regulate cell cycle progression and differentiation – ultimately controlling the their availability and activity. By using various strategies to immobilize and order these complex proteins and small oligopeptide ligands, ECMs control the spatial and temporal profiles of many cellular-responsive signals and generate gradients necessary for vectorial responses. Moreover, structural elements within ECMs, namely collagens, elastin, and proteoglycans, contribute to the mechanical integrity, rigidity, and viscoelasticity of skin, cartilage, vasculature, and other tissues. Furthermore, cells within the ECM can dynamically modulate its composition and structure, leading to a high regulated and bi-directional communication between both cells and the ECM.

Therefore, it is no surprise that that cell-material interaction both *in vivo* and *in vitro* systems are highly dependent on the ECM. By designing simplified proteins sequences, we can take an engineered approach to decoding, and possible controlling, these complex interactions with cells.

2.1.2 Protein Structure

Proteins are structurally complex and functionally sophisticated biomolecules present in all living systems. Their efficiency and effector actions been tuned by natural selection over millions of years and serve a variety of functions in all living organisms. In the following section, we explore the basic chemistry and structure of proteins so that we can better understand protein interactions with biomaterial surfaces.

Proteins are polymer chains that consist of an exact sequence of amino acids [3]. There are 20 known basic amino acids in nature and a number of amino acid derivatives that have slightly modified structure. All amino acids contain conserved structural regions, including an alpha-carbon (α-carbon), an amino group, a carboxyl group, and a variable side chain (R group). This side chain determines the chemical properties of each amino acid. There are non-polar, polar, acidic, basic side chains; as a result, the combined action of all side chains largely dictates a proteins overall 3-dimensional structure, biochemical activity, electrostatic interactions, and adsorption kinetics.

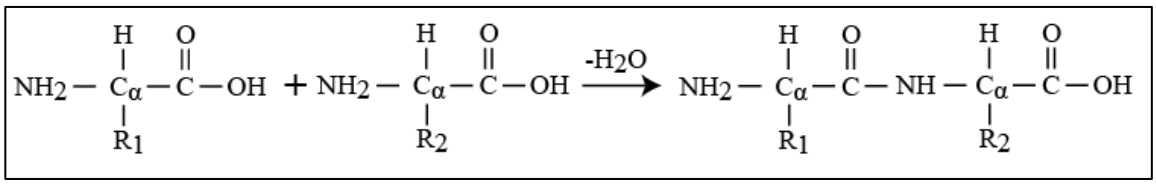

Figure 1. Structural diagram of amino acid and peptide bond. C_α is the alpha carbon; R_1/R_2 are functional groups. There are 20 basic functional groups.

Proteins are made of individual amino acids that are linked via a peptide bond (Figure 1). This bond has a resonance-stabilized structure that keeps the peptide bond in a planar conformation. A chain of many amino acids creates a polypeptide. Most polypeptides, with the exception of certain cyclic peptides, have two free ends – a carboxy terminus (C-terminus) and an amino terminus (N-terminus).

Protein structure can be broken into four discrete levels of organization: primary (1°), secondary (2°), tertiary (3°), and quaternary structure (4°). The physical arrangement or sequence of amino acids in a chain is known as the primary structure. Hydrogen bonding interactions between the functional groups of an amino acid chain cause the formation of local ordered or repeating units known as the secondary

structure. Examples of secondary structures include α-helices, β-sheets, and turns. The tertiary structure of a protein consists of the spatial orientation of various structural units within a single protein chain. These interactions are largely dictated by weaker interactions such as van der Waals, ionic, and hydrophobic interactions. The complex of various individual polypeptide chains forms a protein's quaternary structure. Ultimately, variations in protein structure modulate both its function and activity in biological systems.

2.1.3 The Basics of Protein Adsorption

The first event in the cell adhesion cascade to material surfaces is protein adsorption to a surface, and it is one of the major mechanisms regulating cell-material interactions [4]. Therefore, it becomes no surprise that when engineering biomaterials surfaces control of protein adsorption becomes critical. Protein adsorption is a phenomenon driven by entropy that is influenced by the chemical and physical properties of both the protein and the receiving surface. In general, protein adsorption to surfaces is controlled by non-covalent interactions that are mediated by the amino acid side chains present in different parts of the protein. These interactions include hydrophobic interactions, van der Waals, hydrogen bonding, and electrostatic forces.

While examining the structure of any protein, we can make a couple generalizations about its interactions with surfaces and surrounding fluids. Under physiological conditions, protein folding is highly dictated by hydrophobic interactions to exclude water from highly hydrophilic regions. There are two main types of proteins, those that are membrane bound, and those that largely exist as soluble globular proteins. Soluble proteins often have hydrophobic domains, areas rich in non-polar amino acids, which are buried in the protein core to minimize the entropy of the protein-solution system. The domains of membrane bound or transmembrane proteins often

have outward facing hydrophobic domains that interact with the lipid bilayer. These hydrophobic interactions are all driven by the minimization of free energy of the system and are the primary mediators of protein tertiary structure.

Biomaterial engineers are usually most interested in surface hydrophobicity and surface charge. Hydrophobicity is the manner in which a material responds in the presence of water and it is generally quantified by a contact angle measurement (Figure 2).

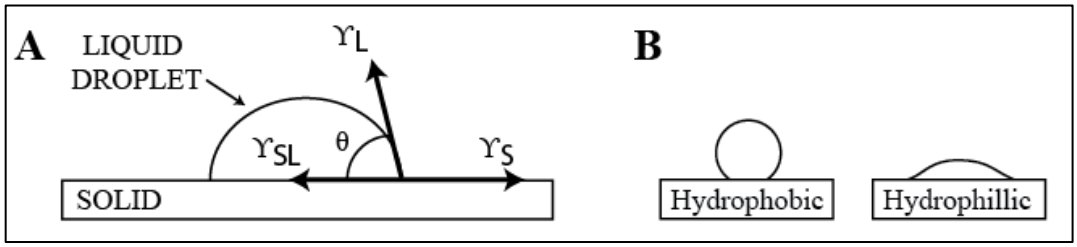

Figure 2. Contact Angle. A) Measurement of contact angle on a surface. Θ denotes contact angle; ϒ denotes respective surface tensions. B) Basic schematic of water droplets on hydrophobic and hydrophilic surfaces.

Generally, with increasing hydrophobicity on the surface, there will be greater protein adsorption; however, this does not mean the protein activity is maintained. The strength of the protein-surface hydrophobic interaction can destabilize a protein's tertiary structure. Protein charge may also influence the conformation of a protein when it adsorbs to a surface. A negatively charged domain interacting with a negatively charged surface will not be energetically favorable; therefore, one would expect counter ions from solution to shield the protein from these entropically unfavorable events.

Other surface properties that can influence protein adsorption to a surface include topography, composition, heterogeneity and electrical potential (Figure 5). The topography of a surface can influence the available surface area for protein adsorption.

The surface composition of a material, or its chemical moieties present will influence interactions with amino acid side chains and determine the intermolecular forces that will be exerted on a protein. The heterogeneity of a material will increase the types of protein "domains" that can interact with a surface. Electrical potential will also affect the conformation of a protein on a surface and perhaps affect the distribution of ions within a protein. Therefore, in engineering surfaces, one must take these factors all into consideration in order to maintain the activity of the protein of interest.

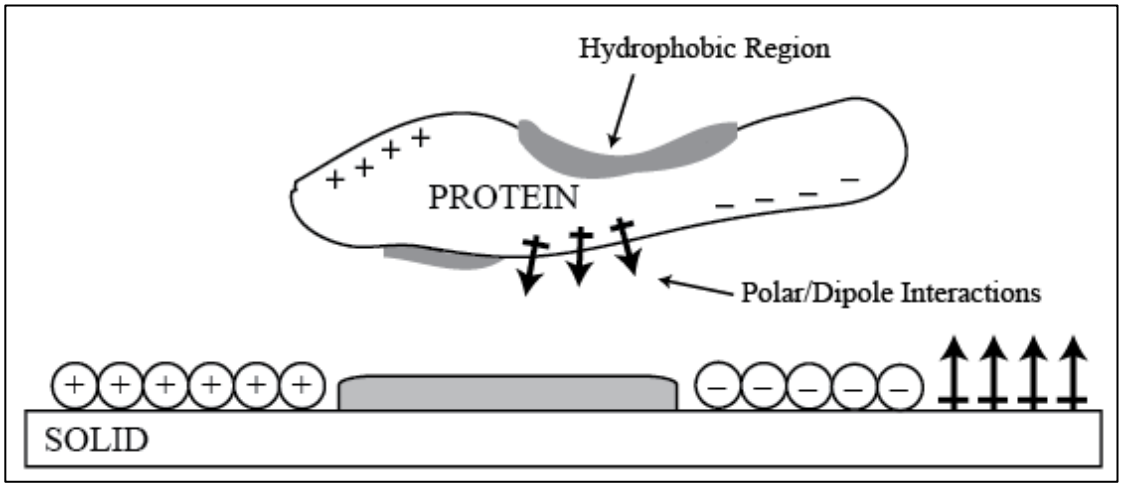

Figure 3. Protein on a heterogeneous surface. + denote positive charged region; - denote negatively charged region; grey areas denote hydrophobic regions; arrows indicate polar regions with dipole.

2.1.4 The Kinetics of Protein Adsorption

Before protein adsorption to a material can occur, proteins must first be transported from the bulk solution phase to a surface. Transport occurs through two main modes: diffusion and convection. The area of transport that is most relevant to cell-material interactions occurs at the boundary layer between the surface and protein solution, where the protein adsorption rate is primarily dictated by diffusion alone.

However, in certain microfluidic systems and blood-contacting surfaces, where active flow occurs, convection mediated adsorption may also be important.

In the adsorption process, proteins are constantly in motion, actively rearranging in the most entropically favorable orientation and packing density. After a protein has begun adsorbing to a surface, as protein density increases, the protein will begin to adopt different conformations for more efficient packing (Figure 4). Interactions between the protein and the surface, as well as other proteins, will influence protein conformation and its interactions with surfaces. Usually, this is accompanied by limited protein unfolding and spreading. After a period of time, protein adsorption is thought to be irreversible since it is unlikely that all of the modalities for interaction between the protein and the surface would fail simultaneously. After adsorption, the final conformation of a protein with respect to the surface ultimately dictates its activity and function. Depending on the orientation of the protein, its activity can be severely hindered (Figure 5).

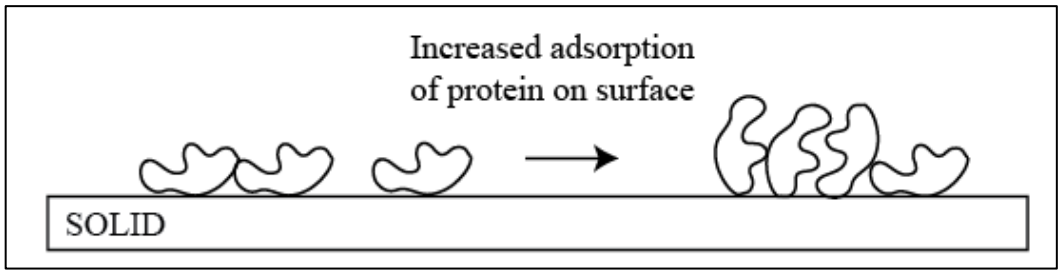

Figure 4. Packing density affects protein adsorption. As packing density of a protein increases on a surface, it can affect its overall orientation, conformation, and activity.

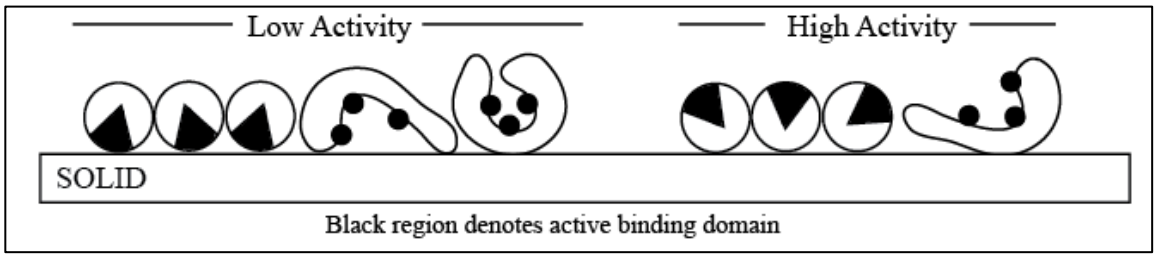

Figure 5. Protein orientation vs. activity. Proteins with active domains oriented upwards towards cells will exhibit higher overall activity compared to proteins with active domains facing towards the substrate surface.

Even though protein adsorption is classically thought to be irreversible, in the context of heterogeneous protein solution, a protein can be displaced from a surface by a protein of higher surface affinity. As mentioned before, proteins on a surface are highly dynamic. In a two protein system, the instant one protein (protein A) changes its orientation or breaks a series of non-covalent interactions with the surface, it is possible for a second protein (protein B) to compete for that physical space on the surface. As a consequence, if this second protein has higher affinity for the surface, it could displace the original protein from the surface. Therefore, the final concentration of proteins on a surface is influenced by the concentration and protein affinity of individual proteins. In a mixed population of proteins, those with higher concentration will be adsorbed first; however, eventually they will be displaced by proteins with higher surface affinity. This is known as the Vroman effect (Figure 6) [4, 5].

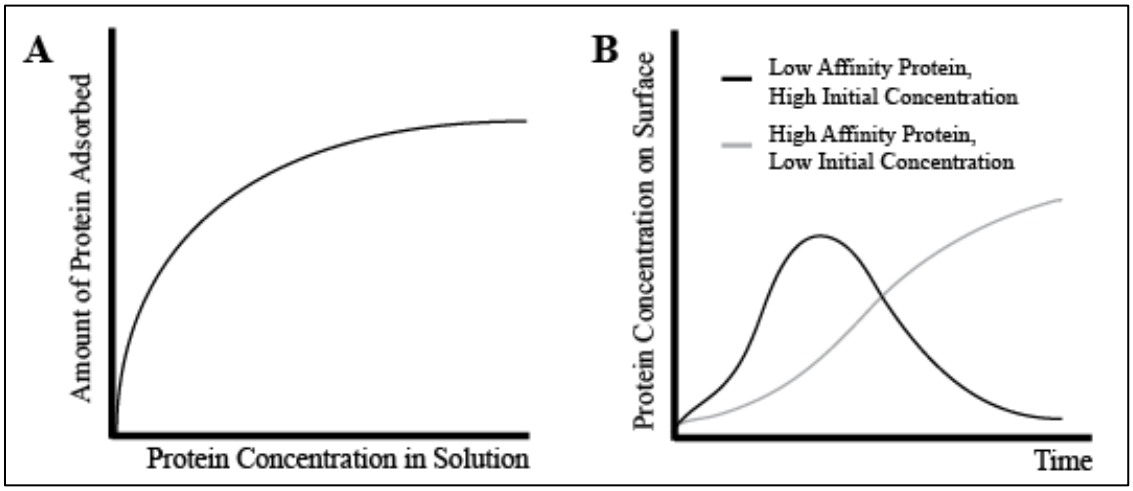

Figure 6. Vroman Effect. A) Protein adsorption isotherm; single protein species. B) Vroman effect with two proteins of different initial concentration and affinities for surface.

2.2 Integrin-Mediated Cell Adhesion

2.2.1 The Importance of Cell Adhesion

Most mammalian cells adhere to ECMs via specific cellular receptor-ligand interactions. In the previous section, we covered how the ECM functions as a scaffold facilitating the transfer of signals to adhering cells via specific proteins such as those containing adhesive domains such as fibrinogen, vitronectin, collagen, and fibronectin. Cells bind these adhesive ligands through a special class of receptors known as integrins [6, 7]. These integrin-ligand interactions regulate a myriad of specific cellular processes ranging from adhesion, migration, proliferation, secretion, gene expression, and apoptosis. In the following section, we highlight the importance of integrin-mediated cell adhesion before we begin our discussion of controlling cell-matrix interactions.

Integrin-mediated cell adhesion to the ECM is central to the organization maintenance, and repair of tissues by providing both mechanical anchorage and signals that direct cell survival, migration, cell cycle progression, and expression of differentiated

phenotypes [8, 9]. In fact, integrin-mediated adhesion is required for mammalian development. Animal models containing deletions for integrin receptors, integrin ligands, or focal adhesion components result in absolute lethality at early embryonic stages [10-13]. Abnormalities in adhesive interactions are often involved in pathological states, including blood clotting and wound healing defects, as well as malignant tumor formation [14, 15]. Furthermore, adhesive interactions are responsible for regulating cellular and host responses to implanted biomedical devices, tissue-engineered, constructs, and biotechnological systems [7].

Whereas significant progress has been achieved in identifying key adhesion components and how these participate in cell spreading, migration, and signaling, the mechanical interactions between a cell and its microenvironment remain poorly understood. It is increasingly evident that mechanotransduction, or signaling triggered by mechanical stimulation, between cells and their environment, regulates gene expression, cell fate, and even malignant transformation [16]. Therefore, engineering and controlling specific cell-matrix interactions are essential to unraveling these complex interactions [17-22].

2.2.2 Integrins and Adhesive Force Generation

Cell adhesion to native ECM components, such as fibronectin (FN) and laminin, is primarily mediated by the integrin family of heterodimeric receptors [23]. The integrin receptor has a large extracellular domain formed by both α and β subunits, a single transmembrane pass, and two short cytoplasmic tails that do not contain catalytic motifs. Integrin-mediated adhesion is a highly regulated process involving receptor activation and mechanical coupling to extracellular ligands [24-27]. Bound integrins rapidly associate with the actin cytoskeleton and cluster together to form focal adhesions (FAs) – discrete supramolecular complexes.

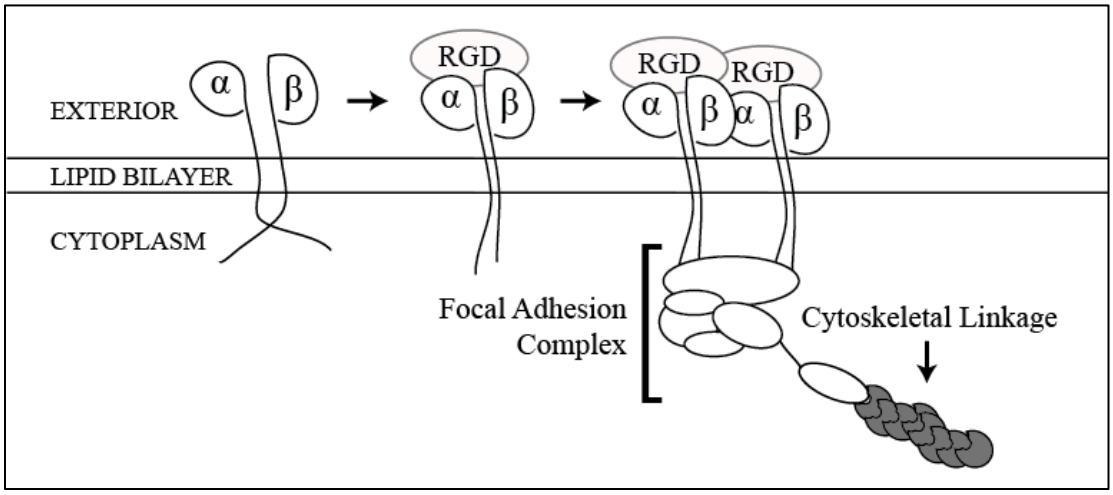

Figure 7. Basic diagram of integrin cascade. Inactive integrin becomes activated, creating a conformation change in the molecule, unfolding the cytoplasmic domains. This allows interactions with focal adhesion proteins, ultimately resulting the linkage with the cell cytoskeleton.

FAs are supramolecular complexes that contain both structural proteins, such as vinculin, talin, and α-actinin, and signaling molecules, including FAK, SRC, and paxillin [28]. Focal adhesions function as structural links, allowing for strong cell adhesive forces and signal transduction elements between the cell and its extracellular environment. These adhesive complexes are dynamic structures that are actively remodeled during cell migration [29, 30]. In response to external stimuli, numerous modalities are responsible for the assembly and disassembly of focal adhesions, including soluble growth factors and mechanical force [31-33]. In particular, the Rho GTPase effector Rho-kinase (also designated ROCK and ROKaII) plays a central role in serum-induced formation of focal adhesions and stress fibers. Rho-kinase controls focal adhesion and stress fiber formation by regulating actomyosin contractility through direct phosphorylation of the myosin light chain (MLC) and inactivation of myosin phosphatase

[34, 35]. Actomyosin contractility then drives the formation of focal adhesions and stress fibers by an unknown mechanism [36, 37].

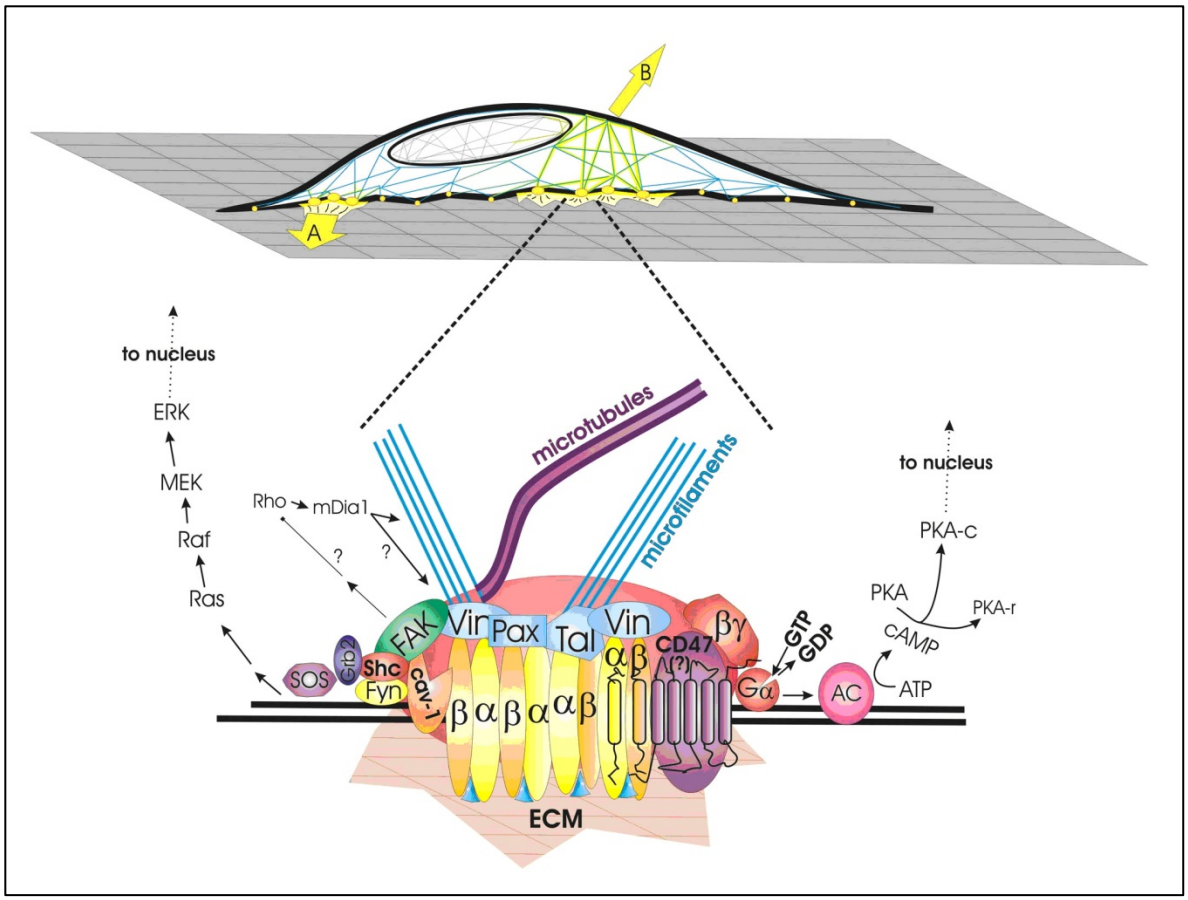

Figure 8. Detailed cartoon of mechanotransduction pathway. Copyright Ingber et al.

Mechanical interactions between a cell and ECM environment comprise of different spatiotemporal force components. For example, migrating cells utilize complex spatiotemporal patterns of traction forces via focal adhesion assembly dynamics that ultimately generate directional cell movement [29, 38]. Also, a cell attached to a surface exhibits an equilibrium balance between its own internal contractile forces and the anchorage forces to the underlying surface. This equilibrium is dictated by the size and distribution of cell-material adhesive structures, cytoskeletal architecture, and

actomyosin contractile forces. What further confounds the analysis is that all these adhesive interactions are inter-related and exhibit complex, often non-linear relationships. For example, migration speed exhibits a biphasic dependence on adhesive strength and ligand density [39], while epithelial cell scattering correlates with adhesion strength and actomyosin contractility but not with migration speed [40].

The accepted model for focal complex-generated adhesive forces, proposed by McClay and Erickson postulates a two-step process consisting of initial integrin-ligand binding followed by a rapid strengthening [41]. The strengthening response is a consequence of (i) increases in cell-substrate contact area (spreading), (ii) receptor recruitment to anchoring sites (recruitments and clustering), and (iii) interactions with cytoskeletal elements that lead to enhanced force distribution among bound receptors via local membrane stiffening (focal adhesion assembly).

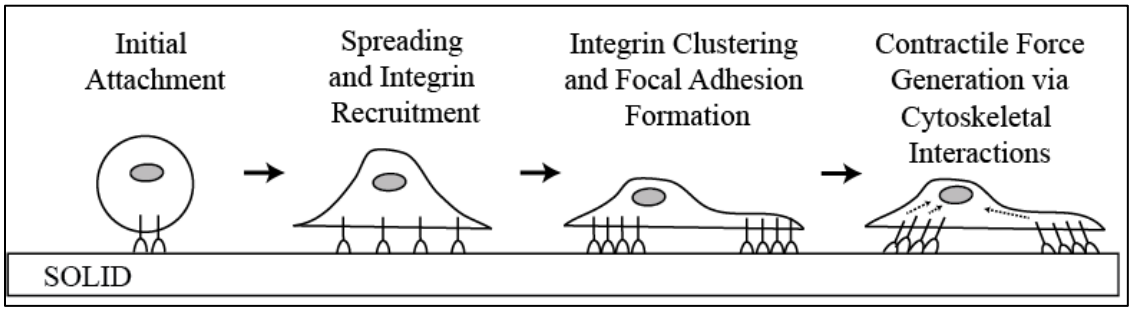

Figure 9. Schematic of cell adhesion cascade to a surface. Initial attachment leads to integrin recruitment, spreading, and integrin clustering; ultimately resulting in the generation of contractile forces by the cell on the surface.

Integrin clustering was one of the first observed and most intensively studied events in the adhesive process. Using chimeric receptors, LaFlamme et al, showed that ligand binding targets integrin receptors to sites of integrin-FN adhesion [42]. Integrin clustering is a critical step in the adhesive process by promoting the recruitment of

cytoskeletal components and initiating activation of signaling molecules. Based on immunostaining analyses, Yamada and colleagues demonstrated that integrin binding and clustering have synergistic effects in integrin function [43, 44]. Integrin occupancy by a single monovalent ligand induced receptor redistribution but no recruitment of cytoskeletal or signaling elements. In contrast, antibody-mediated integrin aggregation induced recruitment of FAK and tensin but no other focal adhesion components. Both integrin occupancy and aggregation are required for the robust assembly of focal adhesions and activation of signaling pathways.

2.2.3 Adhesive Interactions in Cell and Host Response to Biomaterials

Integrins are critically involved in host and cellular responses to biomaterials due to their essential roles in cell adhesion to ECM components. In platelet aggregation, the platelet integrin $\alpha_{IIb}\beta_3$ (GPIIb/IIa) binds to several ligands such as fibrinogen, von Willebrand factor, and fibronectin [6]. This receptor is the essential mediator of initial events in the blood-activation cascade after blood as come into contact with a synthetic material [45, 46]. Leukocyte-specific β_2 integrins, such as $\alpha_M\beta_2$ (Mac-1), mediate monocyte and macrophage adhesion to various ligands, including fibrinogen, fibronectin, IgG, and complement fragment iC3b. These receptors all play central roles in inflammatory responses *in vivo* [47, 48]. Binding of $\alpha_M\beta_2$ integrin to fibrinogen P1 and P2 domains exposed upon adsorption to biomaterial surfaces controls the recruitment and accumulation of inflammatory cells on implanted devices [49]. This integrin also plays a critical role in macrophage adhesion and fusion into giant foreign-body cells [48, 49]. For many types of tissue such as connective, muscular, neural, and epithelial, the β_1-family of integrins is largely responsible for adhesion to extracellular matrix ligands [7].

Integrins mediate cell-materials interactions by binding to adhesive extracellular ligands. These can be adsorbed from solution blood, plasma, or serum; secreted and deposited onto the biomaterial surface by cells; or specifically engineered onto a biomaterial interface. All of these interactions are highly dynamic, and the dominant adhesive mechanism could vary over time and is often different among cell types. For example, in blood plasma, the primary adhesive ligand is fibrinogen; while in serum, vitronectin plays a dominant role [50, 51]. As mentioned in previous sections, adhesive ligands can be displaced and replaced by other proteins in the surrounding medium via the Vroman effect. Therefore, a common surface engineering strategy is to coat a surface with fibronectin to promote cell adhesion and survival, and then allow cells to secrete their own adhesive proteins and extracellular matrix onto the material surface. It is important to note that integrin expression and activity profiles on a particular cell change over time. Most cells exhibit several integrins specific for the same ligand, and the binding activity of these receptions can be rapidly regulated via changes in integrin conformation. However, integrin expression profiles do not necessarily correlate with integrin function on a particular substrate. In most cellular responses, multiple integrins are typically involved.

2.3 Model Systems for Controlling Integrin-Mediated Cell Adhesion

A key to studying and controlling cell-material interactions is starting with a material that provides a "clean-slate" background – one that prevents non-specific protein adsorption and cell adhesion and signaling. Surfaces that are able to resist non-specific adsorption of biomolecules are known as "bio-inert" or "non-fouling". These types of non-fouling surfaces are required for the detailed study of singular bioactive

peptide sequences or molecules. By tethering a single or multiple bioactive species in a highly characterized manner, detailed investigations of specific cell-material interactions can be completed.

Poly(ethylene glycol) (PEG) groups are highly resistant to protein adsorption and remain the benchmark for non-fouling surfaces [52]. The mechanism of resistance to protein adsorption is thought to be the combination of the polymer chain's ability to retain interfacial water (osmotic repulsion) and the resistance of the polymer chain to compression (entropic repulsion) [53]. Well-packed, self-assembled monolayers (SAMs) of ethylene glycol $(EG)_n$ repeats as short as n=3, have excellent non-fouling properties [54, 55]. The non-fouling characteristics of these surfaces are highly dependent on the conformation of the $(EG)_n$ chain. Chains in either a helical or amorphous conformation have significantly higher resistance to protein adsorption than the all trans conformation, probably due to interactions between the EG chains and interfacial water. While PEG groups are excellent at preventing protein adsorption, surfaces that completely abrogate protein adsorption have not been attained.

2.3.1 Self-Assembled Monolayers (SAMs)

Self-assembled monolayers (SAMs) are an organized layer of amphiphilic molecules that contain a head, alkane core, and functional group. In the context of cell adhesion, alkane-thiol based SAMs assembly on gold surfaces have been a extensively used model system to impart both specificity and non-fouling nature to surfaces. In this alkane-thiol based SAM, the head-group contains a –SH, or thiol group, that has a specific, yet reversible affinity for Au (gold). In the assembly of the monolayer, first the head-groups are attached the gold surface via a near-covalent interaction (~100kJ/mol) either in the liquid or gas phase. Then, the tail groups, which consist of long chain alkanes, or single bonded carbon chains, begin to orient and form semi-crystalline to

crystalline structures. These tail group interactions stabilize the close packing of SAM molecules via hydrophobic interactions and van der Waals interactions (VDW).

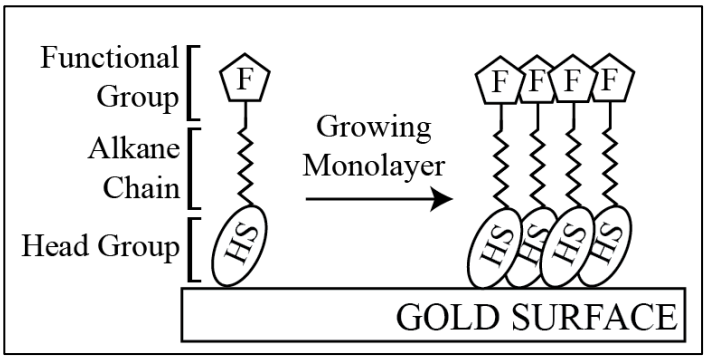

Figure 10. Basic self-assembling monolayer structure for controlling cell adhesion.

In vitro, SAMs present a method to generate and study model substrates presenting specific ligands to which cells can adhere. An advantage of SAMs over other model substrates is the level of control over the composition of the substrate as well as the ability to characterize these biological interactions by surface plasmon resonance [56].

Self-assembling molecules terminated with oligo- or poly(ethylene glycol) units are used to render surfaces non-fouling to cell adhesion. Non-fouling SAMs are an effective way to prevent non-specific protein adsorption to model surfaces. When used in conjunction with bioactive or other functional groups that support protein adsorption, non-fouling SAMs can be used to create a mixed monolayer. Mixed SAMs for the immobilization and attachment of cells only require 0.01-1% of the cell supporting species [57]. Cells can then adhere to these surfaces via non-specific interactions. Nevertheless, cells will continually remodel their microenvironment over time; therefore it might be difficult to control exactly which and what ratio of ECM proteins the cell will

secrete. In order to rigorously study the effects of a single ligand, the ligand can be tethered to a mixed SAM surface, to present integrin binding peptide sequences [58]. Whereas self-assembled monolayers have been used extensively for *in vitro* applications, they suffer several limitations when applied to *in vivo* medical applications. It is difficult to create robust Nobel-metal coatings on biomedical implants, SAM layers are limited to gold and silver substrates, and SAMs still suffer from long-term instability and loss of bioresistance [59-62]. As a consequence, in the last decade there has been a concerted effort developing medical grade polymer-brush systems and hydrogels.

2.3.2 Polymer-Brush Systems

Polymer-brush systems offer a more robust method of tethering biomolecules to biomedical device surfaces. These tethering chemistries utilize the –OH groups on oxidized titanium and silicon substrates for silane immobilization. There are two main methodologies for functionalizing these surfaces, “grafting-to” and “grafting-from” approaches. Grafting-to involves tethering a polymer-brush to the metal surface directly; however, this method suffers from low packing density due to steric hindrances from grafted groups. Grafting-from involves first immobilizing a silane layer on top of the metal to provide a high density of functional groups for direct chain-growth polymerization. Previously, adsorption of end-functionalized PEG onto titanium metal allowed the surface to be non-fouling [63]. Using surface-initiated atom-transfer radical polymerization (SI-ATRP) oligo(ethylene glycol)methacrylate (OEGMA) has been grafted to gold surface modified with a thiol monolayer of α-bromo ester. Furthermore, poly(OEGMA) coatings have been successfully grafted to titanium substrates and have been subsequently modified for tethering to bioactive peptide sequences [64].

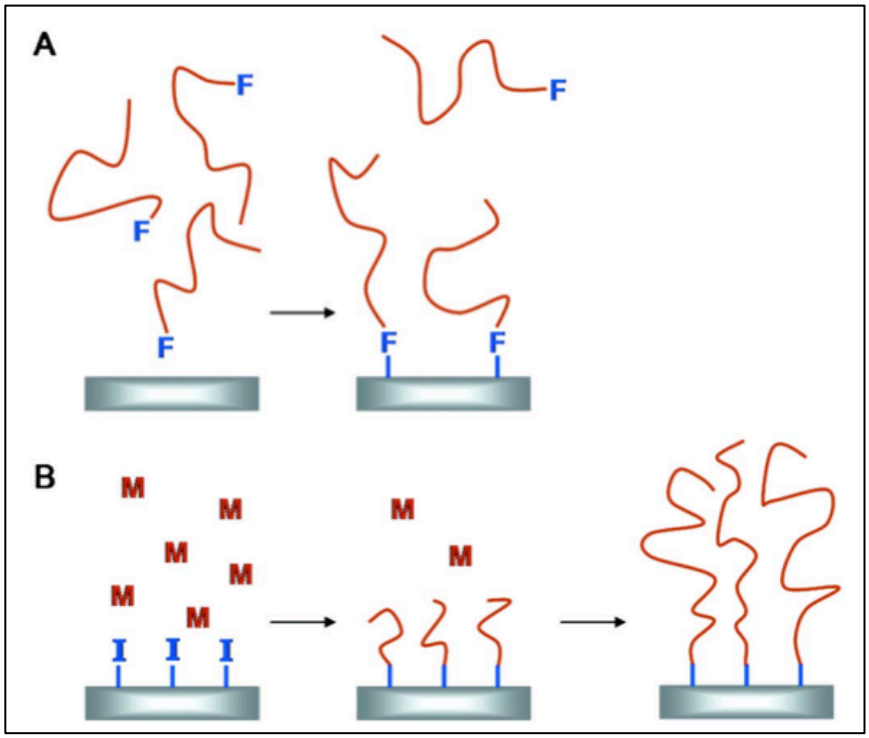

Figure 11. Grafting-to and Grafting-From. A) Grafting-to method; initially tethered polymer impedes further deposition, resulting in low-density of brushes B) Grafting-from method; initiator bearing substrate allows for high density of polymer brushes. Adapted from [65].

2.3.3 Hydrogels

Hydrogel technology has the ability to mimic the 3D architecture of the native ECM to control the function of cells and guide the spatially and temporally complex multicellular process of tissue repair and regeneration. There are two classes of hydrogels, natural and synthetic – each with their own advantages and disadvantages. Natural hydrogels such as collagen and alginate are derived from nature; therefore, they already present receptor-binding ligands and are subject to cell-based enzymatic degradation and modeling. However, there are issues with purification, immunogenicity, and pathogen transmission. Synthetic hydrogels on the other hand are engineered to

have specific structure-function relationships and can be fine-tuned to suit various biological applications via conjugation to bioactive molecules, adhesive moieties, and enzymatically degradable links. In terms of basic science research, synthetic hydrogels have been favored because of the ability to study single and multiple cell receptor-ligand interaction events in a highly empirical and step-wise fashion. For an excellent review regarding the use of ECM mimetic synthetic hydrogels, refer to [66].

2.5 Bio-inspired, Adhesive Materials: New Routes to Promote Tissue Repair and Regeneration

The ECM is naturally complex and presents to cells a myriad of signals that convolute analysis of various cell processes. Using simplified synthetic ECM-mimetic peptides, model surfaces can be constructed that present only a particular signal or adhesive motif. Some of the most prevalent adhesion motifs consist of arginine-glycine-aspartic acid (RGD) tri-peptide for fibronectin [67] and the tyrosine-isoleucine-glycine-serine-arginine (YIGSR) oligopeptide for laminin [68]. These short bioadhesive peptides have been tethered to both synthetic and natural surfaces, as well as three-dimensional scaffolds, to promote adhesion and migration in various cell types (as reviewed in [69-72]). In conjunction with these adhesive peptides, non-fouling, or protein “resistant” supports, such as poly(ethylene glycol), poly(acrylamide) and alginate, are often used to reduce non-specific protein adhesion and background adhesion. The density of tethered peptide is an important design parameter. Cell adhesion, focal adhesion assembly, spreading and migration [73-76], neurite extension and neural differentiation [77, 78], smooth muscle cell activities [79], osteoblast and myoblast differentiation [80-82], all exhibit peptide density-dependent effects. Also, tethering of bioadhesive ligands onto biomaterial surfaces and scaffolds also enhances *in vivo* responses, such as bone

formation and integration [64, 83], nerve regeneration [84, 85], and corneal tissue repair [86].

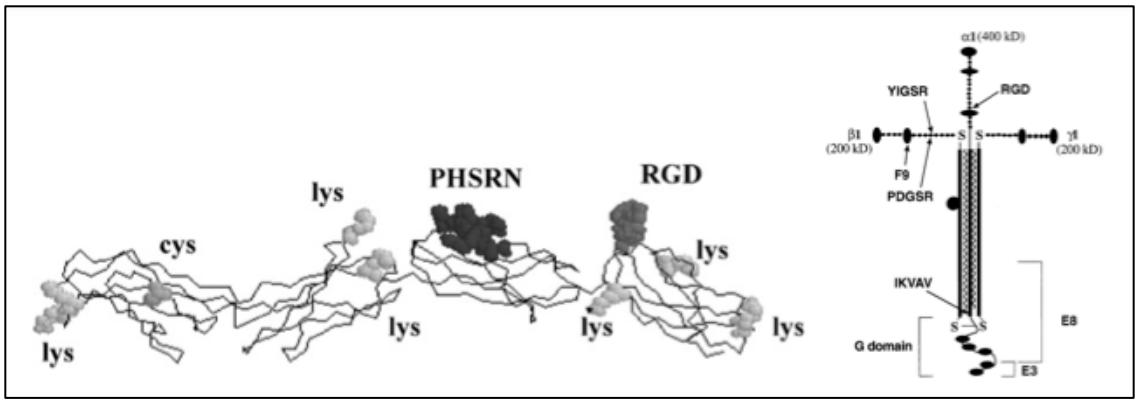

Figure 12. Schematic of RGD and YIGSR sites. A) Schematic diagram of RGD and synergy site PHSRN on the fibronectin III domain. B) Schematic diagram of YIGSR and RGD binding sites on laminin. Adapted from [87] and [88].

These results indicate that functionalization of biomaterials with short adhesive oligopeptides significantly enhances certain cellular activities. In addition, conveying biospecificity while avoiding unwanted interactions with other regions of the native ligand, short bioadhesive peptides allow facile incorporation into synthetic backbones and enhanced stability of the tethered motif. However, these strategies still have their limitations; namely, 1) low activity of oligopeptides compared to native ligand due to the absence of modulatory domains, 2) limited specificity for adhesion receptors and cell types, and 3) inability to bind certain receptors due to conformation differences compared to the native ligand [7]. Strategies to improve ligand activity include conformationally constrained peptides (e.g. cyclic), oligopeptide mixtures, and recombinant protein fragments spanning binding domains of native ligands [64, 89-93]. Also, self-assembling peptides reconstituting the triple helical structure of type I collagen

have been used to target collagen integrin receptors and promote enhanced osteoblastic differentiation and mineralization on biomaterial supports [94, 95]. The improved activity and selectivity of these materials result in enhanced cellular activities and *in vivo* responses [64, 96].

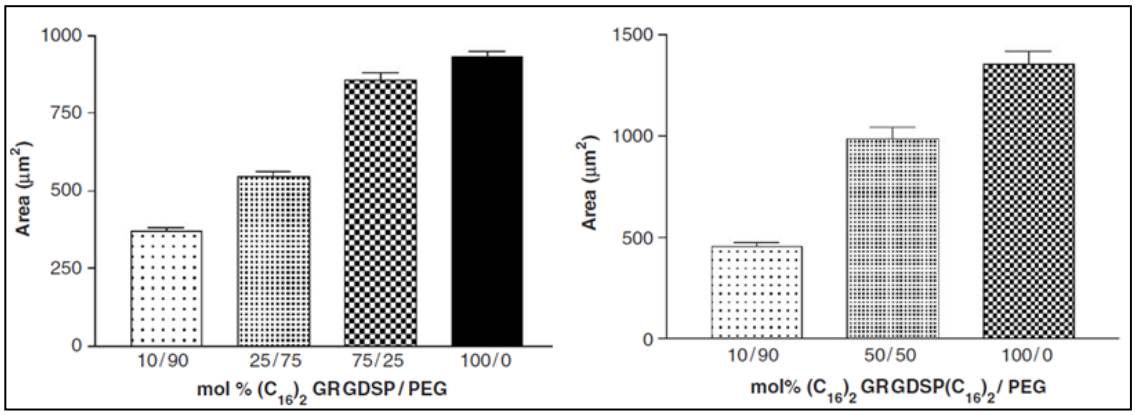

Figure 13. Dose-dependent Spreading on Linear vs. Cyclic RGD. Area of spread HUVEC to supported mixed monolayers of A) (C16)2GRGDSP and PEG and B) looped GRGDSP and PEG, after 60 min incubation at 37 1C in basal medium supplemented with 0.1% BSA (error bars represent S.E.M.). Adapted from [91].

2.6 Triggerable, Dynamic Biomaterials

The previous sections highlighted the importance of bioadhesive ligand presentation in terms of density and specificity. However, current approaches to ligand presentation often comprise of static, constant densities of ligands. In contrast, natural cell adhesive interactions with ECMs exhibit spatiotemporal patterns of binding and activation. Therefore, a key to future research in controlling cell-material interactions will be the development of materials that can respond to external stimuli. The following section presents both the model systems currently being employed and emerging technologies in this field.

There are many modalities to control the presentation of ligands on a biomaterial. Some of these methods include, electrochemical desorption, oxidative release, light controlled desorption, and enzyme controlled activation.

2.6.1 Non-Specific "On" Switches

Electrochemical desorption

Whitesides and co-workers, created a surface that could be used to screen drug candidates via controlling cell migration. Using microcontact printed (μCP) $HS(CH_2)_{17}CH_3$ and $HS(CH_2)_{11}(OCH_2OCH_2)_3OH(C_{11}EG_3)$ as a non-fouling barrier to protein adsorption, bovine capillary endothelial (BCE) cells were seeded and spread on the non-patterned regions. By applying a <-1.2V potential for 30 seconds, the complete desorption of these non-fouling SAMs occurred, and the BCE cells were allowed to migrate and proliferate [97].

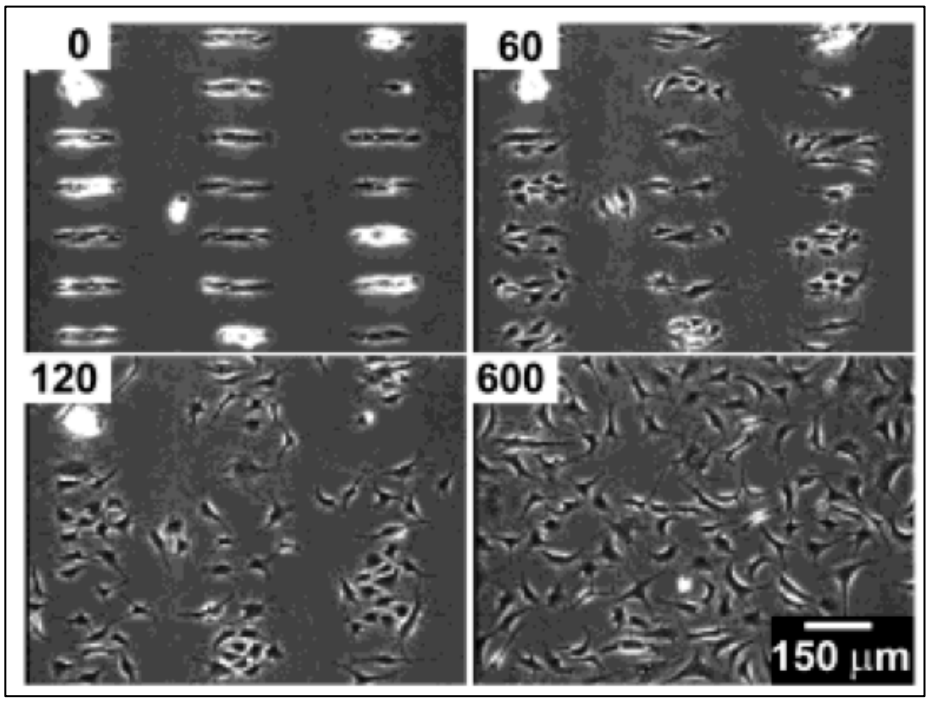

Figure 14. BCE Cells Spread on Patterned Surface with Non-Fouling Barrier C11EG3 and C18. Images show time-lapse after application of cathodic voltage pulse (-1.2V for 30s). The numbers indicate the time elapsed (in minutes) after the voltage pulse. Adapted from [97].

Oxidative Release

Wittstock and co-workers developed an oxidative release mechanism for oligoethylene glycol (OEG)-terminated thiol SAMs using ultra microelectrodes [98]. By generating Br_2 *in situ* using electrochemical processes, an OEG-terminated SAM was oxidized to a cell-adhesive state. This process still had shortcomings in patterning fidelity due to limiting factors of electrode size and diffusion of bromine away from the electrode. The newer method that has been employed by Wittstock and co-workers involves the use of scanning electrochemical microscopy (SECM) to generate bromine *in situ* [99].

Nishizawa and co-workers created a pretreated surface with cell-adhesion resistant bovine serum albumin (BSA) [100]. By the electrochemical generation of hydrobromic acid *in situ*, the BSA was removed, and other serum proteins from media were allowed to attach to the desorbed regions. Nevertheless, these methods also have the same problems as electrochemical desorption methods since they allow ECM proteins to adsorb, with little overall control of composition.

Photo-based Desorption

Light-based control schemes allow for the high resolution patterning of cells in culture in a highly spatially repeatable and specific manner. Strategies by Nakanishi et al were based on silane grafted SAMs containing a 2-nitrobenzyl group. A glass coverslip was modified with 1-(2-nitrophenyl)ethyl-5-trichloro silylpentanoate (NPE-TCSP) that contained nitrobenzyl ester group that could support the hydrophobic adsorption of non-adhesive BSA. Selective areas were irradiated with λ=365nm light, which converted exposed nitrobenzyl ester groups to carboxylic acid groups that could support fibronectin adsorption [101]. Using a photomask, this technology was able to form subcellular adhesive islands to study focal adhesion formation and cell migration [102]. While these surfaces have the added benefit of spatiotemporal control via UV irradiation, it still suffers from the same problems as the previous surfaces in that non-specific protein adsorption can still occur.

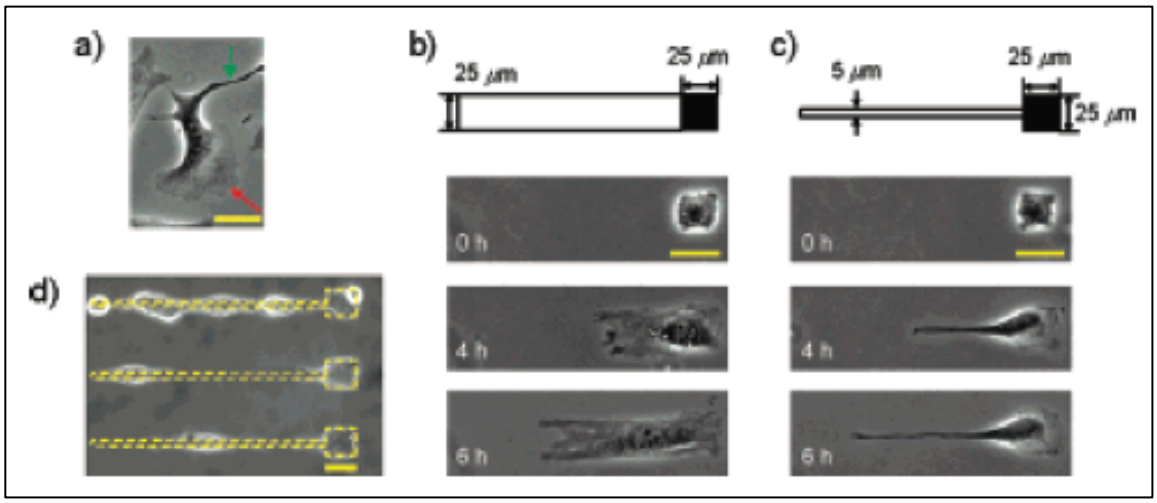

Figure 15. Selective Initiation of Two Different Characteristic Protrusions of NIH3T3s. A) Example of lamellipodia (*red*) and filopodium (*green*) on unpatterned fibronectin surface. B, C) Schematic of photopatterned desorption along with time-lapsed protrusion. D) Cell adhesion onto substrate with patterns illuminated simultaneously. Adapted from [102].

2.6.2 Integrin Specific "On" Switches

Photoactivation

Mrksich and colleagues have generated substrates that used a Diels-Alders reaction for the immobilization of peptide-diene conjugates on quinine-terminated SAMs [103]. The base substrate was a nitroveratryloxy-carbonyl (NVOC)-protected hydroquinone-terminated SAM (1%) with a tri(ethyleneglycol)-terminated alkanethiol background (99%). When selectively irradiated with λ=365nm for 2 minutes, the NVOC protecting group is cleaved, leaving a reactive hydroquinone that can be electrochemically oxidized to yield a benzo-quinone, which then reacts with a peptide-diene. This system allowed for the selective immobilization of cells via the RGD peptide.

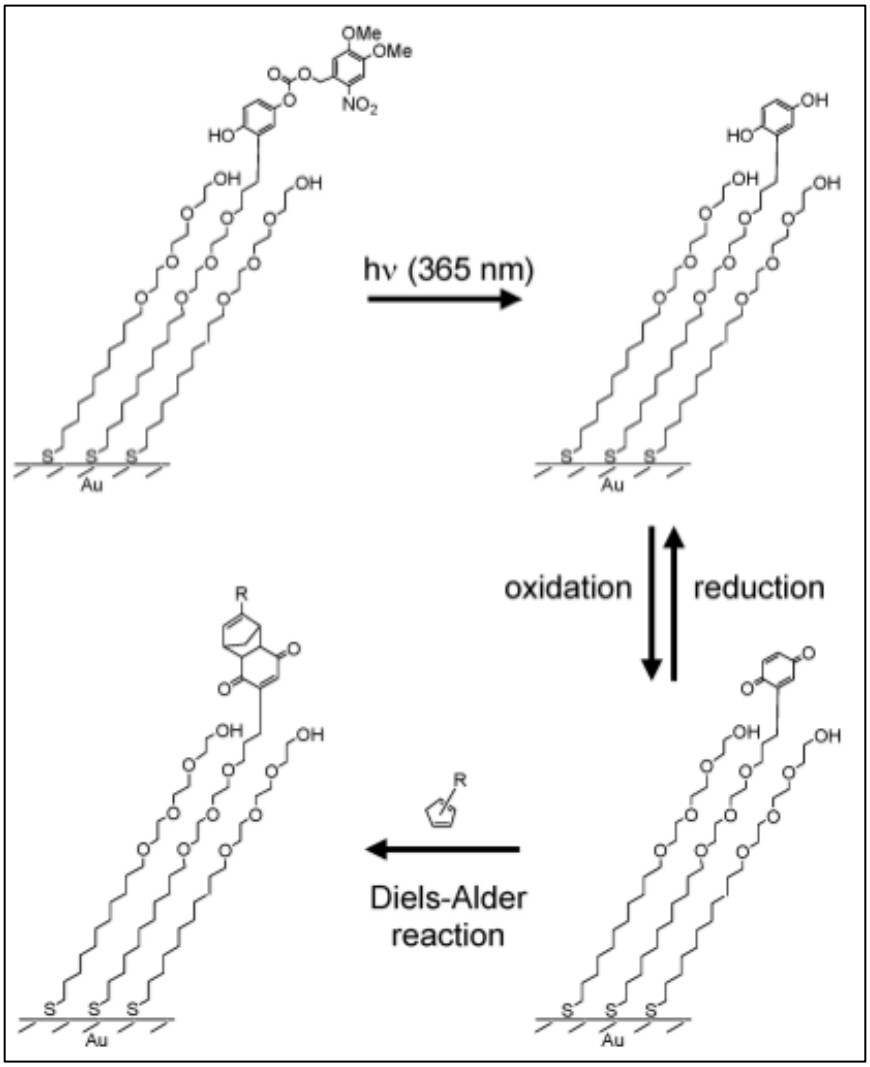

Figure 16. Strategy for Patterning Immobilized Ligands to a Self-Assembled Monolayer via NVOC-Protected Hydroquinone. Upon irradiation with UV-light (365nm), NVOC is cleaved leaving hydroquinone, which is reversibly oxidized to quinine. Quinone undergoes Diels-Alder reaction with cyclopentadiene conjugated ligand, immobilizing ligand on SAM. Adapted from [103].

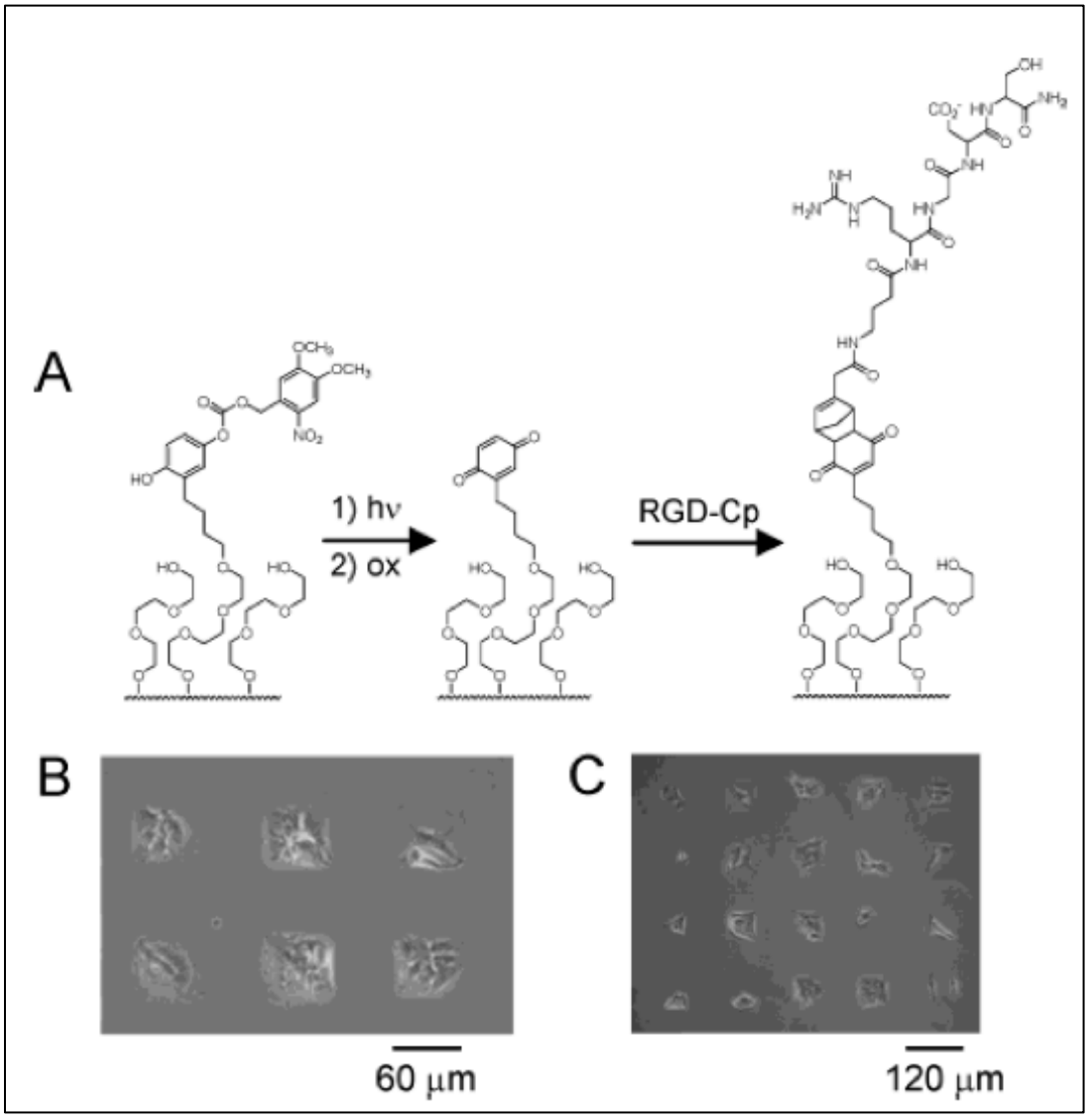

Figure 17. Photodeprotection/Diels-Alder Immobilization Strategy. A) Schematic of overall process flow. B,C) Swiss 3T3 fibroblasts attached to regions of substrate illuminated with UV-light, oxidized (+400mV, 15 sec), and then treated with RGD-Cp (5mM, 4hr). Adapted from [103].

Del Campo and co-workers have demonstrated photo-controlled cell adhesion to self-assembled monolayers via a caged-cyclic RGD containing peptide [104]. A photolabile caging group consisting of a 3-(4,5,dimethoxy-2-nitrophenyl)-2-butyl ester (DMNPB) is tethered to the carboxylic acid side chain of the aspartic acid residue. Upon

UV-irradiation at 361nm, the DMNPB group is cleaved effectively removing the cage, and leaving behind standard cyclic RGDfK. The caging groups mechanism of action has not been fully characterized, but it is possible that additional steric hindrance, conformation restriction or changes in the charge distribution of the peptide are responsible for blocking integrin-recognition.

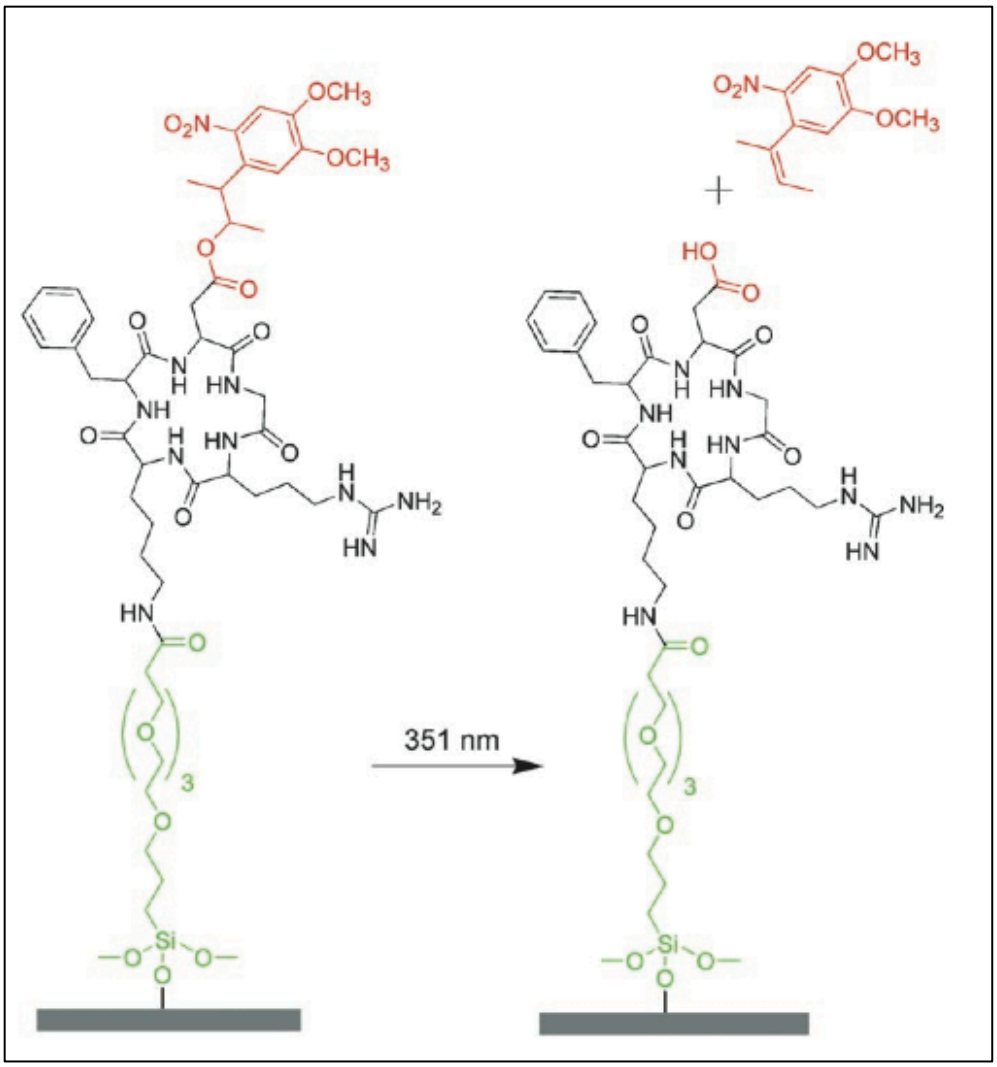

Figure 18. Caged-RGD Compound Immobilized to Surface. Chemical structure of cyclo[RGD(DMNPBfK)] (DMNPB in red) with TEG-based silane immobilization strategy (TEG in green). Upon UV-irradiation @ 365nm, DMNPB group is cleaved from aspartic acid residue, restoring bioactive cyclo(RGD). Adapted from [104].

2.6.3 Adhesion "Off" Switches

Electrochemical Off-switching

An improvement of Mrksich's NVOC system resulted in the generation of an electroactive quinone ester SAM that has a tethered RGD [105]. Upon electrochemical reduction (5min at 550 mV), the quinone forms a hydroquinone, which then performs a rapid cyclization, ultimately cleaving the RGD peptide. A further improvement allowed Mrksich to generate two different redox-active tethers based on the quinone ester and O-silyl hydroquinone which respond to -650mV and 650mV, respectively [106] . This allows for specific dynamic control of two different ligands on the same surface.

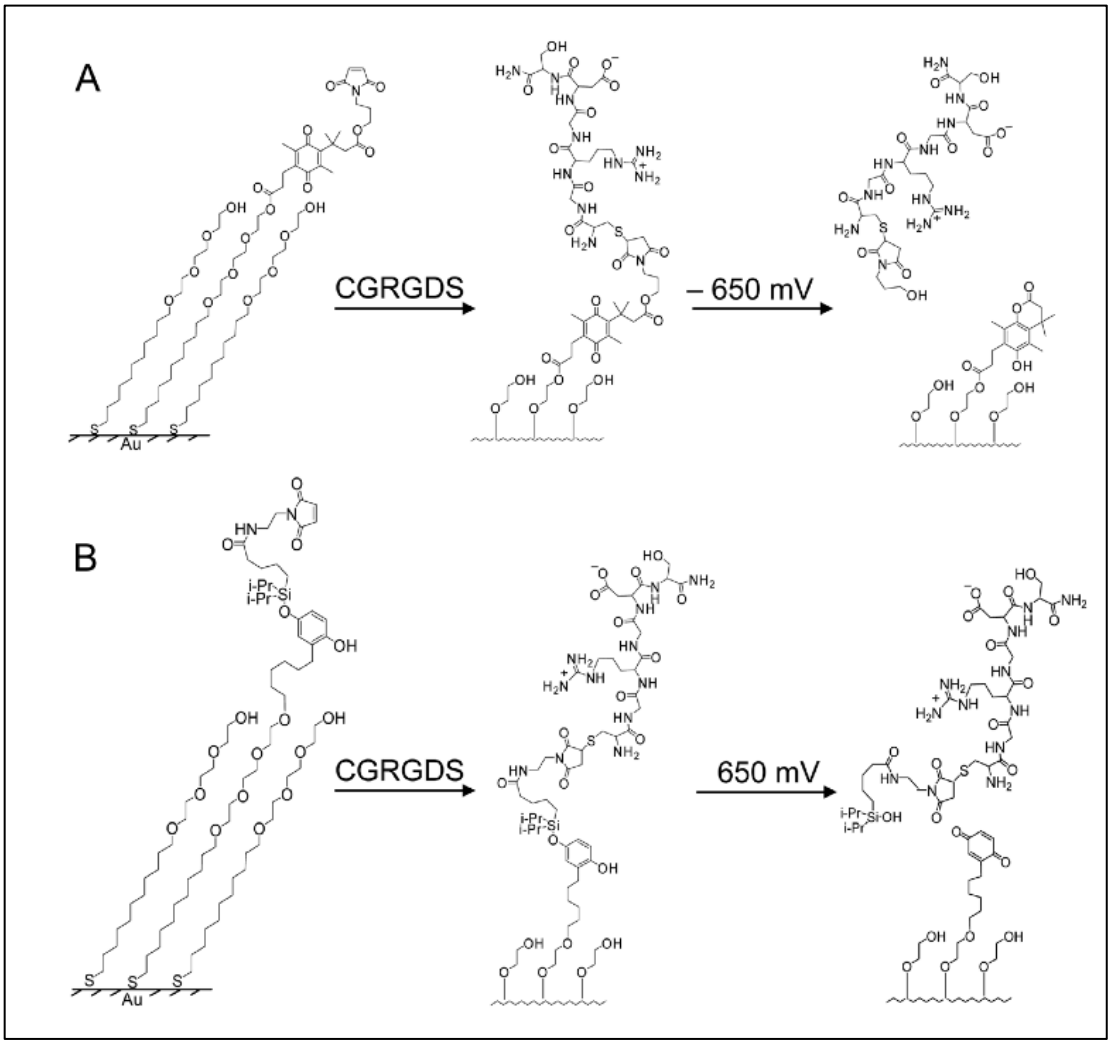

Figure 19. Molecular Strategies to Prepare Dynamic Substrates. A) Monolayer presenting maleimide tethered to electroactive quinine ester reacts with cysteine-terminated RGD peptides to immobilize the ligand, electrochemical reduction of quinine releases RGD ligand. B) Monolayer presenting a maleimide group tethered to an electroactive O-silyl hydroquinone is used to immobilize cysteine-terminated RGD, electrochemical oxidation releases RGD ligand. Adapted from [106].

Del Campo and colleagues have recently developed an intercalated 4,5-dialkoxy 1-(2-nitrophenyl)ethyl photolabile group that can be attached to free amine groups at the surface of a substrate via a carbamate bond [107]. A tetraethyleneglycol (TEG) spacer is

included in the structure in order to provide a protein- and cell-repellent surface before attaching bioactive ligands. A bioactive ligand, such as biotin or RGD oligopeptide, can be attached to the surface by reacting with the free amine at the end of the TEG spacer. When used in conjunction with amine-terminated SAMs, this methodology allowed for the removal of human umbilical vein endothelial cells from model surfaces using irradiation at λ=350. After 8 minutes of irradiation, 70% cleavage of RGD was attained. This system allows for the selective immobilization of a peptide containing a free carboxylic acid and its subsequent cleavage by UV irradiation.

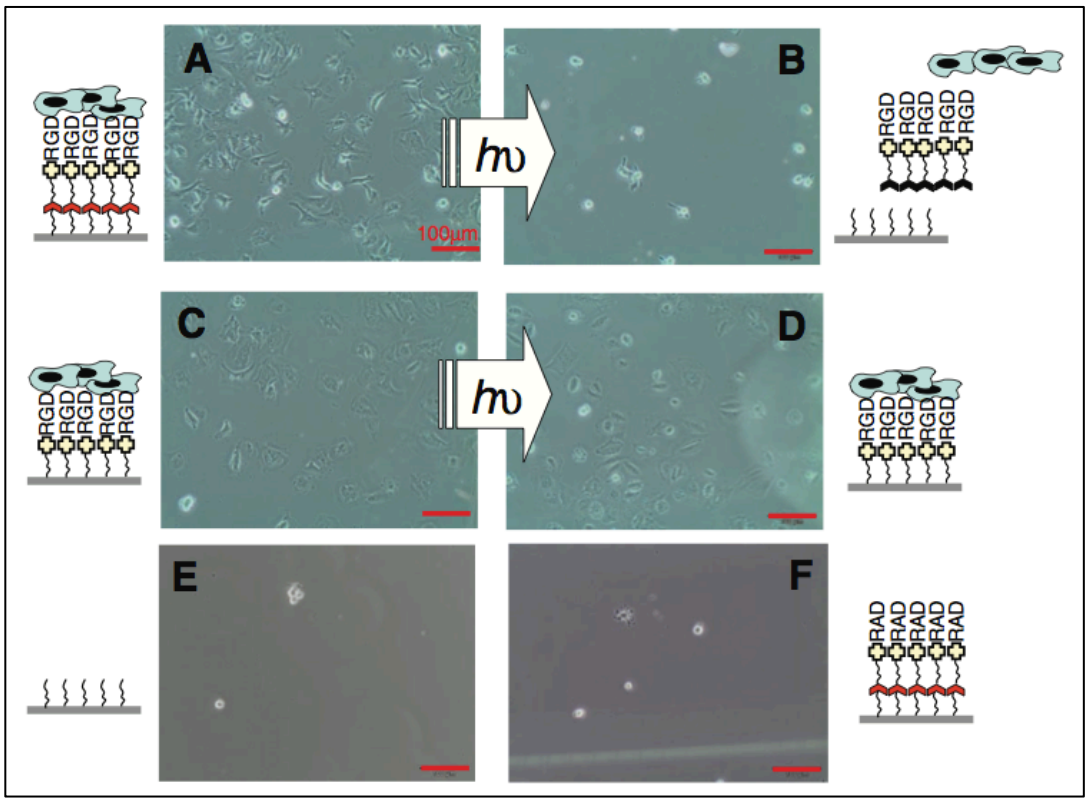

Figure 20. Schematic and Microscopy Images of Intercalated 4,5-dialkoxy 1-(2-nitrophenyl)ethyl Photolabile Linker. A, C) HUVECs attached to RGD immobilized onto photolabile linker and non-cleavable linker control, respectively. B, D) Resulting HUVEC detachment post UV-irradiation. E) HUVECs seeded 2hrs on amine-terminated SAM.

F) HUVECs incubated for 2hr on cyclo(RADfk) non-adhesive control coupled to amine-terminated SAM with linker. Adapted from [107].

2.6.4 Reversible Adhesion Switches

Reversible Photoactive Switching

Liu et al has demonstrated a switchable SAM system that can reversibly modulate RGD presentation [108]. This design employed an azobenzene unit that upon UV irradiation (λ=340-380nm) can be switched from a thermally stable E-isomer to the thermally unstable Z-isomer. Additional irradiation at λ=450-490nm reverts this SAM to its original E-state. When an RGD group is tethered to the end of this molecule, in the E-isomer form, the substrate supports cell adhesion, while in the Z-isomer form, cell binding is significantly attenuated. Using a similar method Kessler et al, used the switching from the E to Z-isomers directly to modulate the percentage of cells on the surface [109]. These methods, however, are potentially limited by damaging pre-adhered cells due to the UV wavelengths.

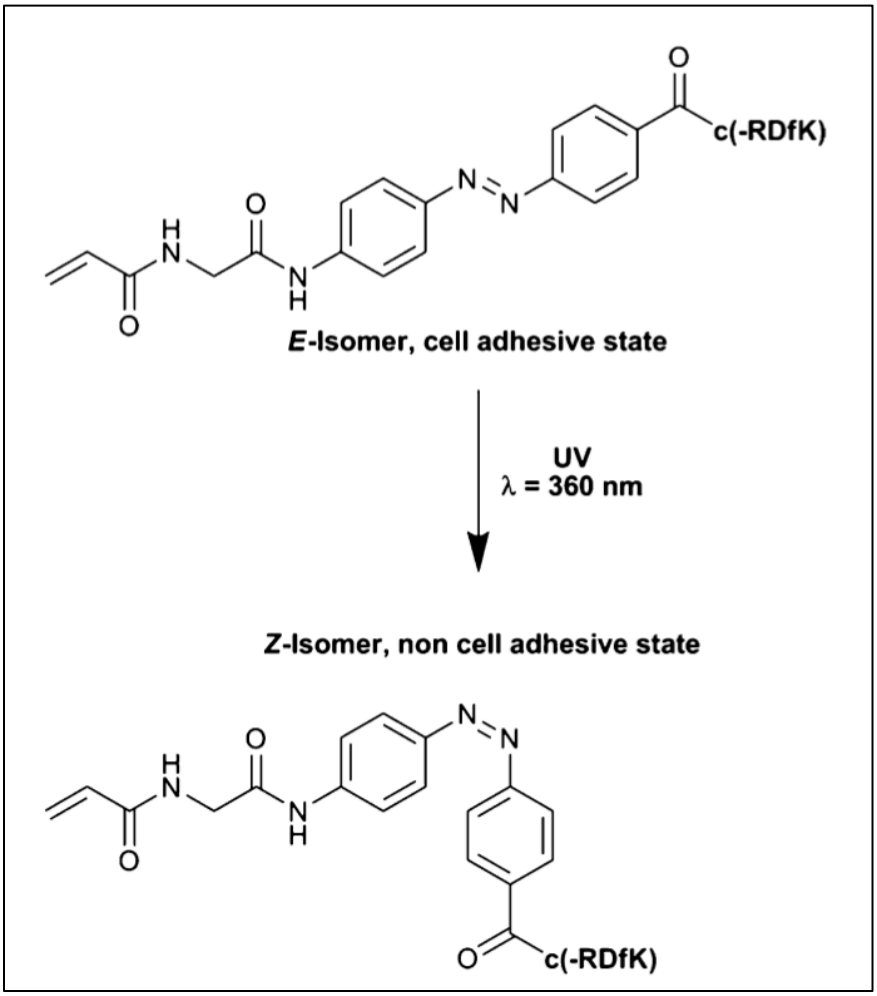

Figure 21. Cyclic RGD Peptide Presented on Photoswitchable 4-[(4-aminophenyl)azo]benzocarbonyl unit]. c-(RDfK) denotes cyclic(RGD) peptide. Adapted from [110].

Reversible Temperature-Based Switching

One of the most promising technologies to control the adhesion of cells and tissues to a substrate has been the temperature responsive polymer poly(N-isopropylacrylamide) (NIPAAm). This polymer that can be covalently tethered to cell culture surface, has the unique characteristic of being able to control protein adsorption based on temperature alone. At temperatures above the lower critical solution temperature (LCST) of 32°C, poly(NIPAMM) surfaces are hydrophobic and support the adsorption of proteins from serum and media, allowing cells to attach and proliferate. Upon, lowering the temperature below the LCST, the surface is rendered hydrophilic and causes a hydrated layer to form between the cell sheet and the culture surface [111]. This causes all cells and ECM components to detach from the polymer surface in a sheet, allowing for "cell-sheet" based tissue engineering. This technology has experienced great success in recent years and is currently being utilized in early phase clinical trials [112].

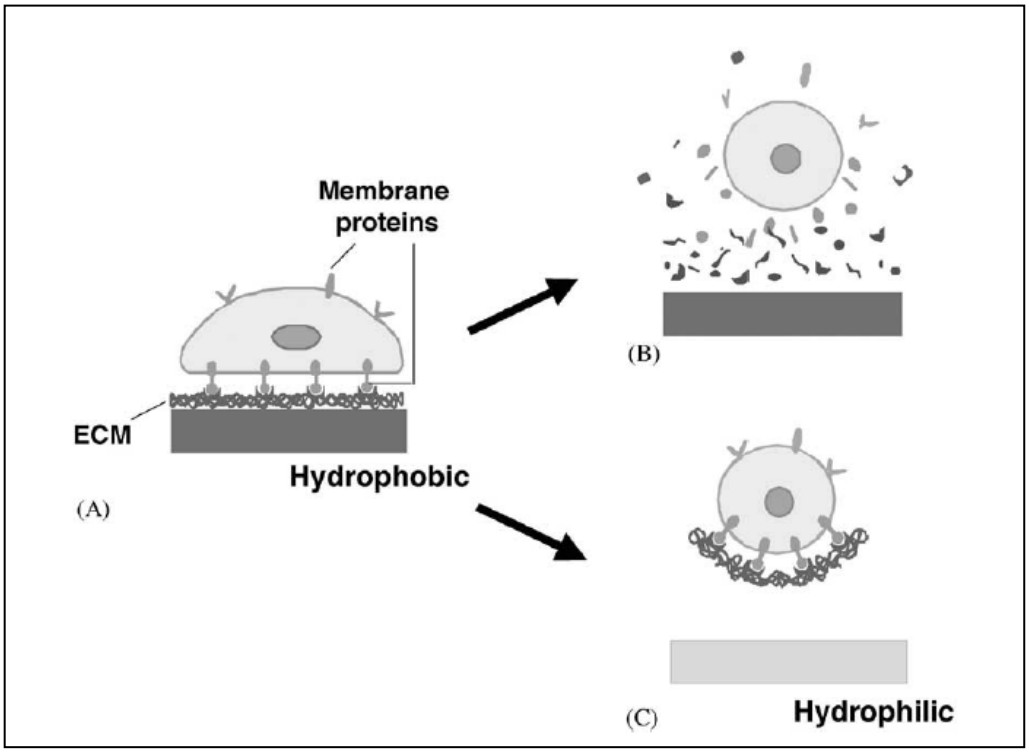

Figure 22. Cell Harvest Mechanism by Using Temperature-Responsive Culture Surfaces. A) Cells attach to hydrophobic surfaces via cell membrane proteins and adsorbed ECM proteins from serum. B) Enzymatic digestion of membrane and ECM components result in cell detachment. C) On poly(NIPAAm) surfaces interconnection between ECM and cells remained intact post-release. Adapted from [113].

2.7 The Multiple Post Array Deflection Substrate (mPADs)

Mechanotransduction has been implicated in many cell processes, from proliferation, differentiation, and cell fate [114]. Early studies attempted to modulate substrate rigidity by growing cells on collagen gels and polyacrylamide (PAA) gels. The first cell traction forces were reported by cells on silicone substrates [115]. Cells spread on these substrates, wrinkle the silicone membrane, and these wrinkles were deconvoluted into strain fields. Later, investigators tried to improve on these approaches by embedding aligned arrays of fluorescent markers to monitor the deformation of

membranes, or used cantilever systems to monitor cell traction forces [116, 117]. All these systems are not amenable to measuring discrete cell traction forces on a surface. The multiple post array deflection substrate allows for the highly defined monitoring of cell traction forces in live-cell applications with the added ability to decouple surface rigidity from cell traction force [118]. The general schematic of mPAD behavior is shown below in Figure 23.

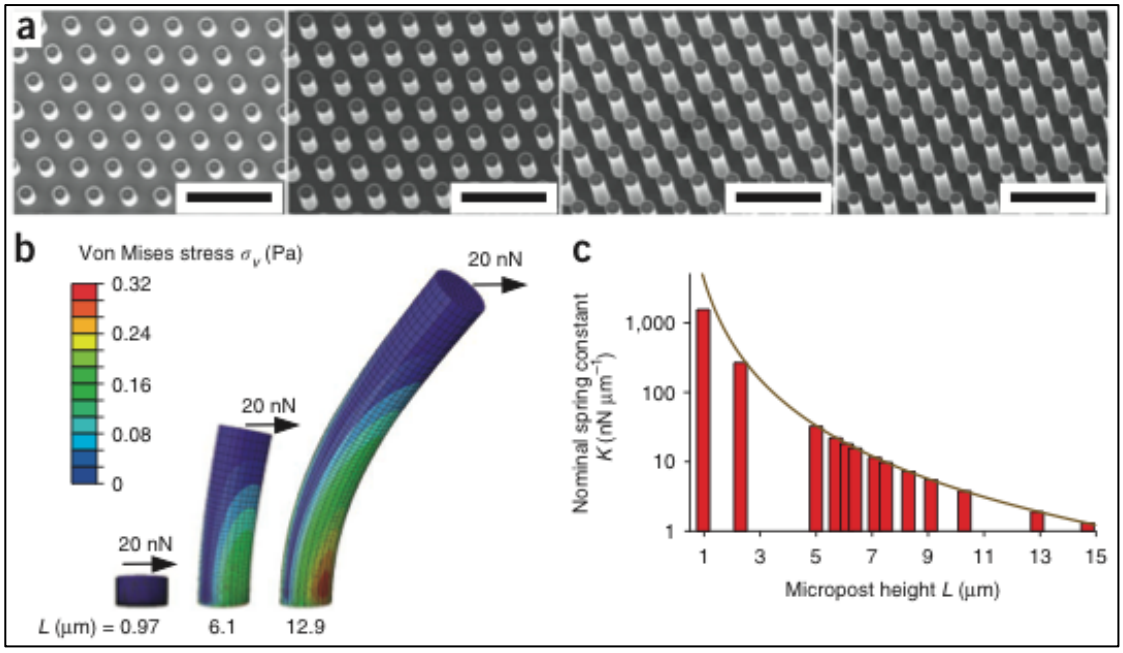

Figure 23. Characterization of mPAD Masters and Substrates. A) SEM images of silicon masters. B) FEM simulation of von Mises stresses on posts of different heights. C) Nominal spring constant of posts of different height. Adapted from [119].

2.8 Summary of Background

In summary, controlling cell-adhesive interactions is paramount to the study of cell mechanical signaling. Cell-matrix interactions rely on specific interactions with either the native or synthetic ECM. This ECM is comprised of various biomolecules including proteins. Proteins are biomolecules with complex structure and can modulate function and activity of biological systems. Engineering surfaces with simplified protein sequences allows for an empirical approach to decoding these complex cell-material interactions. Through the rational design of material surfaces, protein adsorption and receptor-ligand interaction can be tightly controlled both spatially and temporally. Because of this level of control, researchers have begun unraveling the complex symphony of signals for cellular events such as adhesion and cell spreading.

Cell-material interactions are primarily mediated by receptor-ligand interactions between adsorbed or covalently bound ligands to a surface and cell receptors called integrins. Integrin mediated signaling has been implicated in many cellular processes ranging from adhesion, migration, growth, secretion, gene expression, and apoptosis. These adhesive interactions also regulate cellular and host responses to implanted biomedical devices, tissue-engineered constructs, and biotechnological systems. It is increasingly evident that mechanotransduction between cells and their environment regulates gene expression, cell fate, and even malignant transformation.

The cell adhesion cascade involves initial attachment, integrin recruitment and spreading, integrin clustering and focal adhesion formation, and contractile force generation via cytoskeletal interactions. Cell adhesion to native ECM components, such as fibronectin and laminin, is mediated by the activation and mechanical coupling to

integrins. Bound integrins rapidly associate with the actin cytoskeleton and cluster to form focal adhesion complexes.

Model surfaces have been created to explore in-depth specific mechanisms for cell adhesion and spreading to various peptide sequences and adhesive proteins. Simplified protein sequences such as RGD and YIGSR tethered to both synthetic and natural surfaces in order to study the effects of a single protein motif. Dynamic biomaterials can modulate the spatiotemporal presentation of these motifs through electrochemical, enzyme and light controlled modalities. The development of additional dynamic biomaterials is critical to unraveling the complex adhesive interactions between cells and surfaces. Applications of adhesive control in three-dimensions and in *in vivo* applications will undoubtedly provide key insights into cellular behavior in more complex ECM constructs and may also provide new avenues for clinical therapies and treatments.

CHAPTER 3

AIM 1: *IN VIVO* TRIGGERABLE LIGAND PRESENTATION USING CAGED-RGD PRESENTING HYDROGELS

3.1 ABSTRACT

PEG-based hydrogels provide a novel platform to elucidate cell-ECM interactions through a highly defined, non-fouling surface. Through the use of simplified ECM-peptides such as RGD, specific integrin-ECM interactions can be studied. We have demonstrated the uses of a novel caged-RGD molecule that can be activated by UV irradiation in the context of PEG-based hydrogels. Delayed activation of caged-RGD presenting hydrogels, via transdermal irradiation was able to modulate macrophage recruitment and downstream fibrous capsule formation in subcutaneously implanted PEGDA-based hydrogels. When applied to PEG-maleimide based hydrogels, caged-RGD was effective at controlling *in vitro* cell outgrowth into a degradable hydrogel with protease sensitive crosslinks. In an *in situ* polymerized subcutaneous model, caged-RGD was effective at controlling vasculogenesis through the modulation of RGD presentation via transdermal UV irradiation. Therefore, we demonstrate that caged-RGD in conjunction with PEG-based hydrogels is a versatile platform that offers unparalleled spatiotemporal control of RGD ligand presentation. Through UV-activation we demonstrated that ex vivo control of RGD-mediated cell adhesion is a critical regulator of many events including inflammation and vasculogenesis. We show that that caged-

compounds provide a versatile and effective means of controlling the presentation of signals and ligands in both *in vitro* and *in vivo* systems.

3.2 INTRODUCTION

Fibrous capsule formation has long been an undesirable inflammatory response to implantable medical devices. Immediately following implantation, proteins and other biomolecules quickly adsorb to the surface of an implant, creating a surface rich for inflammatory cell adhesion and activation [120]. The inflammatory cascade that begins with neutrophil and macrophage recruitment and activation, followed by foreign body giant cell response and fibroblast-based fibrosis, results in the formation of a dense collagen matrix around the implant [120]. This natural barrier, between the host tissue and the implant surface, is a critical limiter of device performance and engraftment in a variety of applications ranging from implantable sensors to cosmetic applications [121, 122]. Although studies have attempted to elucidate methods of abrogating fibrous capsule formation through the use of specialized materials, surface coatings, and drug eluting polymers, until now there have been few ways to study the effects of time-dependent regulation of integrin-ligand based cell adhesion on downstream inflammatory pathways.

Integrin-mediated cell adhesion to the ECM is essential for the maintenance and repair of tissues by providing both mechanical anchorage, and biochemical cues that direct cell survival, migration, cell cycle progression, and the expression of differentiated phenotypes [8, 9]. Abnormalities in adhesive interactions have also been implicated in pathological states, including blood clotting, wound healing defects, and malignant tumor formation [14, 15]. Inflammatory cell adhesion to ECM components, specifically integrin mediated binding to adhesive extracellular ligands, are responsible for regulating cellular

and host responses to implanted biomedical devices, tissue-engineered constructs, and biotechnological systems [7]. These ligands can be adsorbed from solution blood, plasma, or serum; secreted and deposited onto the biomaterial surface by cells; or specifically engineered onto a biomaterial interface. All of these interactions are highly dynamic, and the dominant adhesive mechanism could vary over time and is often different among cell types. In platelet aggregation, the platelet integrin $\alpha_{IIb}\beta_3$ (GPIIb/IIa) binds to several ligands such as fibrinogen, von Willebrand factor, and fibronectin [6]. This receptor is the essential mediator of initial events in the blood-activation cascade after blood as come into contact with a synthetic material [45, 46]. Leukocyte-specific β_2 integrins, such as $\alpha_M\beta_2$ (Mac-1), mediate monocyte and macrophage adhesion to various ligands, including fibrinogen, fibronectin, IgG, and complement fragment iC3b. These receptors all play central roles in inflammatory responses *in vivo* [47, 48]. Binding of $\alpha_M\beta_2$ integrin to fibrinogen P1 and P2 domains exposed upon adsorption to biomaterial surfaces controls the recruitment and accumulation of inflammatory cells on implanted devices [49]. This integrin also plays a critical role in macrophage adhesion and fusion into giant foreign-body cells [48, 49].

Clearly, cell-material interactions are governed by a complex symphony of integrin-ligand binding and downstream signaling events that that act in a coordinated time-dependent manner. Thus, controlling specific cell-matrix interactions is essential to unraveling these complex interactions [17-22]. Synthetic hydrogels can be engineered to elicit specific structure-function relationships and can be fine-tuned to suit various biological applications via conjugation to bioactive molecules, adhesive moieties, and enzymatically degradable links [66]. These ECM-mimetic matrices have been popular because of the ability to study single and multiple cell receptor-ligand interaction events in a highly empirical and step-wise fashion. In this study, poly(ethylene glycol)-based

hydrogels are used as a “clean-slate” model surface that is highly resistant to non-specific protein adsorption, cell adhesion, and signaling [52, 53].

Using simplified synthetic ECM-mimetic peptides, model surfaces can be engineered to present only a particular signal or adhesive motif, such as arginine-glycine-aspartic acid (RGD) tri-peptide for fibronectin [67]. These short bioadhesive peptides have been tethered to both synthetic and natural surfaces, as well as three-dimensional scaffolds, to promote adhesion and migration in various cell [69-72]. These ligands also enhance *in vivo* responses, such as bone formation and integration [64, 83], nerve regeneration [84, 85], and corneal tissue repair [86].

Traditional investigations of cell-matrix interactions, however, have often relied on static ligand presentation; in contrast, natural cell adhesive interactions with ECMs exhibit spatiotemporal patterns of binding and activation. Nevertheless, recent advances have resulted in a new class of “dynamic” biomaterials that provide triggerable, real-time control of mechanical and biomolecular cues in response to external stimuli. These materials can be triggered by changes in temperature, pH, chemical concentration, light, and electrical field [104, 123-125].

Previously, it has been shown the adhesive sequence RGD (arginine-glycine-aspartic acid) has the ability to modulate inflammatory response as measured by cytokine production and downstream fibrous capsule formation [126]. Also it has been shown that the RGD ligand is required for *in vivo* vasculogenesis into VEGF-presenting degradable hydrogels. In this study, we used a novel UV-labile DMNPB-“caged”-cRGD(fk) [104] to demonstrate *in vivo* control of biomaterial implant associated inflammation, as measured by fibrous capsule formation, immunohistochemistry, and quantitative *in vivo* reactive oxygen species imaging, and also cell infiltration into implants via whole-mount fluorescence imaging.

3.3 RESULTS AND DISCUSSION

3.3.1 Synthesis of PEG-Conjugates and Fabrication of PEGDA Hydrogels

We have engineered poly(ethylene glycol) di-acrylate (PEGDA) based hydrogels that have covalently tethered adhesive ligands on the surface. The first step in the generation of adhesive PEGDA hydrogels is the synthesis of "adhesive ligand"-poly(ethylene glycol)-acrylate derivatives (Figure 24, B). Acrylate-PEG-SVA contains a NHS ester that is readily displaced by the free amine in any peptide in 50mM sodium bicarbonate solution (pH 8.2). RGD and caged-RGD derivatives were synthesized. These PEG-conjugates were then dialyzed and lyophilized to obtain a stable solid. Successful functionalization of the Acrylate-PEG-caged-RGD and Acrylate-PEG-cyclic(RGD) were confirmed using MALDI mass spectrometry; and, the overall increase in molecular weight of the product is consistent with the tethering of the adhesive ligands (Figure 24, C).

The detailed fabrication protocol can be found in Figure 25. The final hydrogels are cast in sterilized silicon grommets affixed to glass surfaces treated with Sigmacote (to facilitate mold release). In the interest of using the minimal amount of caged-RGD, we first create the bottom bulk 10% (w/v) PEDGA hydrogel, using a combination of PEGDA and UV-activated BASF (Ciba) Irgacure 2959 crosslinker. A Sigmacote treated coverslip was then placed on top of the mold to generate a flat disk. After UV-based free radical crosslinking, coverslip was removed from the bulk PEGDA gel. At this point the bulk gels were ready for a separate layer of functionalized PEGDA hydrogel (Figure 24, D-E). We cast a thin layer of functionalized gel (8% PEGDA (w/v) and 2% (w/v) PEG-conjugate) on top of the PEGDA bulk gel because we are only interested in studying the tissue/implant interface at the top functionalized surface. The bulk portion

of the gel primarily serves to increase ease of handing during surgical implantation. However, this caged-RGD was UV labile at the wavelength required for photopolymerization; therefore, the functional layer crosslinked via TEMED/APS chemistry to preserve the intact caging group.

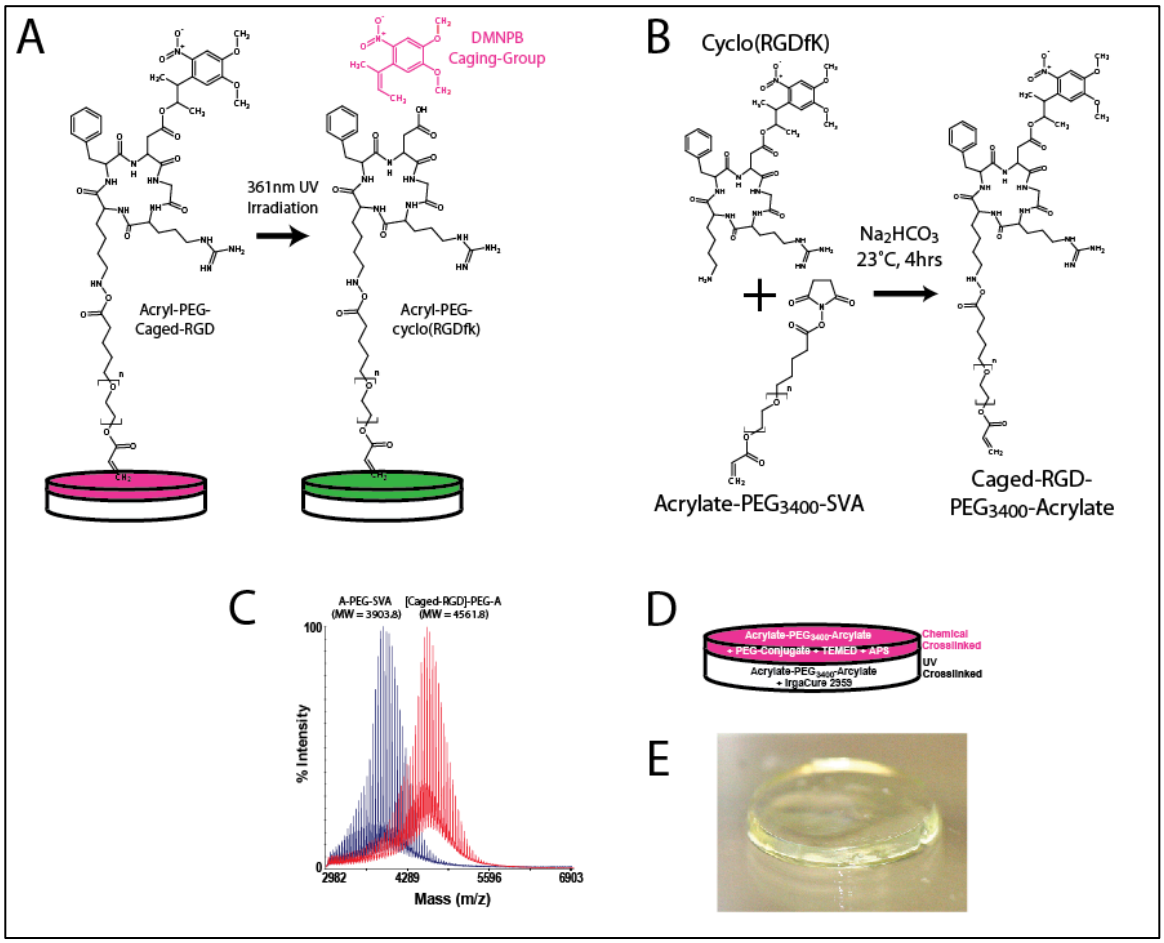

Figure 24. PEGDA-based Caged-RGD Hydrogels. A) Acryl-PEG-Caged-RGD tethered to Acryl-PEG-Acryl Hydrogels; red hydrogel denotes "caged" RGD molecule, green hydrogel denotes "uncaged" RGD molecule on surface. **B)** Reaction Scheme for tethering Caged-RGD molecule to Acryl-PEG-SVA (NHS ester terminated). **C)** MALDI-MS curves showing successful tethering of Caged-RGD to PEG-Acryl, forming Caged-RGD-PEG-Acryl. **D)** Overall schematic of hydrogel layering. **E)** Photo example of two-layer hydrogel.

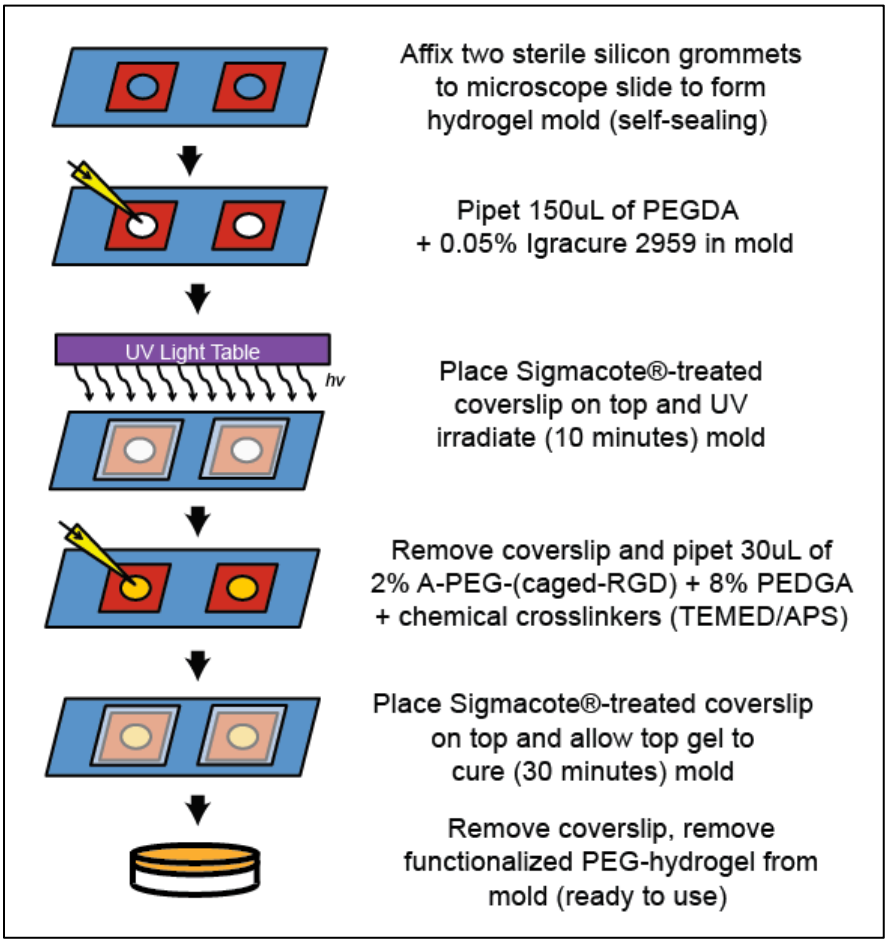

Figure 25. Fabrication Schematic for Caged-RGD Presenting PEGDA Hydrogels.

3.3.2 Caged-RGD Presenting Hydrogels Modulate Cell Adhesion and Spreading

In vitro characterization of functionalized hydrogels was completed using NIH3T3 fibroblasts in a 24hr cell adhesion and spreading assay (Figure 26). PEGDA, RDG (scrambled, inactive peptide), and linear(RGD) controls were compared to unexposed and exposed caged-RGD gels. NIH3T3s cells were seeded at 20k/cm^2 density, and allowed to spread overnight, washed to remove minimally attached and dead cells, and then treated with Calcein-AM/ethidium homodimer I (live/dead) stain. Calcein signal indicates that even on the non-adhesive controls the cells were still alive. The lack of

ethidium homodimer II positive staining is not surprising because all the dead and minimally adherent cells would have been removed during washing.

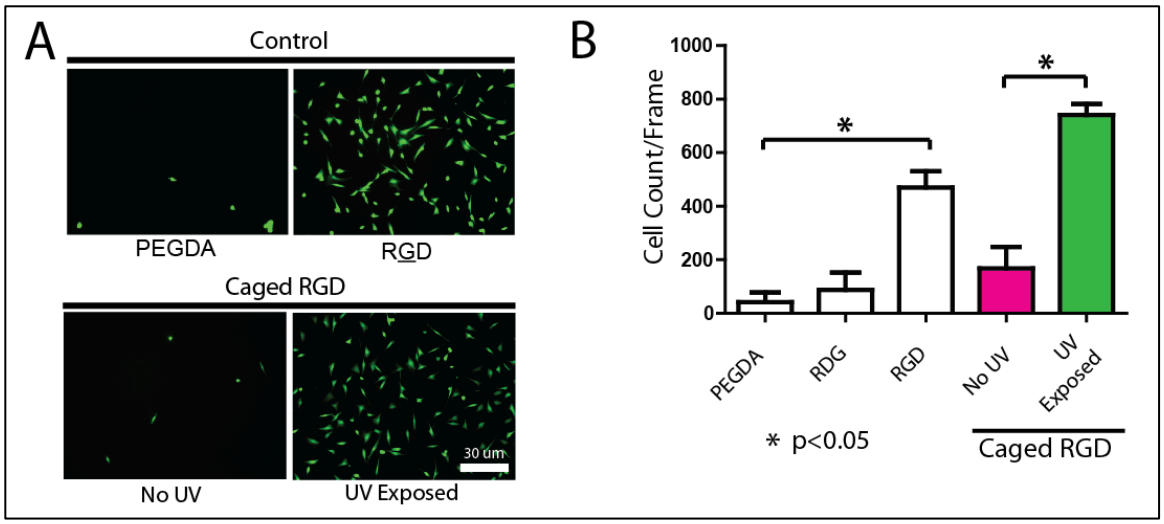

Figure 26. Caged-RGD Modulates Cell Adhesion and Spreading to PEGDA-based hydrogels. A) NIH3T3 24hrs post seeding on various conditions. Not exposed caged-RGD presenting hydrogels show similar cell adhesion and spreading as the PEGDA and RDG non-adhesive controls. Exposed caged-RGD and RGD positive control support cell adhesion and spreading. Live/dead stain; Calcein AM (*green*) and ethidium homodimer II (*red*). B) Quantification of cell attachment to functionalized PEGDA hydrogels.

Low levels of NIH3T3 fibroblast spreading were observed in the PEGDA, RDG, and "No UV" caged-RGD conditions. The cells that attached to these surfaces were largely rounded or bipolar in morphology indicating poor adhesion to surface by lack of adhesive ligands. High levels of adhesion and spreading were observed in the RGD and "UV Exposed" caged-RGD conditions (Figure 26, A). These cells exhibited normal spreading morphology and were well spread. There was no statistical difference in cell density in controls PEGDA and scrambled peptide RDG (Figure 26, B), which is expected due to the lack of adhesive ligands. Also, this validates the non-fouling nature

of PEG surfaces, where adhesive proteins from serum are unable to adsorb and facilitate cell attachment. There was a statistical difference between the “No UV” and “UV Exposed” condition, showing that caged-RGD was effective in controlling cell adhesion/spreading through controlling RGD ligand presentation in the presence/absence of UV irradiation. Another important conclusion was that poor adhesion and spreading on the “No UV” caged-RGD conditions confirm that the DMNPB caging group was not compromised while incorporating the Acrylate-PEG-caged-RGD conjugate into the PEGDA gel via free radical crosslinking.

3.3.3 *In vivo* Subcutaneous Model for Caged-RGD/fluorescein Hydrogels

The subcutaneous implantation of hydrogels in Balb/c mice was performed via the schematic described in Figure 27. All procedures were approved by the Georgia Tech Institutional Animal Care and Use Committee. First, incisions were made left and right proximal of the dorsum. Hemostats were used to create a subcutaneous pocket, ensuring the subcutaneous space was large enough to accept the hydrogel implant. The hydrogel was implanted, and wound clips were used close the wound. Wound clips were taken off at Day 10. Mice were single housed to prevent biting and reopening of wound. At designated time points, UV lamp-based 361nm UV irradiation was performed on each implant while mice under anesthesia. For the Day 0 condition, mice were exposed to UV irradiation immediately after closure of wound clips.

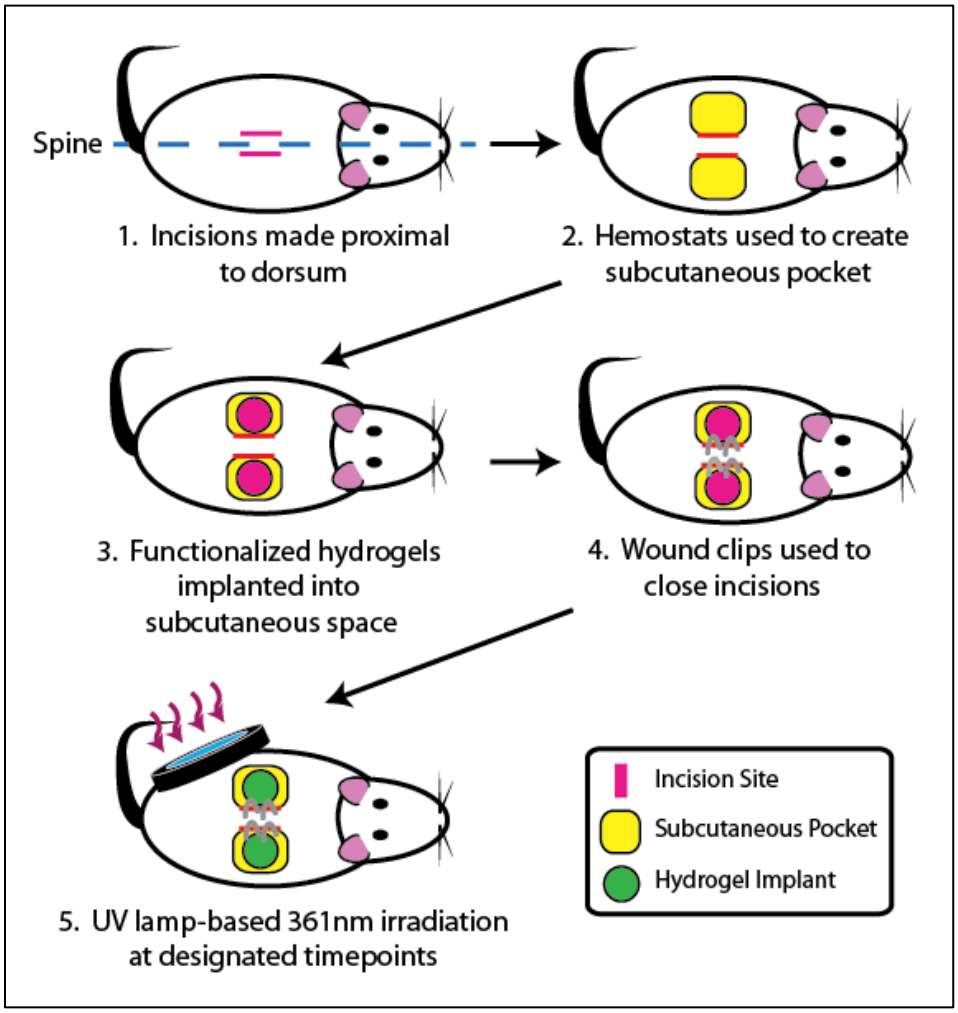

Figure 27. Subcutaneous Implantation of Pre-cast PEDGA Hydrogels. Incisions are made on dorsum of mouse, just proximal to spine. Hemostats are used to create subcutaneous pocket. Functionalized hydrogels are implanted. Wound clips are used to close incisions. UV lamp-based 361 nm irradiation at designated timepoints is used to transdermally activate hydrogels.

3.3.4 *In vivo* Uncaging Efficiency Validated Using Caged-fluorescein

In order to validate the efficacy of transdermal uncaging, Caged-fluorescein functionalized hydrogels were used to characterize the transdermal *in vivo* un-caging efficiency of the DMNPB group. The tethering scheme and mechanism of action is illustrated in Figure 28.

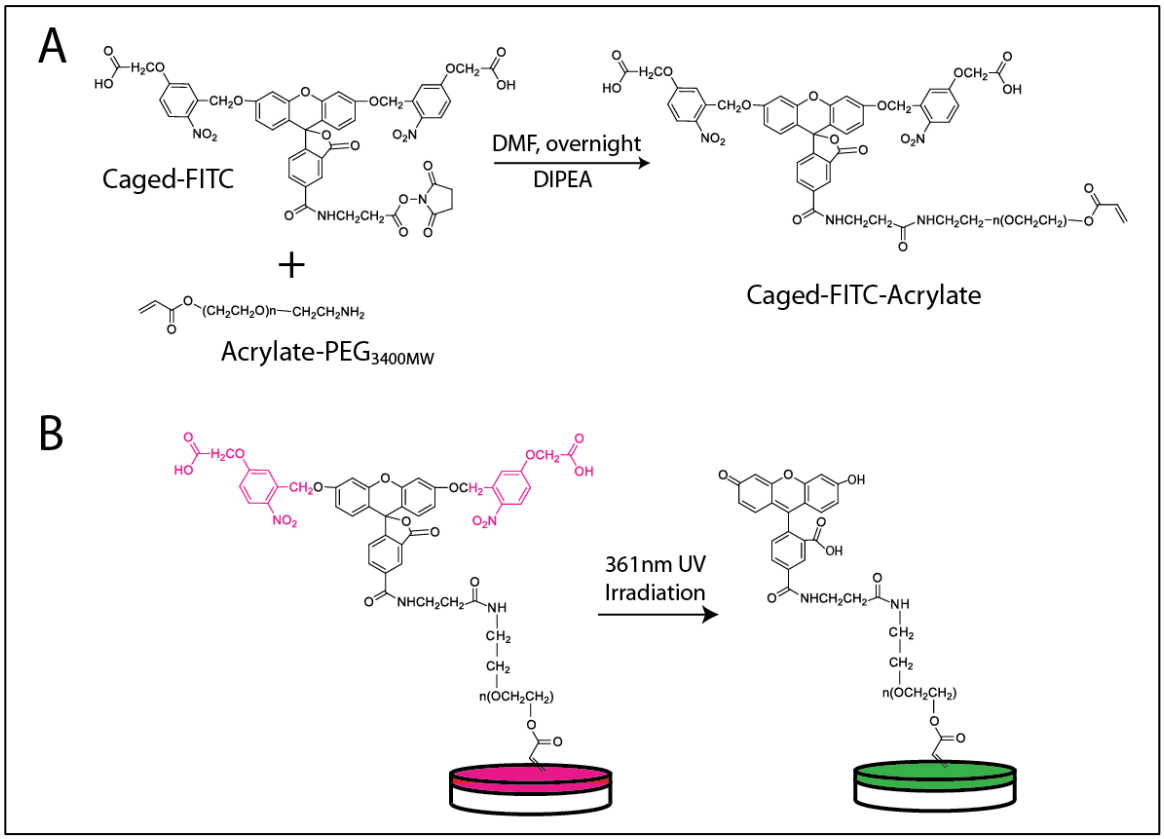

Figure 28. Schematic of Caged-fluorescein-Acrylate Synthesis and Mechanism of Action. A) Caged–fluorescein is reacted with a PEG-Acrylate in DMF and DIPEA overnight to yield caged-fluorescein-acrylate. B) Schematic representation of caged-fluorescein conjugated to PEGDA hydrogels. Upon 361 nm irradiation the caging groups (*red*) are cleaved.

Caged-fluorescein hydrogels and blank PEDGA controls were fabricated (Figure 29, A) and implanted subcutaneously in Balb/c mice. All implants were irradiated using a UV-lamp with bandpass filter at 361nm. After designated takedown points of one week and two weeks, explants were whole-mount imaged using an epifluorescent microscope. For the 7-day explant condition, PEGDA, and caged-fluorescein gels were implanted, and half of the caged-fluorescein gels were irradiated immediately following

implantation. For the 14-day takedown condition, PEGDA, caged-fluorescein, and pre-exposed caged-fluorescein hydrogels were implanted in Balb/C mice.

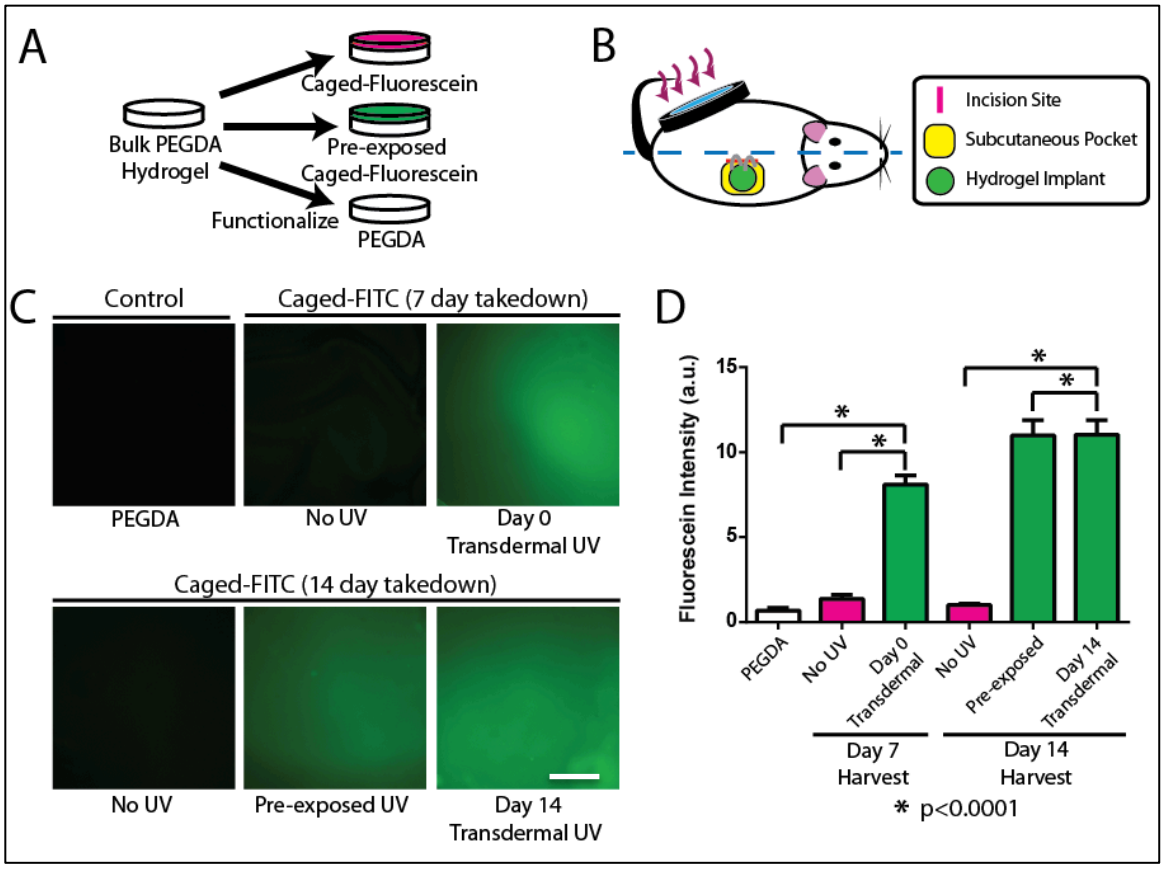

Figure 29. *In vivo* Characterization of Caged-fluorescein. A) Schematic of PEGDA hydrogel functionalization for caged-fluorescein characterization. B) Schematic of subcutaneous implantation of caged-fluorescein presenting hydrogels and subsequence 361nm UV irradiation. C) Whole-mount explants of caged-fluorescein implants at designated takedown points. Blank PEGDA control has minimal fluorescence signal similar to the 7-day takedown and 14-day takedown "No UV" conditions. 7-day takedown "Day 0 Transdermal UV", 14-day takedown "pre-exposed UV" and "Day 14 Transdermal UV" conditions all exhibit strong fluorescein signal. Scale bar 1mm. D) Quantification of fluorescein signal of hydrogel explants at designated takedown points. Uncaged conditions exhibit strong fluorescein signal when compared to unexposed conditions and PEGDA control. Differences are statistically significant ($p<0.0001$).

At both time points, the “No UV,” non-exposed, caged-fluorescein hydrogels exhibited minimal fluorescence signal, similar to the PEGDA non-functionalized control. This indicates that even after hydrogel preparation, surgical implantation, and exposure to animal facility lighting, the caging group was still intact and exhibited no measureable uncaging. In the 7-day explants, transdermally irradiated caged-fluorescein hydrogels exhibited markedly increased fluorescein intensity compared to the non-irradiated Day 0 control (Figure 29, C, top row, middle and right panel). In order to confirm the long-term un-caging efficiency at two weeks, explants of pre-exposed caged-fluorescein controls (irradiated before implantation) were compared to Day 14 transdermally irradiated conditions and exhibited similar fluorescence intensity (Figure 29, C, bottom row, middle and right panel). Both the transdermal activation at both Day 0 and Day 14, and the pre-exposed caged-fluorescein conditions have significantly higher fluorescein intensity than the PEGDA, Day 0 non-exposed, and Day 14 non-exposed conditions (Figure 29). This data shows that DMNPB caging group after 10 minutes of 361 nm irradiation is UV labile at similar efficiency regardless of whether it is pre-exposed, transdermally exposed at Day 0, or transdermally exposed at Day 14. These results are important because they show the stability of the caging group through out the whole experiment and how caging efficiency remains unchanged regardless of fibrous capsule formation or inflammation around the implant in the weeks after surgery.

3.3.5 GMA Based Histology Preserves Tissue/Implant Interface

Histology is especially difficult at tissue/hydrogel interfaces. A traditional cryosectioning medium is a mixture of poly(ethylene glycol) [PEG] and poly(vinyl alcohol) [PVA], commonly known as OCT. Cryosectioning, due to freezing fracturing, caused by the different freezing rates of tissue vs. hydrogels, often leads to the destruction of the

hydrogel and damage to the interface. We have developed a new method of embedding tissue/hydrogel explants that preserves the hydrogel interface using Polymer Science Immunobed, a resin-based embedding system based on poly(gylcidyl methacrylate) [GMA].

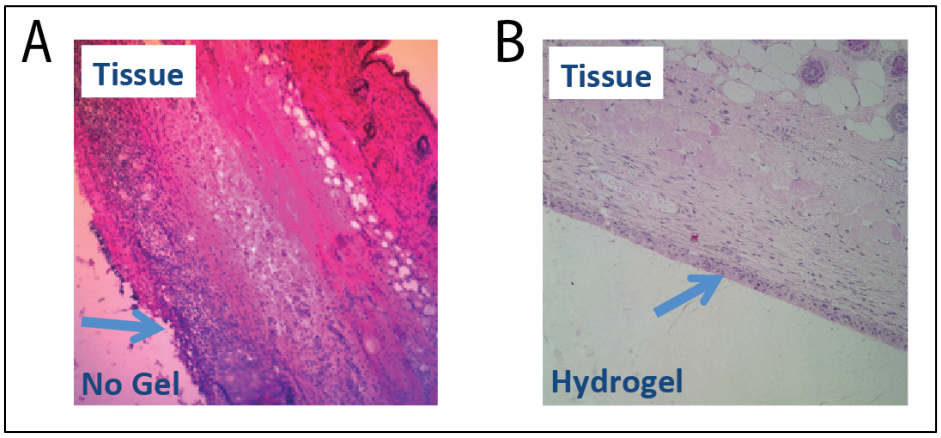

Figure 30. GMA Histology Preserves Implant/Tissue Interface. A) OCT-based cryosection (10µm thickness) of caged-RGD functionalized hydrogel explant; gel is no longer present after cutting, implant interface is badly damaged with infiltrate front completely missing. B) Polymer Sciences Immunobed plastic section (2µm thickness) of caged-RGD functionalized hydrogel explant; implant interface is perfectly preserved with hydrogel intact, staining/antigen retrieval is adequate.

After optimization of the Immunobed system, we were able to take 2 µm thick sections, compared to the minimum thickness of 10 µm in OCT-based cryosections. It is clear that the GMA embedding method (Figure 30, B) leads to a preserved tissue/hydrogel interface, whereas in the traditional cryosectioning method (Figure 30, A) the interface is destroyed. These resin-embedded sections can be de-plasticized using solvents and antigen retrieval methods can be used in downstream immunostaining. We

demonstrate in future sections that Hematoxylin and Eosin, Mason's Trichrome, and fluorescent-based immunohistochemistry is still possible.

3.3.6 *In vivo* Subcutaneous Implantation of Caged-RGD Presenting Hydrogels

After demonstrating the caged system allowed for efficient triggerable ligand presentation *in vivo*, we investigated the effects of delayed activation of caged-RGD surfaces on the localized inflammatory response. PEGDA, RGD, and caged-RGD hydrogels are implanted subcutaneously in mice. All conditions are exposed to UV (n=6) at different time points (Day 0, 7, 14) yielding 72 total implants. A brief outline of experimental setup is outlined in Figure 31. Hydrogels were prepared using a PEGDA bulk base layer, and functionalized with caged-RGD, and cyclic(RGD) ligand using the PEGDA-conjugates discussed in earlier sections (Figure 31, A). Two implants of the same condition are implanted in left/right proximal to dorsum in Balb/c mice. The reason mice were implanted with the same implants was to minimize the chance of unwanted UV-irradiation from other timepoints. From the caged-fluorescein study we have confidence that caging group is not labile from standard fluorescent bulbs present in mouse housing areas. Mice are irradiated at designated timepoints outlined in Figure 31, C.

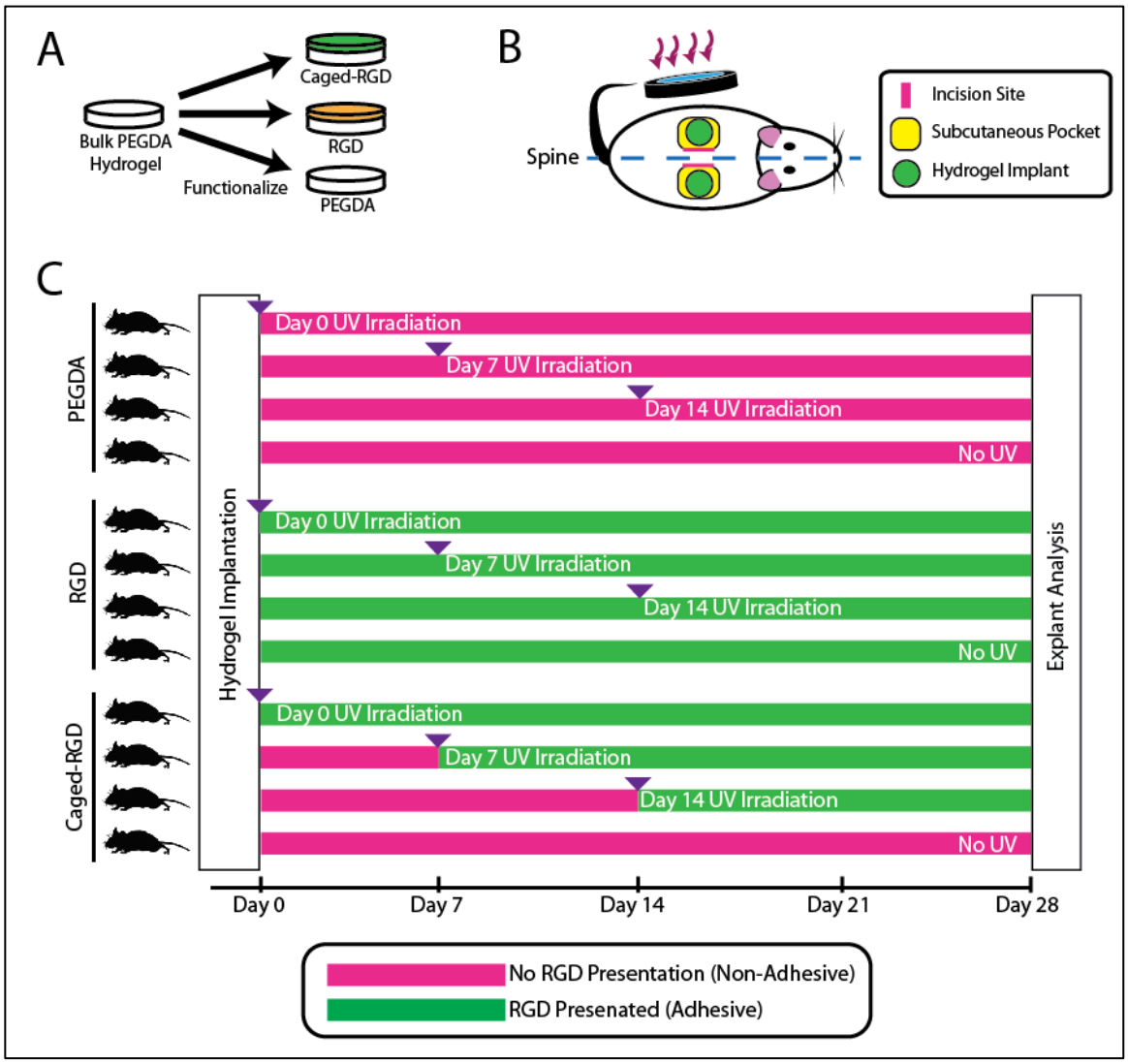

Figure 31. Outline of *In vivo* Subcutaneous Implantation of Caged-RGD Presenting Hydrogels. A) Functionalization of bulk PEGDA hydrogels with RGD, caged-RGD, or blank PEGDA. B) Schematic of implantation sites on dorsum of Balb/c mice, two implants per mouse, transdermal UV irradiation. C) Timeline representation of implantation conditions and designated irradiation timepoints. Each condition has n=6 implants. Red bars indicate no adhesive ligand presentation; green bars indicate when RGD is presented.

3.3.7 *In vivo* Activation of Caged-RGD Presenting Hydrogels Modulates Macrophage Localization

Using a CD68 antibody, macrophage localization to the implant was visualized through immunohistochemistry; results for the 28 day (4 week) takedown are summarized in Figure 32, A. Using the GMA-based embedding technique, the implant/tissue interface is well preserved. CD68+ staining is shown in green, and DAPI nuclear stain is in red. The nominal infiltrate thickness for all conditions was measured by taking the average thickness of the dark purple infiltrate band in Mason's Trichrome images or the CD68+ band in immunofluorescence images (data not shown). These infiltrate thickness measurements were consistent regardless of measurement method. PEGDA non-adhesive control exhibits a nominal CD68+ band thickness of 21.57 ± 0.57 μm, and the cyclic(RGD) adhesive control exhibits a nominal thickness of 26.71 ± 0.65 μm, these results are statistically significant ($p<0.01$). Results for the "No UV" caged-RGD condition (20.95 ± 0.44μm) are consistent with the PEGDA non-adhesive control and the differences are not statistically significant. The "Day 0" transdermal irradiation of caged-RGD (24.56 ± 0.96 μm) exhibits a similar CD68+ band thickness as the RGD control, and the differences are not statistically significant. These results indicate that transdermal irradiation of caged-RGD is able to modulate macrophage recruitment to the implant (Figure 32, B).

Interestingly, in "Day 7 UV" caged-RGD, the macrophage band thickness (20.44 ± 0.87 μm) is significantly lower than the "Day 0 UV", "Day 14 UV", and cyclic(RGD) control (Figure 32, B). This indicates that activation of caged-RGD, and subsequent presentation of cyclic(RGD) ligand, delayed after 7 days, perhaps after the end of acute phase inflammation, can elicit a lower inflammatory response. When a biomaterial is implanted with adhesive ligands present, it is known that the first cells that arrive at the implantation site are neutrophils and macrophages. RGD ligation to integrins has been

known the play a critical role in macrophage adhesion and activation, all which serve initiated a FBGC response [48, 49]. By delaying the activation of RGD ligand to day 7, we would be able to delay integrin-mediated macrophage adhesion and activation until acute phase inflammation subsided [120], this would result in a lower infiltrate band thickness when compared to conditions were RGD ligand we present since Day 0.

This does not explain, however, why the “Day 14 UV” caged-RGD condition exhibits infiltrate band thickness similar to “Day 0 UV” caged-RGD and static cyclic(RGD) conditions (25.65 ± 1.03 μm). This result is statistically significant when compared to “Day 7 UV” caged-RGD and PEGDA conditions ($p<0.01$). It is possible that after two weeks, over a week after the remission of acute phase inflammation, the delayed activation of RGD ligand starts a new inflammatory cascade. It is known that active remodeling of the infiltrate front occurs during chronic inflammation, with many macrophages fusing in to FBGC cells [120]. Day 0 activated caged-RGD hydrogels would have had 4 weeks to remodel, Day 7 with only three weeks to remodel. Therefore, if Day 14 activation of caged-RGD ligand began a new inflammatory response, it is possible that its infiltrate band thickness would be thicker than Day 7 conditions by virtue of recruiting macrophages to the implant without as much time to fully convert to the FBGC response and remodel the infiltrate band.

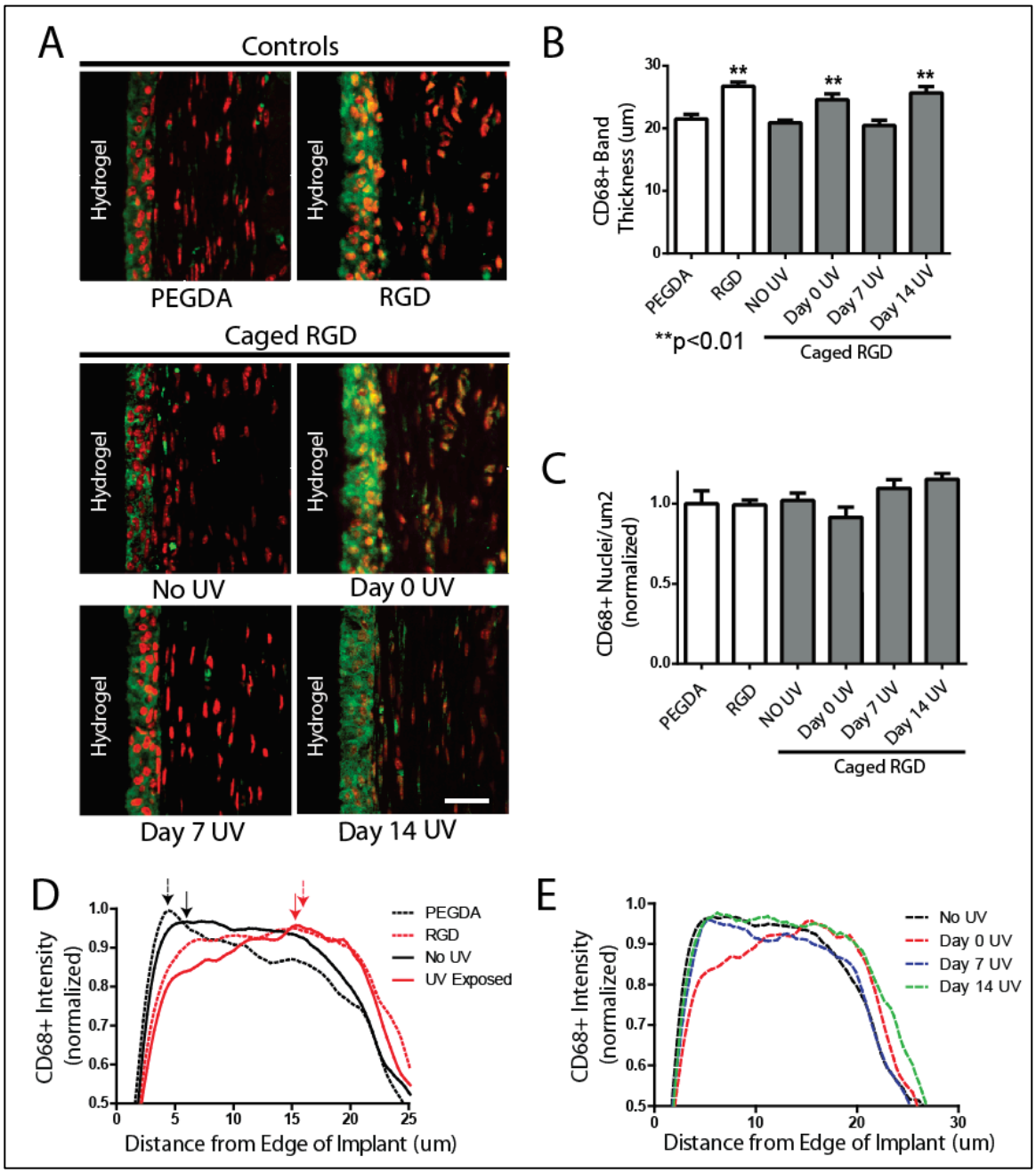

Figure 32. Triggerable Ligand Presentation of Caged-RGD Modulates Macrophage Localization. A) GMA-based immunohistochemistry showing CD68 localization to implant surface; CD68 (*green*), DAPI (*red*). Scale bar 30µm. B) CD68+ band thickness for all implant conditions. PEGDA (non-adhesive control) has a band thickness, similar to the caged-RGD "No UV" and "Day 7 UV" condition. RGD (static cyclic(RGD) control) has a band thickness, similar to the caged-RGD "Day 0 UV" condition and "Day 14 UV" condition. ** denotes statistical significance ($p<0.01$) C) Quantification of CD68+ cell

density as measured by co-localization of CD68+ and DAPI staining. No statistical differences between conditions. D) CD68+ intensity profiles of PEGDA, RGD, and Caged-RGD (No UV and UV exposed).

There are no differences in density of macrophages as measured by CD68+/DAPI co-localization (Figure 32, C). Unfortunately, due to higher background of GMA-based embedding, it is impossible to see cell outlines to quantify FBGC formation. We next assessed the spatial distribution of CD68+ staining across the infiltrate band by measuring the CD68+ staining vs. distance from the implant, normalizing each trace, and then finding the average normalized CD68+ thickness over the band (Figure 32, D and E). The PEGDA and No UV caged-RGD conditions exhibit a similar profile of CD68+ intensity, both with peak intensity at 3.41μm and 2.48 μm, respectively, from the implant surface. The static RGD control and Day 0 caged-RGD condition have also have a profile of CD68+ intensity, with peak occurring further from implant surface (17.4μm and 12.12 μm). This shows that transdermal irradiation of caged-RGD, and subsequent RGD presentation is effective at modulating macrophage CD68+ density (as measured by CD68+ intensity) to the implant surface (Figure 32, D).

The CD68+ intensity profiles were also generated for the delayed activation of caged-RGD conditions (Figure 32, E). Interestingly, for all conditions where RGD was not activated immediately, “No UV”, “Day 7 UV” and Day 14 UV (*black*, *green*, *blue*), the peak CD68+ localization occurs relatively close to the implant surface (2.48 μm, 5.28 μm, 3.41 μm, respectively), similar to the PEGDA control (3.41 μm). This is consistent with the fact that “Day 7 UV”, “Day 14 UV”, and “No UV” conditions did not present any adhesive ligands for over a week (during acute phase inflammation), resulting in similar profiles of macrophage recruitment and localization in the infiltrate band. It seems that

delayed presentation did have an effect on the tissue side CD68+ density; however, by that point the FBGC response on the implant surface had already resulted in high CD68+ density and localization.

When RGD is presented immediately, in both static cyclic(RGD) and “Day 0 UV” caged-RGD conditions, macrophage density is concentrated towards the tissue side, perhaps suggesting, a active recruitment of additional macrophages to the infiltrate band via RGD presentation. This taken in conjunction with the increased infiltrate band thickness in RGD and Day 0 UV conditions suggest that these conditions elicit the strongest macrophage recruitment. However, because the peak occurs at the tissue side in RGD and “Day 0 UV”, conditions it is not possible to say that the FBGC response on the implant side is lower than in PEGDA, “Day 7 UV” and “Day 14 UV” conditions. The fact that “Day 14 UV” condition exhibits a flatter CD68+ intensity plot as well as a thicker band thickness could suggest that after the FBGC response was already established by day 14, and that subsequent activation of RGD ligand served to recruit more macrophages, changing the profile from a implant side CD68+ bias, to more of a flat profile. It is important to note that because these curves are normalized, quantitative generalizations of the relative CD68+ densities cannot be made. Nevertheless, this data shows that transdermal activation of RGD-ligand at delayed timepoints is effective at modulating macrophage response to implant associated inflammation.

3.3.8 Delayed Activation of Caged-RGD Attenuates Fibrous Capsule Formation

The fibrous capsule thickness was determined by Mason’s Trichrome staining of 2µm GMA sections (Figure 33A). The fibrous capsule is determined as the fibrotic, aligned tissue (alanine blue collagen stain) that extends from the left edge of the dark purple, inflammatory cell band to the right edge of the light purple smooth muscle layer.

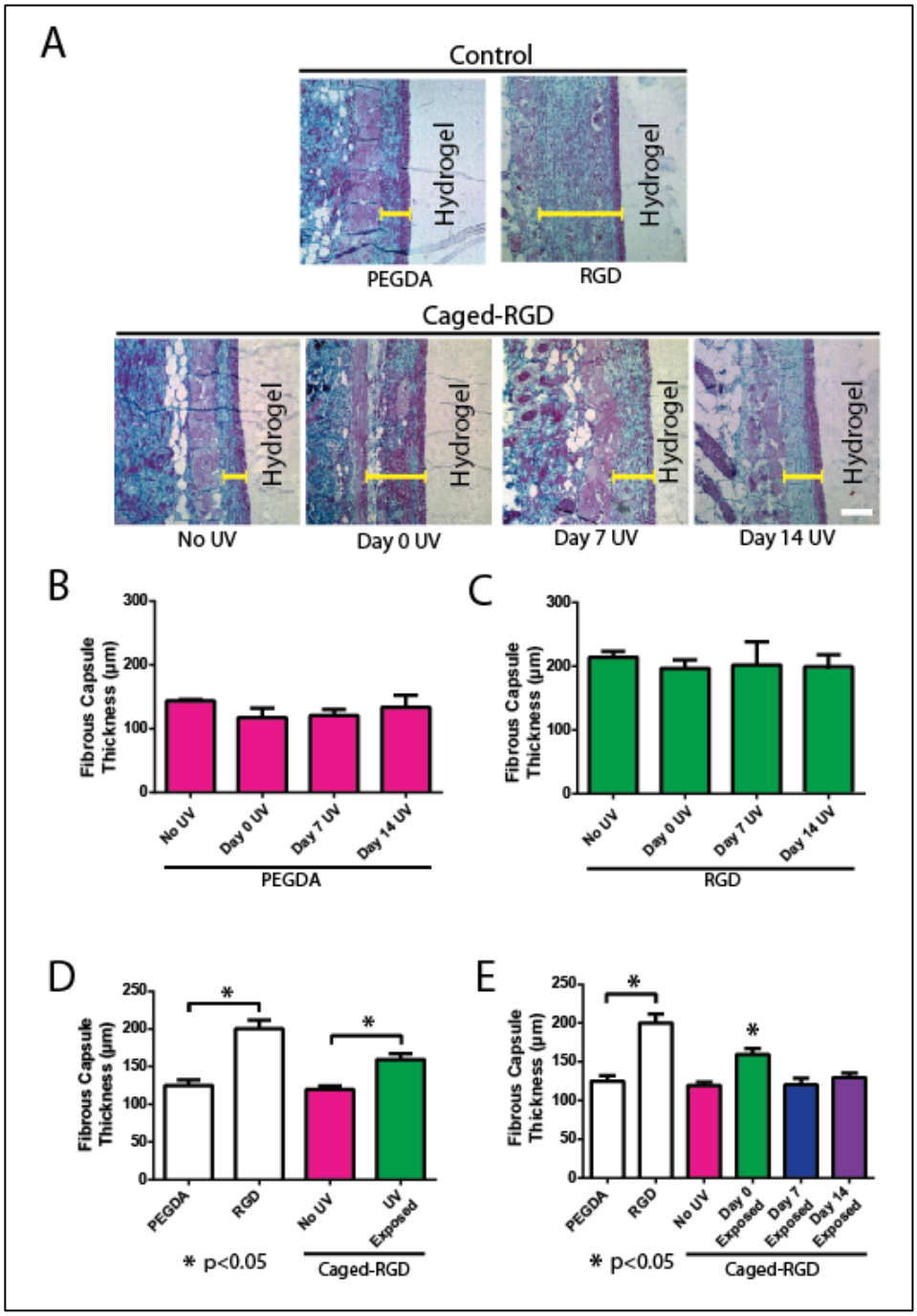

Figure 33. Delayed activation of caged-RGD modulates downstream fibrous capsule thickness. A) GMA-based Mason's Trichrome 4wk explants. The dark purple band denotes the infiltrate rich cell band. The dark blue, aligned tissue, in between the smooth muscle layer and the infiltrate band is the fibrous capsule. Tissue/implant interface is perfectly preserved. Scale bar 150µm. B) Quantification of fibrous capsule thickness of all PEGDA conditions. No statistical difference, regardless of UV irradiation.

C) Quantification of fibrous capsule thickness of all static cyclic(RGD) conditions. No statistical difference, regardless of UV irradiation. D) Comparison of controls (PEGDA, RGD) to analogous caged-RGD conditions. PEGDA and No UV caged-RGD condition (*red*) exhibit fibrous capsule thickness around 120μm, which is consistent with non-specific FBCG response. RGD and UV exposed caged-RGD condition (*green*) exhibit statistically significant increases in fibrous capsule thickness ($p<0.05$). E) Delayed activation of caged-RGD attenuates fibrous capsule thickness.

Fibrous capsule thickness was quantified for all conditions, results summarized in Figure 33. For all PEGDA and RGD controls, regardless of UV irradiation, the difference in fibrous capsule thickness is not statistically significant. This is the expected result, as UV irradiation should not affect implants presenting either no ligands (PEGDA) or static cyclic(RGD) (Figure 33, B and C). In Figure 33 D and C, the PEGDA and RGD controls have been pooled for all irradiation conditions. PEGDA and caged-RGD No UV conditions have similar fibrous capsule thickness, which is expected since they both present no RGD ligands. Static cyclic(RGD) conditions (denoted by RGD) and caged-RGD Day 0 UV conditions exhibit similar fibrous capsule thickness due to presenting RGD ligand for exactly the same amount of time (4 weeks). These results are consistent with previous studies that have compared PEGDA hydrogels to RGD presenting PEGDA hydrogels [90, 126]. These results demonstrate it is possible to directly modulate fibrous capsule formation via triggerable presentation of RGD ligand.

We have already established that the DMNPB caging group uncaged with the same efficiency even after 14 days (Figure 29). Interestingly, delayed activation of caged-RGD ligand (Day 7 and Day 14) both exhibit statistically significant lower fibrous capsule thickness, even though these conditions should still be presenting equal amounts of RGD ligand, only at different time points after implantation (Figure 33, E).

This is not particularly surprising because the Day 7 UV and Day 14 UV conditions presented RGD ligand for a shorter amount of time than the Day 0 condition by 7 days and 14 days, respectively. It should be noted that the caged-RGD Day 0 exposure condition has a slightly lower, but not statistically significant fibrous capsule thickness when compared to the RGD control. Therefore, we have shown that delayed activation of adhesive ligands is effective at modulating a second order inflammatory response, the downstream fibrous capsule formation.

3.3.9 *In vitro* Cell Sprouting Modulated by Caged-RGD Presenting Hydrogels

The previous sections described the ability of caged-RGD to modulate cell and inflammatory processes on a two-dimensional surface. To further demonstrate the applications of caged-RGD we have applied the use of triggerable ligand presentation in a three-dimensional environment. While it is known that caged-RGD ligand can effect macrophage recruitment and fibrous capsule formation at the implant site, these studies only demonstrate second order effects of caged-RGD in an *in vivo* system. In order to demonstrate a directly functional link between ligand presentation and cell or tissue level behavior, we decided to perform two functional assays, *in vitro* cell outgrowth model and an *in vivo* vasculogenesis assay. In both cases, there should be stark differences in cell and tissue behavior between irradiated and non-irradiated caged-RGD conditions.

Caged-RGD presenting PEG-maleimide (PEG-MAL) gels were used to demonstrate the ability of triggerable RGD ligand presentation to modulate IMR90 cell migration and sprouting in the 3-dimensional hydrogel system. It has been previously shown that PEGDA-based hydrogels are not effective at promoting cell infiltration, even when crosslinked with protease-sensitive crosslinks; therefore, we ported the caged-RGD technology to a PEG-MAL-based hydrogel system [127]. Caged-RGD analogs

were created with a cysteine termination (Figure 34, A) for compatibility with PEG-MAL chemistry (Figure 34, B). These caged-RGD analogs still have exactly the same DMNPB caging group and UV labile linker, therefore the uncaging efficiency and peptide behavior should be exactly the same as in the PEGDA-based gels.

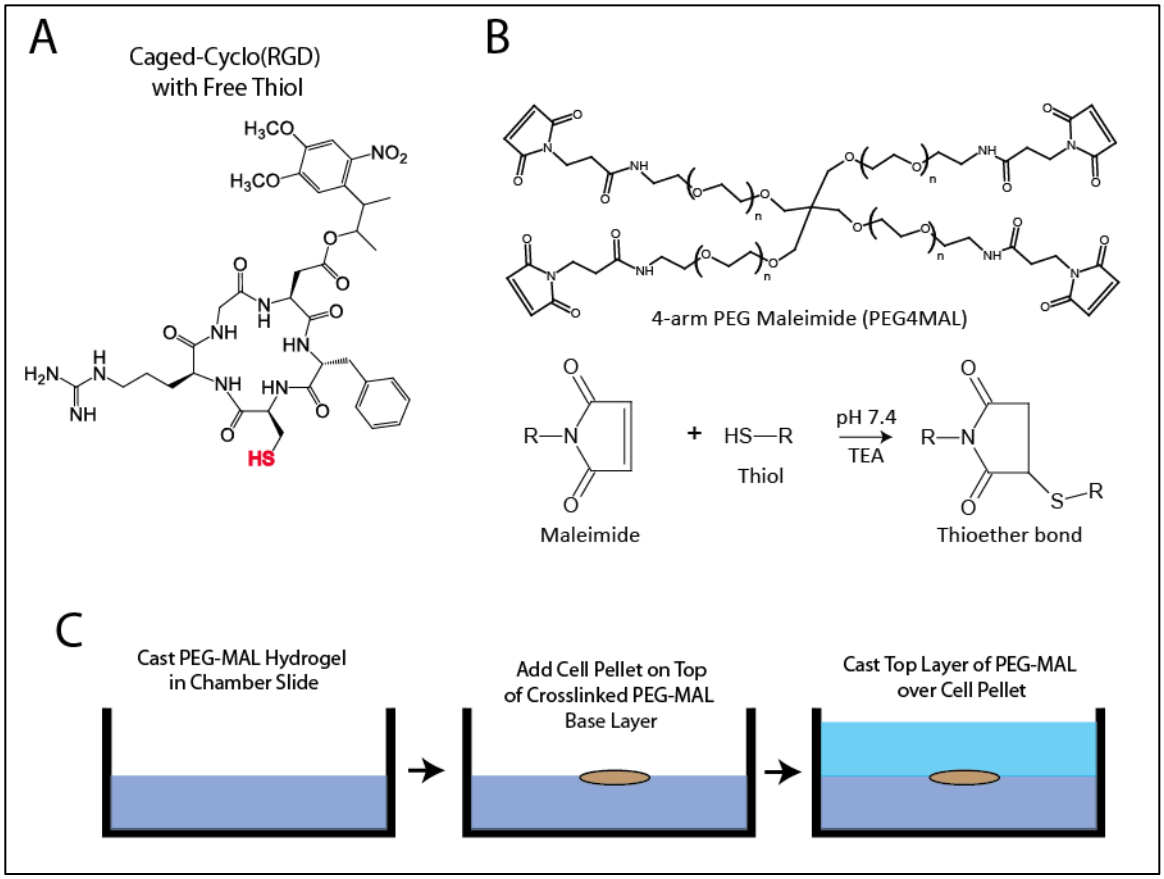

Figure 34. PEG-Maleimide Caged-RGD Presenting Hydrogels. A) Chemical formula of cysteine contained caged-RGD. B) Schematic representation of PEG-Maleimide based peptide tethering and crosslinkers. The maleimide group in combination with a free thiol under in TEA buffer at pH 7.4 leads to the formation of a covalent thioester bond. C) Schematic representation of sandwiched PEG-MAL hydrogel with embedded cell pellet.

4% PEG-MAL hydrogels were created with 10 mM VPM (protease-sensitive crosslinker), 10 µg/mL VEGF, and 2 mM ligand (RDG, RGD and caged-RGD). VEGF was used not to promote IMR90 cell outgrowth, but to maintain the same gel formulation

in all PEG-MAL studies. The gels were directly crosslinked in a #1 coverslip bottomed 8-chamber slide. The bottom of each well was coated with a small amount of PEG-MAL hydrogel so that cells seeding into wells would not be able to spread on the bottom glass. This gel was allowed to crosslink. A cell pellet of IMR90 cells (~1 mm in diameter) was pipetted into the center of the bottom gel. Immediately after, a top layer of PEG-MAL gel was pipetted on top, with great care not to disturb the cell pellet. After allowing the gel to fully crosslink at 37°C for 20 minutes, growth media was added to each well. This method is summarized in Figure 34, C. Gels were UV irradiated using a UV-lamp based setup already described in previous sections. Dosage optimization of UV irradiation time was performed, as too much UV irradiation directly to cells resulted in cell death (data not shown), too little irradiation resulting in not enough uncaging of caged-RGD ligand. Optimal dosage was determined to be 12 mW/cm^2 intensity for 3 minutes.

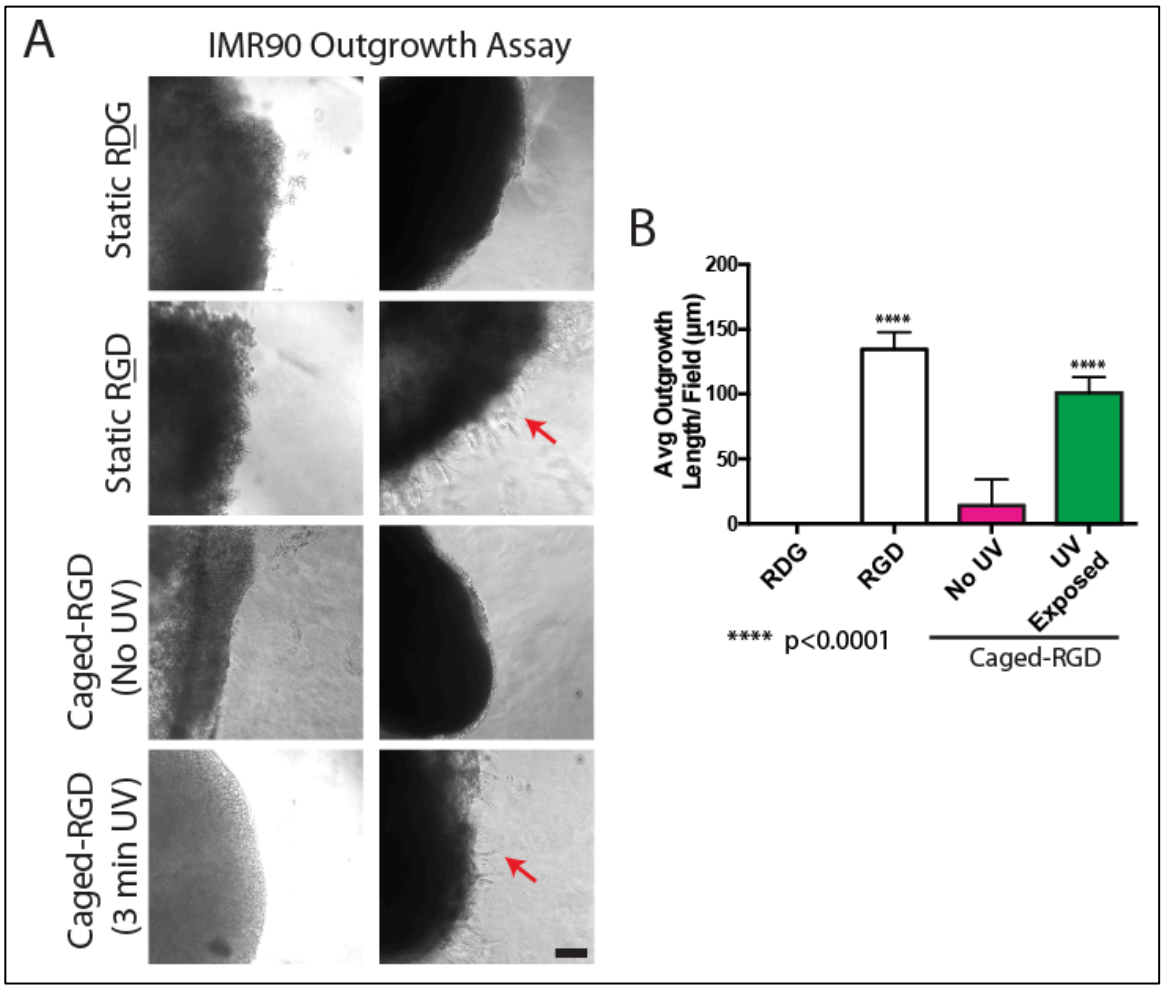

Figure 35. Quantification of Outgrowth in Caged-RGD containing PEG-MAL Hydrogels. A) *In vitro* characterization of caged-RGD containing PEG-MAL gels using IMR90 cells in a cell outgrowth assay. Outgrowth was observed in RGD and caged-RGD "UV Exposed" conditions. No outgrowth was observed in RDG negative control and caged-RGD "No UV" conditions. Red arrows denote outgrowths. Scale bar 100 µm. B) Degree of outgrowth of RGD vs. "UV Exposed" caged-RGD. Both hydrogels that presented RGD ligand exhibited cell outgrowth between 100-150µm. There is no significant difference between degrees of outgrowth in RGD control vs. UV exposed caged-RGD conditions.

The results of this study are summarized in Figure 35, A. In the static RDG controls and in the "No UV" caged-RGD condition, there was no cell sprouting after three days. After three days in culture, the static RGD and "UV Exposed" caged-RGD

condition both exhibited IMR90 cell outgrowths of 134.33 ± 13.96 μm and 100.95 ± 12.08 μm, respectively. "UV exposed" caged-RGD conditions exhibited slightly less sprouting presumably due to poorer cell health due to UV damage from irradiation, however, these differences were not statistically significant. Taken in whole, these results show that caged-RGD presenting PEG-MAL hydrogels can control IMR90 cell outgrowth through the modulation of cyclic(RGD) presentation via UV irradiation.

3.3.10 *In vivo* Vasculogenesis Modulated by Caged-RGD Presenting Hydrogels

To show *in vivo* efficacy of caged-RGD presenting PEG-MAL hydrogels, an *in vivo* vasculogenesis assay was performed. Hydrogels were prepared with the same formulation described in the previous section: 4% PEG-MAL hydrogels were created with 10 mM VPM (protease-sensitive crosslinker), 10 μg/mL VEGF, and 2 mM ligand (RDG, RGD and caged-RGD). Instead of pre-casting hydrogels as in caged-RGD presenting PEGDA gels, caged-RGD PEG-MAL gels were crosslinked *in situ* for better vasculogenesis (data not reported, Garcia Lab). A subcutaneous implantation study using Balb/c mice was performed in the manner outlined in Figure 36. The same UV-lamp source described in previous sections was used to irradiate mice at designated time points (Day 0 and Day 7). RDG negative controls were also irradiated to show that UV irradiation has no effect on vasculogenesis.

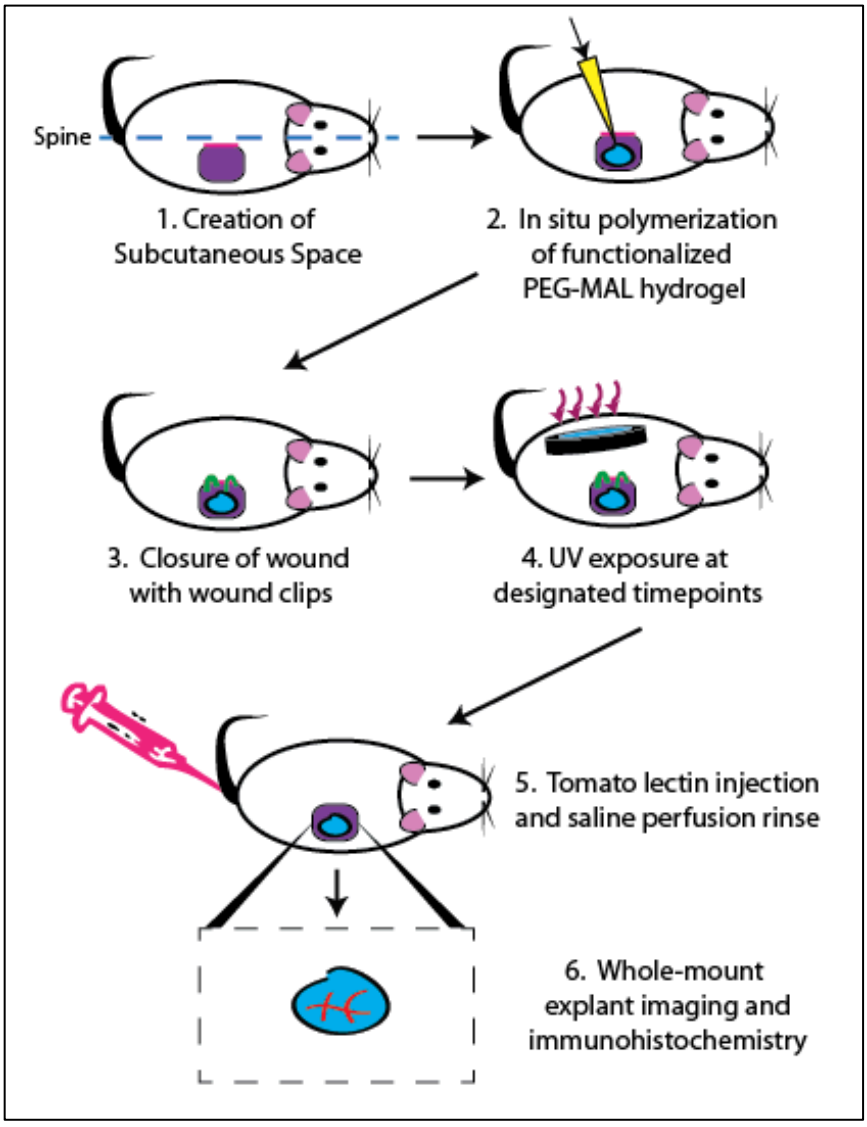

Figure 36. *In situ* Crosslinking of PEG-MAL Hydrogels in Subcutaneous Implant. A subcutaneous space is created using an incision along right of mouse back, hemostats are used to create subcutaneous pocket, PEG-MAL hydrogel containing degradable crosslinkers and ligands are polymerized *in situ*, wound is closed. After designated time point of 14 days, mouse is perfused with tomato lectin to label vasculature via tail vein injection; mouse vasculature is rinsed with saline containing papaverine. Explants are then removed for whole mount fluorescent microscopy.

After the designated 2-week time-point, all mice were perfused with tomato lectin-DyLight488 through the tail vein to label the vasculature. The tomato lectin was allowed to circulate for 20 minutes to ensure that there was good staining of small vessels. Afterwards, the mice were perfused with papaverine containing saline and are bled from the inferior vena cava. This was to ensure that all of the blood was removed from the vasculature for better fluorescent imaging. Afterwards, all of the implants were explanted from the mice and placed in 4% formalin for preservation. After overnight incubation in formalin, implants were washed three times in DPBS and imaged on the Nikon C2+ confocal with attached Nikon Eclipse Ti, 20x. Z-stacks of 20um were taken of each condition.

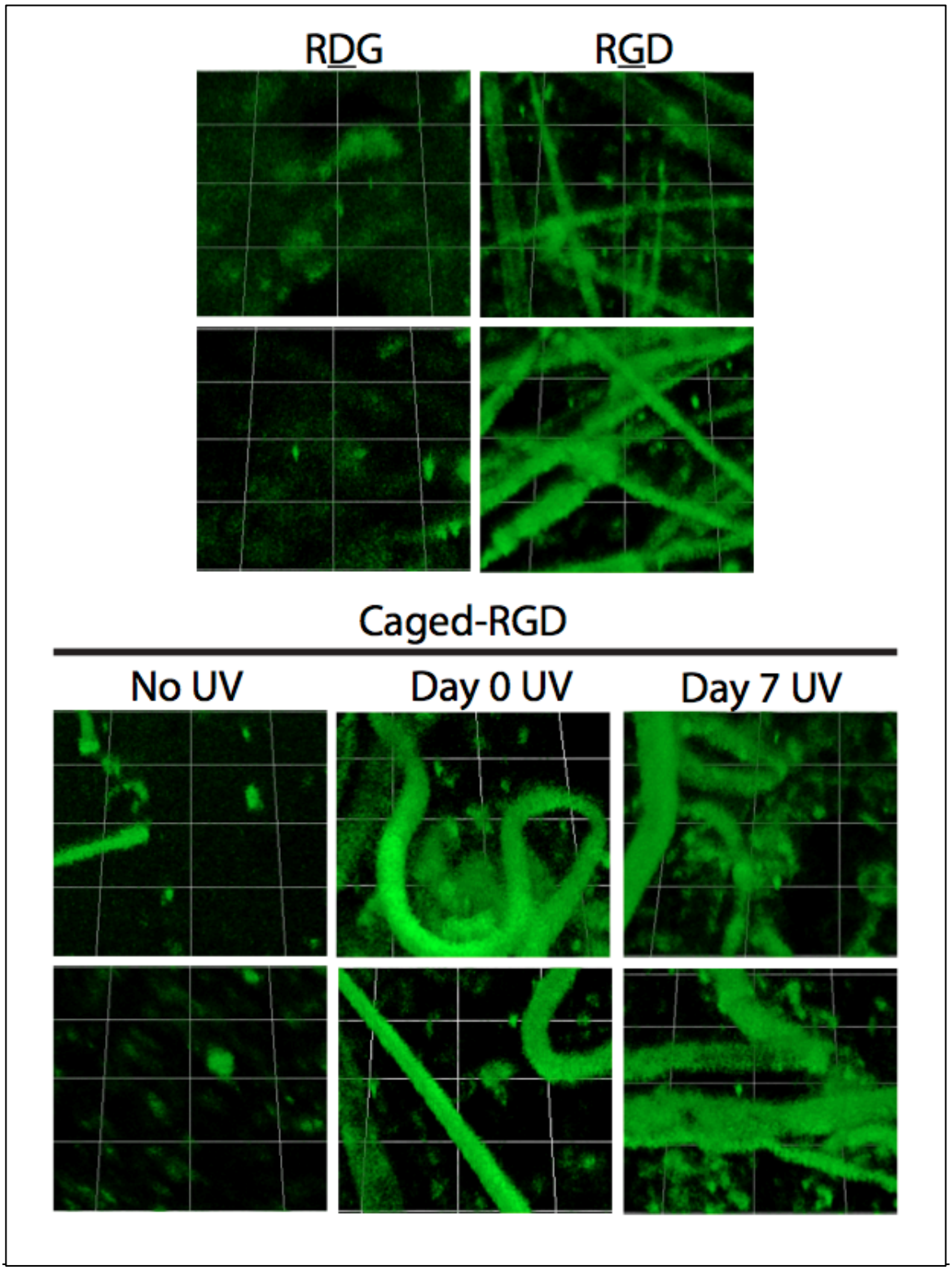

Figure 37. Tomato Lectin Dylight488 Staining of Vasculogenesis in PEG-MAL Caged-RGD Hydrogels. Three-dimensional reconstructions using alpha blending of z-stacks. Stack height approx. 22µm. Squares indicate 100µm^2.

Upon analysis, all hydrogels were still visible in the microscope as visualized by air bubbles trapped in the hydrogel. Z-stacks were taken in and around these regions to ensure that imaged vasculature was in hydrogel. These image stacks were then converted to three-dimensional reconstructions for cursory visualization of results (Figure 37). The RDG negative control exhibited no vasculogenesis, with no structures resembling blood vessels labeled above background level. The RGD positive control exhibited robust vasculogenesis with a dense blood vessel network with both large and small diameter blood vessels throughout the implant site. In accordance with the control groups, the "No UV" caged-RGD condition extremely low levels of vasculogenesis comparable to the RDG negative control. The "Day 0 UV" and "Day 7 UV" caged-RGD conditions exhibited vasculogenesis, but not the same extent as the RGD positive control. The UV exposed caged-RGD conditions only had large blood vessels throughout the gel at much lower density. These differences will be investigated in more detail and quantified in the following section.

Using ImageJ we created the maximum intensity projections of each field so that we could quantify the number of blood vessels and determine the average diameter of each blood vessel. We ensured that vessel counts and diameters were accurate by ensuring that we were imaging the area with the hydrogel. During *in situ* polymerization the gels were mixed with a pipet tip and this introduces some small air bubbles into the hydrogel. Therefore, these air bubbles were an excellent guide to ensure that the vasculogenesis regions that were imaged indeed within the hydrogel (Figure 38, A). From the images it is clear that there is some tissue autofluorescence from collagen and in some images you can see the smooth muscle layer behind some of the blood vessels.

However, the vasculature signal via tomato lectin is significantly higher, and in conjunction with the morphology of the blood vessels it is easy to discriminate between vasculature in the gel and bulk tissue.

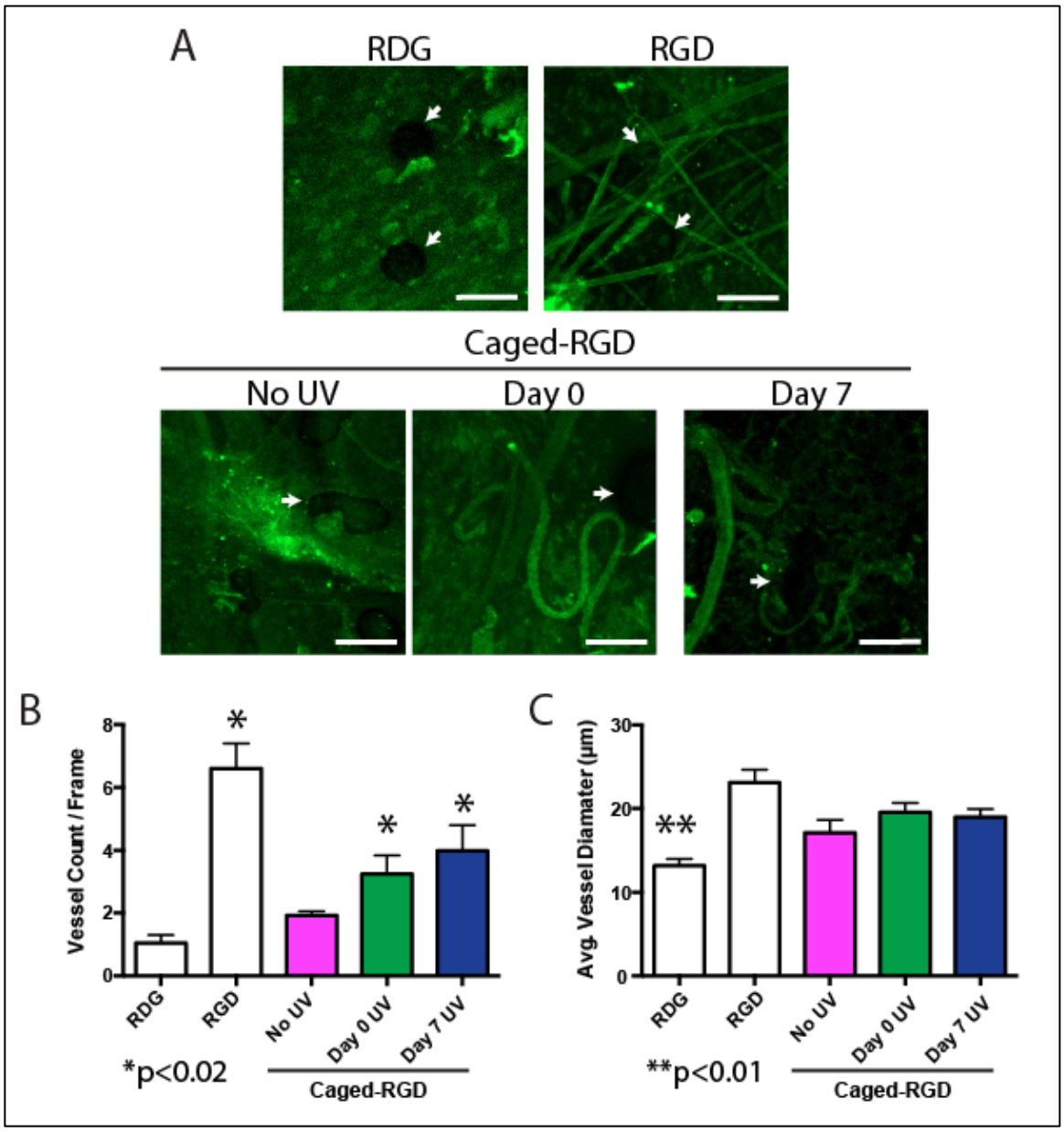

Figure 38. Quantification of Vasculogenesis. A) Maximum intensity projections of representative images. White arrow denotes air bubble in hydrogel, used to confirm hydrogel location. Scale bar 80 µm. B) Quantification of number of blood vessels per field. RGD Day 0 UV, and Day 7 UV exhibit higher numbers of blood vessels per field

when compared to No UV and RDG control, differences are statistically significant ($p<0.02$). C) Quantification of average diameter of blood vessels. RDG control has significantly lower diameter of blood vessels when compared to all other conditions, results are statically significant ($p<0.01$).

In the RDG and "No UV" caged-RGD condition, there is minimal vasculature within the gel, which is consistent with previous studies that demonstrated that RGD is required for vascular infiltration of the hydrogel [127]. In the RGD condition there is robust formation of vasculature with a significant amount of blood vessel formation. In "Day 0 UV" and "Day 7 UV" conditions, there was also blood vessel formation, however, not as much as in the RGD condition. There are several possibilities for this result. There could be reduced uncaging efficiency stemming from larger irradiation distances of three-dimensional PEG-MAL gels, when compared to previous uncaging studies that occurred directly below the surface of the skin. Furthermore, inefficient uncaging could lead to lower RGD presentation leading to fewer blood vessel sprouting events into the hydrogel bulk. Also, there could be side effects from the solvents used to solubilize the cys-containing caged-RGD in DPBS that may have had an effect on vasculogenesis. Compared to the "No UV" caged-RGD condition, both the "Day 0 UV" and "Day 7 UV" caged-RGD conditions, exhibited significantly higher amounts of blood vessels per frame ($p<0.02$). These results are consistent with previous studies that have shown that RGD tethered to PEG-based hydrogels is required for *in vivo* vasculogenesis in PEG-based hydrogels [127, 128]. Taken in whole, transdermal UV irradiation of caged-RGD containing PEG-MAL gels was effective at providing ex vivo control of *in vivo* vasculogenesis in a simple reproducible manner without requiring additional surgeries or invasive procedures. This shows the promise of caged-compounds, *in vivo*, to study various tissue level processes in a robust and non-invasive fashion.

3.4 CONCLUSION

PEG-based hydrogels provide a novel platform to elucidate cell-ECM interactions through a highly defined, non-fouling surface. Through the use of simplified ECM-peptides such as RGD, specific integrin-ECM interactions can be studied. We have demonstrated the uses of a novel caged-RGD molecule in the context of PEG-based hydrogels.

Caged-RGD conjugated PEGDA based hydrogels were able to effectively modulate cell attachment and spreading *in vitro*. We were able to demonstrate that DMNPB-based caged compounds were effectively controlled ex vivo using UV irradiation, after a subcutaneous implantation and the uncaging efficiency was unchanged even after 14 days. Furthermore, delayed activation of caged-RGD presenting hydrogels was able to modulate macrophage recruitment and downstream fibrous capsule formation in subcutaneously implanted PEGDA-based hydrogels.

When applied to PEG-maleimide based hydrogels, caged-RGD was effective at controlling *in vitro* cell outgrowth into a degradable hydrogel with protease sensitive crosslinks through the control of RGD presentation via wide-field UV irradiation. When this PEG-maleimide system was combined with protease sensitive crosslinks and VEGF in an *in situ* polymerized subcutaneous model, caged-RGD was effective at controlling vasculogenesis through the modulation of RGD presentation via transdermal UV irradiation. Therefore, we have demonstrated that caged-RGD in conjunction with PEG-based hydrogels is a versatile platform that offers unparalleled spatiotemporal control of RGD ligand presentation. Through UV-activation we have demonstrated that ex vivo control of RGD-mediated cell adhesion is a critical regulator of many events including inflammation and vasculogenesis. This study has shown that caged-compounds provide

a versatile and effective means of controlling the presentation of signals and ligands in both *in vitro* and *in vivo* systems and have demonstrated the potential of this class of compounds in future biomaterials research.

3.5 METHODS

Cell Culture and Reagents

NIH3T3 fibroblasts cell and IMR90 cells were purchase from the ATCC (Manassas, VA). Growth media was DMEM (Gibco), 10% fetal bovine serum (Gibco), 100 U/mL penicillin G sodium (Gibco), 100 µg/mL streptomycin sulfate (Gibco), 1% non-essential amino acids (Gibco). Live dead staining completed via Calcein AM and ethidium homodimer II (Invitrogen).

Generation and characterization of PEG-conjugates and hydrogels

Caged-RGD is synthesized in the manner described previously and generously provided by Arancha del Campo's Lab at Max-Planck-Institut für Polymerforschung, Mainz, Germany [104]. Poly(ethylene glycol)-based caged-RGD conjugates were generated by reacting Acryl-PEG-SVA (Laysan Bio, AL) with the primary amine of the caged-RGD molecule for 4hrs in sodium bicarbonate (Sigma-Aldrich) buffer, pH 8.2. Pegylated-RGD was generated in the same fashion using A-PEG-SVA and cyclo(RGDfk) (Peptides International; AL). The pegylated derivatives were dialyzed using a Slide-A-Lyzer dialysis cassette with a 3400MW cutoff (Pierce; IL) for 2 days in ultra-pure diH_2O and lyophilized using a freeze-dying system (Labconco; MO). These PEG-conjugates were stable at -20°C for long-term storage. The tethering of caged-RGD to the acryl-PEG-SVA was confirmed using MALDI-MS.

Hydrogel casting and functionalization

Bulk PEGDA hydrogels were created using a mixture of 10% PEGDA (Laysan Bio, AL) and 0.05% Irgacure 2959 (BASF, Germany) in DPBS. These precursor solutions were sterile filtered using a 0.22 µm filter. These precursors were cross-linked in a sterilized silicon isolator mold (GraceBio, OR) mounted to a glass slide sealed by a

Sigmacote (Sigma-Aldrich) coated microscope slide. A 15mm Sigmacote coated coverslip was used to squeeze out excess precursors and generate a flat top surface of the hydrogel. Hydrogels were crosslinked using a UV light table for 10 minutes. The top coverslip was removed and these bulk gels were then functionalized with a thin top gel consisting of 8% PEGDA, 2% adhesive PEG-conjugate crosslinked via TEMED (IBI Scientific, IA) and APS (Fluka) in the same mold. Another Sigmacote coated coverslip was placed on top of the crosslinking gel to ensure that the top surface was also flat.

In vitro characterization of cell adhesion

Caged-RGD, RGD, RDG, and blank PEGDA hydrogels were generated and NIH3T3 were seeded on top at 20k/cm^2 density overnight. Live-dead assay was performed (Invitrogen), epifluorescent images captured at 20x using a Nikon TE-300 (Nikon; Japan) and quantified via ImageJ.

Subcutaneous implantation of caged-RGD presenting hydrogels

Hydrogels precursors are sterile filtered and verified to be endotoxin-free. Cast hydrogels are further sterilized in 0.2% sodium azide (Sigma-Aldrich) for overnight, and washed with DPBS -/- (Gibco) over the course of 3 days to remove remaining azide. Caged-RGD samples are protected from light.

Sterile, endotoxin-free PEGDA-based hydrogels, (8 mm) diameter, were implanted subcutaneously following IACUC-approved procedures in 6-8wk old male Balb/c mice (Jackson Laboratories, ME) that have been anesthetized by isofluorane. Two 1 cm incisions were made on the dorsum proximal to the spine, on both left and right sides, and a subcutaneous pocket was created that laterally spanned the dorsum. Two hydrogels were implanted in each animal, and the incision was closed using sterile wound clips. A X-Cite 120 Arc Lamp (Exfo; Canada) with an attached collimator (Nikon, Japan), bandpass filter (Edmund Optics, NJ), a VS14/25 shutter and VMM-T1 Shutter

Driver Controller (Uniblitz; NY) is used to transdermally expose UV-liable implants and controls at Day 0, 7, and 14. When needed, any hair over implant site was removed with Nair™.

In vivo characterization of DMNPB-group via Caged-fluorescein

Caged-Fluorescein-Acrylate was generously provided by Arancha del Campo's Lab at Max-Planck-Institut für Polymerforschung, Mainz, Germany. fluorescein is modified with an acrylate group and a DMNPB-caging group. Preliminary characterization is performed via NMR. Caged-fluorescein hydrogels are generated in the same manner as described as Caged-RGD hydrogels. Pre-exposed, unexposed caged-fluorescein, and control blank hydrogels were implanted subcutaneously in mice, one per animal. A X-Cite 120 Arc Lamp (Exfo; Canada) with an attached collimator (Nikon, Japan), bandpass filter (Edmund Optics, NJ), a VS14/25 shutter and VMM-T1 Shutter Driver Controller (Uniblitz; NY) is used to transdermally expose UV-liable implants and controls at Day 0 and 7. Implants were imaged by Nikon TE-300 using epifluorescence microscopy using a 4x objective. Fluorescence intensity over several fields was quantified using ImageJ (NIH).

GMA-based implant analysis

Mice were sacrificed at 4 weeks with implants explanted without disturbing the implant-tissue interface. Explants were fixed in 4% formalin for 24hrs, washed with DPBS three times, incubated in 70% denatured alcohol reagent in H_2O, and dehydrated in a tissue processor (Thermo, MA). Processed explants were incubated in 50% Immunobed infiltration solution (Polysciences; PA)/50% ethanol (Decon Labs; PA) for 24 hours, then two times in 100% Immunobed infiltration solution for two more 24 hours incubations. Explants were embedded using the Immunobed Kit in plastic molds. Embedded tissues were removed from molds after 48 hours of curing at 4°C, and

allowed to air dry at room temperature. Molds are sliced into 2µm tissue sections using a microtome (Thermo; CA) with a tungsten-carbide blade (DDK; DE). Tissue sections were stained in an autostainer (Lecia; Germany) for Mason's Trichrome stain. Masons's Trichrome stain contained: Alanine Blue (Sigma), Phosphomolybdic-phosphotungstic acid (ACS Chem), Biebrich's Scarlet-Acid fuchsin (ACS Chem), Hematoxylin (ACS Chem). Other processing reagents included xylene (check), xylene sub (ACS Chem), reagents alcohol (ACS Chem). Macrophage and neutrophil recruitment is monitored by immunofluorescence analysis of CD68 and NIMP-14 (Abcam, MA), respectively. Nuclei are monitored using DAPI (Invitrogen). Image analysis is completed in ImageJ (NIH).

PEG-maleimide based fibroblast outgrowth assay

PEG-maleimide (Laysan Bio) was incubated with Caged-RGD, RGD, RDG in separate vials to conjugate the thiol-terminated peptides to one arm of the PEG-maleimide molecule. The final gel formulation called for a 100uL per well, 4% PEG-MAL gels, 2mM peptide concentration, 5ug/mL VPM, and 10ug/mL VEGF. These 50uL of these gels were then formed in LAB-TEK 8 chamber #1 coverslip glass bottomed wells. The gels were then allowed to crosslink for 2 minutes. A cell pellet was seeded into the middle of the hydrogel, and another 50uL of functionalized hydrogel was placed on top. Gels were allowed to fully crosslink for 30 minutes in an incubator. Media was then added to wells after gels were fully crosslinked.

Vasculogenesis in PEG-MAL hydrogels presenting caged-RGD

4-arm PEG-MAL polymer precursors were sterilized using ethanol and then rotary evaporated to remove all ethanol. 4% (w/v) PEG-MAL (Laysan Bio) hydrogels were prepared with 2mM peptide, 5ug/mL VPM (Apptec), and 10ug/mL VEGF (Invitrogen). First PEG-MAL hydrogels were allowed to incubate with 2mM peptide (RGD (Peptides International), RDG, and caged-RGD (del Campo Lab; M) in a 3:1 molar

ratio for 30 minutes in 10-20mM TEA (Sigma-Aldrich), in order to pre-conjugate, on average, one peptide per maleimide arm. During this incubation step, one 1 cm incision was made on the dorsum proximal to the spine, on the right side, and a subcutaneous pocket was created that laterally spanned the dorsum. PEG-MAL-peptide precursors were then combined with VPM and VEGF (total volume 80µL) and were pipetted into the subcutaneous space and allowed to crosslink *in situ*. After crosslinking for one minute, the incision was closed using sterile wound clips. A X-Cite 120 Arc Lamp (Exfo; Canada) with an attached collimator (Nikon, Japan), bandpass filter (Edmund Optics, NJ), a VS14/25 shutter and VMM-T1 Shutter Driver Controller (Uniblitz; NY) is used to transdermally expose UV-liable implants and controls at Day 0 and 7.

Whole-mount explant analysis

At the Day 14 takedown point, 1 mg/mL tomato lectin was injected through the tail vein of the anesthetized mice and allowed to circulate for 20-30 minutes. Following this incubation time, the mice were terminally perfused with 0.4% papaverine in saline through the left ventricle and allowed to bleed through the inferior vena cava. This procedure was completed by opening up the chest cavity and performing a Y-cut to the sternum in order to expose the heart. Then a butterfly needle with tubing was connected to a 50mL syringe filled with papaverine containing saline. First, the inferior vena cava was cut using scissors, and the blood was allowed to bleed into the abdominal cavity. Immediately following this step, the butterfly needle was inserted into the left ventricle and the whole circulatory system was perfused with 50mL of papaverine containing saline for 5 minutes. Following this, the implants were explanted from the back of the mice, and placed into 4% formalin overnight. These implants were than rinsed with successive washes of DPBS, and then where placed on microscope slides for whole-

mount confocal imaging. Tomato lectin was imaged using the 488nm laser on a Nikon C2+ laser scanning confocal head attached to a Nikon Eclipse-Ti.

CHAPTER 4

AIM 2: *IN SITU* TRIGGERABLE LIGAND PRESENTATION FOR THE REAL-TIME TRACKING OF FOCAL ADHESION FORMATION AND FORCE GENERATION

4.1 ABSTRACT

We demonstrate the use triggerable ligand presentation using a caged-RGD molecule covalently tethered to the surface of the multiple post array deflection substrate (mPADs). Using a silane-PEG-NHS ester we developed a novel method of tethering small ligands and peptides to PDMS surfaces. The ability to microcontact print silane onto surfaces furthers its utility in complicated microfabricated softlithography tethering schemes. Caged-RGD tethering to mPADs in conjunction with WT-eGFP-MEF cells was able to support normal cell adhesion, spreading, and vinculin localization to focal adhesions. The efficiency of uncaging using the 403nm confocal laser was validated using caged-fluorescein tethered to mPADs surfaces and a full titration of stimulation conditions was performed. Using a mixture of 50% static RGD and 50% caged-RGD, we have demonstrated the first real-time tracking of vinculin localization and cell traction force generation on multiple post array deflection substrates following triggered RGD presentation via *in situ* laser-based uncaging. These studies have shown that vinculin recruitment to increased RGD ligand presentation occurs independently of force generation. Additional RGD presentation to established, mature focal adhesions resulted in immediate increase in traction force generation, while vinculin localization is

delayed by over 200 seconds. Taken in whole, this study demonstrates the power of *in situ* triggerable ligand presentation and the real-time tracking of focal adhesion formation and force generation, and it has shown two possible pathways for vinculin localization to focal adhesions depending on the amount of contractile force across a single focal adhesion.

4.2 INTRODUCTION

Integrin-mediated cell adhesion to ECM provides both mechanical anchorage and signals that mediate cell migration, proliferation, and differentiation [23, 129], processes that are central organization, maintenance, and repair of tissues. Adhesion to ECM components, such as fibronectin (FN), and laminin, is primarily mediated by the integrin receptor family [23]. After ligand binging and activation, integrins form focal adhesion (FA) complexes that transmit adhesive and traction forces [118, 130-132]. Focal adhesions consist of integrins and actins separated by a ~40nm core that includes cytoskeleton (CSK) elements such as vinculin and talin, and signaling molecules such as focal adhesion kinase and paxillin [133].

Focal adhesions are dynamic structures whose size and composition are actively remodeled during cell migration [29, 30]. Assembly of focal adhesions is regulated by numerous pathways in response to external stimuli – including signaling by growth factors and stimulation by mechanical force [31-33]. Focal adhesions mediate responses to internal and external stresses by modulating force transfer between integrins and the actin cytoskeleton [33, 132, 134]. This function is analogous to a "mechanical clutch" between and engine and a transmission [135].

Vinculin (116 kDa, 1066 amino acids) is an actin binding protein consisting of a globular head linked to a tail domain by a proline-rich strap and its interaction with

binding partners has been well mapped for all three domains [136]. Vinculin contains a talin binding site in its globular head (V_H) and an actin binding site in its tail domain (V_T). Interactions between V_H and V_T are regulated by an auto-inhibited conformation arising from strong head-tail binding [137]. V_H contains talin, α-actinin, and α- and β-catenin binding sites. V_T contains actin, paxillin, and phosphatidylinositol 4,5 biphosphate (PIP2) binding sites. The proline rich region contains binding sites for vasodilator stimulated phosphoprotein (VASP), actin-related protein 2/3 (Arp2/3), and vinexin. One case of vinculin activation includes the simultaneous binding of to talin and actin. When vinculin localizes to focal adhesions, vinculin forms a complex with β1 integrin and talin [138]. FRET studies in live cells indicate that vinculin exhibits a spatial gradient of activation that correlates with FA dynamics [139]. While vinculin is not required for FA assembly, vinculin deletion is embryonically lethal and leads to aberrant cell spreading and migration, cardiomyopathies, and defects in hematopoietic stem cell repopulation [13, 140-143]. It has recently been shown that vinculin a critical mediator of force generation between adhesive clusters and the cytoskeleton that stabilizes focal adhesions [144, 145].

Dumbauld et. al., performed through characterization of vinculin-null mouse embryonic fibroblasts (MEFs) that re-expressed WT, T_{12}, and V_H eGFP-vinculin mutants [145]. These studies on FN-coated mPADs showed that vinculin regulates the transmission of adhesive forces by modulating ECM-integrin complexes through its head (V_H) domain and acted as a link to the actin cytoskeleton via the tail domain (V_T). Furthermore, vinculin regulated the cell area-traction force coupling and myosin contractility-dependent traction force. They also showed that in WT MEF cells, vinculin residence time at a focal adhesion correlates linearly with the force applied to the focal adhesion. The data supported a model for vinculin stabilization in which forces applied

across vinculin maintain the molecule in its active conformation and to increase residence times at focal adhesions to promote force transfer.

Despite extensive characterization of vinculin and its role in force generation on native full-length ECM proteins, these systems still rely on static presentation of ECM molecules. There have been no studies that utilize the dynamic materials that can modulate adhesive ligand presentation in real-time to study the correlation between vinculin recruitment and force generation. In this study, we demonstrate the use of caged-RGD presenting mPADs, that can through confocal-based laser irradiation can effectively trigger additional RGD ligand presentation and track downstream vinculin recruitment and force generation.

4.3 RESULTS AND DISCUSSION

A significant limitation of the traditional mPADs system is that it relies on the passive adsorption of ECM proteins (e.g., fibronectin) onto the PDMS posts. Surfaces based on synthetic simplified ECM peptides have shown promise as a model system to study integrin specific interactions with materials. However, due to the small size of these oligopeptides (typically <500 Da), they cannot be adsorbed stably to a surface. Herein, we will describe two strategies to tether these peptides to a PDMS surface: "protein μCP" and "direct tether".

4.3.1 Streptavidin-based Protein μCP for Small Molecule Immobilization

The streptavidin-biotin interaction has long been used as a coupling chemistry in affinity purification and surface immobilization strategies. Since streptavidin is a 52kDa protein, it can be readily adsorbed to the PDMS surface. With the use of biotinylated-peptides, we can exploit the biotin-streptavidin interaction to tether small peptides to the PDMS surface. By using microcontact printing (μCP), we are able to pattern streptavidin islands onto PDMS, and then couple biotinylated-peptides to the streptavidin islands (Figure 39).

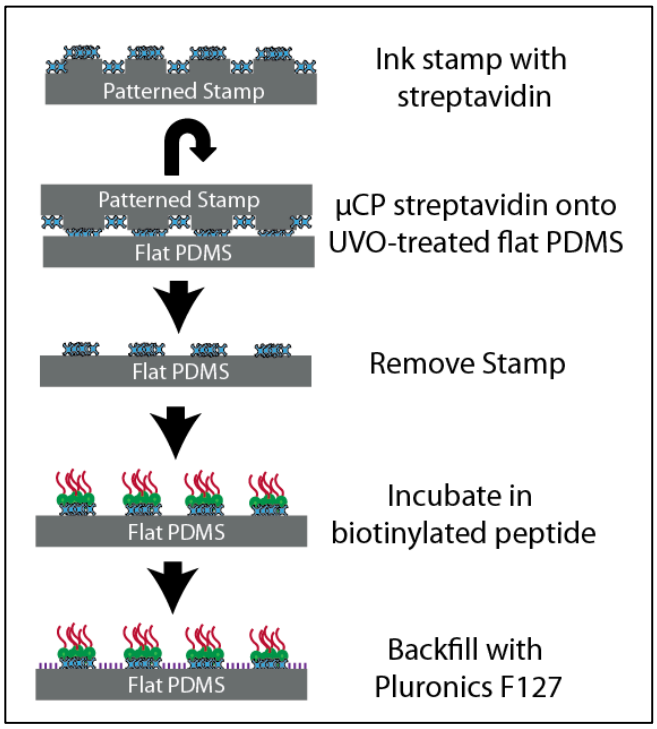

Figure 39. Schematic of Small Biomolecule Immobilization via μCP of Streptavidin. Schematic of fabrication flow for small molecule tethering to PDMS via streptavidin-biotin. Stamps are inked with streptavidin and microcontact printed onto UV ozone treated PDMS, the stamp is removed, and the PDMS surface is incubated with biotinylated peptide, the surface is then backfilled with Pluronics F127 to passivated the surface against non-specific protein absorption.

In order to perform characterization on the efficiency of this tethering methodology, we employed the use of fluorescently tagged streptavidin and biotin proteins. We demonstrate the successful patterning of labeled-streptavidin on a flat PDMS surface with high efficiency (Figure 40, A). Using a labeled-biotin conjugate, we are also able to show specific tethering of biotin to the streptavidin islands (Figure 40, B). The co-localization of the tagged-biotin (*red*) to tagged-streptavidin islands (*blue*), demonstrates the specificity of biotin-conjugates to patterned streptavidin (Figure 40, C).

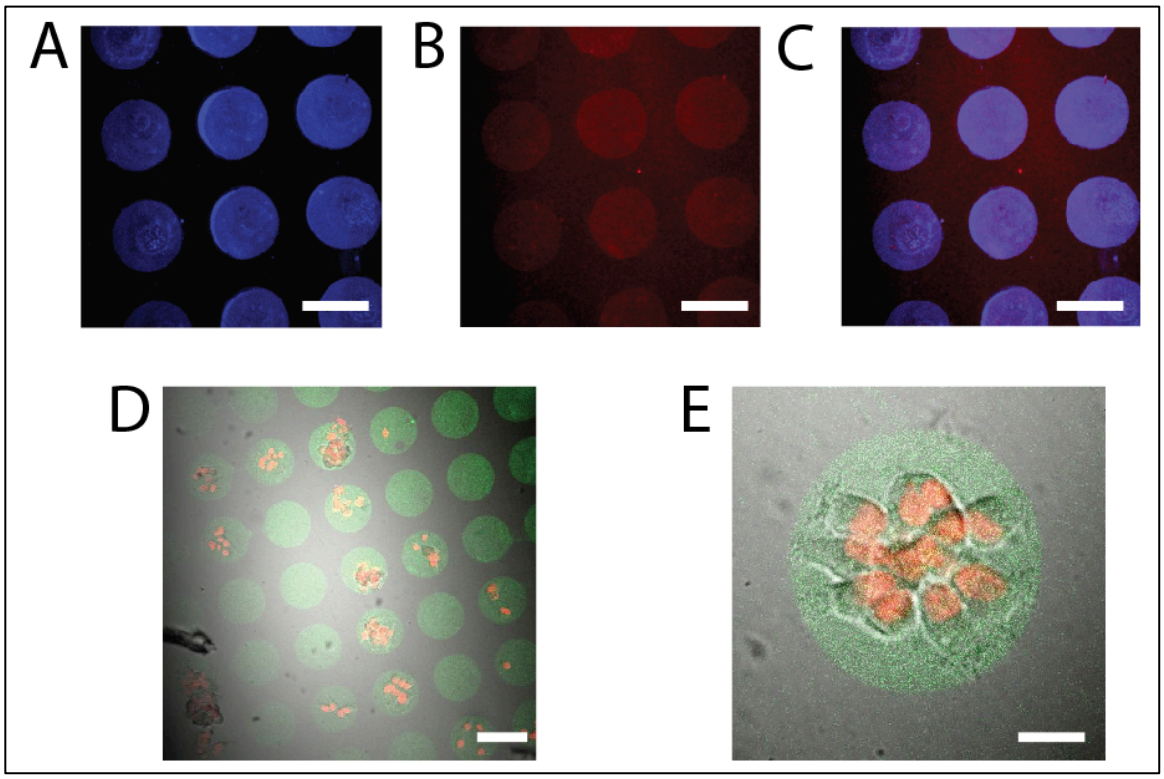

Figure 40. Immunofluorescence Characterization of µCP Surface and Cell Attachment. A) Alexaflour488-labeled streptavidin (*blue*) patterned in 100um islands. Scale bar 50µm B) Atto-655 conjugated biotin (*red*) tethered to streptavidin islands. Scale bar 50µm C) Overlay of Atto655-biotin (*red*) colocalized to streptavidin islands (*blue*). Scale bar 50µm D) Low magnification view of HT1080 cell attachment to array of patterned streptavidin with bound biotinylated-RGD. Images taken at 60x: transmission (brightfield), streptavidin (*green*), cell nuclei (DAPI, *orange*). Scale bar 50µm. E) High magnification view of a single patterned streptavidin island with bound biotinylated-RGD, and HT1080 attachment. Streptavidin (*green*), cell nuclei (DAPI, *orange*). Scale bar 15µm.

In order to test the viability of this method for controlling cell attachment to PDMS, streptavidin islands were patterned and tethered with biotinylated-cyclic(RGD) peptide. HT1080 cells were seeded overnight and allowed to spread. There was generally poor cell attachment to these surfaces indicating inadequate density of RGD ligand (Figure 40, D). When looking at a single island, it is clear that cells have higher

cell-cell contacts, are not spread, and are mostly bipolar in morphology, even though HT1080s should be able to anchor to a single island and become fully spread (Figure 40, E). This low RGD density was either caused by poor streptavidin transfer efficiency during μCP, due to its relatively low weight, or denaturing of the streptavidin during the μCP process from ethanol washes. Therefore, while in principle this streptavidin μCP immobilization method does immobilize RGD ligand; its tethering efficiency is inadequate for the purpose of our study. If cell spreading and attachment was inadequate on a flat PDMS surface, it would be woefully inadequate on mPADs surfaces that have less the 25% of the available surface area for cell attachment in the same cell spread area.

4.3.2 Silane-PEG-NHS-based Direct Covalent Tethering of Small Biomolecules

Clearly, a new approach was needed to address the limited RGD tethering efficiency. Using a "direct tether" approach, we have developed a simple way to tether any small peptide/biomolecule to –OH presenting surfaces, such as silicon, glass and PDMS. The silane-PEG-NHS ester molecule was ideal for our application. It contains a silane group that readily reacts with –OH moieties in organic phase at extremely high efficiency. Its long PEG chains will allow for high density packing on a suitable surface and at the same time prevent non-specific cell adhesion in tethered regions. The NHS-ester is ideal for tethering to the amino-terminus of linear peptides or primary amines on cyclic peptides and larger biomolecules. A simple two-step, two-phase tethering scheme was developed in order to react each side of the silane-PEG-NHS ester at maximum efficiency (Figure 41, A). The silane group was tethered to the PDMS in organic phase, dissolved in DMSO. This prevented premature hydrolysis of the NHS ester. Then the surfaces were rinsed in ethanol for sterilization, and then transferred to peptides that were dissolved in sodium bicarbonate (aqueous phase). This allowed for the direct

tethering of peptides to the surface via displacement of the NHS ester. These surfaces were rinsed to remove excess silane and unconjugated peptides.

Using this method, cyclic(RGD) was immobilized onto a flat PDMS surface, and HT1080 cells seeded overnight. Cells were fixed and stained with V284 antibody (vinculin localization) and phalloidin (actin cytoskeleton). Cells exhibited normal cell attachment, spreading, and formation of robust focal adhesions (Figure 41, B). These results indicate that for direct incubation of silane onto surfaces, followed by tethering of cyclic(RGD), there was adequate adhesive ligand density to support normal cell spreading and focal adhesion formation.

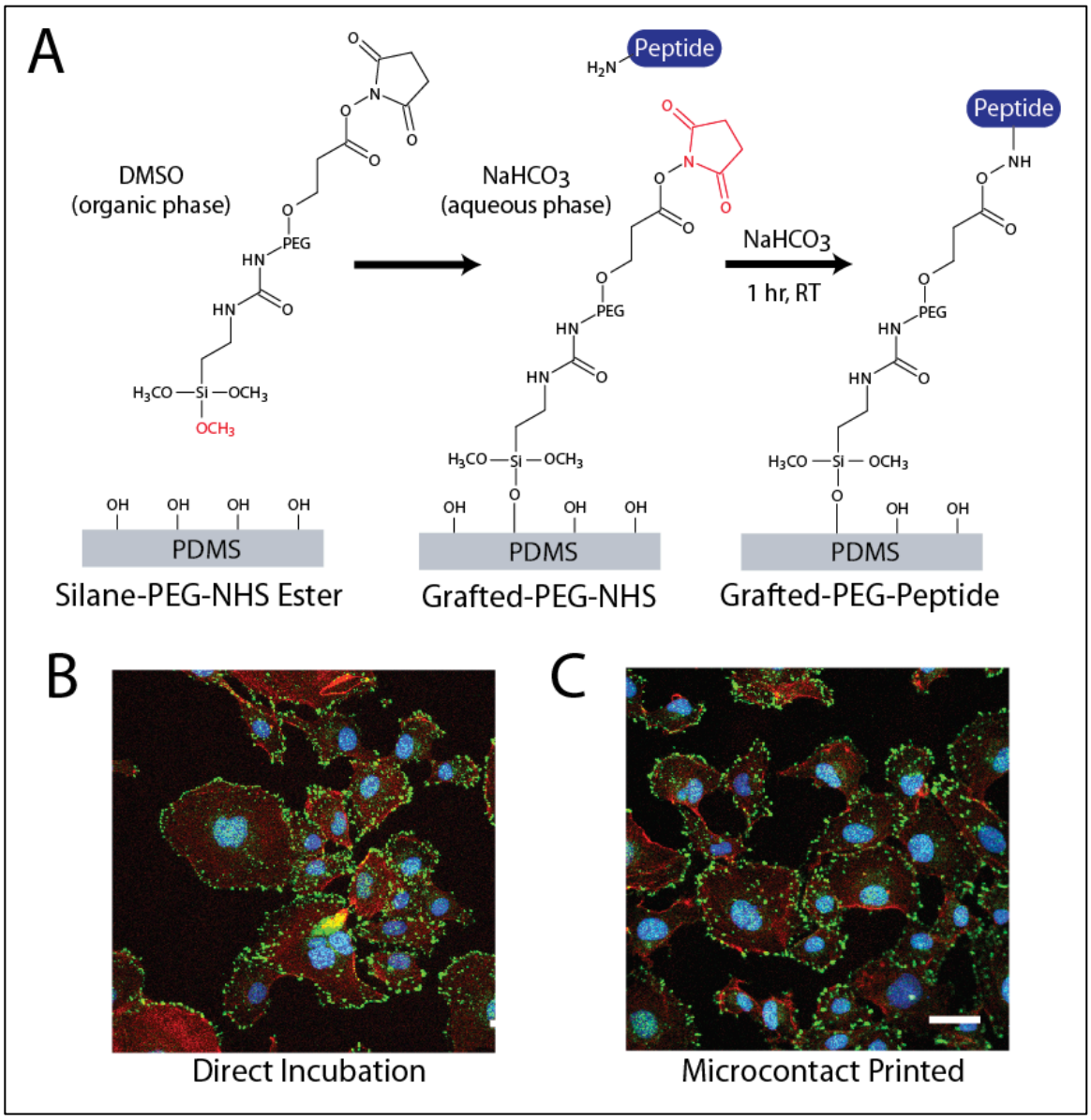

Figure 41. Silane-PEG-NHS Ester *In vitro* Characterization. A) Tethering Chemical Schematic. Silane-PEG-NHS Ester reacts with –OH groups on PDMS surface in organic phase, NHS-ester is displaced by primary amine containing peptide in aqueous phase. B) Direct Incubation vs. Microcontact printing silane; HT1080s seeded overnight. FA staining shown; DAPI (*blue*), vinculin (*green*), phalloidin (*red*). Scale bar 5µm.

On mPADs surfaces, however, direct incubation with silane was not possible. Tethered peptides had to be localized only to the tips of the posts, and any direct

incubation in silane solution would results in unwanted peptide tethering to the regions between posts. Therefore we had to assess the possibility of microcontact printing (μCP) silane, instead of direct silane incubation. By applying silane-PEG-NHS ester dissolved in DMSO to an untreated PDMS stamp, there should be minimal silane coupling. After blow-drying under a stream of nitrogen, there should still be silane adsorbed on the surface on the stamp. By inverting the stamps onto an oxygen-plasma treated PDMS surface, the silane should then covalently tethered to the receiving surface. Following incubation with cyclic(RGD) and the subsequent immobilization of the adhesive peptide, HT1080 cells seeded and allowed to spread overnight. Cells were fixed and stained with V284 antibody (vinculin localization) and phalloidin (actin cytoskeleton). When compared to the direct incubation approach (Figure 41, C), the μCP method appears to support normal cell attachment, spreading, morphology, and focal adhesion formation (Figure 41, C). Therefore, we validated μCP-based approach to peptide tethering.

4.3.3 Silane-PEG-NHS Ester-based Tethering of Cyclic(RGD) Supports Cell Adhesion and Focal Adhesion Formation

μCP of silane-PEG-NHS ester appeared to be the ideal candidate for immobilizing small biomolecules and peptides to mPADs surfaces. This method was validated for the mPADs system through cell attachment and focal adhesion formation assay. A flat PDMS stamp was inked in 4% (w/v) silane-PEG-NHS ester dissolved in DMSO to prevent the premature cell hydrolysis of the NHS ester. The stamp was then dried under a stream of nitrogen, inverted, and brought into contact with an oxygen plasma-treated mPADs device. This plasma treatment increases the density of –OH presenting groups on the surface and is critical for high efficiency silane tethering. The

samples were then washed in ethanol and then three serial washes of sodium bicarbonate buffer ($NaHCO_3$, pH 8.2), and incubated with peptide dissolved in $NaHCO_3$. Efficient NHS ester-mediated tethering must be done at near pH 8.2, under aqueous conditions. Following tethering, samples are labeled with Δ9DiI and passivated with Pluronics F127.

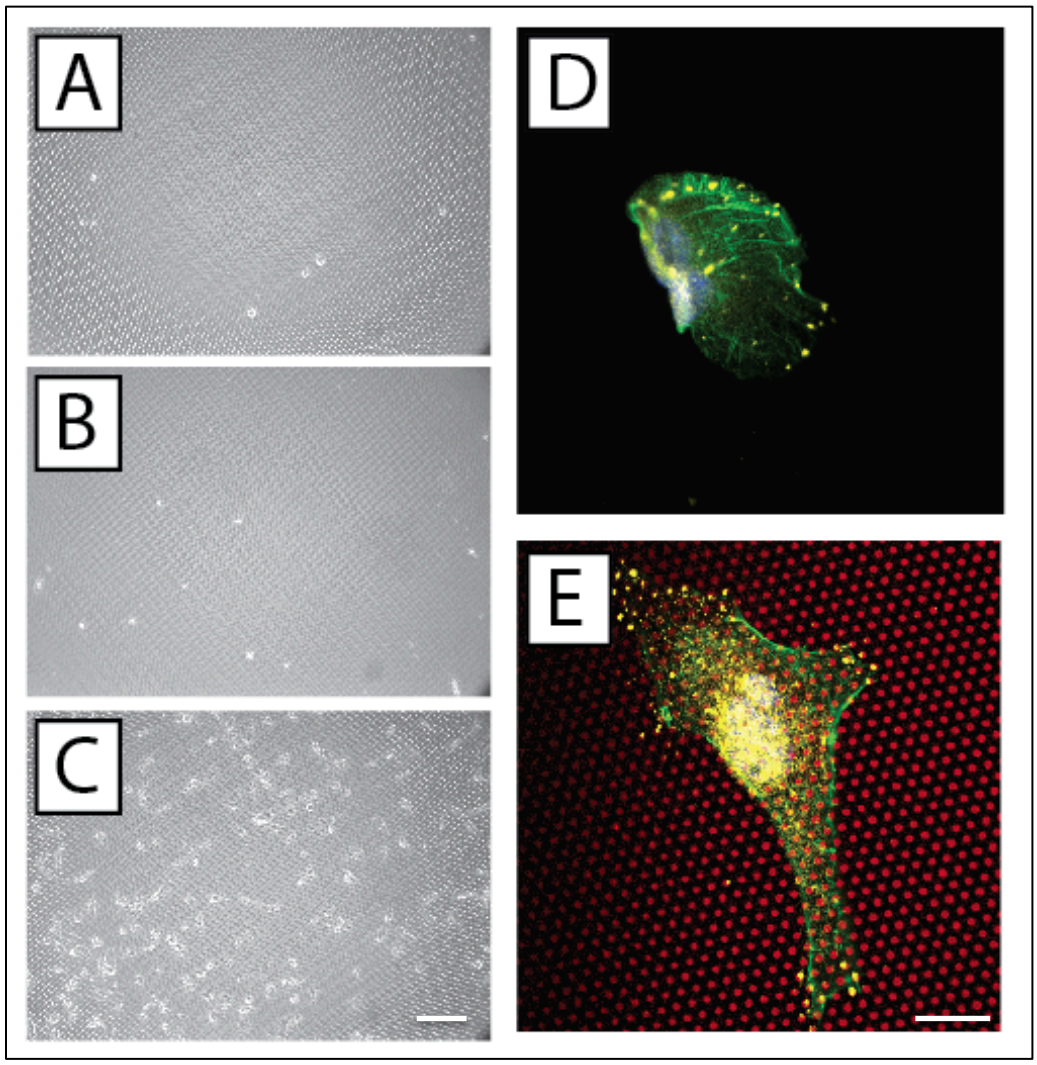

Figure 42. Silane-PEG-NHS on mPADs Characterization. A) (-)silane (+)RGD control. B) (+)silane (-)RGD control. C) (+)Silane (+)RGD condition. [A-C: Images taken 20x Ph1, 24 hours post seeding on mPADs, scale bar 50μm]. D) Microcontact printed (+)silane (+)RGD flat control on mPAD device. E) Microcontact printed (+)silane

(+)RGD, cell spread on mPADs. [D-E: Images are >60x on Laser Scanning Confocal; DAPI (*blue*), phalloidin (*green*), vinculin (*yellow*), posts (*red*), scale bar 20μm].

HT1080 cells were seeded overnight in order to determine the viability of this direct tether approach for mPADs traction force studies (Figure 42). Cells were fixed and stained with V284 antibody (vinculin localization) and phalloidin (actin cytoskeleton). In the controls that either contained (-)silane or (-)cyclic(RGD) peptide, there was minimal cell spreading and attachment (Figure 42, A and B). The (-)silane result is consistent with the fact that cyclic(RGD) peptide is too small to passively adsorb to PDMS surfaces. The (-)cyclic(RGD) condition was used to demonstrate the efficacy of silane tether to effectively resist non-specific protein adsorption. Standard tethering with (+)silane and (+)cyclic(RGD) show normal cell spreading and proliferation on a mPADs surface (Figure 42, C). Both on a flat region on the mPAD device and the normal pillar array cells exhibit standard cell spreading, normal morphology, and focal adhesion formation (Figure 42, D and E). Therefore, the mPADs system in conjunction with the silane-PEG-NHS ester tether was shown to be a promising platform for detailed investigation of mechanotransduction and cell traction force events on highly defined engineered small biomolecule surfaces.

4.3.4 Tethered RGD vs. FN on mPAD Surfaces

Traditional studies of cell traction force on mPADs have been performed with passively adsorbed fibronectin (FN). The RGD peptide is known to be the minimal adhesive sequence of the FN molecule. Fibronectin has multiple RGD binding sites and synergy sites (i.e. PHRSN) that all serve to stabilize and reinforce focal adhesions. In order to perform detailed investigations of single mechanotransduction and cell traction

force events, we must use simplified engineered surfaces that present only single ligands. The RGD peptide is specific a small family of integrins, including $\alpha_1\beta_1$ and $\alpha_v\beta_3$.

Traction force vs. cell area measurements were performed on RGD and FN coated mPADs. The cells used in these mPADs studies were a stable line of vinculin-null MEFs with retroviral expressed WT-eGFP-vinculin, and from this point will be referred to as WT MEFs. WT MEFs were seeded on mPADs (FN and RGD surfaces) and allowed to spread overnight to reach steady state. WT MEF cells on RGD surfaces exhibited markedly lower traction forces and cell spreading when compared to FN surfaces (Figure 43, A). On FN surfaces, there was a linear relationship between cell traction force and cell area, which is consistent with previous findings [118]. Interestingly, on RGD surfaces there was also a linear relationship between cell traction force and cell area. Linear regressions were performed on both data sets, and they exhibited similar slopes (Figure 43, B). It appears that RGD is a critical regulator of cell spreading the cell area in MEF cells, and when in combination with the PHSRN or other sites on the FN molecule, the MEF cells can exert spread more and exert higher traction forces.

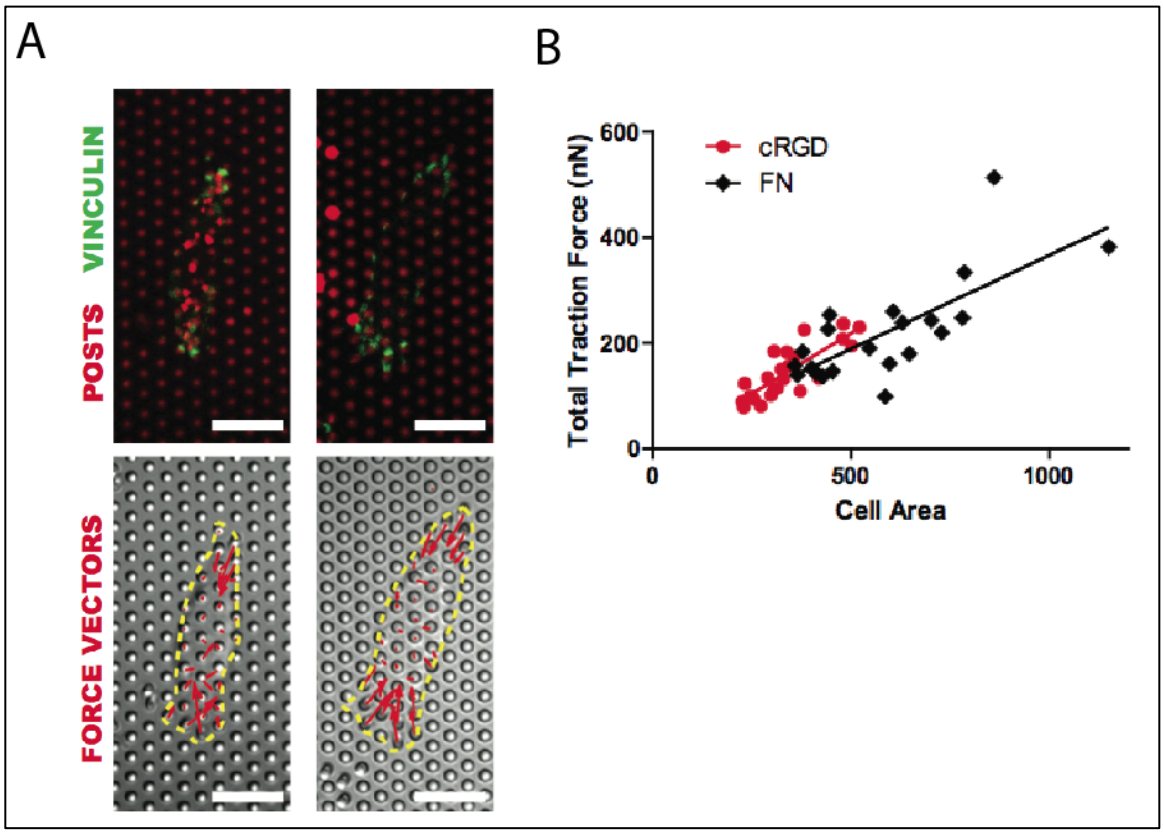

Figure 43. Traction forces of MEFs on Tethered Cyclic(RGD) vs. Passively Adsorbed Fibronectin mPADs . A) WT eGFP-vinculin expressing MEF cells on mPADs. Left column, RGD condition. Right column, FN condition. Top row, vinculin localization (*green*), and posts (*red*). Bottom row, traction forces (red arrows), and cell outline (yellow). Scale bar 10µm. FN conditions exhibit better cell spreading and traction force generation. B) Total traction Force vs. Cell Area of WT eGFP-vinculin expressing MEF cells for cyclic(RGD) conditions vs. FN. Note: regression lines are similar in slope, MEF cells on RGD surfaces have proportionally lower cell traction force and cell spreading.

4.3.5 Cell Adhesion to Silane-PEG-RGD Surfaces Is Mediated by β1 and β3 Integrins

In order to confirm that the mechanism of RGD adhesion via silane-PEG-NHS ester tethering was indeed due to integrin-receptor interactions, an antibody blocking experiment was performed. Flat PDMS surfaces were prepared with tethered

cyclic(RGD) and passivated with Pluronics F127. WT MEF cells were incubated with blocking antibodies for β1, β3, or both β1 and β3. These cells were then seeded on cyclic(RGD) surfaces. WT MEF cells without antibodies were seeded on cyclic(RGD) and RDG surfaces to serve as positive and negative controls.

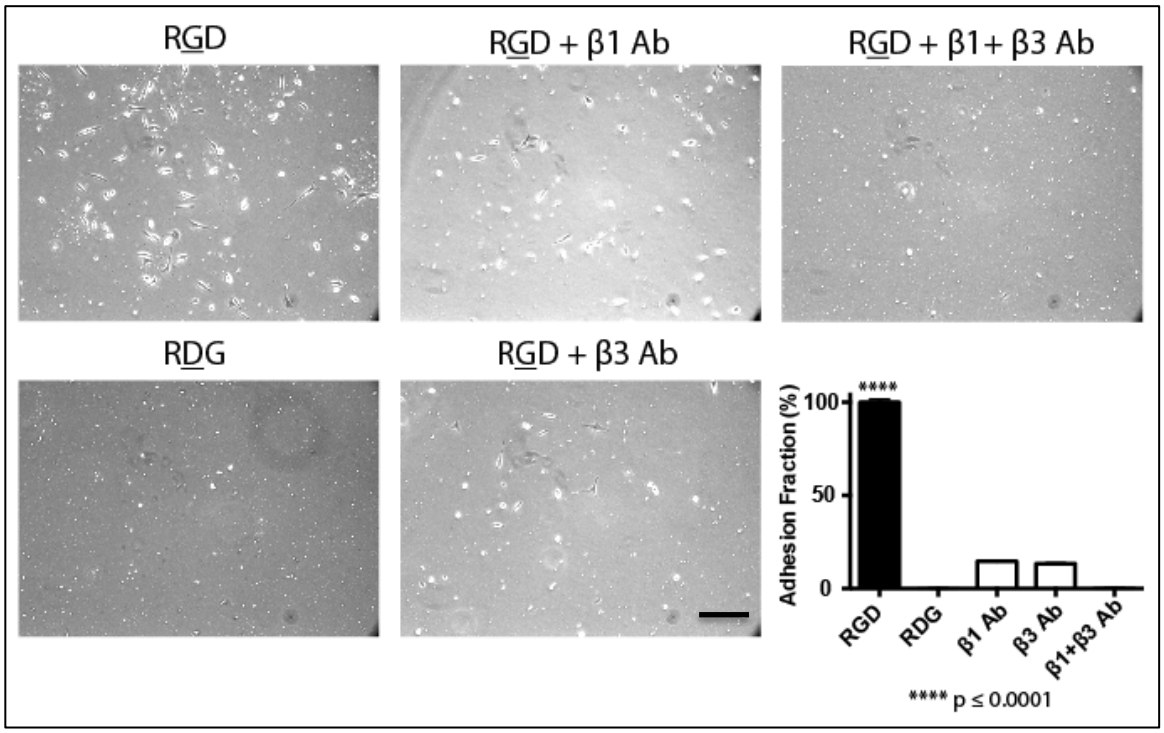

Figure 44. Antibody Blocking of β1 and β3 on Silane-PEG-Peptide Surfaces. RGD control exhibits normal cell spreading and adhesion. RDG control has no cell attachment. RGD surface with β1 antibody and RGD surface with β3 antibody have minimal cell attachment and poor cell spreading. RGD surface with both β1 and β3 antibodies exhibit no cell attachment or spreading. Results are quantified in graph, all conditions except RGD have low cell adhesion fraction ($p<0.0001$). Scale Bar 100μm.

WT MEFs attached and spread normally to the RGD control and no cells attached to the RDG surfaces. Both β1 and β3 blocking conditions exhibited low levels of cell attachment and had poor spreading, characterized by the bipolar morphology of

cells. Under the combined β1 and β3 blocking condition, there was almost no cell attachment or spreading. Therefore, we can conclude that β1 and β3 integrins are responsible for RGD dependent adhesion and spreading in WT MEFs.

4.3.6 WT MEF Cells on Silane-PEG-caged-RGD Surface Exhibit Cell Spreading and Focal Adhesion Formation

We then validated the efficacy of tethering the caged-RGD ligand using the silane-PEG-NHS ester direct tether approach using WT MEF cells. Static RGD and caged-RGD was tethered to mPADs using the chemistry outlined Figure 41, A. Samples were irradiated at 361nm wavelength, using a wide-field UV lamp with a bandpass filter, before cell seeding. WT MEF cells were seeding onto mPADs substrates after preparation and were allowed to spread overnight (Figure 45, A). The controls either without silane or without caged-RGD exhibited no cell attachment and spreading, which is consistent with the absence of adhesive ligands on the mPADs surface. With the tethering of static RGD ligand, in both the presence and absence of UV irradiation, WT MEF cells exhibited normal cell attachment and spreading. In contrast, in the caged-RGD conditions, in the absence of UV irradiation, there was minimal cell attachment and spreading, consistent with the assertion that the caging group remains intact, and no RGD was presented. With UV irradiation, the caged-RGD presenting mPADs exhibit normal cell attachment and spreading, validating the ability of caged-RGD to modulate cell attachment and spreading on mPADs. Therefore, the efficacy of the UV labile DMNPB caging group, using the wide-field UV irradiation, was validated on the mPADs system. It is clear that WT MEF cells can exhibit measureable traction forces and eGFP vinculin localization—sample confocal images of posts (*red*) and vinculin localization (*green*) are shown in Figure 45, B and C.

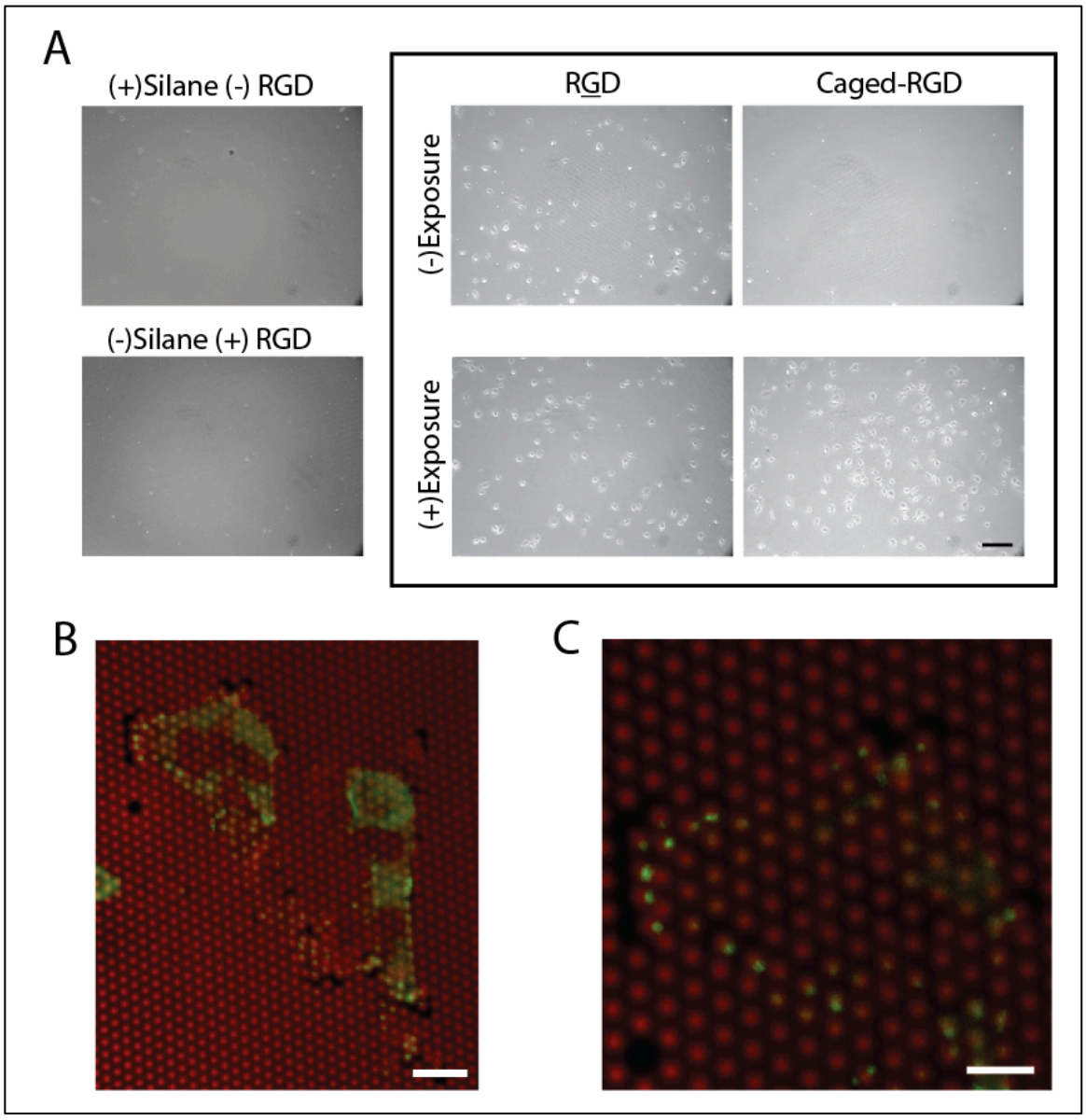

Figure 45. Validation of Caged-RGD tethering to mPADs Surface. A) *In vitro* Characterization of caged-RGD surfaces. (+)silane (–)RGD and (–)silane (+)RGD controls exhibit no cell attachment. Both unirradiated and irradiated static cyclic(RGD) surfaces exhibit normal cell attached and adhesion. Unirradiated caged-RGD exhibits no cell attachment. Irradiated caged-RGD condition exhibits normal cell spreading and attachment similar to static cyclic(RGD) controls. Scale bar 50µm. B) Multiple WT eGFP-vinculin MEF cells on mPADs exhibiting normal cell spreading, vinculin localization and force generation. Scale bar 20µm. C) Zoomed view of WT eGFP-

vinculin MEF cells on mPADs showing vinculin localization and force generation. Scale bar 10μm.

4.3.7 Validation of Uncaging Efficiency on mPADs Surface Using Tethered Caged-fluorescein

The previous section demonstrated the ability of the silane tethering system to immobilize small peptides to PDMS surfaces, specifically caged-RGD and the preservation of function of the UV labile caging group via wide-field UV irradiation. We demonstrated in the previous section that the silane tethering chemistry did not impact the stability and integrity of the DMNPB caging group of caged-RGD on mPADs surfaces. While the UV labile moiety on caged-RGD is optimized for maximum efficiency at 361 nm, our confocal microscope only has a UV laser at 403 nm. Thus, the efficiency of the UV labile caging group at 403 nm was investigated using a fluorescent analog of the caged-RGD molecule, caged-fluorescein. Caged-fluorescein contains a similar caging group and utilizes the same linker chemistry as the caged-RGD. In its caged form, caged-fluorescein is not fluorescent. Through 361 nm UV irradiation, the caged-fluorescein molecule becomes “uncaged,” thereby restoring its fluorescence emission. The uncaging efficiency of caged-fluorescein was determined when tethered to surface of mPADs (scheme shown in Figure 46).

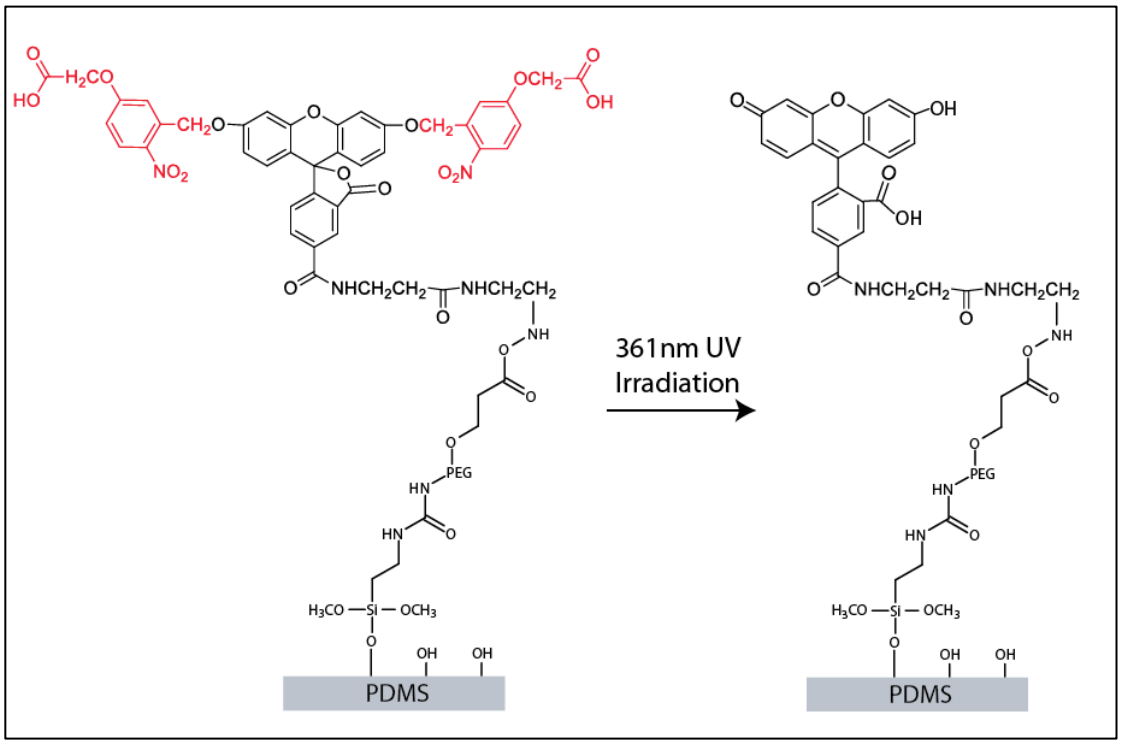

Figure 46. Covalent Tethering of Caged-fluorescein to mPADs. Caged-fluorescein is immobilized to PDMS surface via reaction with silane-PEG-NHS ester. Caging groups are highlighted in RED. Caging groups are cleaved via 403 nm laser scanning confocal-based irradiation.

Using the stimulation function of the Nikon Elements software, a 2 µm diameter circular ROI was defined and centered on a single post. Using 1.96% laser power of the 403 nm laser and a 1 frame per second (fps) stimulation speed, the caged-fluorescein molecule was successfully uncaged at maximum efficiency. The 403 nm ROI-based laser stimulation offers unparalleled spatial control of fluorescein presentation using sequential stimulations (Figure 47). Although the mPADs device is excellent at scattering and diffracting light, we can see that using laser-based 403 nm irradiation, there is minimal activation of adjacent posts (Figure 47, C). This specific activation is already far superior than a photolithography based approach because a photomask

cannot be brought into conformal contact with the mPADs and cell substrate. A titration of laser power and scan speed was performed to demonstrate the ability of the 403 laser to modulate exactly the degree of uncaging on a single post (Figure 47). These stimulation events were performed sequentially using the Nikon Elements software.

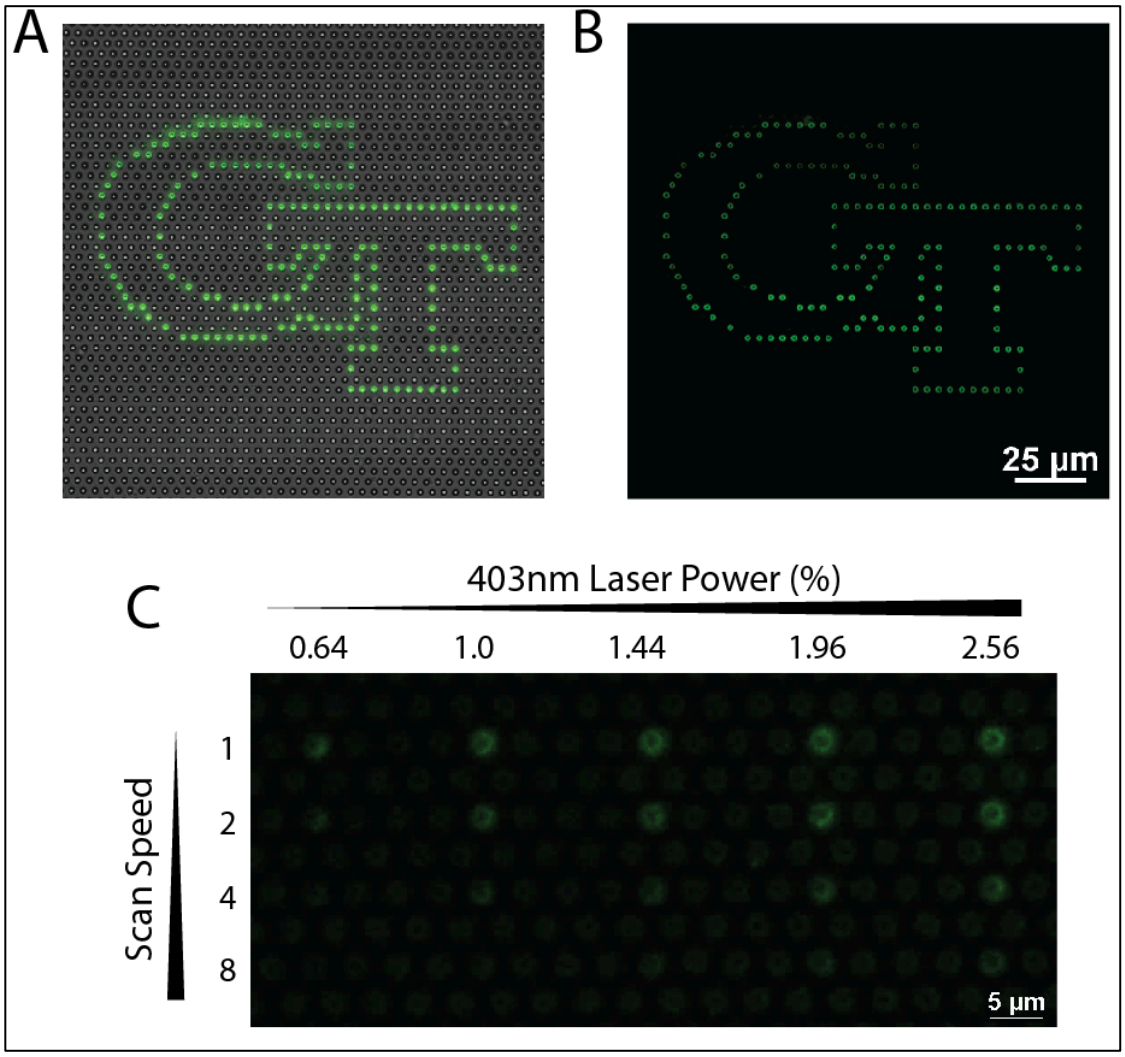

Figure 47. Caged-fluorescein Characterization on mPADs. Georgia Tech logo patterned on mPADs using 403 nm laser on individual posts. A) Transmission and fluorescein B) fluorescein only, scale bar 25 µm C) Stimulation laser power and scan speed titration; laser power varied from 0.64% to 2.56%, scan speed varied from 1 to 8 frames per second.

In the previous section, we demonstrated real-time *in situ* confocal-based uncaging was a promising platform for the spatiotemporal presentation a single molecule on a single post. Applied to the caged-RGD molecule, it is clear that in conjunction with WT MEF cells, we would be able to track in real-time the effects of RGD-ligand presentation of a single post or focal adhesion on vinculin recruitment and force reinforcement. This type of spatiotemporal control is currently unprecedented in the cell mechanotransduction world.

4.3.8 Real-time Tracking of Vinculin and Force Generation in WT MEFs

Following successful characterization of the kinetics of the UV-labile DMNPB caging group during confocal-based 403 nm irradiation, mPADs experiments using caged-RGD could now be performed. Caged-RGD and static RGD was tethered to the mPADs in equal molar ratios so that cells were allowed to minimally attach and spread, but still have enough caged-RGD on the surface to later irradiate. These molar ratios can be modified; however, this ratio was determined to be a good balance between steady-state cell contractile force, while still having adequate amounts of caged-RGD to uncage at later timepoints. A limitation of this system however is that there is no good way to characterize this actual concentration of RGD ligand on the surface without using radiometric methods. Using this setup, 403 nm laser stimulation of a single post can dynamically increase the ligand presentation on a single post within the 951 ms, which is the same time it takes for the laser scanning confocal to raster across the post. Therefore, using this caged-RGD, mPADs, and WT MEF cells system, we can modulate

ligand density almost instantaneously and begin tracking force generation and vinculin localization concurrently.

Using time-lapse live-cell confocal microscopy, we dynamically tracked the recruitment of vinculin (WT eGFP-vinculin (488 nm) and subsequent force generation through the deflection of posts (DiI, 561 nm). Using position list-based time-lapse microscope utilizing many stimulation regions of interest (ROI), we could track as many as three different cells, with stimulation of three separate posts. This speed and number of stimulation ROIs was limited by the acquisition speed of the Nikon C2+ confocal system and limitations of the software. Theoretically, using spinning disc confocal microscopy, this system should be able image at least 10 cells, concurrently, and track force and vinculin recruitment with sub-second resolution.

Live cell microscopy using the Nikon C2+ system had to be optimized as to not kill the cells from phototoxicity. It was determined (data not shown) that 0.16% 488 nm laser power, using a 4.3 µsec dwell time, at 512x512 resolution, one frame captured every 10 seconds was a good balance of signal/noise ratio and cell survival. 488 nm laser power higher than 2% was shown to be the upper limit before acute cell phototoxicity (data not shown). 403 nm laser power higher than 5% was shown to bleach 488nm signal and cause phototoxicity (data not shown).

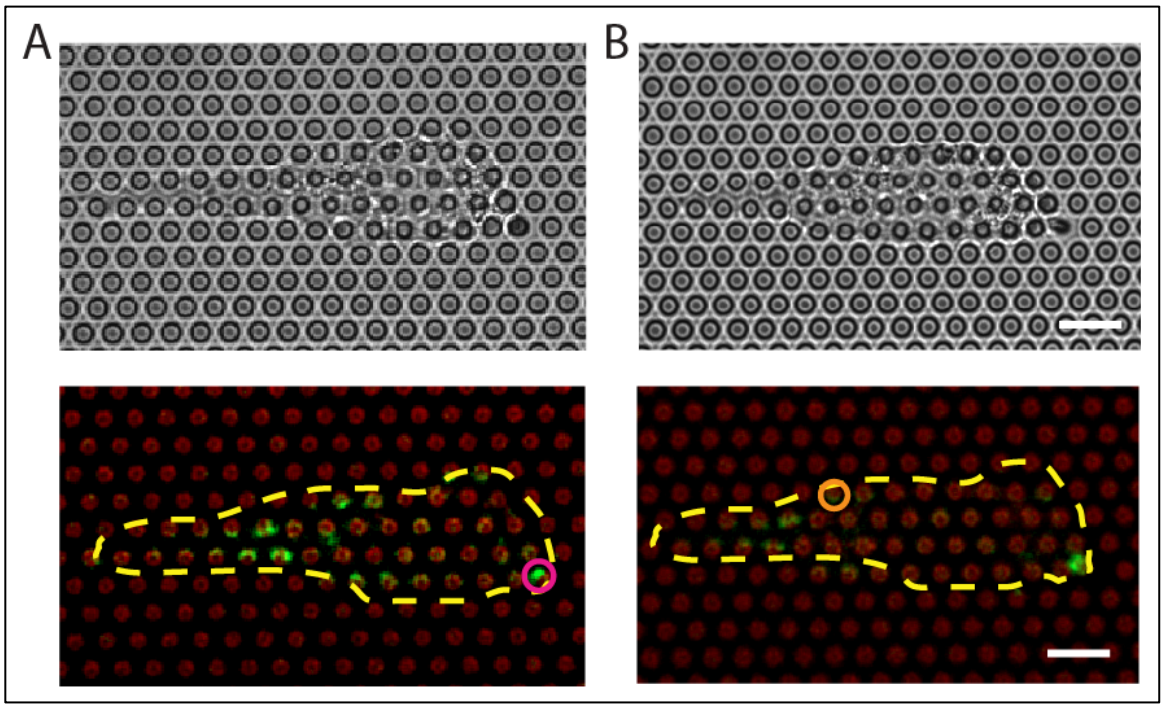

Figure 48. Stimulation of Individual Focal Adhesions of a Single WT MEF on mPAD#5. Panel A (top) shows transmission image of cell, (bottom) shows vinculin localization (*green*), post deflections (*red*), stimulation ROI 1 (*pink*), and cell outline (*dotted yellow*). Panel B (top) shows transmission image of cell, (bottom) shows vinculin localization (green), post deflections (red), stimulation ROI 2 (*pink*), and cell outline (*dotted yellow*). Stimulation ROI 1 and stimulation ROI 2 were performed sequentially, 20 minutes per time-lapse movie. Scale bar 6µm.

For our pilot study, WT MEF cells were seeded on 50% caged-RGD/50 static cyclic(RGD) mPADs #5 (stiffness 18.19nN/um). Cells were allowed to spread overnight to reach a quazi-steady state. Cells were minimally adhesive mostly in rounded or bipolar morphologies, with small focal adhesions being formed on posts. In Figure 48, above, depicts the ROI based irradiation of two separate posts in the same cell (outlined in *yellow*). These two adhesions (Figure 48, A and B) differ in their original amount of contractile force and vinculin localization. In the ROI outlined in *pink*, there is already significant force on the post and strong vinculin localization. In contrast, in the ROI

outlined in *orange*, there is no force on the post, and minimal vinculin localization. In the proceeding section we will investigate this cell in detail.

Using particle-tracking software developed by Mosaic in ImageJ, we are table to track the deflection of every post using the DiI fluorescently labeled posts. This fluorescent labeling of posts is critical because the transmission image of the cells on posts is marred with many artifacts and refraction patterns Figure 48, A. As seen in Figure 48, B, the fluorescent channel image of posts (*red*) is far clearer and leads to simple and accurate tracking of post deflection. By binarizing the image in ImageJ and setting the search parameters for the particle-tracking algorithm, it is able to automatically detect all of the posts in each from of a time-lapse study (Figure 49, A, left). Once the software has found the posts it can automatically track the displacement of each post and plot it onto a user interface (Figure 49, A, right).

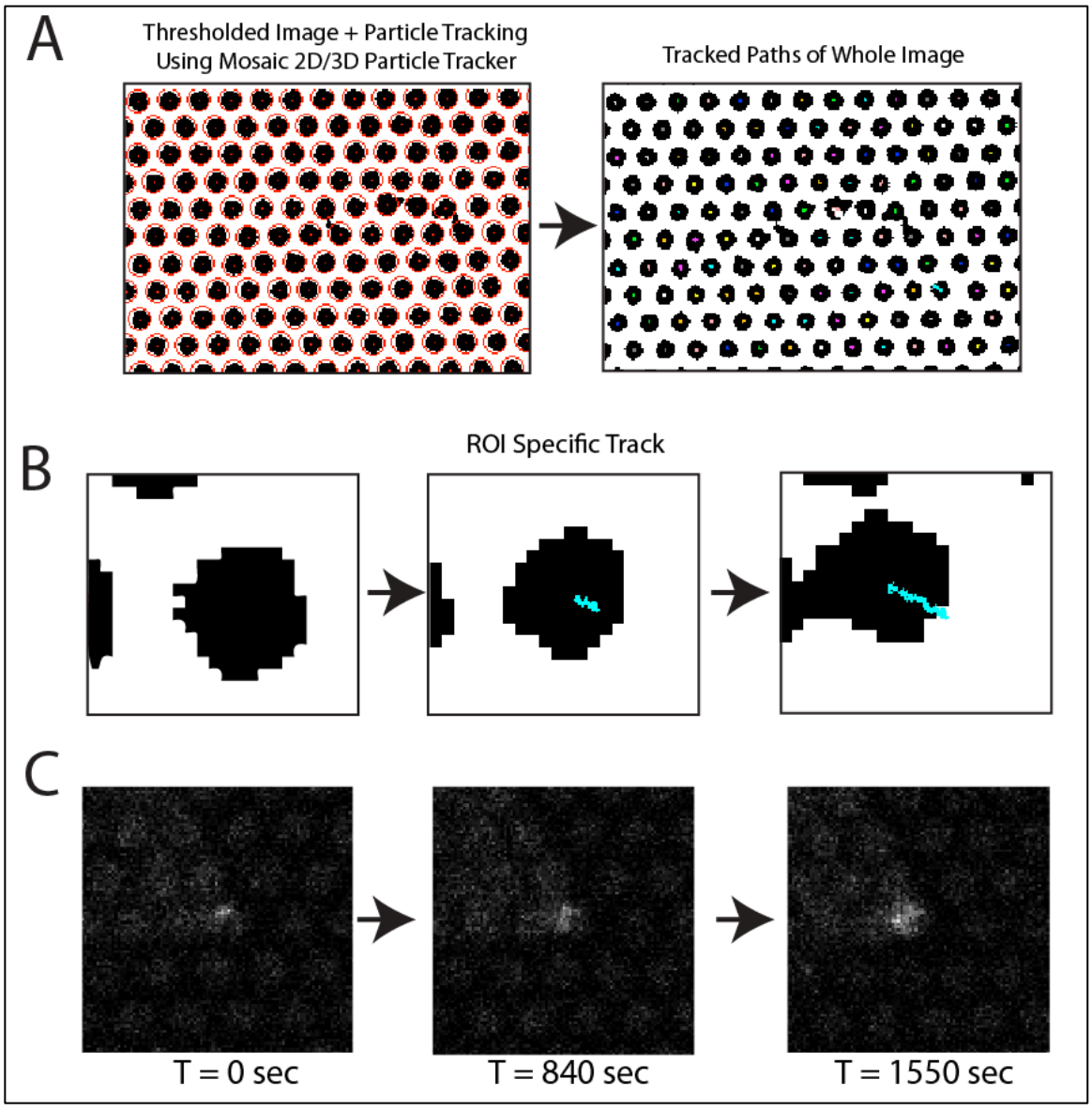

Figure 49. Particle Tracking to Quantify Force and Vinculin Localization. A) ImageJ based analysis of post images using binarization and 2D particle tracking algorithm. B) Output of particle tracking algorithm of a single post, binarized image and path shown in time-lapse form at 0, 840, and 1550 seconds. C) Tracking of vinculin intensity on single post after irradiation in time-lapse faction. Note: there is increased vinculin localization after 1550 seconds.

By selecting an individual post, the software automatically plots the displacement of the post, providing both a path and X-Y coordinates (Figure 49, C). These

coordinates can be exported for graphing purposes. Using this displacement data, combined with the stiffness of the mPADs substrate, we quantified the force that the cell exerted on the post in response to the triggered ligand presentation of RGD. Using the 488 nm eGFP-vinculin images, we tracked the real-time trafficking of vinculin to the irradiated post (Figure 49, C) and exported this data using ImageJ's [stack->"plot z-intensity"] functionality. Using these two data sets, the correlation between force generation and vinculin localization in response to changes in RGD ligand presentation was quantified (Figure 50).

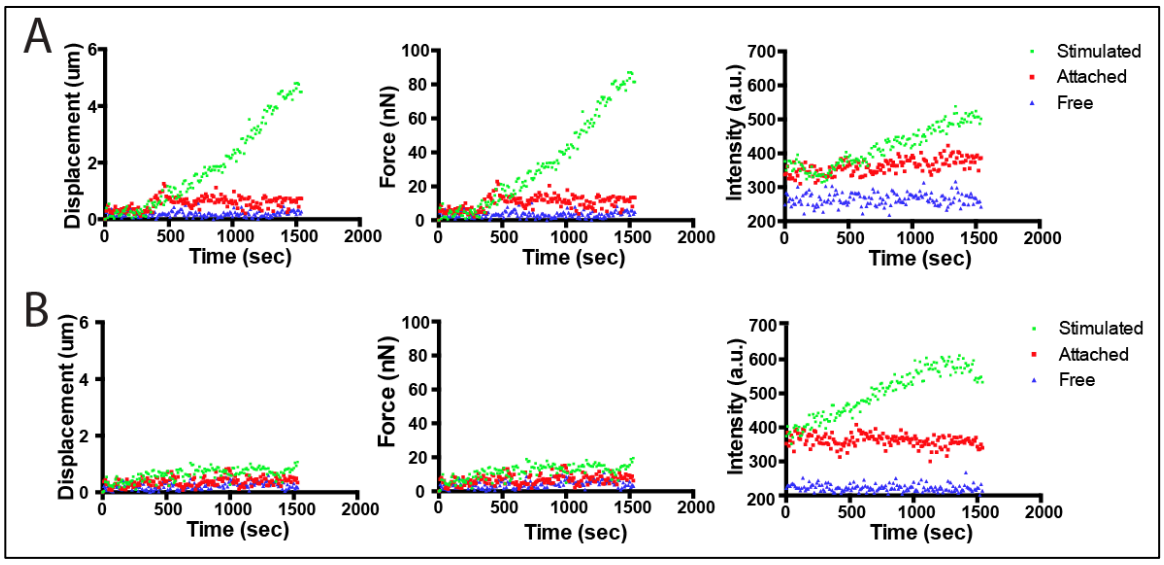

Figure 50. Quantifying the Difference in Force Generation and Vinculin Recruitment in Mature vs. Nascent Focal Adhesions. A) Summary data of stimulation ROI 1 (mature focal adhesion with preexisting deflection) time lapse videos of displacement, force, and intensity vs. time. B) Summary data of stimulation ROI 2 time lapse videos of displacement, force, and intensity vs. time. Green denotes stimulated post, red denotes unstimulated post with cell attached, blue denotes free post with no cell. Note: vinculin recruitment occurs independently of force generation.

In the first ROI, the post is already moderately deflected, and contains a small amount of vinculin localization; this type of adhesion we will classify as a *mature* adhesion. This adhesion was selected because it was already bearing the most force in the cell; therefore, should be strongly coupled to the cytoskeletal machinery for maximal response to uncaging. In control conditions, a post where the cell was attached (attached post) and a free post with no cell (free post), there was no appreciable increase in force generation or vinculin localization over the course of the time-lapse study. Also, it is important to note that there is no photobleaching in the vinculin channel during acquisition as evidenced by no change in vinculin signal in the control attached post; therefore, no post processing of vinculin signal is required. After the first ROI stimulation, both vinculin and force generation increase in response to increased RGD presentation. In this case, increase in force generation precedes an increase in vinculin localization by almost 250 seconds (Figure 50, A, *middle* and *right*). The implications of this will be discussed in the following sections.

A second adhesion was selected in the same cell to demonstrate the versatility of this system to perform independent measurements of force generation and vinculin recruitment in a single cell. This adhesion was selected because there was a very small amount of vinculin localization and no force generation, this type of adhesion we will classify as a *nascent* adhesion. After the second ROI stimulation of a post in the same cell, it appears that there is no force generation, however there is still appreciable vinculin recruitment to the post (Figure 50, B, *middle* and *right*).

This dichotomy in behavior of these adhesions can be explained in several ways. In a mature adhesion, the focal adhesion complex is already stabilized through the formation of a robust adhesive plaque, and vinculin is likely stabilized in a active conformation, linking the focal adhesion complex to the actomyosin-cytoskeletal

machinery. Therefore, when an increase RGD-dependent ligand is detected, the main constituents of the focal adhesion such as talin, paxillin, and FAK are already localized in the area and therefore the stimulated FA can immediately generate more contractile force. Interestingly however, in the mature adhesion, increases in vinculin recruitment over baseline is delayed ~250-500 seconds from the onset of force generation. These results are consistent with recent findings on cell spreading experiments on flat nanopatterned RGD membranes that there is a delayed recruitment of vinculin to RGD clusters while talin, paxillin, and FAK are all recruited almost instantaneously [146]. Furthermore, studies on tension-mediated FA maturation have suggested that FA recruitment of vinculin and FAK are myosin II dependent and that phosphorylation of paxillin is responsible for vinculin recruitment to reinforce the ECM to cytoskeletal linkage and drive FA maturation [147]. Therefore, if myosin II dependent FAK phosphorylation of paxillin were required for vinculin recruitment, then logically vinculin recruitment to contractile FAs would be delayed.

In the case of the nascent adhesion, increases in vinculin recruitment occur immediately after post stimulation, even in the absence of force generation. This is consistent with previous studies have shown that both talin and paxillin is recruited to adhesions even in the absence of myosin II contractility [147]. Additionally, it is known that vinculin can be recruited to focal adhesions in the absence of paxillin [148]. Therefore, these results suggest, vinculin localization to new focal adhesions could be mediated by association with talin-integrin complexes, before the onset of downstream paxillin/FAK mediated myosin II contractility. However, these assertions are beyond the scope of this study.

This novel platform of triggerable RGD-presentation on mPADs has many applications for studying integrin clustering, kinetics and properties of FA formation, and

force generation. Through the generation of new stable cell lines containing both vinculin and other fluorescently labeled FA constituents, such as paxillin and talin, we could elucidate which mechanism is responsible for contractility and force mediated vinculin recruitment. Furthermore, with the use of either FAK (focal adhesion kinase) or SRC FRET based biosensors we could obtain an in-depth understanding of the kinetics of these critical mediators of mechanotransduction in both mature and nascent focal adhesions.

4.4 CONCLUSION

We have demonstrated a novel method of tethering small ligands and peptides to PDMS surfaces using a silane-PEG-NHS ester. This scheme opens up new avenues of research in small molecule presentation on PDMS, glass, and silicon surfaces. The ability to microcontact print silane onto surfaces furthers its utility in complicated microfabricated softlithography tethering schemes. RGD tethering to microcontact printed silane was shown to support normal cell adhesion and focal adhesion formation comparable to the RGD tethered direct incubated approach. Caged-RGD tethering to mPADs in conjunction with WT-eGFP-MEF cells was able to support normal cell adhesion, spreading, and vinculin localization to focal adhesions.

The efficiency of uncaging the DMNPB group using the 403nm confocal laser was validated using caged-fluorescein tethered to mPADs surfaces and a full titration of stimulation conditions was performed. Using a mixture of 50% static RGD and 50% caged-RGD, we have demonstrated the first real-time tracking of vinculin localization and cell traction force generation on multiple post array deflection substrates following triggered RGD presentation via *in situ* laser-based uncaging. These studies have shown that vinculin recruitment to increased RGD ligand presentation occurs independently of force generation. Additional RGD presentation to established, mature focal adhesions, results in immediate increase in traction force generation, while vinculin localization is delayed by over 200 seconds, suggesting that vinculin localization in these adhesions is regulated by signals downstream of myosin II-mediated increases in cytoskeletal tension. In nascent adhesions, however, vinculin localization occurs immediately even in the absence of force generation. This suggests that local focal adhesion adaptor proteins such as talin could be responsible for vinculin localization under low force

regimes. Taken in whole, this study suggests that that there are two pathways for vinculin localization to focal adhesions depending on the amount of contractile force across a single focal adhesion.

4.5 METHODS

Cells and reagents

Mouse embryonic fibroblasts (MEF) vinculin mutants (null, WT, T12, Vh) were provided by David Dumbauld. Growth media was DMEM (Gibco), 10% fetal bovine serum (Gibco), 100 U/mL penicillin G sodium (Gibco), 100 μg/mL streptomycin sulfate (Gibco), 1% non-essential amino acids (Gibco), 1% sodium pyruvate (Gibco). Vinculin antibody (V284; Sigma-Aldrich), actin stain (Phallodin-Alexafluor555; Invitrogen), and nuclear stain (DAPI; Sigma-Aldrich) were used for immunostaining. Human plasma fibronectin was purchased from Invitrogen (Carlsbad, CA). Cyclic(RGD) peptide and RDG peptides were purchased from Peptides International (Louisville, KY). Caged-RGD and caged-fluorescein were generously provided by Arancha del Campo's lab from Max-Planck-Institut für Polymerforschung, Mainz, Germany.

mPADs fabrication

mPADs silicon masters were prepared as previously described [149] and were provided by Jianping Fu's lab from the University of Michigan. The elastomeric micropost arrays were fabricated using Sylgard 184 PDMS (Dow-Corning) via replica molding. To make a microfabricated post array template, PDMS prepolymer was cast on top of mPAD silicon masters, cured at 110˚C for 1 hr, peeled off, oxidized with oxygen plasma (Plasma-Preen; Terra Universal), and silanized with (tridecafluoro-1,1,2,2,-tetrahydrooctyl)-1-trichlorosilane (Sigma-Aldrich) vapor overnight under vacuum. To make the final PDMS mPAD device, PDMS prepolymer was cast on the template, degassed under vacuum, and cured at 110˚C for 20 hrs and peeled off the template. Peeling induces collapse of the mPADs was rectified by sonication in 100% ethanol

(Decon Labs), followed by super-critical drying in liquid CO_2 using a critical point dryer (Samdri-PVT-3D; Tousimis).

Peptide tethering and cell seeding

Flat PDMS stamps were generated by casting PDMS prepolymer on silanized silicon wafers. Stamps were coated in saturating concentration of fibronectin (50 µg/mL in DPBS) for 1 hr. These stamps were washed in distilled water and dried under a stream of N_2. 4% Silane-PEG-NHS ester (Nanocs) dissolved in DMSO was then incubated on the stamp surfaces for 5-10 minutes. During this time, mPAD substrates were oxygen plasma treated at 100 mW/cm^2 for 5 seconds (Plasma-Preen; Terra Universal). Immediately following, the silane-PEG-NHS ester stamps were dried under a stream of N_2. These stamps were then inverted onto the plasma treated mPADs surface for around 10 seconds. These substrates with stamp were then sequentially washed in 100% ethanol, and three times in 50mM sodium bicarbonate buffer, and then directly into 100 µL of peptide reconstituted in sodium bicarbonate buffer (1 mg/mL). Peptides used in study were caged-RGD and cyclic(RGD). mPAD substrates were labeled with 5 µg/mL of Δ^9-DiI (Invitrogen) in distilled water for 1 hr. mPAD substrates were then transferred to a solution of 0.1% Pluronics F127 (Sigma-Aldrich) to prevent non-specific protein absorption. WT, Null eGFP-vinculin MEF cells were seeded in growth medium and then allowed to spread overnight.

Characterization of confocal-based uncaging efficiency of DMNPB group

Caged-fluorescein was tethered to mPADs in the described in the previous section. mPAD substrates were labeled with 5 µg/mL of Δ^9-DiI (Invitrogen) in distilled water for 1 hr. Substrates were washed three times in DPBS and allowed to sit at RT. Samples were stable for over two days.

Time-lapse microscopy and laser confocal based stimulation of caged-RGD

mPAD substrates were transferred to an aluminum coverslip holder (Attoflour Cell Chamber; Invitrogen) for live cell microscopy and placed in an stage top incubator that regulated temperature, humidity, and CO_2 (Live Cell; Pathology Devices). Confocal images were taken with a Nikon-C2+ Laser Scanning Confocal connected to a Nikon Ti-Eclipse Inverted Microscope using a high magnification objective (CFI Plan Apochromat TIRF 60x oil, N.A. 1.45; Nikon). Uncaging of the caged-RGD was completed by single-post ROI stimulation using the Nikon Elements software to control the 403 nm laser at 1.96% power, 1fps. Post images were captured using a 561 nm channel, and vinculin images were captured using a 488 nm channel. Capture settings were the following: 0.16% 488 nm laser power, 0% 561 nm laser power, 4.18 µs pixel dwell time, 7.1 AU pinhole, 512x512 resolution, scan area gated on single cell.

Image analysis to quantify force generation and vinculin recruitment

Time-lapse movies were saved in .nd2 format and imported into Fiji (ImageJ, NIH) using the "BioFormats Importer" plugin. These time-lapse series were split into their transmission, 488, and 561nm channels. The 488nm channel was used to visualize vinculin localization. By placing a ROI box around the expected displacement area of a stimulated, attached, and free post, using the [stack->plot z intensity], the 488nm vinculin signal vs. time was automatically extracted and exported to Excel. 561nm post time-lapses were smoothed to remove noise artifacts, and then binarized using the [Image->Adjust->Threshold] tool. Using the "2D/3D Particle Analyzer" (Mosaic, Germany) plugin, and setting the search parameters to 6um-10um, all of the posts, in each field, were automatically detected. Then the particle analysis and path-tracking algorithm was run, the output contained an image of all of the posts with superimposed displacements. Upon clicking on a single post its time-lapse displacement path could be visualized and data exported to Excel. Displacement was converted to force by

multiplying values with the stiffness of the mPADs device. Final data output was graphed in GraphPad Prism 6 (Graphpad Software, CA).

CHAPTER 5

CONCLUSION AND FUTURE DIRECTIONS

This thesis presents a *significant* contribution to field of biomaterials research by demonstrating the utility of dynamic, triggerable biomaterials using novel caged-compounds. By having unparalleled spatiotemporal control of RGD ligand presentation, we demonstrated two novel tools for discovery: 1) *in vivo* ligand presentation to probe downstream tissue behavior and cell infiltration to biomaterial implants, and 2) *in vitro* ligand presentation *in situ* using confocal-based live cell microscopy to investigate real-time vinculin recruitment and cell traction force generation.

In Aim 1, PEG-based hydrogels provided a novel platform to elucidate cell-ECM interactions through a highly defined, non-fouling surface. Through the use of simplified ECM-peptides such as RGD, specific integrin-ECM interactions can be studied. We have demonstrated the uses of the novel caged-RGD molecule in the context of PEG-based hydrogels. Caged-RGD conjugated PEGDA based hydrogels were able to effectively modulate cell attachment and spreading *in vitro*. We were able to demonstrate that DMNPB-based caged compounds were effectively controlled ex vivo using UV irradiation, after a subcutaneous implantation and the uncaging efficiency was unchanged even after 14 days. Furthermore, delayed activation of caged-RGD presenting hydrogels was able to modulate macrophage recruitment and downstream fibrous capsule formation in subcutaneously implanted PEGDA-based hydrogels.

When applied to PEG-maleimide based hydrogels, caged-RGD was effective at controlling *in vitro* cell outgrowth into a degradable hydrogel with protease sensitive

crosslinks through the control of RGD presentation via wide-field UV irradiation. When this PEG-maleimide system was combined with protease sensitive crosslinks and VEGF in an *in situ* polymerized subcutaneous model, caged-RGD was effective at controlling vasculogenesis through the modulation of RGD presentation via transdermal UV irradiation. Therefore, we have demonstrated that caged-RGD in conjunction with PEG-based hydrogels is a versatile platform that offers unparalleled spatiotemporal control of RGD ligand presentation. Through UV-activation we have demonstrated that ex vivo control of RGD-mediated cell adhesion is a critical regulator of many events including inflammation and vasculogenesis. This study has shown that caged-compounds provide a versatile and effective means of controlling the presentation of signals and ligands in both *in vitro* and *in vivo* systems and have demonstrated the potential of this class of compounds in future biomaterials research.

With the ability to modulate presentation of ligands/compound after implantation, the caged-system has wide ranging applications in vivo. First, it can be used to dynamically control the presentation of chemical moieties immobilized on biomaterial surfaces. This will have wide ranging effects in the field of immunomodulation. With the rise of personalized medicines and cell-based biopharmaceuticals, there is a need to study spatiotemporal presentation of antigens in immunological synapses. Current methods of inducing antigenicity in t-cell populations only rely on the mixing antigen in a solution of white blood cells, which utilizes only the static presentation of antigens. Also, in the study of CD8+ T-cells, that are already antigen specific, researchers could use a substrate presenting caged-antigen to visualize the formation of an immunological synapse in real-time and uncover antigen density dependent patterns of activation.

Wound healing and cell migration studies would also be greatly aided by the use of caged compounds. Restenosis of vascular stents has long been a problem in the treatment of atherosclerosis due to wounding of the epithelial layer of blood vessels. This causes the a wound healing response in which smooth muscle cells migrate over the stent, eventually causing blockage. Perhaps using a caged-adhesive ligand system, we can control the migration of specific cell types over the stent in order to stabilize the stent inner diameter.

In Aim 2, we have demonstrated a novel method of tethering small ligands and peptides to PDMS surfaces using a silane-PEG-NHS ester. This scheme opens up new avenues of research in small molecule presentation on PDMS, glass, and silicon surfaces. The ability to microcontact print silane onto surfaces furthers its utility in complicated microfabricated softlithography tethering schemes. RGD tethering to microcontact printed silane was shown to support normal cell adhesion and focal adhesion formation comparable to the RGD tethered direct incubated approach. Caged-RGD tethering to mPADs in conjunction with WT-eGFP-MEF cells was able to support normal cell adhesion, spreading, and vinculin localization to focal adhesions.

The efficiency of uncaging the DMNPB group using the 403nm confocal laser was validated using caged-fluorescein tethered to mPADs surfaces and a full titration of stimulation conditions was performed. Using a mixture of 50% static RGD and 50% caged-RGD, we have demonstrated the first real-time tracking of vinculin localization and cell traction force generation on multiple post array deflection substrates following triggered RGD presentation via *in situ* laser-based uncaging. These studies have shown that vinculin recruitment to increased RGD ligand presentation occurs independently of force generation. Additional RGD presentation to established, mature focal adhesions,

results in immediate increase in traction force generation, while vinculin localization is delayed by over 200 seconds, suggesting that vinculin localization in these adhesions is regulated by signals downstream of myosin II-mediated increases in cytoskeletal tension. In nascent adhesions, however, vinculin localization occurs immediately even in the absence of force generation. This suggests that local focal adhesion adaptor proteins such as talin could be responsible for vinculin localization under low force regimes. Taken in whole, this study suggests that that there are two pathways for vinculin localization to focal adhesions depending on the amount of contractile force across a single focal adhesion.

Spatiotemporal control of RGD ligand presentation on spread cells has many applications when used in conjunction with other sensing modalities, such as FRET biosensors. Using either sensors of FA proteins (vinculin tension sensor) or essential signaling molecules (FAK and SRC biosensors), in conjunction with caged-RGD presenting mPADs, researchers would be able to track signaling cascades in addition to FA localization and force generation. Furthermore, because this system allows researchers to perform the same studies on new vs. established focal adhesions, important insights into the dichotomy of these types of adhesions can be uncovered.

Designing new caging chemistries, based on maleimide chemistry, will extend the use of caged compounds from only short peptides to medium or large sized globular proteins. Most proteins have free cysteine sites, and if it is determined that the active site of a protein is near one of these cysteines, a maleimide –based caging group may be able to disrupt the proteins activity. If caging groups were shown to influence activity of whole proteins, this would greatly increase the use of caged compounds in the research world, and may even extend the use of caged compounds into the clinic.

Ultimately, these studies provided the biomaterials community with new tools for detailed investigation into the role of spatiotemporal ligand presentation in both hydrogel and PDMS-based systems. Triggerable *in vivo* adhesive ligand presentation was evaluated in both a biomaterial-associated implant inflammation model and an *in vivo* vasculogenesis study. These studies demonstration the power of triggerable adhesive ligand presentation *in vivo* and demonstrated the utility of caged-compounds in probing specific receptor-ligand responses on highly defined PEG-based synthetic hydrogels. Triggerable *in vitro* ligand presentation, combined with traction force microscopy, demonstrated the first real-time tracking of vinculin recruitment and traction force generation in response to additional ligand presentation. It also represented a new research platform for investigating the temporal control of ligand presentation and its effect on integrin activation, focal adhesion formation, and downstream force generation. Taken in whole, this thesis demonstrates the potential of UV-light mediated temporal control of adhesive ligand presentation in a variety of systems and created several new platforms for discovery that can be used in future biomaterials and cell biology research.

APPENDIX

A1. PUBLICATIONS

A1.1 *Multivalent integrin-specific ligands enhance tissue healing and biomaterial integration*. Science Translational Medicine.

RESEARCH ARTICLE

TISSUE ENGINEERING

Multivalent Integrin-Specific Ligands Enhance Tissue Healing and Biomaterial Integration

Timothy A. Petrie,[1,2] Jenny E. Raynor,[3] David W. Dumbauld,[1,2] Ted T. Lee,[1,2] Subodh Jagtap,[3] Kellie L. Templeman,[1,2] David M. Collard,[3] Andrés J. García[1,2]*

(Published 18 August 2010; Volume 2 Issue 45 45ra60)

Engineered biointerfaces covered with biomimetic motifs, including short bioadhesive ligands, are a promising material-based strategy for tissue repair in regenerative medicine. Potentially useful coating molecules are ligands for the integrins, major extracellular matrix receptors that require both ligand binding and nanoscale clustering for maximal signaling efficiency. We prepared coatings consisting of well-defined multimer constructs with a precise number of recombinant fragments of fibronectin (monomer, dimer, tetramer, and pentamer) to assess how nanoscale ligand clustering affects integrin binding, stem cell responses, tissue healing, and biomaterial integration. Clinical-grade titanium was grafted with polymer brushes that presented monomers, dimers, trimers, or pentamers of the $\alpha_5\beta_1$ integrin–specific fibronectin III (7 to 10) domain ($FNIII_{7-10}$). Coatings consisting of trimers and pentamers enhanced integrin-mediated adhesion in vitro, osteogenic signaling, and differentiation in human mesenchymal stem cells more than did surfaces presenting monomers and dimers. Furthermore, ligand clustering promoted bone formation and functional integration of the implant into bone in rat tibiae. This study establishes that a material-based strategy in which implants are coated with clustered bioadhesive ligands can promote robust implant-tissue integration.

INTRODUCTION

An overarching goal in materials engineering and medicine is the development of biomaterials to control cell function in order to promote tissue healing and regeneration (*1*, *2*). Cell-biomaterial interactions are primarily governed by cell adhesion, which arises from the binding of cellular integrin receptors to biomacromolecules adsorbed, tethered, or deposited onto a surface or the extracellular matrix (*3*). Engagement of distinct integrin αβ heterodimers activates specific signaling pathways that regulate survival, proliferation, and phenotypic cellular programs (*4*, *5*). For instance, binding of cell surface integrin to extracellular fibronectin promotes osteoblast survival, cell cycle progression, differentiation, and matrix mineralization (*6*–*9*). Strategies to control integrin-mediated adhesion to bioinspired materials have been developed to regulate tissue repair and maintenance. For example, presentation of short oligopeptides such as the Arg-Gly-Asp (RGD) sequence derived from fibronectin on substrates allows for the selective activation of integrin signaling pathways (for example, $\alpha_v\beta_3$-mediated signaling by RGD) (*2*, *10*–*12*). Other approaches make use of macromolecular ligands, including extracellular matrix–derived proteins such as collagen, elastin, and fibronectin (*11*, *12*). These strategies have typically relied on the immobilization of the bioadhesive ligand onto a solid support in a relatively static arrangement, without the possibility of substantial ligand mobility or directed receptor clustering. This presentation is in contrast to the state of cell membrane integrin receptors, which are mobile and cluster together to attain maximal function (*13*, *14*). Integrin clustering drives the assembly of focal contacts that serve as mechanotransducers and signaling nexuses for cells (*5*, *15*, *16*).

Synthetic clustering of multiple copies of the RGD sequence in polyvalent dendritic polymers enhances cell attachment, migration, and targeting (*17*–*20*). For optimal effect, clustered ligands should be spaced far enough apart to avoid steric hindrance to binding (integrin receptor diameter, ~10 nm) but close enough to promote synergistic interactions. Integrin ligand spacings on the order of 80 to 140 nm are required for the assembly of focal adhesion domains (*21*, *22*). However, in rats and dogs, coating of implants with individual linear RGD-containing peptides does not promote or enhance implant integration or bone formation compared to the surface treatments that are used in the clinic (*23*–*26*), including porous and hydroxyapatite-coated implants. These findings suggest that such RGD-based approaches have limited therapeutic application.

We hypothesized that immobilization of a flexible macromolecular assembly that presents multiple tethered copies of bioligands could promote cellular integrin clustering and signaling and thereby enhance integration of an implant. We therefore tested whether recombinant constructs displaying specified numbers of the 7 to 10 type III repeats of fibronectin ($FNIII_{7-10}$)–binding domain (*27*) could promote implant integration into bone.

RESULTS

$FNIII_{7-10}$ presents the PHSRN (Pro-His-Ser-Arg-Asn) and RGD integrin-binding sites of fibronectin in an arrangement that results in high binding specificity for integrin $\alpha_5\beta_1$ (*23*, *28*). In previous studies, we have shown that the presentation of $FNIII_{7-10}$ on a substrate enhances osteoprogenitor cell differentiation and implant osseointegration when compared to a coating of simple immobilized RGD-containing oligopeptides (*23*). By combining the $FNIII_{7-10}$ fragment, a flexible linker derived from tenascin ($TNfnIII_{3-8}$), and a multiplex-forming coiled-coil sequence at the C terminus (Fig. 1A), we assembled

[1]Woodruff School of Mechanical Engineering, Georgia Institute of Technology, 315 Ferst Drive, Room 2314 IBB, Atlanta, GA 30332-0363, USA. [2]Petit Institute for Bioengineering and Bioscience, Georgia Institute of Technology, Atlanta, GA 30332, USA. [3]School of Chemistry and Biochemistry, Georgia Institute of Technology, Atlanta, GA 30332, USA.
*To whom correspondence should be addressed. E-mail: andres.garcia@me.gatech.edu

the bioadhesive domains into a supramolecular construct that presented defined numbers of copies of the cell-adhesive domain on a flexible linker (Fig. 1A). Constructs presenting one, two, three, or five nanoclustered adhesive ligands were generated with different coiled-coil domains. The linker within the $FNIII_{7–10}$ multimeric construct provided flexibility to allow for the rearrangement of the bioadhesive ligands within a range of about 10 to 50 nm.

We expressed recombinant constructs in *Escherichia coli* and purified them with anion-exchange chromatography. The hydrodynamic radii of the multimers were assessed by dynamic light scattering to verify the assembly of the subunits into the expected dimers, trimers, and pentamers. Size histograms (Fig. 1B) show the expected hydrodynamic radius for the monomer (8.5 nm), dimer (12 nm), trimer (22 nm), and pentamer (41 nm) constructs. Smaller peaks corresponding to partially assembled multimers were observed for the trimer and pentamer preparations, but these constituted <15% of the total amount of material.

To precisely control the presentation of biological ligands on clinically relevant materials, while preventing nonspecific adsorption of biomacromolecules, we used a nonfouling oligo(ethylene glycol)-substituted polymer brush system on clinical-grade titanium (Ti). This thin polymeric coating, generated by surface-initiated atom transfer radical polymerization of poly[oligo(ethylene glycol) methacrylate] [poly(OEGMA)] brushes on Ti, provides a robust coating that can be engineered to present well-defined densities of covalently tethered biological ligands in a background that is resistant to nonspecific biomacromolecule adsorption and cell adhesion (*29*). This coating technology is compatible with in vivo applications and can be used to rigorously evaluate biomaterial integration and function in animal models (*23*). Multimeric $FNIII_{7–10}$ constructs were covalently tethered onto these materials, and the density of tethered multimers was controlled by varying the ligand concentration in solution and measured via surface plasmon resonance (SPR) (fig. S1) (*28*).

The ability of $\alpha_5\beta_1$ integrin to bind to our multivalent constructs was examined by SPR in a cell-free system. In a first set of experiments, SPR chips coated with polymer brushes were modified with the different multimers to present the same density of the $FNIII_{7–10}$ integrin-binding sites (Fig. 2A) (that is, surfaces modified with five times as much monomer as pentamer present the same density of $FNIII_{7–10}$ ligand). Binding of soluble integrin $\alpha_5\beta_1$ to these surfaces was the same for all multimers. In a complementary set of experiments, polymer-coated SPR chips presenting equimolar densities of constructs were used (Fig. 2B). For the same construct densities, integrin binding increased linearly (R^2 = 0.994) with the valency. These results demonstrate that the multivalent constructs support integrin $\alpha_5\beta_1$ binding, that integrin-binding sites within the constructs are accessible for receptor binding, and that they are not subject to steric inhibition.

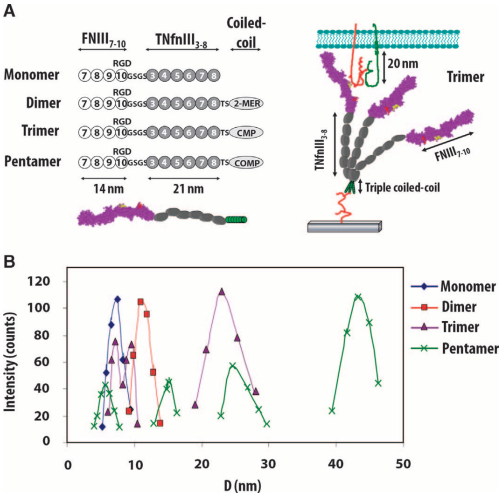

Fig. 1. Multimeric constructs with precise nanoclustered integrin-binding domains. (**A**) Constructs consisting of the $FNIII_{7–10}$ integrin-binding domain at the N terminus, flexible spacer arm comprising the FNIII domains 3 to 8 from tenascin, and a distinct oligomerization sequence at the C terminus: K6 peptide for dimer, cartilage matrix protein (CMP) for trimer, and cartilage oligomeric matrix protein (COMP) for pentamer. Schematic of trimer tethered to a surface and interacting with integrins via the $FNIII_{7–10}$–binding domain. (**B**) Histograms of construct hydrodynamic diameter (D) for purified multimer fractions. A mixture of complete and incompletely assembled multimers was detected; the majority (>85%) of multimers were completely assembled as the desired dimer, trimer, and pentamer constructs.

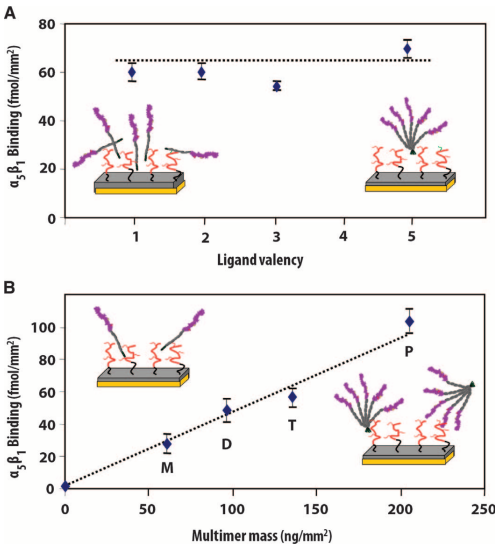

Fig. 2. The integrin-binding sites within the multivalent ligand constructs are accessible for receptor binding and support robust $\alpha_5\beta_1$ binding. Binding of soluble human $\alpha_5\beta_1$ integrin to multimers immobilized on polymer brushes (orientation uncontrolled). (**A**) Equimolar average densities of $FNIII_{7–10}$–binding domains. (**B**) Surfaces presenting equimolar densities of multimers. Integrin binding increased linearly with ligand valency (R^2 = 0.994).

The effects of ligand clustering on cellular responses were examined by culturing human mesenchymal stem cells under osteogenic conditions (growth medium supplemented with Osteogenic SingleQuots kits) on biomaterials presenting multimeric constructs. These stem cells have the potential to differentiate into various lineages and represent a promising cell source for regenerative medicine (*30*). Biomaterial surfaces were engineered to present equivalent average density (150 fmol/cm^2) of the FNIII$_{7–10}$ domain as quantified by SPR. Because of differences in molecular weight among constructs, the saturation density of tethered constructs was different for each construct (fig. S1). The density of FNIII$_{7–10}$ used (150 fmol/cm^2) represents the highest density of the integrin-binding domain that could be tethered onto the polymer coating while still having equivalent average densities of the FNIII$_{7–10}$ domain for all of the multimeric constructs. Integrin binding in adherent cells was quantified with a biochemical cross-linking and extraction method (*31*). Surfaces that presented trimeric and pentameric ligands exhibited twice as much integrin binding as the monomeric and dimeric ligands at equivalent ligand densities ($P < 0.05$) (Fig. 3A). No differences in integrin binding were observed between monomeric and dimeric ligands, or between trimers and pentamers, suggesting a threshold response rather than a monotonic increase with valency. Cells did not adhere to control surfaces that presented no multimeric constructs or in the presence of antibodies against the integrin subunit α_5. Using Ti surfaces coated with passively adsorbed monomeric and pentameric ligands, we also examined the effects of ligand nanoclustering on integrin binding at higher multimer surface densities (fig. S2). Adsorption of multimers on unmodified Ti yielded about five times higher FNIII$_{7–10}$ surface density (680 fmol/cm^2) compared to tethered multimers on polymer brush–coated Ti. Experiments to determine binding of soluble integrin to substrates modified with adsorbed monomer and pentamer constructs confirmed equivalent integrin receptor accessibility for these coated densities (fig. S2A). Consistent with our observations with ligands tethered onto polymer brushes, cells on surfaces that presented pentameric constructs exhibited greater levels of integrin binding (fig. S2B) and adhesion strength (fig. S3C) than the monomeric ligand at equivalent FNIII$_{7–10}$ densities. Together, these results demonstrate that nanoclustering enhances integrin binding to adhesive ligands presented on biomaterial surfaces.

The differences in binding of soluble integrins (linear with total FNIII$_{7–10}$ density) (Fig. 2B) and cell-bound integrins (enhanced binding to trimer and pentamer over monomer and dimer at equal overall densities of FNIII$_{7–10}$) (Fig. 3A and fig. S2) demonstrate that ligand clustering improves cell-adhesive activity. The effects of ligand clustering on cell signaling were explored further by quantification of phosphorylation of focal adhesion kinase (FAK) by Western blotting (Fig. 3B). FAK is a central signaling molecule that is activated by phosphorylation and is involved in integrin-mediated signal transduction, focal adhesion formation, and the osteogenic differentiation pathway (*32*). We used a phosphotyrosine-specific antibody to examine the phosphorylation of Y^{397}, a tyrosine autophosphorylation site critical for FAK function. We previously demonstrated that blocking the binding of integrin $\alpha_5\beta_1$ to fibronectin inhibits FAK-Y^{397} phosphorylation and osteoblastic differentiation (*23*, *33*). Here, FAK-Y^{397} exhibited more phosphorylation on pentamer-presenting surfaces than on the other multimer-functionalized materials ($P < 0.05$) (Fig. 3B). This result is consistent with the valency-dependent threshold effects observed for integrin binding.

We next examined the effects of ligand clustering on lineage commitment and osteoblastic differentiation for mesenchymal stem cells. Cells cultured on surfaces displaying trimeric and pentameric bioadhesive ligands exhibited significantly more alkaline phosphatase activity

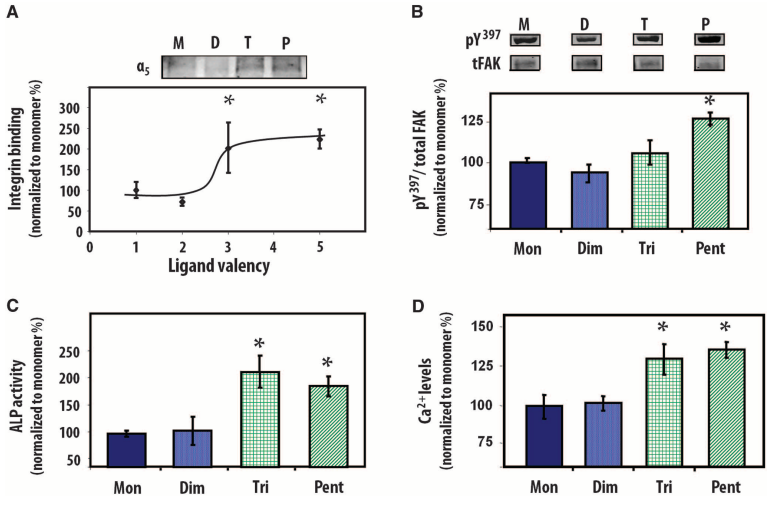

Fig. 3. Human mesenchymal stem cell responses to biomaterials presenting multivalent adhesive ligands at equimolar average density of FNIII$_{7–10}$ domains. (**A**) Integrin binding to multimeric constructs in whole cells (1 hour, 37°C), showing threshold response [pentamer (P) and trimer (T) versus monomer (M) and dimer (D): *$P < 0.05$, $n = 6$]. (**B**) Phosphorylation of FAK-Y^{397} in whole-cell lysates (2 hours, 37°C) is enhanced on surfaces presenting higher-valency ligands [pentamer (Pent) versus monomer (Mon), dimer (Dim), and trimer (Tri): *$P < 0.05$, $n = 4$]. (**C** and **D**) Biomaterials presenting trimers and pentamers enhance alkaline phosphatase (ALP) activity (pentamer and trimer versus monomer and dimer: *$P < 0.01$) and mineralization as measured by extracellular Ca^{2+} in 14-day cultures of mesenchymal stem cells (pentamer and trimer versus monomer and dimer: *$P < 0.04$).

than did cells on materials functionalized with monomeric or dimeric constructs ($P < 0.01$) (Fig. 3C). Deposition of calcium phosphate mineral within a collagen matrix is considered an endpoint marker of differentiation. Mineralization, as measured by Ca^{2+} levels, was up-regulated in human stem cells cultured on biomaterials presenting trimers and pentamers of $FNIII_{7–10}$ compared to substrates functionalized with monomeric and dimeric constructs ($P < 0.04$) (Fig. 3D), in agreement with our results on alkaline phosphatase activity. Together, these results demonstrate that adhesive ligand multivalency (trimers and pentamers) enhanced integrin binding, signaling, and osteoblastic differentiation in human stem cells.

Enhancements of tissue repair and device integration represent the ultimate goal for biomaterial-based therapeutic strategies. As a relevant test of such behavior, we examined the effects of our multivalent ligands on implant osseointegration. Ti rods functionalized with the multimeric constructs ($FNIII_{7–10}$ average density, 150 fmol/cm^2) were press-fit into circular defects drilled into rat proximal tibia (Fig. 4A). This model mimics dental and orthopedic clinical procedures, such as endosteal dental implants and joint arthroplasties, where the mechanical and biological integration of the implant and surrounding bone is critical to function. Therefore, this in vivo model provides a platform to rigorously evaluate the effects of implant coating in a relevant dental and orthopedic setting (*23*, *34*, *35*). Tibiae were harvested after 4 and 12 weeks and analyzed for bone-implant contact by histomorphometry (4 weeks) and implant-bone fixation by mechanical testing (4 and 12 weeks). Histological sections revealed more extensive and contiguous bone in close apposition to the trimer- and pentamer-functionalized implants than for the monomer- and dimer-coated implants (Fig. 4B). Control implants presenting poly(OEGMA) brushes without tethered bioadhesive ligands displayed limited bone-implant contact. No evidence of multinucleated cells, fibrous capsule, or chronic inflammation was observed for any of the groups. Histomorphometric analysis demonstrated a 50% increase in bone-implant contact area for the trimer- and pentamer-functionalized implants compared to monomer-coated rods ($P < 0.04$), a 250% increase compared to the polymer brush–coated Ti in the absence of tethered ligand ($P < 0.01$), and a 75% increase over unmodified Ti (33 ± 3% bone-implant contact), the current clinical standard ($P < 0.02$) (Fig. 4C).

Mechanical fixation provides a rigorous metric of functional implant osseointegration. Pullout mechanical testing at 4 and 12 weeks of implantation revealed ligand valency–dependent differences ($P < 0.01$; Fig. 4D). Trimer- and pentamer-functionalized implants exhibited a 250% enhancement in fixation over monomer- and dimer-tethered implants ($P < 0.002$), and ~400% improvement relative to the unmodified polymer coating ($P < 0.001$). Furthermore, implants presenting trimers and pentamers required twice as much force to be pulled out as did unmodified Ti (17 ± 4.2 N pullout force at 12 weeks, $P < 0.001$), the current clinical standard.

DISCUSSION

Our results demonstrate that clinical implants coated with nanoclustered biological ligands enhance integrin binding and signaling, stem cell differentiation, and in vivo implant integration relative to coatings displaying equivalent densities of monovalent ligand. We attribute the effects of ligand multivalency and clustering on these biological responses to enhancements in binding of integrin $\alpha_5\beta_1$. How does ligand clustering exert its influence over binding to integrins in a cell membrane? For integrins located in the cell membrane, ligand clustering results in greater integrin binding by increasing the local density of ligand and increasing the effective affinity by spatially constraining the receptors to the plane of the membrane. We observed this cooperative binding behavior for integrin receptors in cells but not for freely diffusing soluble receptors. These findings agree with simulations of integrin binding and clustering (*36*, *37*). Our observation of a threshold for optimal binding (trimer and pentamer exhibit greater in vitro and in vivo biological responses than monomer and dimer) is consistent with previous suggestions that a trimer is the minimal matrix complex causing integrin-cytoskeleton connections (*27*, *38*).

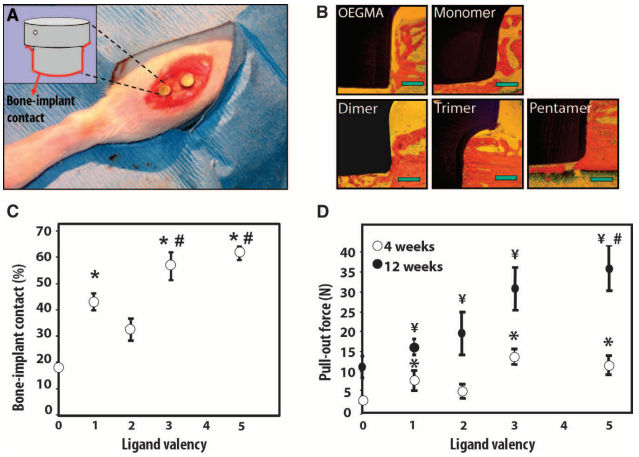

Fig. 4. Nanoclustered ligand coatings enhance functional in vivo implant osseointegration. (**A**) Bone implantation model for assessment of implant integration by measuring bone-implant contact and mechanical fixation. Photograph shows placement of two implants. (**B**) Micrographs of bone-implant longitudinal sections showing mineralized bone (red/orange) and implant (black) contact. Scale bars, 0.2 mm. (**C**) Quantification of bone-implant contact at 4 weeks after implantation demonstrating valency-dependent enhancements (pentamer versus monomer and dimer: $^{\#}P < 0.04$; pentamer versus no ligand: $^{*}P < 0.0001$, $n = 4$; trimer versus monomer, dimer, and no ligand: $^{*}P < 0.05$, $n = 4$; monomer versus no ligand: $^{*}P < 0.01$, $n = 4$). (**D**) Biomaterials presenting trimers and pentamers significantly increased mechanical fixation (4 weeks: pentamer, trimer, and monomer versus no ligand: $^{*}P < 0.01$, $n = 8$; 12 weeks: pentamer versus monomer and dimer: $^{\#}P < 0.002$, $n = 7$; pentamer, trimer, and monomer versus no ligand: $^{¥}P < 0.01$, $n = 7$).

Integrin clustering is a critical step in the cell adhesion process that promotes recruitment of cytoskeletal components and activation of signaling molecules (*13*, *14*). Our data show that integrin clustering can be exploited by engineering materials that present well-defined, multivalent adhesive ligands. This affords control over mesenchymal stem cell lineage commitment and differentiation, as well as biomaterial integration. Moreover, our work demonstrates that substrate manipulation alone can be used to directly influence essential functions of the entire tissue, confirming the utility of a material-based strategy in regenerative medicine. The use of recombinant multimeric constructs has important advantages over the stochastic presentation of many other adhesive RGD-based peptides, including the ability to have precise control over valency ligand spacing and integrin-binding specificity. Specifically, this study establishes bioadhesive ligand clustering as a key parameter for the rational engineering of bioactive materials for regenerative medicine and demonstrates methods to exploit this strategy.

MATERIALS AND METHODS

Multimer preparation and characterization

Recombinant multimeric $FNIII_{7-10}$ proteins presenting the central cell-binding domain of fibronectin were expressed as described (*27*). DNA constructs were transformed into *E. coli* BL21(DE3), and cells were lysed with lysozyme. Protein was precipitated with ammonium sulfate. Pellets were resuspended in buffer (0.02 M tris, 0.1 M NaCl) and run through a Sephacryl 500 column. Peak fractions were then run through a RESOURCE Q column (Amersham Pharmacia). High-purity proteins were eluted at 0.22 M NaCl (pentamer and trimer), 0.24 M NaCl (dimer), and 0.27 M NaCl (monomer). Dynamic light scattering was performed on purified protein samples dialyzed in ultrapure water at protein concentrations of 2 mg/ml.

Biomaterial supports

Poly(OEGMA) brushes (135 Å thick) were grown on commercial clinical-grade Ti as described (*29*). For ligand tethering, brushes were first incubated in a 4-nitrophenyl chloroformate (NPC) solution containing triethylamine, followed by incubation in ligand solution for 1 hour, and residual activated NPC sites were quenched in 20 mM glycine in phosphate-buffered saline (PBS). Brush synthesis and functionalization reactions were verified by x-ray photoelectron spectroscopy and Fourier transform infrared spectroscopy. Ligand surface density measurements were obtained via SPR with a Biacore X instrument.

Cells

Human mesenchymal stem cells were obtained from Lonza, cultured in Lonza MSCM and SingleQuots, and passaged every 3 to 4 days before 60% confluency. Osteogenic SingleQuots kits (PT-4120, Lonza) were used in Lonza Basal Medium (replaced every 3 to 4 days) for subsequent osteoblast differentiation assays.

Integrin binding, adhesion, and FAK signaling assays

SPR measurements were conducted with soluble human $\alpha_5\beta_1$ integrin by means of a Biacore X instrument. Gold-coated SIA chips (Biacore) were coated with 50 Å Ti, and brushes were deposited on the surface as described (*29*). Surfaces were activated with NPC for 20 min. Ligands were tethered on chips by flowing a solution containing them at 8 μl/min for 30 min. A solution (200 μg/ml) of human recombinant soluble $\alpha_5\beta_1$ (R&D Systems) was passed over the multimer-functionalized chips for 10 min in integrin-activating conditions (PBS + 1 mM Mn^{+2}), the surfaces were washed, and the baseline was allowed to stabilize before the amount of bound integrin was quantified. Resonance units (RUs) were converted to surface density values (10 RUs = 1 ng/cm^2).

Integrin binding in cells was quantified with a cross-linking–extraction–reversal procedure with 3,3′-dithiobis[sulfosuccinimidyl propionate] cross-linker (*31*). For FAK activation assays, human mesenchymal stem cells were plated on multimer-tethered substrates for 2 hours at 37°C under serum-free conditions. Cells were lysed in radioimmunoprecipitation assay buffer [1% Triton X-100, 1% sodium deoxycholate, 0.1% SDS, 150 mM NaCl, 150 mM tris-HCl (pH 7.2), phenylmethylsulfonyl fluoride (350 μg/ml), leupeptin (10 μg/ml), and aprotinin (10 μg/ml)], and equal amounts of total protein were loaded on 8% SDS–polyacrylamide gel electrophoresis (SDS-PAGE) gels, separated by SDS-PAGE, and transferred to nitrocellulose membranes. FAK activation was assessed by subsequent Western blotting with antibodies specific for FAK phosphotyrosines (Invitrogen) and normalized to total FAK levels.

Osseointegration study

Implantations into the tibiae of mature Sprague-Dawley male rats were conducted in accordance with an Institutional Animal Care and Use Committee–approved protocol (*35*). Ti rods and polymer brushes were prepared as described (*23*). Multimeric constructs were tethered to yield equimolar densities of the $FNIII_{7-10}$ domain (150 fmol/cm^2). Two 2-mm-diameter defects were drilled into the medial aspect of the proximal tibial metaphysis of each leg, and implants were press-fit into the defects (four implants per animal). After euthanasia, tibiae were explanted and either fixed in neutral buffered formalin (histology) or wrapped in PBS for immediate mechanical testing. Formalin-fixed tibiae were embedded in poly(methyl methacrylate), dehydrated, and stained with Sanderson's Rapid Bone Stain (Surgipath) and Van Gieson counterstain (Surgipath). This procedure stained mineralized bone (yellow-orange) and soft tissue and osteoid (blue-green). Bone apposition was quantified as the percentage of the implant's surface in contact with the bone, and six to eight fields per implant were quantified. Pullout testing was performed to quantify implant mechanical fixation to surrounding bone tissue with an EnduraTEC Bose ELF 3200. The ends of each excised tibia were secured, and the exposed head of the implant was connected to a load cell via a customized grip apparatus. Preloaded samples (<2 N) were then subjected to a constant pull rate of 0.2 N/s. The pullout force (*N*), parallel to the long axis of implant, was the maximum load achieved before implant detachment or failure.

Statistics

Results are presented as mean ± SEM. Results were analyzed by analysis of variance (ANOVA) in SYSTAT 8.0 (SPSS). If deemed significant, pairwise comparisons were performed with Tukey post hoc test, and a confidence level of 95% was considered significant. In vitro assays were conducted in at least triplicate and replicated in two separate experiments.

SUPPLEMENTARY MATERIAL

www.sciencetranslationalmedicine.org/cgi/content/full/2/45/45ra60/DC1
Materials and Methods
Fig. S1. Surface density for constructs tethered onto polymeric brushes as a function of coating concentration.

Fig. S2. Cell-adhesive responses to surfaces presenting high density of multivalent ligands at equimolar average density (680 fmol/cm^2) of FNIII$_{7–10}$ domains.
References

REFERENCES AND NOTES

1. M. P. Lutolf, J. A. Hubbell, Synthetic biomaterials as instructive extracellular microenvironments for morphogenesis in tissue engineering. *Nat. Biotechnol.* **23**, 47–55 (2005).
2. R. Langer, D. A. Tirrell, Designing materials for biology and medicine. *Nature* **428**, 487–492 (2004).
3. J. M. Anderson, A. Rodriguez, D. T. Chang, Foreign body reaction to biomaterials. *Semin. Immunol.* **20**, 86–100 (2008).
4. R. O. Hynes, Integrins: Bidirectional, allosteric signaling machines. *Cell* **110**, 673–687 (2002).
5. V. Vogel, M. P. Sheetz, Cell fate regulation by coupling mechanical cycles to biochemical signaling pathways. *Curr. Opin. Cell Biol.* **21**, 38–46 (2009).
6. R. K. Globus, D. Amblard, Y. Nishimura, U. T. Iwaniec, J. B. Kim, E. A. Almeida, C. D. Damsky, T. J. Wronski, M. C. van der Meulen, Skeletal phenotype of growing transgenic mice that express a function-perturbing form of β1 integrin in osteoblasts. *Calcif. Tissue Int.* **76**, 39–49 (2005).
7. R. K. Globus, S. B. Doty, J. C. Lull, E. Holmuhamedov, M. J. Humphries, C. H. Damsky, Fibronectin is a survival factor for differentiated osteoblasts. *J. Cell Sci.* **111**, 1385–1393 (1998).
8. A. M. Moursi, R. K. Globus, C. H. Damsky, Interactions between integrin receptors and fibronectin are required for calvarial osteoblast differentiation in vitro. *J. Cell Sci.* **110**, 2187–2196 (1997).
9. S. L. Cheng, C. F. Lai, S. D. Blystone, L. V. Avioli, Bone mineralization and osteoblast differentiation are negatively modulated by integrin αvβ3. *J. Bone Miner. Res.* **16**, 277–288 (2001).
10. A. J. García, Get a grip: Integrins in cell–biomaterial interactions. *Biomaterials* **26**, 7525–7529 (2005).
11. A. J. García, C. D. Reyes, Bio-adhesive surfaces to promote osteoblast differentiation and bone formation. *J. Dent. Res.* **84**, 407–413 (2005).
12. E. Ruoslahti, M. D. Pierschbacher, New perspectives in cell adhesion: RGD and integrins. *Science* **238**, 491–497 (1987).
13. S. Miyamoto, S. K. Akiyama, K. M. Yamada, Synergistic roles for receptor occupancy and aggregation in integrin transmembrane function. *Science* **267**, 883–885 (1995).
14. S. Miyamoto, H. Teramoto, O. A. Coso, J. S. Gutkind, P. D. Burbelo, S. K. Akiyama, K. M. Yamada, Integrin function: Molecular hierarchies of cytoskeletal and signaling molecules. *J. Cell Biol.* **131**, 791–805 (1995).
15. B. Geiger, A. Bershadsky, R. Pankov, K. M. Yamada, Transmembrane crosstalk between the extracellular matrix and the cytoskeleton. *Nat. Rev. Mol. Cell Biol.* **2**, 793–805 (2001).
16. B. Geiger, J. P. Spatz, A. D. Bershadsky, Environmental sensing through focal adhesions. *Nat. Rev. Mol. Cell Biol.* **10**, 21–33 (2009).
17. L. Y. Koo, D. J. Irvine, A. M. Mayes, D. A. Lauffenburger, L. G. Griffith, Co-regulation of cell adhesion by nanoscale RGD organization and mechanical stimulus. *J. Cell Sci.* **115**, 1423–1433 (2002).
18. G. Maheshwari, G. Brown, D. A. Lauffenburger, A. Wells, L. G. Griffith, Cell adhesion and motility depend on nanoscale RGD clustering. *J. Cell Sci.* **113**, 1677–1686 (2000).
19. V. Villard, O. Kalyuzhniy, O. Riccio, S. Potekhin, T. N. Melnik, A. V. Kajava, C. Rüegg, G. Corradin, Synthetic RGD-containing α-helical coiled coil peptides promote integrin-dependent cell adhesion. *J. Pept. Sci.* **12**, 206–212 (2006).
20. E. Garanger, D. Boturyn, P. Dumy, Tumor targeting with RGD peptide ligands—design of new molecular conjugates for imaging and therapy of cancers. *Anticancer Agents Med. Chem.* **7**, 552–558 (2007).
21. J. Huang, S. V. Grater, F. Corbellini, S. Rinck, E. Bock, R. Kemkemer, H. Kessler, J. Ding, J. P. Spatz, Impact of order and disorder in RGD nanopatterns on cell adhesion. *Nano Lett.* **9**, 1111–1116 (2009).
22. S. P. Massia, J. A. Hubbell, An RGD spacing of 440 nm is sufficient for integrin $\alpha_v\beta_3$-mediated fibroblast spreading and 140 nm for focal contact and stress fiber formation. *J. Cell Biol.* **114**, 1089–1100 (1991).
23. T. A. Petrie, J. E. Raynor, C. D. Reyes, K. L. Burns, D. M. Collard, A. J. García, The effect of integrin-specific bioactive coatings on tissue healing and implant osseointegration. *Biomaterials* **29**, 2849–2857 (2008).
24. H. Schliephake, D. Scharnweber, M. Dard, S. Rössler, A. Sewing, J. Meyer, D. Hoogestraat, Effect of RGD peptide coating of titanium implants on periimplant bone formation in the alveolar crest. An experimental pilot study in dogs. *Clin. Oral Implants Res.* **13**, 312–319 (2002).
25. T. A. Barber, J. E. Ho, A. De Ranieri, A. S. Virdi, D. R. Sumner, K. E. Healy, Peri-implant bone formation and implant integration strength of peptide-modified p(AAM-*co*-EG/AAC) interpenetrating polymer network-coated titanium implants. *J. Biomed. Mater. Res. A* **80**, 306–320 (2007).
26. K. M. Hennessy, W. C. Clem, M. C. Phipps, A. A. Sawyer, F. M. Shaikh, S. L. Bellis, The effect of RGD peptides on osseointegration of hydroxyapatite biomaterials. *Biomaterials* **29**, 3075–3083 (2008).
27. F. Coussen, D. Choquet, M. P. Sheetz, H. P. Erickson, Trimers of the fibronectin cell adhesion domain localize to actin filament bundles and undergo rearward translocation. *J. Cell Sci.* **115**, 2581–2590 (2002).
28. T. A. Petrie, J. R. Capadona, C. D. Reyes, A. J. García, Integrin specificity and enhanced cellular activities associated with surfaces presenting a recombinant fibronectin fragment compared to RGD supports. *Biomaterials* **27**, 5459–5470 (2006).
29. J. E. Raynor, T. A. Petrie, A. J. García, D. M. Collard, Controlling cell adhesion to titanium: Functionalization of poly[oligo(ethylene glycol)methacrylate] brushes with cell-adhesive peptides. *Adv. Mater.* **19**, 1724–1728 (2007).
30. M. F. Pittenger, A. M. Mackay, S. C. Beck, R. K. Jaiswal, R. Douglas, J. D. Mosca, M. A. Moorman, D. W. Simonetti, S. Craig, D. R. Marshak, Multilineage potential of adult human mesenchymal stem cells. *Science* **284**, 143–147 (1999).
31. B. G. Keselowsky, A. J. García, Quantitative methods for analysis of integrin binding and focal adhesion formation on biomaterial surfaces. *Biomaterials* **26**, 413–418 (2005).
32. Y. Tamura, Y. Takeuchi, M. Suzawa, S. Fukumoto, M. Kato, K. Miyazono, T. Fujita, Focal adhesion kinase activity is required for bone morphogenetic protein—Smad1 signaling and osteoblastic differentiation in murine MC3T3-E1 cells. *J. Bone Miner. Res.* **16**, 1772–1779 (2001).
33. B. G. Keselowsky, D. M. Collard, A. J. García, Integrin binding specificity regulates biomaterial surface chemistry effects on cell differentiation. *Proc. Natl. Acad. Sci. U.S.A.* **102**, 5953–5957 (2005).
34. T. A. Petrie, C. D. Reyes, K. L. Burns, A. J. García, Simple application of fibronectin–mimetic coating enhances osseointegration of titanium implants. *J. Cell. Mol. Med.* **13**, 2602–2612 (2009).
35. C. D. Reyes, T. A. Petrie, K. L. Burns, Z. Schwartz, A. J. García, Biomolecular surface coating to enhance orthopaedic tissue healing and integration. *Biomaterials* **28**, 3228–3235 (2007).
36. D. J. Irvine, K. A. Hue, A. M. Mayes, L. G. Griffith, Simulations of cell-surface integrin binding to nanoscale-clustered adhesion ligands. *Biophys. J.* **82**, 120–132 (2002).
37. C. J. Brinkerhoff, J. J. Linderman, Integrin dimerization and ligand organization: Key components in integrin clustering for cell adhesion. *Tissue Eng.* **11**, 865–876 (2005).
38. G. Jiang, G. Giannone, D. R. Critchley, E. Fukumoto, M. P. Sheetz, Two-piconewton slip bond between fibronectin and the cytoskeleton depends on talin. *Nature* **424**, 334–337 (2003).

39. **Acknowledgments:** We thank H. Erickson for providing complementary DNA for fibronectin constructs and M. Mathews for implant machining. **Funding:** This work was supported by NIH grants R01 EB-004496 and R01 GM-06591. T.A.P. acknowledges support from the Medtronic Foundation. **Author contributions:** T.A.P., J.E.R., D.W.D., T.T.L., S.J., and K.L.T. contributed to collection of experimental data; T.A.P. and A.J.G. analyzed the data; T.A.P., D.M.C., and A.J.G. contributed to writing the paper. **Competing interests:** A.J.G. has consulted for Synthes Inc. Georgia Tech Research Corporation has applied for a U.S. patent on the use of FNIII$_{7–10}$ for orthopedic repair. The authors declare that they have no competing interests.

Submitted 22 February 2010
Accepted 30 July 2010
Published 18 August 2010
10.1126/scitranslmed.3001002

Citation: T. A. Petrie, J. E. Raynor, D. W. Dumbauld, T. T. Lee, S. Jagtap, K. L. Templeman, D. M. Collard, A. J. García, Multivalent integrin-specific ligands enhance tissue healing and biomaterial integration. *Sci. Transl. Med.* **2**, 45ra60 (2010).

A1.2 *Role of material-driven fibronectin fibrillogenesis in cell differentiation.* Biomaterials.

Biomaterials 32 (2011) 2099–2105

Contents lists available at ScienceDirect

Biomaterials

journal homepage: www.elsevier.com/locate/biomaterials

Role of material-driven fibronectin fibrillogenesis in cell differentiation

Manuel Salmerón-Sánchez [a,b,c,*], Patricia Rico [a,b], David Moratal [a], Ted T. Lee [d,e], Jean E. Schwarzbauer [f], Andrés J. García [d,e,**]

[a] Center for Biomaterials and Tissue Engineering, Universidad Politécnica de Valencia, Spain
[b] CIBER de Bioingeniería, Biomateriales y Nanomedicina, Valencia, Spain
[c] Regenerative Medicine Unit, Centro de Investigación Príncipe Felipe, Valencia, Spain
[d] Woodruff School of Mechanical Engineering, Georgia Insitute of Technology, Atlanta, GA, USA
[e] Petit Institute for Bioengineering and Bioscience, Georgia Insitute of Technology, Atlanta, GA, USA
[f] Department of Molecular Biology, Princeton University, Princeton, NJ, USA

ARTICLE INFO

Article history:
Received 3 November 2010
Accepted 25 November 2010
Available online 24 December 2010

Keywords:
Fibronectin
Cell adhesion
Integrin
Interface

ABSTRACT

Fibronectin (FN) is a ubiquitous extracellular matrix protein (ECM) protein that is organized into fibrillar networks by cells through an integrin-mediated process that involves contractile forces. This assembly allows for the unfolding of the FN molecule, exposing cryptic domains that are not available in the native globular FN structure and activating intracellular signalling complexes. However, organization of FN into a physiological fibrillar network upon adsorption on a material surface has not been observed. Here we demonstrate cell-free, material-induced FN fibrillogenesis into a biological matrix with enhanced cellular activities. We found that simple FN adsorption onto poly(ethyl acrylate) surfaces, but not control polymers, triggered FN organization into a fibrillar network via interactions in the amino-terminal 70 kDa fragment, which is involved in the formation of cell-mediated FN fibrils. Moreover, the material-driven FN fibrils exhibited enhanced biological activities in terms of myogenic differentiation compared to individual FN molecules and even type I collagen. Our results demonstrate that molecular assembly of FN can take place at the material interface, giving rise to a physiological protein network similar to fibrillar matrices assembled by cells. This research identifies material surfaces that trigger the organization of extracellular matrix proteins into biological active fibrils and establishes a new paradigm to engineer ECM-mimetic biomaterials.

1. Introduction

Fibronectin (FN) is a glycoprotein which forms dimers consisting of two subunits (~220 kDa) linked by a single disulfide bond near the carboxyl termini [1,2]. Each subunit contains three types of repeating modules (types I, II and III), which mediate interactions with other FN molecules, other ECM components, and cell surface receptors [3]. Cells primarily interact with FN via integrins, a family of transmembrane cell adhesion receptors [4]. Integrin-mediated adhesion is a complex process that involves integrin association with the actin cytoskeleton and clustering into supramolecular complexes that contain structural proteins (vinculin, talin, tensin, etc.) and signaling molecules [4,5].

Most cells assemble rich matrices via an integrin-dependent contractile process that incorporates FN molecules, either synthesized by cells or reorganized from their surroundings, into matrix fibrils [6,7]. The thickness of FN matrix fibrils ranges from 10 to 1000 nm in diameter and these fibrils consist of a few to hundred of FN molecules across. FN fibril assembly involves the 70 kDa amino-terminal domain of FN, through binding of I_{1-5} either to III_{1-2} or III_{12-14} domains [8].

Significant efforts have focused on engineering materials that recapitulate characteristics of ECM, such as the presentation of cell adhesive motifs or protease degradable cross-links, in order to direct cellular responses [9,10]. However, materials-based approaches to reconstitute the network structure and bioactivity of FN fibrillar matrices have not been established. The use of denaturing or unfolding agents and applied forces to promote FN fibril assembly indicate that changes in the structure of FN are required to expose sites within the molecule to drive assembly into fibers [11–16]. We hypothesized that adsorption of individual FN molecules onto particular surface chemistries would induce exposure of self-

* Corresponding author. Tel.: +34 96 3877275.
** Corresponding author. Tel.: +1 404 894 9384.
E-mail addresses: masalsan@fis.upv.es (M. Salmerón-Sánchez), andres.garcia@me.gatech.edu (A.J. García).

0142-9612/$ – see front matter © 2010 Elsevier Ltd. All rights reserved.
doi:10.1016/j.biomaterials.2010.11.057

a

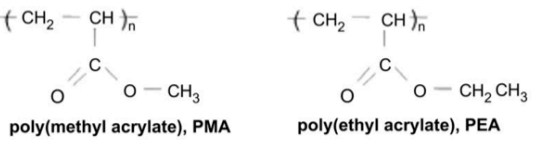

b

Substrate	WCA (°)	FN surface density (ng/cm^2)
PMA	74 ± 2	470 ± 43
PEA	80 ± 2	450 ± 45

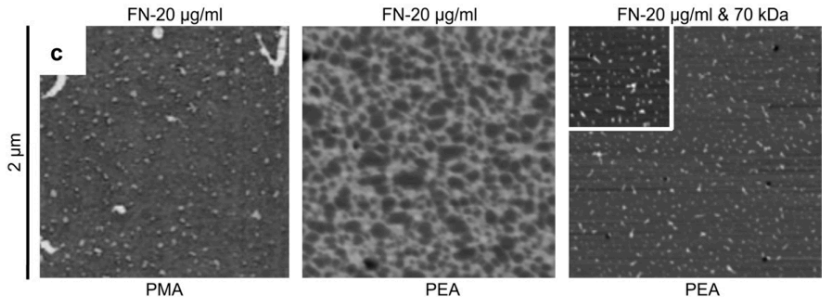

Fig. 1. FN adsorption on material substrates. a, chemical structure of the polymers PEA and PMA. b, water contact angle on the different substrates and equilibrium surface density of adsorbed FN from a solution of concentration 20 µg/mL. c, FN distribution on material substrates as obtained by AFM: globular aggregates on PMA and FN network on PEA after adsorption from a solution of concentration 20 µg/mL. FN fibrillogenesis is blocked on PEA in the presence of the amino-terminal 70 kDa FN fragment, leading to dispersed molecular aggregates.

assembly sites to drive FN fibril assembly and identified poly(ethyl acrylate) (PEA) as a potential surface chemistry to generate FN fibrils [17,18]. Here, we investigate the organization of FN molecules at the material (PEA) interface and the analogy with the physiologically cell-induced FN fibrillogenesis [19]. Additionally, we also compare cell differentiation on the substrate-assembled FN network versus those substrates that do not promote FN fibrillogenesis.

2. Materials and methods

2.1. Materials

Polymer sheets were obtained by radical polymerization of a solution of the corresponding alkyl acrylate, i.e. methyl (MA) and ethyl (EA), (Sigma–Aldrich, Steinheim, Germany) using 0.2 wt% benzoin (98% pure, Scharlau, Barcelona, Spain) as a photoinitiator. The polymerization was carried out up to limiting conversion. After polymerization, low molecular-mass substances were extracted from the material by drying in vacuo to constant weight. Thin films were prepared by making use of a spin-coater (Brewer Science, Rolla, USA). Each one of the synthesized polymers was dissolved in toluene at a concentration of 2 wt%. Spin casting was performed on 12 mm glass coverslips at 2000 rpm for 30 s. Samples were dried in vacuo at 60 °C before further characterization. The obtained films are not porous and approximately 500 nm thickness. Water contact angles were measured using a Dataphysics OCA. The volume of the drop was 20 µL and the measurement was performed after 10 s of substrate-water contact.

2.2. Atomic force microscopy

AFM experiments were performed using a Multimode AFM equipped with NanoScope IIIa controller from Veeco (Manchester, UK) operating in tapping mode; the Nanoscope 5.30r2 software version was used. Si-cantilevers from Veeco (Manchester, UK) were used with force constant of 2.8 N/m and resonance frequency of 75 kHz. The phase signal was set to zero at a frequency 5–10% lower than the resonance one. Drive amplitude was 600 mV and the amplitude setpoint A_{sp} was 1.8 V. The ratio between the amplitude setpoint and the free amplitude A_{sp}/A_0 was kept equal to 0.8.

2.3. Protein adsorption

FN from human plasma (Invitrogen, Carlsbad, CA) was adsorbed on the different substrates by immersing the material sheets in FN solutions at concentrations of either 2 or 20 µg/mL in PBS. After adsorption, samples were rinsed in PBS to eliminate the non-adsorbed protein. AFM was performed in the tapping mode immediately after sample preparation. Height, phase and amplitude magnitudes were recorded simultaneously for each image. To quantify the amount of adsorbed FN, we measured the remaining protein in the supernatant, i.e. the amount of protein that remained in solution without adsorbing on the material surface as explained elsewhere [17].

2.4. Cells

Murine C2C12 myoblasts (ATCC CRL-1772) were maintained in Dubelcco's Modified Eagle Medium (DMEM) supplemented with 20% fetal bovine serum and 1% penicillin-streptomycin in a humidified atmosphere at 37 °C and 5% CO_2. Cells were subculture before to reaching confluence (approximately every 2 days). For experiments, C2C12 cells were seeded at 2000 cells/cm^2 on the different surfaces after coating with different concentrations of FN in DMEM supplemented with 1% insulin-transferin-selenium and 1% penicillin-streptomycin to induce myogenic differentiation.

2.5. Myogenic differentiation

C2C12 cells were cultured on FN-coated materials for 4 days under differentiation conditions and immunostained for sarcomeric myosin. Briefly, cultures were fixed in 70% ethanol/37% formaldehyde/glacial acetic acid (20:2:1) and then blocked in 5% goat serum in DPBS for 1 h. Samples were sequentially incubated in MF-20 mouse antibody (Developmental Studies Hybridoma Bank, University of Iowa, USA) and anti-mouse AlexaFluor-488 conjugated secondary antibody; cell nuclei were counter-stained with ethidium homodimer-2 (200 nM). Cultures were scored by fluorescence microscopy for differentiation as the percentage of cells positive for sarcomeric myosin using an in-house image analysis routine. For experiments

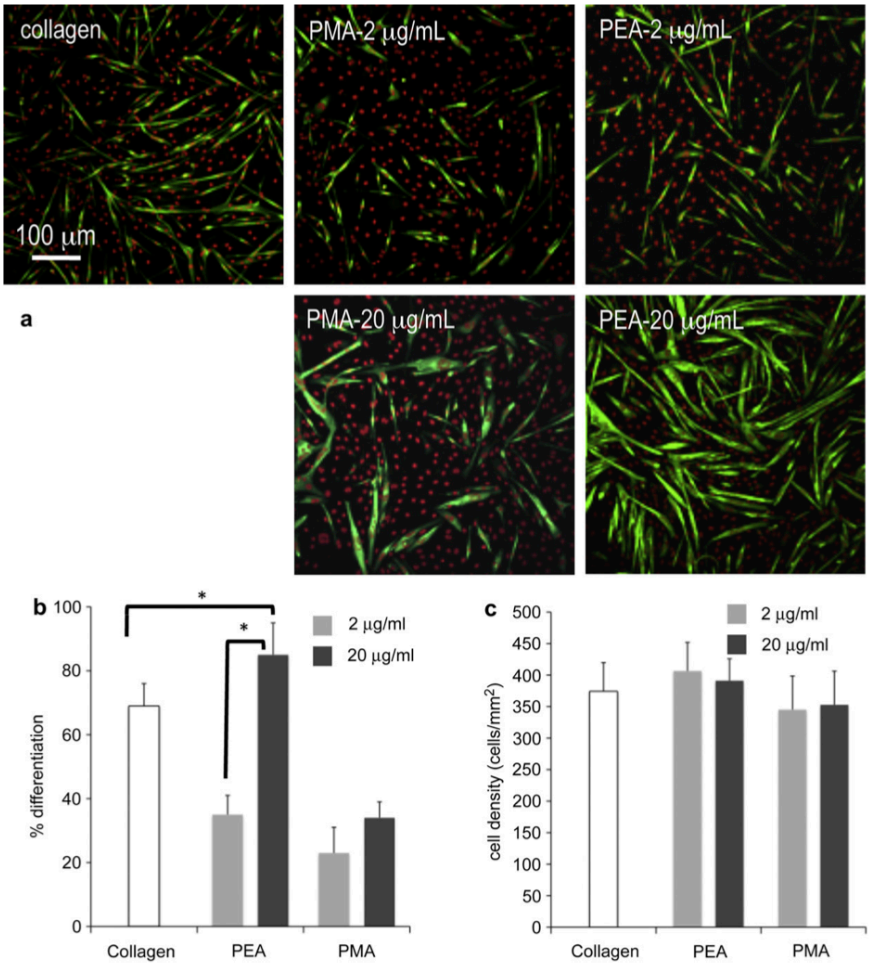

Fig. 2. Myogenic differentiation on the different substrates. a, fluorescence staining showing sarcomeric myosin-positive cells (green) and cell nuclei (red) on FN-coated surfaces (from solutions of concentration 2 and 20 μg/mL) and control collagen. b, myogenic differentiation as determined by the percentage of sarcomeric myosin-positive cells on the different substrates after adsorbing FN from solutions of concentrations 2 and 20 μg/mL. c, cell density on each substrate.

including integrin blocking, HFN7.1 antibody (7.3 μg/mL final concentration) was added to culture media on day 1 in order to avoid altering initial adhesion. For experiments including contractility inhibitors, Y-27632 or blebbistatin was added to culture medium at different concentrations (10, 20 and 40 μM) after 2 h and maintained for 4 days.

2.6. Integrin binding and FAK

Integrin binding to FN-coated materials was analyzed via immunostaining following cross-linking of bound integrins to FN and extraction of cellular components. Cells were seeded on FN-coated materials for 4 h. Cultures were rinsed in DPBS and incubated in ice-cold DTSSP (1.0 mM final concentration in DPBS + 2 mM dextrose) for 30 min. Unreacted cross-linker was quenched with 50 mM Tris in DPBS for 15 min and bulk cellular components were extracted in 0.1% SDS + 350 mg/mL phenylmethylsulfonyl fluoride in DPBS. After blocking with 5% FBS + 0.1% Tween-20 for 1 h, bound integrins were immunostained with anti-α_5 and AlexaFluor488-conjugated secondary antibody. For FAK assays, cells were detached and gently agitated in suspension under serum-free conditions for 45 min to reduce background. Cells were then seeded on FN-coated materials serum-free for 2 h. Cells were lysed in RIPA buffer containing protease inhibitors (1% Triton X-100, 1% sodium deoxycholate, 0.1% SDS, 150 mM NaCl, 150 mM Tris–HCl (pH 7.2), 350 μg/mL PMSF, 10 μg/mL leupeptin, and 10 μg/mL aprotonin) for 20 min at room temperature. Total protein was quantified using micro-BCA (Pierce). Identical amounts of cell lysates were mixed in sample buffer (50 mM Tris–HCl pH 6.8, 100 mM DTT, 2% SDS, 10% glycerol, and 0.1% bromophenol blue) and separated by SDS–PAGE. After transferring to nitrocellulose membranes and blocking with Blotto (5% nonfat dry milk, 0.2% Tween-20) overnight at 4 °C, membranes were gently rocked in antibodies

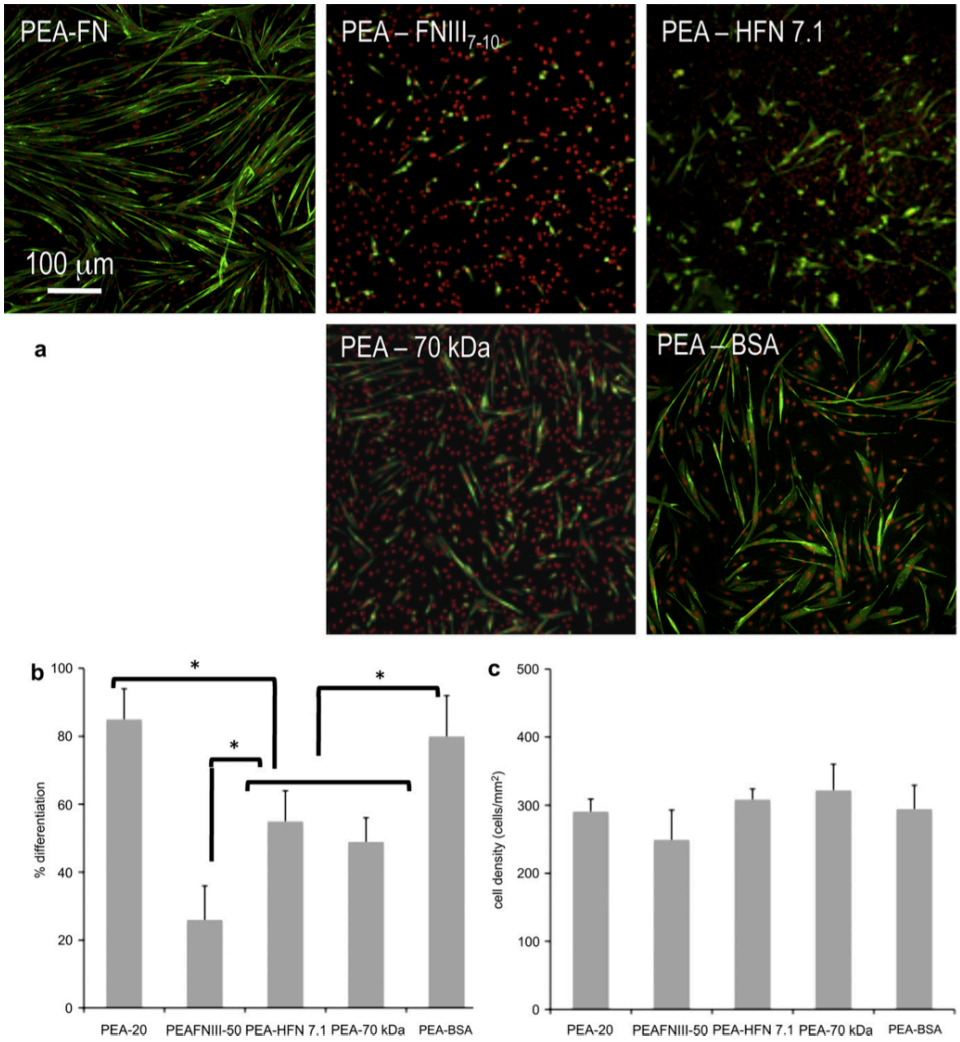

Fig. 3. Both the central FN domain ($FNIII_{7-10}$) and the amino-terminal fragment (70-kDa) involved in FN fibrillogenesis enhance myogenic differentiation on the material-driven FN network on PEA. a, fluorescence staining showing sarcomeric myosin-positive cells (green) and cell nuclei (red) on the substrate-induced FN network (PEA-FN), after coating PEA with a recombinant fragment of FN ($FNIII_{7-10}$), blocking the central FN domain with HFN7.1 antibody (PEA-HFN7.1), after adsorbing FN altogether with the 70 kDa fragment, which blocked the formation of the FN network (PEA-70 kDa), control experiment for the 70 kDa fragment using BSA instead (PEA-BSA). b, myogenic differentiation as determined by the percentage of sarcomeric myosin-positive cells on the different substrates with the conditions explained in a. c, cell density for each condition.

against FAK and specific phosphorylated FAK tyrosine residues (anti-total FAK at 1 μg/mL, anti-FAK pY397 at 0.35 μg/mL) for 1 h. After washing with TBS-Tween (20 mM Tris–HCl pH 7.6, 137 mM NaCl, 0.1% Tween-20), secondary antibody (biotin-conjugated anti-rabbit IgG; 1:20,000) was added for 1 h, followed by alkaline phosphatase-conjugated anti-biotin antibody (1:10,000) in Blotto. FAK bands were visualized by a Fuji Image Analyzer and phosphorylation levels normalized to total FAK.

2.7. Phosphorylation of myosin light chain

C2C12 cells were cultured on FN-coated materials for 1 day under differentiation conditions and immunostained for phosphorylated myosin light chain. Briefly, cultures were fixed in 4% formaldehyde in PBS for 15 min at room temperature and then blocked in blocking buffer (5% goat serum and 0.3% Triton-1X-100 in DPBS) for 1 h. Samples were sequentially incubated in pMLC rabbit antibody (1:200, Cell

Signalling), and goat anti-rabbit AlexaFluor-488 conjugated secondary antibody (1:100); cell nuclei were counter-stained with Hoescht (200 nM). For experiments including contractility inhibitors, Y-27632 or blebbistatin was added to culture medium at different concentrations (10, 20 and 40 μM) after 2 h.

2.8. Statistics

All experiments were performed at least three times in triplicate unless otherwise noted. Data are reported as mean ± standard error. Results were analyzed by one-way ANOVA using SYSTAT 8.0 (SPSS). If treatment level differences were determined to be significant, pair-wise comparisons were performed using a Tukey post hoc test. A 95% confidence level was considered significant.

3. Results and discussion

3.1. Material-driven FN fibrillogenesis

We compared the organization of FN at the material interface on two similar chemistries: poly(ethyl acrylate) (PEA) and poly(methyl acrylate) (PMA) which differ in one single carbon in the side chain (Fig. 1a). Both surface chemistries show similar wettability and total amount of adsorbed FN (Fig. 1b). However, the conformation and distribution of the protein following passive adsorption onto these surfaces are completely different (Fig. 1c). Interconnected FN fibrils are organized upon adsorption from a solution of concentration 20 μg/mL on PEA (Fig. 1c) whereas only dispersed molecules are present on PMA (Fig. 1c). FN fibril formation on PEA is dependent on the FN solution concentration, as lower concentrations result in dispersed adsorbed molecules (Supplementary Fig. S1). We next examined the requirements for the 70 kDa amino-terminal domain of FN in this material-driven fibrillogenesis. The 70 kDa amino-terminal regions are essential for cell-mediated FN assembly, and within this region, the I_{1-5} repeats confer FN binding activity [20]. This domain is not accessible in the folded, compact structure of FN in solution and a conformational change of the molecule is mandatory for physiological matrix assembly to occur [6]. Strikingly, material-driven fibrillogenesis absolutely requires the 70 kDa amino-terminal region of FN. Addition of the 70 kDa fragment completely blocks the organization of FN at the material interface and only discrete molecular aggregates can be observed (Fig. 1c) without any trace of the assembled FN network. The resulting adsorbed FN resembles the FN adsorbed onto the control PMA polymer. These results demonstrate that a particular polymer chemistry (PEA) drives assembly of adsorbed FN molecules into FN fibrils and this material-driven fibrillogenesis requires the 70 kDa amino-terminal domain of FN.

3.2. Cell differentiation on material-assembled FN

We hypothesized that material-driven FN fibrils have enhanced biological activity compared to adsorbed FN molecules because the fibrillar structure recapitulates the native structure of FN matrices. We evaluated the biological activity of the material-driven FN networks by examining the myogenic differentiation process [21]. Sarcomeric myosin expression and cell bipolar alignment and fusion into myotubes, markers of myogenesis, were significantly higher on the substrate-induced FN network (Fig. 2, PEA-20) as compared to the same substrate coated with a lower density of FN that does not lead to the fibrillar organization of the protein at the material interface (Fig. 2, PEA-2), and PMA polymer coated with the same density of FN but lacking any fibrillar organization (Fig. 2, PMA-20). Surprisingly, myogenic differentiation was considerably more robust on the PEA-assembled FN matrix than on collagen type I, which represents that standard substrate for myogenic differentiation (Fig. 2b) [22]. It is important to emphasize that these differences in myogenic differentiation are not due to differences in the number of cells on the substrates (Fig. 2c).

To further evaluate the biological activity of the material-driven FN fibrils, we used different blocking antibodies and FN fragments to assess the importance of different parts of the FN molecule on the myogenic differentiation process (Fig. 3). Addition of the adhesion-blocking HFN7.1 antibody inhibited differentiation on PEA to levels found for those substrates on which FN is not organized into a network (Fig. 3, PEA-HFN7.1). The HFN7.1 antibody binds to the flexible linker between the 9th and 10th type III repeats of FN where the integrin-binding domain is located, demonstrating that the integrin-binding domain of FN is essential for myogenic differentiation on FN fibrils. Moreover, HFN7.1 is specific for human FN and does not cross-react with mouse FN, indicating that the human FN adsorbed onto the substrate prior cell seeding provided the dominant signal for differentiation. We next examined whether a recombinant fragment of FN spanning the 7th–10th type III repeats ($FNIII_{7-10}$) that encompass the integrin-binding domain recapitulates the material-dependent differences in myogenic differentiation [23]. In contrast to complete FN, adsorption of $FNIII_{7-10}$ onto PEA yielded minimal levels of myogenic differentiation (Fig. 3, PEA-$FNIII_{7-10}$). $FNIII_{7-10}$ does not contain domains involved in FN–FN interactions (I_{1-5} and III_{1-2} or III_{12-14} domains), demonstrating that both integrin-binding domains and domains involved in FN–FN interactions are required for the enhanced myogenic differentiation on PEA-driven FN matrices.

Consistent with our observations for FN network formation, addition of the 70 kDa amino-terminal fragment during the adsorption process of FN blocked the differentiation of myoblasts on PEA (Fig. 3, PEA-70 kDa). This result demonstrates the importance of FN–FN interactions and the fibrillar structure of the protein on the cell differentiation process – only when the FN network is assembled on PEA via interactions involving the 70 kDa amino-terminal fragment does the differentiation process occurs. As a control, when albumin (a protein with similar molecular weight to the 70 kDa fragment) is added at the same concentration during the network assembly process of FN at the material interface, the formation of the network is not disturbed and myoblast differentiation levels remain as in the original material-assembled FN network (Fig. 3, PEA-BSA). Importantly, the addition of the 70 kDa FN fragment once the FN network is already assembled on the material surface has no effect on subsequent myoblast differentiation (Supplementary Fig. S2).

3.3. Cell contractility on material-assembled FN

To gain insights into the mechanisms controlling the enhanced cellular responses to material-driven FN networks, we examined binding of $\alpha_5\beta_1$ integrin to the adsorbed FN since this receptor provides the primary adhesion mechanism in this cell model [22]. Immunofluorescence staining following crosslinking of bound integrins to FN and extraction of cellular components revealed no significant differences in integrin binding among FN on different surfaces, demonstrating that the substrate-assembled FN network does not alter integrin binding (Supplementary Fig. S3). Similarly, no differences in FAK phosphorylation, a critical signal related to integrin-binding and myoblast differentiation, were observed between FN molecules on PEA and control PMA substrates (Supplementary Fig. S3) [24,25].

Contractile forces generated within the cell regulate several functions, including muscle cell contraction and differentiation [26]. Contractility results from dynamic interactions between actin filaments and myosin, which are regulated via phosphorylation of myosin light chain (MLC) [27]. Rho GTPases control the formation of stress fibers and focal adhesion assembly by modulating MLC phosphorylation and generating actin-myosin contractility. Myoblast differentiation is characterized by the synthesis of the proteins of the contractile apparatus and the fusion of single myoblasts into multinucleated

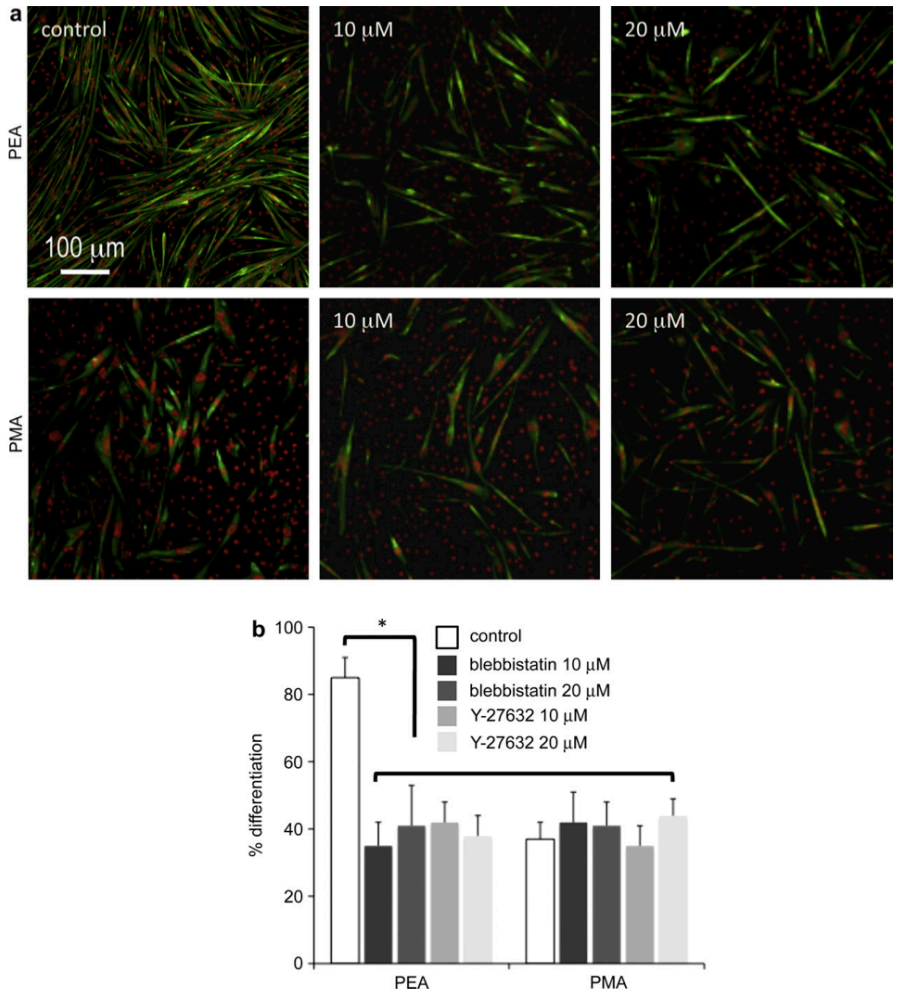

Fig. 4. The FN network upregulates differentiation by enhancing cell contractility. a, fluorescence staining showing sarcomeric myosin-positive cells (green) and cell nuclei (red) on the substrate-induced FN network (PEA-control) and the reference polymer (PMA-control). The effect of adding Y-27632 at different concentrations in the culture medium is shown. b. myogenic differentiation as determined by the percentage of sarcomeric myosin-positive cells on the different substrates (PEA, PMA) in the presence of contractility inhibitors at different concentrations (Y-27632, blebbistatin) in the culture medium.

myotubes [28]. Immunofluorescence staining for phosphorylated MLC revealed the presence of well-defined fibers, coincident with the actin cytoskeleton, on cells cultured on the FN network (PEA) but not on either PMA or collagen (Supplementary Fig. S4). We used pharmacological inhibitors that impair contractility to examine the contributions of contractility on myogenic differentiation on the substrate-induced FN network. Y-27632 is a specific inhibitor of Rho-kinase, and blebbistatin is a specific inhibitor of myosin II activity [29,30]. Staining for phosphorylated MLC was reduced in a dose-dependent manner in the presence of these inhibitors on the different substrates (Supplementary Fig. S4). More importantly, myoblast differentiation was drastically arrested by these contractile inhibitors only on the substrate-induced FN network (Fig. 4). Differentiation levels diminished from 85% to 40% on PEA, but were not altered on PMA, which remains approximately equal to 40% independently of the presence of either Y-27632 or blebbistatin (Supplementary Fig. S5, S6). These results reveal the importance of the material-assembled FN network on myoblast differentiation and show that actin-myosin contractility is

activated by the physiological material-assembled FN fibrils to drive differentiation.

4. Conclusions

We have identified a synthetic material – poly(ethyl acrylate) – that drives cell-free, physiological organization of FN into fibrillar networks upon adsorption. This material promotes the biomimetic assembly of FN in absence of cells. This research facilitates the preparation of new tools to advance in the investigation of the biological process of FN fibrillogenesis and establishes a new strategy for engineering of biomimetic materials.

Acknowledgements

This work was supported by NSF DMR-0909002 and MAT2009-14440-C02-01. MSS was supported by the Spanish Government through PR2009-0351 to stay in Atlanta (Georgia Institute of Technology) for a sabbatical during 2010.

Appendix

Figures with essential color discrimination. Figs. 2–4 in this article are difficult to interpret in black and white. The full color images can be found in the online version, at doi:10.1016/j.biomaterials.2010.11.057.

Appendix. Supplementary material

Supplementary data related to this article can be found online at doi:10.1016/j.biomaterials.2010.11.057.

References

[1] Erickson HP, McDonagh J. FN molecule visualized in electron microscopy: a long, thin, flexible strand. J Cell Biol 1981;91:673–8.
[2] Erickson HP, Carell NA. FN in extended and compact conformations. Electron microscopy and sedimentation analysis. J Biol Chem 1983;258:14539–44.
[3] Pankov R, Yamada KM. FN at a glance. J Cell Sci 2002;115:3861–3.
[4] Hynes RO. Integrins: bidirectional, allosteric signaling machines. Cell 2002;110:673–87.
[5] García AJ. Get a grip: integrins in cell-biomaterial interactions. Biomaterials 2005;26:7525–9.
[6] Mao Y, Schwarzbauer JE. FN fibrillogenesis, a cell-mediated matrix assembly process. Matrix Biol 2005;24:389–99.
[7] Altankov G, Grinnell F, Groth T. Studies of the biocompatibility of materials: fibroblast reorganization of substratum-bound FN on surfaces varying in wettaability. J Biomed Mater Res 1996;30:385–91.
[8] Geiger B, Bershadsky A, Pankov R, Yamada KM. Transmembrane extracellular matrix – cytoskeleton crosstalk. Nat Rev Mol Cell Bio 2001;2:793–805.
[9] Lutolf MP, Gilbert PM, Blau HM. Designing materials to direct stem-cell fate. Nature 2009;462:433–41.
[10] Petrie TA, Raynor JE, Dumbauld DW, Lee TT, Jagtap S, Templeman KL, et al. Multivalent integrin-specific ligands enhance tissue healing and biomaterial integration. Sci Transl Med 2010;2:45ra60.
[11] Mosher DF, Johnson RB. In vitro formation of disulfide-bonded FN multimers. J Biol Chem 1983;258:6595–601.
[12] Williams EC, Janmey PA, Johnson RB, Mosher DF. FN effect of disulfide bond reduction on its physical and functional properties. J Biol Chem 1983;258:5911–4.
[13] Morla A, Zhang Z, Rouslahti E. Super FN is a distinct form of FN. Nature 1994;367:193–6.
[14] Baneyx G, Vogel V. Self-assembly of FN into fibrillar networks underneath dipalmitoyl phosphatidylcholine monolayers: role of lipid matrix and tensile forces. Proc Natl Acad Sci USA 1999;96:12518–23.
[15] Ulmer J, Geiger B, Spatz JP. Force-induced FN fibrillogenesis. Soft Matter 2008;4:1998–2007.
[16] Kaiser P, Spatz JP. Differential adhesion of fibroblasts and neuroblastoma cells on size- and geometry-controlled nanofibrils of the extracellular matriz. Soft Matter 2010;6:113–9.
[17] Rico P, Rodríguez Hernández JC, Moratal D, Altankov G, Monleón Pradas M, Salmerón-Sánchez M. Substrate-induced assembly of fibronectin into networks: influence of surface chemistry and effect on osteoblast adhesion. Tissue Eng Part A 2009;15:3271–81.
[18] Gugutkov D, González-García C, Rodríguez Hernández JC, Altankov G, Salmerón-Sánchez M. Biological activity of the substrate-induced FN network: insight into the third dimension through electrospun fibers. Langmuir 2009;25:10893–900.
[19] Aguirre KM, McCormick RJ, Schwarzbauer JE. FN self-association is mediated by complementary sites within the amino-terminal one-third of the molecule. J Biol Chem 1994;269:27863–8.
[20] Schwarzbauer JE. Identification of FN sequences required for assembly of a fibrillar matrix. J Cell Biol 1991;113:1463–73.
[21] Sabourin LA, Rudnicki MA. The molecular regulation of myogenesis. Clin Genet 2000;57:16–25.
[22] García AJ, Vega MD, Boettiger D. Modulation of cell proliferation and differentiation through substrate-dependent changes in FN conformation. Mol Biol Cell 1999;10:785–98.
[23] Petrie TA, Raynor JE, Reyes CD, Burns KL, Collard D, García AJ. The effect of integrin-specific bioactive coatings on tissue healing and implant osteointegration. Biomaterials 2008;29:2849–57.
[24] Michael KE, Dumbauld DW, Burns KL, Hanks SK, García AJ. FAK modulates cell adhesion strengthening via integrin activation. Mol Biol Cell 2009;20:2508–19.
[25] Quach NL, Biressi S, Reichardt LF, Keller C, Rando TA. Focal adhesion kinase signaling regulates the expression of caveolin 3 and β1 integrin, genes essential for normal myoblast fusion. Mol Biol Cell 2009;20:3422–35.
[26] Griffin MA, Sen S, Sweeney HL, Discher DE. Adhesion-contractile balance in myocite differentiation. J Cell Sci 2004;117:5855–63.
[27] Kaibuchi K, Kuroda S, Amano M. Regulation of the cytoskeleton and cell adhesion by the Rho family GTPases in mammalian cells. Annu Rev Biochem 1999;68:459–86.
[28] Andres V, Walsh K. Myogenin expression, cell cycle withdrawal, and phenotypic differentiation are temporally separable events that precede cell fusion upon myogenesis. J Cell Biol 1996;132:657–66.
[29] Narumiya S, Ishizaki T, Uehata M. Use and properties of ROCK-specific inhibitor Y-27632. Methods Enzymol 2000;325:273–84.
[30] Kovács M, Tóth J, Hetényi C, Málnási-Csizmadia A, Sellers JR. Mechanism of blebbistatin inhibition of myosin II. J Biol Chem 2004;279:35557–63.

Materials Views
www.MaterialsViews.com

ADVANCED MATERIALS
www.advmat.de

Triggered Cell Release from Materials Using Bioadhesive Photocleavable Linkers

*Melanie Wirkner, José María Alonso, Verona Maus, Marcelo Salierno, Ted T. Lee, Andrés J. García, and Aránzazu del Campo**

The ability to trigger or turn "on" or "off" material properties with external stimuli in order to control biological responses is critically important to biotechnological and biomedical applications. One such application is the use of light to trigger cell adhesion to synthetic materials by controlling the presentation of the bioadhesive arginine-glycine-aspartic acid (RGD) oligopeptide. Successful strategies for photoactivation of cell adhesion include direct modification of the chemical structure of the RGD peptide with photoresponsive molecules,[1] using a light-triggered phase transition of a RGD-containing amphiphilic peptide,[2] and linking the RGD peptide to the surface using azobenzene units.[3] However, no light-based approaches are available to specifically promote cell adhesion to materials with the ability to precisely deactivate or detach the cells at later time points or spatial locations. This is a relevant issue in cell biology because cells need to be removed from the culture plate during culture and before application and in tissue engineering, i.e., cell sheet engineering therapies. In this article, we introduce a flexible and facile strategy for controlled light-triggered cell release from surfaces based on the use of photocleavable linkers to couple the RGD ligand to the surface. Upon light exposure, the linker is cleaved by means of a photolytic reaction,[4] thereby untethering the RGD peptide from the surface and releasing adhering cells. Our approach represents a more specific and controlled alternative to enzymatic digestion, temperature-driven changes in substrate hydrophobicity,[5] or electrochemical dissolution of polyelectrolyte coatings[6] or self-assembled monolayers (SAMs)[7] onto conductive substrates for cell release (see ref. [8] for a recent review on this topic). Our strategy is applicable to any material, provided that there is proper linker design, and provides direct control over the molecular interactions involved in cell adhesion.

The general strategy is presented in **Figure 1**. The photocleavable linker contains an intercalated 4,5-dialkoxy 1-(2-nitrophenyl)-ethyl photolabile group and can be attached to free amine groups at the surface of the material via a carbamate bond. A tetraethyleneglycol (TEG) spacer is included in the structure in order to provide a protein- and cell-repellent surface before attaching bioactive ligands. A bioactive ligand, such as biotin or RGD oligopeptide, can be attached to the surface by reacting with the free amine at the end of the TEG spacer (I). The biological ligand then mediates specific binding to the surface of a particular target, such as streptavidin for biotin or cells for RGD peptides (II). Upon light exposure, the chromophore is photocleaved (III) and the linker, along with its target, is effectively removed from the surface (IV). As with photolithographic techniques, full control over the spatiotemporal resolution of the release process is possible. By using a photomask for the illumination steps, patterns of active and nonactive sites can be previously generated, and immobilized species can be site-selectively detached in the last step.

The detailed synthesis of the linker is included in the Supporting Information. The linker was successfully reacted with amine-terminated substrates and the coupling reaction was monitored by UV spectroscopy on modified quartz substrates (where the characteristic bands of the chromophore were visible) and by ellipsometry on modified silicon wafers (an increase in the layer thickness of 1.4 nm was detected). The photocleavage of the linker from the surface was followed by UV spectroscopy after irradiating quartz substrates at λ_{max} = 350 nm for increasing times and washing with tetrahydrofurane and water. Exposure of *o*-nitrobenzyl derivatives to light induces an intramolecular redox reaction and cleavage of the cage from the surface (see scheme in **Figure 2**). Washing removed the photocleaved part of the molecule from the surface, and this was reflected in a significant decrease in absorbance in the UV spectrum, most visible around λ_{max} (Figure 2). The ratio between the absorbance pre- and post-irradiation at λ_{max} represents the amount of photocleaved linker upon exposure (conversion). After 8 min irradiation, no significant changes were visible in the UV spectrum with time, indicating that a maximum conversion of 70% was reached (inset in Figure 2). The residual absorbance indicates that part of the chromophore and/or photolytic by-products remained attached to the surface or entrapped by the surface layer.[9] The residual attached chromophore could be a potential limitation in the performance of the light-induced detachment step.

M. Wirkner, V. Maus, M. Salierno, A. del Campo
Max-Planck-Institut für Polymerforschung
Ackermannweg 10, 55128 Mainz, Germany
E-mail: delcampo@mpip-mainz.mpg.de
J. M. Alonso[+]
Max Planck Institute für Metallforschung
Heisenbergstrasse 3, 70569 Stuttgart, Germany
T. T. Lee, A. J. García
Woodruff School of Mechanical Engineering
Georgia Institute of Technology
315 Ferst Drive, Atlanta, GA 30332–0363, USA
T. T. Lee, A. J. García
Petit Institute for Bioengineering and Bioscience
Georgia Institute of Technology
315 Ferst Drive, Atlanta, GA 30332–0363, USA
[+] Present address: CIC nanoGUNE Consolider, Tolosa Hiribidea, 76, 20018 San Sebastián, Spain

DOI: 10.1002/adma.201100925

ADVANCED MATERIALS
www.advmat.de

Materials Views
www.MaterialsViews.com

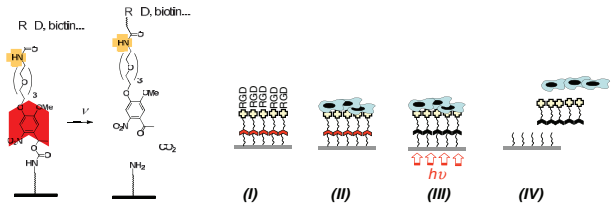

Figure 1. Left: Chemical structure of the photocleavable linker after reaction with the surface and the ligand before and after light exposure. Right: Working principle of phototriggered release, specifically for cell detachment from surfaces using photocleavable linkers with an intercalated cage.

In order to assess the ability of the photolabile moiety to mediate specific binding and detachment, we tested the attachment and controlled removal of the fluorophore AlexaFluor 647 succinimidyl ester and of streptavidin after functionalization with biotin. **Figure 3** and Figure A (Supporting Information) show schemes of the process. A substrate modified with the photosensitive linker was irradiated through a mask containing 100 µm wide chrome stripes separated by 200 µm wide gaps. Irradiation cleaved the linker from the exposed regions (Figure 3, I). The remaining linker molecules in the nonexposed areas were reacted with the fluorophore (Figure B, II, Supporting Information) or with *N*-(+)-biotin *N*-hydroxysuccinimide ester and then incubated with fluorescently labelled streptavidin (Figure 3, II). Figure 3A shows the fluorescent protein pattern observed through the microscope. The nonirradiated regions appeared bright, indicating preferential and site-controlled attachment of the protein. In a second irradiation step, the substrate was exposed through the same mask rotated 90°. After washing, fluorescence decreased in the irradiated regions (III and cross pattern in Figure 3B and Figure A, Supporting Information) as a consequence of the cleavage of the intercalated cage and removal of the attached specie (protein or fluorophore) from the surface. Low levels of residual fluorescence were observed in the irradiated regions due to uncleaved chromophore (up to 30%) remaining attached to the surface after full exposure, as anticipated from the photolysis studies (see conversion plot Figure 2). Negative controls were performed in order to prove that the loss of fluorescence was not due to bleaching of the fluorophore. No cross pattern was visible in the photobleached control. Taken together, these

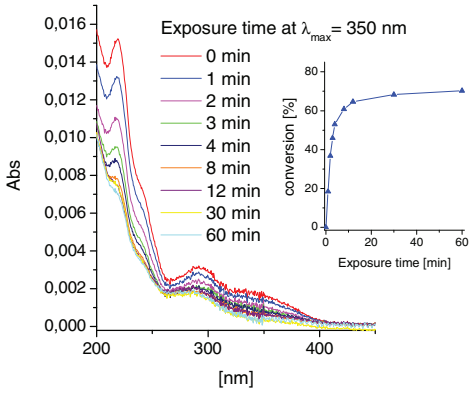

Figure 2. UV spectra of quartz substrates modified with the photosensitive linker after irradiation at 350 nm (0.6 mW cm^{-2}) for increasing exposure times and washing for removal of the photolysis products. Inset represents the photolytic conversion calculated from the decay in the absorbance.

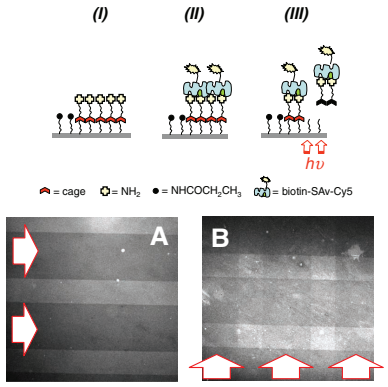

Figure 3. Phototriggered protein release and the possibility of site control. The scheme represents the coupling and irradiation steps. The fluorescent micropatterns correspond to A) step II (site-selective immobilization) and B) step III (site-selective release). The arrows indicate the exposed stripes (200 µm).

results demonstrate the potential of this approach to selectively attach and release molecules from surfaces with spatiotemporal control, in contrast to other work that requires additional blocking steps to prevent non-specific protein adsorption onto the surface.[10] The inclusion of the TEG segment in the linker provides an effective protein-repellent surface background.

We next examined the ability of photolabile linker to mediate precise cell attachment to and subsequent light-triggered detachment from surfaces via the presence or absence (via photocleavage) of RGD. For this purpose, mixed SAMs of amine- and methoxy-terminated thiols with oligo(ethylene glycol) spacers were used to modify gold-coated surfaces and obtain a cell-repellent surface. A non-adhesive background is crucial in order to guarantee only RGD-mediated cell attachment and minimize non-specific interactions of the cell with the surface. Cell experiments were performed on SAMs using a 2% surface concentration of the amine-terminated thiol to which the photolabile linker and cyclo(RGDfK) were attached. As a positive control, cyclo(RGDfK) was attached directly to the amine-terminated SAMs without the photolabile linker. Substrates were seeded with human umbilical vascular endothelial cells (HUVECs) for 2 h. No cell adhesion was observed on surfaces that did not present RGD peptide (**Figure 4**E). For surfaces modified with photocleavable linker and RGD, cells attached and spread, extending cellular processes (Figure 4A). Similar levels of spreading were observed on surfaces modified with photocleavable linker presenting RGD and surfaces modified directly with RGD (Figure 4C). This result demonstrates that the RGD peptide coupled to the photocleavable linker displays full bioadhesive activity. Importantly, control surfaces presenting cyclo(RADfK) as inactive peptide displayed minimal cell adhesion, confirming that adhesion to the surfaces is mediated by integrin cellular receptors (Figure 4F). Next, substrates were irradiated under conditions for photocleavage of the linker. On surfaces modified with photocleavable linker presenting RGD peptide, the cells rounded up and detached from the surface (Figure 4C). Over 85% of the original, adherent cells were removed from the surface by simple washing with saline, and the remaining cells displayed a round morphology, indicative of poor adhesion to the surface. We attribute the small fraction of remaining cells to incomplete cleavage of the photolabile linker as shown in the photolysis analysis. Importantly, cells remained attached and spread on the positive control substrates where the RGD was directly immobilized (without photolinker, Figure 4D), confirming that the cell release is associated with the cleavage of the linker and that the irradiation dose used in the experiments did not affect cell adhesion and spreading. In fact, cell staining with the Live/Dead kit showed no differences in viability between irradiated and not irradiated cell cultures under these exposure conditions (data not shown). These results demonstrate a flexible and facile strategy for the specific attachment of cells with the ability of subsequent controlled

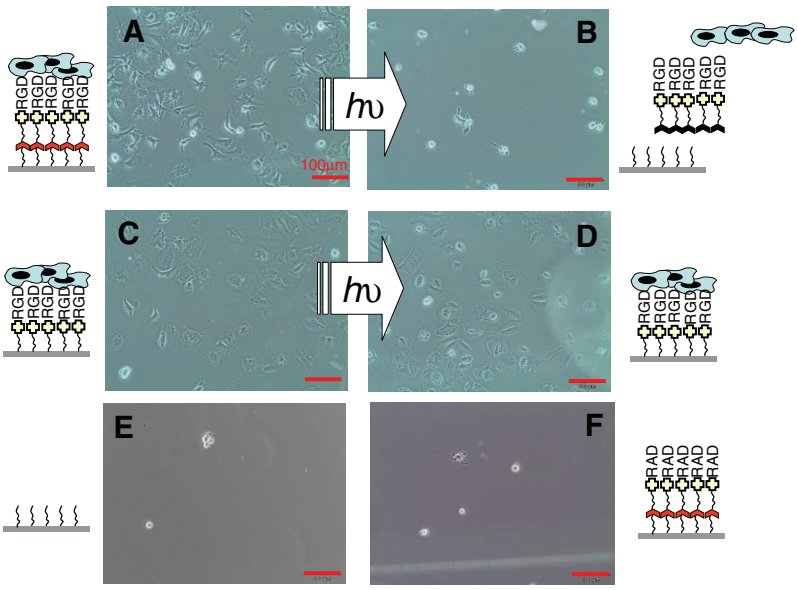

Figure 4. Microscopy images of HUVECs after 2 h incubation on RGD-modified substrates anchored to A) an amine-terminated SAM with the photosensitive linker and C) without the photosensitive linker (control experiment). In (B,D) the same substrates after irradiation are shown. E) HUVECs after a 2 h incubation on an amine-terminated SAM. F) HUVECs incubated for 2 h on cyclo(RADfK) non-adhesive peptide coupled to the amine-terminated SAM with the photosensitive linker. Scale bars represent 100 μm.

light-triggered release from surfaces. This strategy represents a more specific and controlled alternative to trypsination or to temperature-driven changes in substrate hydrophobicity,[5] or to the recently demonstrated cell release by addition of soluble RGD.[11] Reported cell release strategies relying on dissolution of the underlying electroactive coatings[6–8] or photodegradable gels[12] are material- and substrate-specific and less flexible than these photocleavable linkers. This approach is applicable to any material, provided that the linker is properly designed, and provides direct control over the molecular interactions involved in cell adhesion.

In summary, we have demonstrated that phototriggered cleavage of the RGD peptide can lead to subsequent cell release from surfaces. To our knowledge this is the first demonstration of a dynamic variation of RGD concentration at surfaces and its consequences in cell detachment by means of photosensitive molecules.

Experimental Section

The detailed synthesis and characterization of the linker, conditions for surface modification irradiation, and coupling protocols are provided as Supporting Information.

Supporting Information

Supporting Information is available from the Wiley Online Library or from the author.

Acknowledgements

A.d.C., M.W., T.T.L., and A.J.G. thank the Materials World Network (DFG AOBJ 569628, NSF DMR-0909002) for financial support. AdC and MS thank the DFG (444ARG113/8) and the MPG-FhG Project "Biomimetic matrices" for financial support.

Received: March 11, 2011
Revised: April 29, 2011
Published online: May 25, 2011

[1] a) Y. Ohmuro-Matsuyama, Y. Tatsu, *Angew. Chem.* **2008**, *47*, 7527; b) S. Petersen, J. M. Alonso, A. Specht, P. Duodu, M. Goeldner, A. Del Campo, *Angew. Chem.* **2008**, *47*, 3192.
[2] T. Muraoka, C. Y. Koh, H. G. Cui, S. I. Stupp, *Angew. Chem.* **2009**, *48*, 5946.
[3] a) J. Auernheimer, C. Dahmen, U. Hersel, A. Bausch, H. Kessler, *J. Am. Chem. Soc.* **2005**, *127*, 16107; b) M. Schutt, S. S. Krupka, A. G. Milbradt, S. Deindl, E. K. Sinner, D. Oesterhelt, C. Renner, L. Moroder, *Chem. Biol.* **2003**, *10*, 487; c) A. G. Milbradt, M. Loweneck, S. S. Krupka, M. Reif, E. K. Sinner, L. Moroder, C. Renner, *Biopolymers* **2005**, *77*, 304.
[4] C. G. Bochet, *J. Chem. Soc. Perkins Trans. 1* **2002**, 125.
[5] T. Okano, N. Yamada, M. Okuhara, H. Sakai, Y. Sakurai, *Biomaterials* **1995**, *16*, 297.
[6] O. Guillaume-Gentil, Y. Akiyama, M. Schuler, C. Tang, M. Textor, M. Yamato, T. Okano, J. Voros, *Adv. Mater.* **2008**, *20*, 560.
[7] E. W. L. Chan, S. Park, M. N. Yousaf, *Angew. Chem.* **2008**, *47*, 6267.
[8] O. Guillame-Gentil, O. Semenov, A. S. Roca, T. Groth, R. Zahn, J. Voros, M. Zenobi-Wong, *Adv. Mater* **2010**, *22*, 5443.
[9] a) J. M. Alonso, A. Reichel, J. Piehler, A. del Campo, *Langmuir* **2008**, *24*, 448; b) A. del Campo, D. Boos, H. W. Spiess, U. Jonas, *Angew. Chem.* **2005**, *44*, 4707; c) P. Stegmaier, J. M. Alonso, A. del Campo, *Langmuir* **2008**, *24*, 11872; d) P. Stegmaier, A. del Campo, *ChemPhysChem* **2009**, *10*, 357.
[10] a) K. Nakayama, T. Tachikawa, T. Majima, *Langmuir* **2008**, *24*, 6425; b) K. Nakayama, T. Tachikawa, T. Majima, *Langmuir* **2008**, *24*, 1625.
[11] S. H. Shabbir, J. L. Eisenberg, M. Mrksich, *Angew. Chem.* **2010**, *49*, 7706.
[12] G. Pasparakis, T. Manouras, A. Selimis, M. Vamvakaki, P. Argitis, *Angew. Chem.* **2011**, *50*, 4142.

Adhesion strength–based, label-free isolation of human pluripotent stem cells

Ankur Singh[1,2,8], Shalu Suri[1–3,8], Ted Lee[1], Jamie M Chilton[4], Marissa T Cooke[5], Weiqiang Chen[6], Jianping Fu[6,7], Steven L Stice[4], Hang Lu[2,3], Todd C McDevitt[2,5] & Andrés J García[1,2]

We demonstrate substantial differences in 'adhesive signature' between human pluripotent stem cells (hPSCs), partially reprogrammed cells, somatic cells and hPSC-derived differentiated progeny. We exploited these differential adhesion strengths to rapidly (over ~10 min) and efficiently isolate fully reprogrammed induced hPSCs (hiPSCs) as intact colonies from heterogeneous reprogramming cultures and from differentiated progeny using microfluidics. hiPSCs were isolated label free, enriched to 95%–99% purity with >80% survival, and had normal transcriptional profiles, differentiation potential and karyotypes. We also applied this strategy to isolate hPSCs (hiPSCs and human embryonic stem cells) during routine culture and show that it may be extended to isolate hPSC-derived lineage-specific stem cells or differentiated cells.

Generation of hiPSCs from somatic cells is a promising strategy to produce autologous cells for regenerative therapies and novel models of human development and disease[1–3]. However, the reprogramming process is inefficient (0.001%–2% reprogrammed cells)[4], and hiPSC cultures are often heterogeneous because of the presence of undifferentiated stem cells, parental and partially reprogrammed cells and differentiated derivatives[5], thereby introducing variability, potential immunogenicity[6] and problems in directed differentiation[7–11].

hiPSC survival and 'stemness' require compact colonies with E-cadherin–mediated cell-cell adhesion[12]. Current methods for maintenance of hiPSC cultures rely on manual isolation, either alone or in combination with enzymatic dissociation[13–17]. Such methods are time intensive, require skilled labor and are dependent on morphologic recognition of undifferentiated cells. Although many reagents have been developed for enzymatic passaging, such methods are not selective for hPSCs, and unwanted cells are often transferred during passaging[14,18]. Furthermore, enzymatic methods have been reported to be associated with karyotypic abnormalities when compared to manual passaging[13–15,19] and require reaggregation of dissociated hPSCs for improved survival[20]. Although FACS[21] can enrich undifferentiated populations, this method requires single-cell dissociation of hPSCs, which induces cell death[12], and replated cells fail to form compact colonies (**Supplementary Fig. 1**).

There remains a need to develop unbiased, high-throughput technologies that can efficiently separate colonies of hiPSCs from nonreprogrammed and partially reprogrammed cells, feeder cells or differentiated cells. In this study, we demonstrate a unique 'adhesive signature' for hPSCs that is a multifactorial function of extracellular matrix (ECM)-bound integrins, assembly of focal adhesions and the resulting cell-ECM adhesion strength. We present a platform technology that exploits differences in the adhesion strength among nonreprogrammed and partially reprogrammed cells, hiPSCs and differentiated cells to selectively isolate hiPSCs using microfluidics.

RESULTS

Changes in adhesive signature with reprogramming

During reprogramming to pluripotency, cells undergo changes in morphology resulting in an epithelial phenotype indicative of the pluripotent state (**Fig. 1a**). IMR90 and dermal fibroblasts, common somatic cell sources[1,2] for reprogramming, exhibited an elongated ('spread') morphology and lack of pluripotency markers (**Supplementary Fig. 2a–c**) as compared to hiPSCs, which existed as tightly packed colonies (**Supplementary Fig. 2d,e**). Typically we observed that <1% of fibroblasts were converted to fully reprogrammed hiPSCs[22] positive for OCT4, SSEA4, TRA-1-60, NANOG and TRA-1-81 (**Supplementary Fig. 2e–g**). Residual nonreprogrammed and partially reprogrammed cells exhibited a less elongated morphology than that of parental fibroblasts and expressed some, but not all, pluripotency markers (**Supplementary Fig. 2e**).

The adhesive strength of a cell to its ECM is dependent on ECM-ligated integrins and their association to cytoskeletal elements[23]. Using flow cytometry and adhesion-inhibition studies (**Supplementary Fig. 3**), we determined that whereas parental fibroblasts expressed predominantly $\alpha_5\beta_1$-integrin, hiPSCs expressed high levels of $\alpha_6\beta_1$-integrin, regardless of whether the cells were cultured on fibronectin, laminin or Matrigel.

[1]Woodruff School of Mechanical Engineering, Georgia Institute of Technology, Atlanta, Georgia, USA. [2]Petit Institute for Bioengineering and Bioscience, Georgia Institute of Technology, Atlanta, Georgia, USA. [3]School of Chemical and Biomolecular Engineering, Georgia Institute of Technology, Atlanta, Georgia, USA. [4]ArunA Biomedical, Inc., Athens, Georgia, USA. [5]Wallace H. Coulter Department of Biomedical Engineering, Georgia Institute of Technology, Atlanta, Georgia, USA. [6]Department of Mechanical Engineering, University of Michigan, Ann Arbor, Michigan, USA. [7]Department of Biomedical Engineering, University of Michigan, Ann Arbor, Michigan, USA. [8]These authors contributed equally to this work. Correspondence should be addressed to A.J.G. (andres.garcia@me.gatech.edu).

RECEIVED 24 SEPTEMBER 2012; ACCEPTED 7 MARCH 2013; PUBLISHED ONLINE 7 APRIL 2013; DOI:10.1038/NMETH.2437

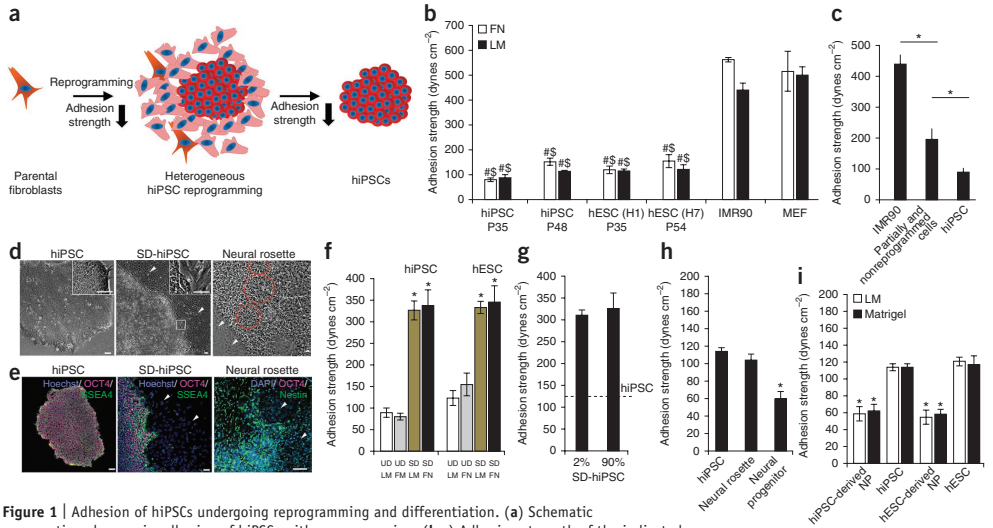

Figure 1 | Adhesion of hiPSCs undergoing reprogramming and differentiation. (**a**) Schematic representing changes in adhesion of hiPSCs with reprogramming. (**b**,**c**) Adhesion strength of the indicated cell types on fibronectin (FN) and laminin (LM) (**b**) and of cells during reprogramming (**c**). MEFs, mouse embryonic fibroblasts; P, passage number; H1 and H7 indicate embryonic stem cell lines. (**d**,**e**) Morphology (**d**) and expression of pluripotency markers (**e**) in hiPSCs in spontaneously differentiating cultures of hiPSCs (SD-hiPSC; white arrowheads indicate differentiated cells), and expression of nestin in neural rosettes (red circles). Scale bars, 50 µm. (**f**) Adhesion strength for undifferentiated (UD) and spontaneously differentiating (SD) cultures of hiPSCs and hESCs on FN or LM. (**g**–**i**) Adhesion strength for cells in hiPSC cultures with different levels of spontaneous differentiation (2% and 90% TRA-1-60$^+$) cultured on LM (**g**), cells in hiPSC cultures differentiated into neural rosettes and neural progenitors (NPs) on LM (**h**) and hPSC-derived NPs on LM and Matrigel (**i**). All bar graphs represent mean ± s.d. $^*P < 0.05$; $^{\#}P < 0.05$ stem cells vs. IMR90; $^{\$}P < 0.05$ stem cells vs. MEFs; $n = 3$.

These results are consistent with those of human embryonic stem cell (hESC) studies[24]. Fibroblasts possessed actin stress fibers, and vinculin and talin were enriched at focal adhesions (**Supplementary Figs. 4** and **5**). In contrast, hiPSCs exhibited substantially fewer actin fibers, with diffuse vinculin and talin throughout the cytoplasm or localized to cell-cell junctions. Nonpluripotent cells in reprogramming cultures showed mixed regions of spread cells with well-defined focal adhesions and round cells without distinct focal adhesions (**Supplementary Fig. 4**). We therefore hypothesized that alterations in the adhesive signature related to integrin binding and cytoskeletal components accompany reprogramming to induced pluripotency and differentiation of hiPSCs.

We evaluated the steady-state cell-ECM adhesion strength for hiPSCs and IMR90 cells using a spinning-disk device[23] (**Supplementary Fig. 6a**). We observed that adhesion strength to fibronectin for hiPSCs was one-seventh that for parental fibroblasts (**Fig. 1b**). Analyses among fibroblastic parental and feeder cells, hESCs and hiPSCs revealed significantly lower adhesion strength to fibronectin, laminin and Matrigel for hPSCs than for fibroblasts ($P < 0.02$; **Fig. 1b** and **Supplementary Fig. 6b**), indicating that the adhesive properties of cells shift during reprogramming. These results were independent of passage number, underlying matrix, parental fibroblast source and colony size (**Supplementary Figs. 6c** and **7**). The differences in adhesive strength correlated to more focal adhesions in parental cells than in hiPSCs. Nonreprogrammed and partially reprogrammed cells that expressed some but not all pluripotency markers (for example, OCT4$^+$SSEA4$^-$) exhibited higher adhesion strength than hiPSCs but lower adhesion strength than parental cells (**Fig. 1c**).

Distinct adhesive properties of differentiated cells

We next determined the adhesive signature of hiPSCs undergoing spontaneous or directed differentiation (**Fig. 1d**,**e**). We detected significant increases in the adhesion strength to the ECM of spontaneously differentiated cultures of hiPSCs (~10% TRA-1-60$^+$) as compared to undifferentiated hiPSCs (**Fig. 1f**, $P < 0.006$); we obtained similar results in hESCs. Cells in spontaneously differentiating cultures of hiPSCs displayed actin stress fibers and localized talin and vinculin to focal adhesions (**Supplementary Figs. 5** and **8**), which we did not observe in undifferentiated colonies. Differences in adhesion strength between undifferentiated and differentiated cells were independent of the levels of spontaneous differentiation (**Fig. 1g**).

During directed differentiation, we observed early-stage multipotent neural stem cells (neural rosettes[10]) with a radial pattern of epithelial morphology (**Fig. 1d**), which stained for nestin (**Fig. 1e**) and Musashi (**Supplementary Fig. 9a**), distinct from hiPSCs. The adhesion strength of these cells was comparable to that of hiPSCs (**Fig. 1h**) but significantly lower than that of fibroblast-like cells ($P < 0.05$). We manually isolated rosettes and differentiated them to neural progenitors and neurons (**Supplementary Fig. 9b**). Neural progenitors exhibited adhesion strength comparable to that of neurons but 50% lower than that of hiPSCs (**Fig. 1h**,**i**)

and about 85% lower than that of spontaneously differentiated fibroblastic cells (**Fig. 1g**), independent of hPSC type and matrix (**Fig. 1i**). These analyses demonstrate that hPSCs, progenitors and differentiated cells exhibit distinct adhesive signatures.

Hydrodynamic isolation of hPSCs

We exploited the unique adhesive signature of hiPSCs to isolate undifferentiated hPSCs from a heterogeneous cell population. We used adhesive force–based separation via a simple microfluidic system, a label-free technique that requires minimal cell processing. We termed this technology µSHEAR (micro–stem cell high-efficiency adhesion-based recovery). We fabricated µSHEAR devices for a range of culture surface areas (**Fig. 2a** and **Supplementary Fig. 10a**). Cells remained viable in the device and retained their distinct morphologies, and hiPSCs remained undifferentiated (**Supplementary Fig. 10b**,**c**).

The application of laminar flow generated fluid shear stresses on adherent cells in the device. hiPSC colonies detached at a shear stress of 85–125 dynes cm^{-2} within 4 min of fluid-flow application and were completely detached in 10–14 min (**Fig. 2b**,**c**) irrespective of the underlying ECM (**Supplementary Fig. 10d**,**e**), whereas fibroblasts remained attached. To quantify the efficiency of hiPSC purification, we incubated recovered cells with StainAlive DyLight 488–conjugated TRA-1-60 antibody (Stemgent) to stain for live hiPSCs and with CellTracker Red dye (CMPTX; Life Technologies). Flow cytometry analysis of

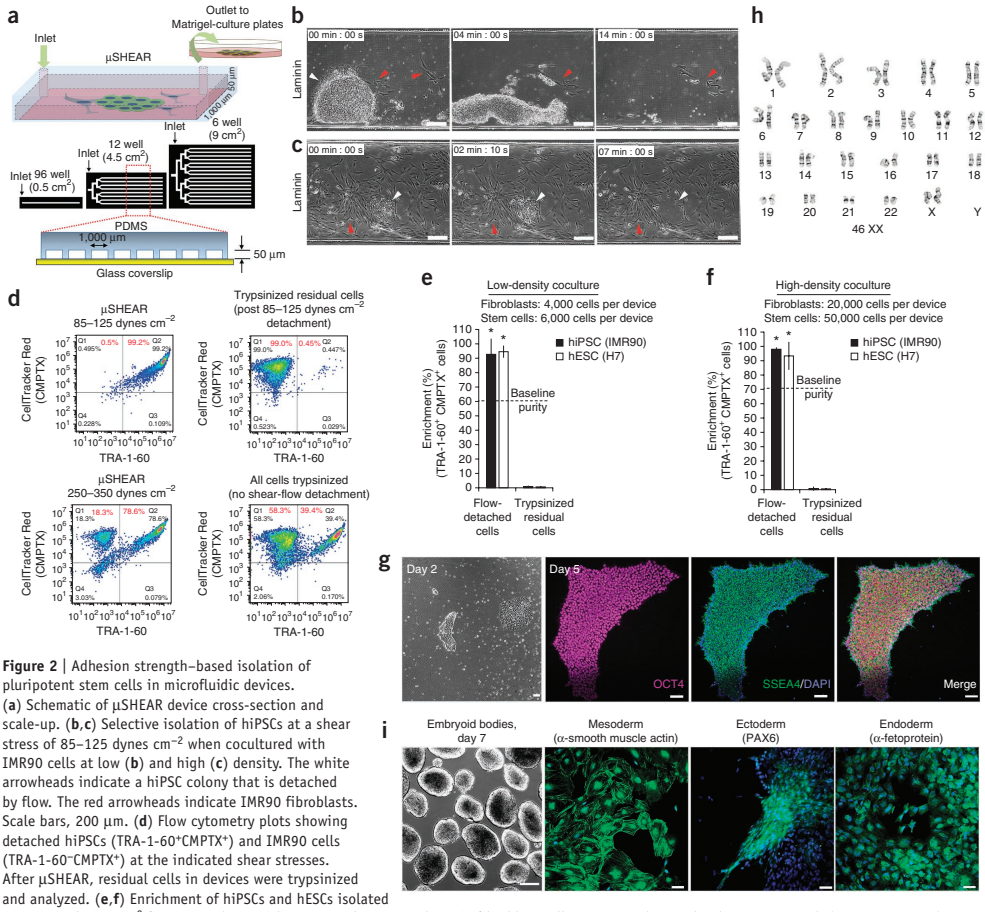

Figure 2 | Adhesion strength–based isolation of pluripotent stem cells in microfluidic devices. (**a**) Schematic of µSHEAR device cross-section and scale-up. (**b**,**c**) Selective isolation of hiPSCs at a shear stress of 85–125 dynes cm^{-2} when cocultured with IMR90 cells at low (**b**) and high (**c**) density. The white arrowheads indicate a hiPSC colony that is detached by flow. The red arrowheads indicate IMR90 fibroblasts. Scale bars, 200 µm. (**d**) Flow cytometry plots showing detached hiPSCs (TRA-1-60$^+$CMPTX$^+$) and IMR90 cells (TRA-1-60$^-$CMPTX$^+$) at the indicated shear stresses. After µSHEAR, residual cells in devices were trypsinized and analyzed. (**e**,**f**) Enrichment of hiPSCs and hESCs isolated at 85–125 dynes cm^{-2} from a coculture with IMR90 and mouse embryonic fibroblast cells, respectively. Graphs show mean ± s.d. ($^*P < 0.05$, $n = 3$). (**g**) Detached hiPSC colonies readhered to Matrigel and immunostained for the indicated markers. Scale bars, 50 µm. (**h**) Karyotype analysis of hiPSCs isolated twice using µSHEAR, with passages 7–8 d apart. (**i**) Embryoid bodies generated from µSHEAR-isolated hiPSCs immunostained with markers for the three germ layers (21 d). Scale bars, 50 µm, except the phase-contrast embryoid bodies (left; scale bar, 200 µm).

the recovered cells revealed significant ($P < 0.05$) enrichment of hiPSCs when detached at 85–125 dynes cm^{-2} with up to 99% purity (**Fig. 2d**) as compared to the initial purity of 39% hiPSCs. Exposure to higher fluid forces (250–350 dynes cm^{-2}) resulted in contamination with IMR90 cells (18%), whereas we observed <1% fibroblast contamination in cultures exposed to 85–125 dynes cm^{-2}. When we increased the fluid force to 750–850 dynes cm^{-2}, we observed high proportions of IMR90 cells in the detached populations, similar to those in trypsinized samples under no-flow conditions (**Fig. 2d**). The μSHEAR isolation efficiency was independent of hiPSC purity in the initial coculture (**Fig. 2e**,**f** and **Supplementary Fig. 11a**). Less than 3% of residual cells in devices after fluid detachment were hiPSCs, indicating high recovery yield of hiPSCs by μSHEAR (**Fig. 2e**,**f**). Similar results were observed with hESCs cultured on mouse embryonic fibroblast (MEF) feeders (**Fig. 2e**,**f** and **Supplementary Fig. 10f**). We observed similar enrichment with varying levels of hiPSCs in a fibroblast-hiPSC coculture (baseline hiPSC purity, 1%–70%). Finally, we

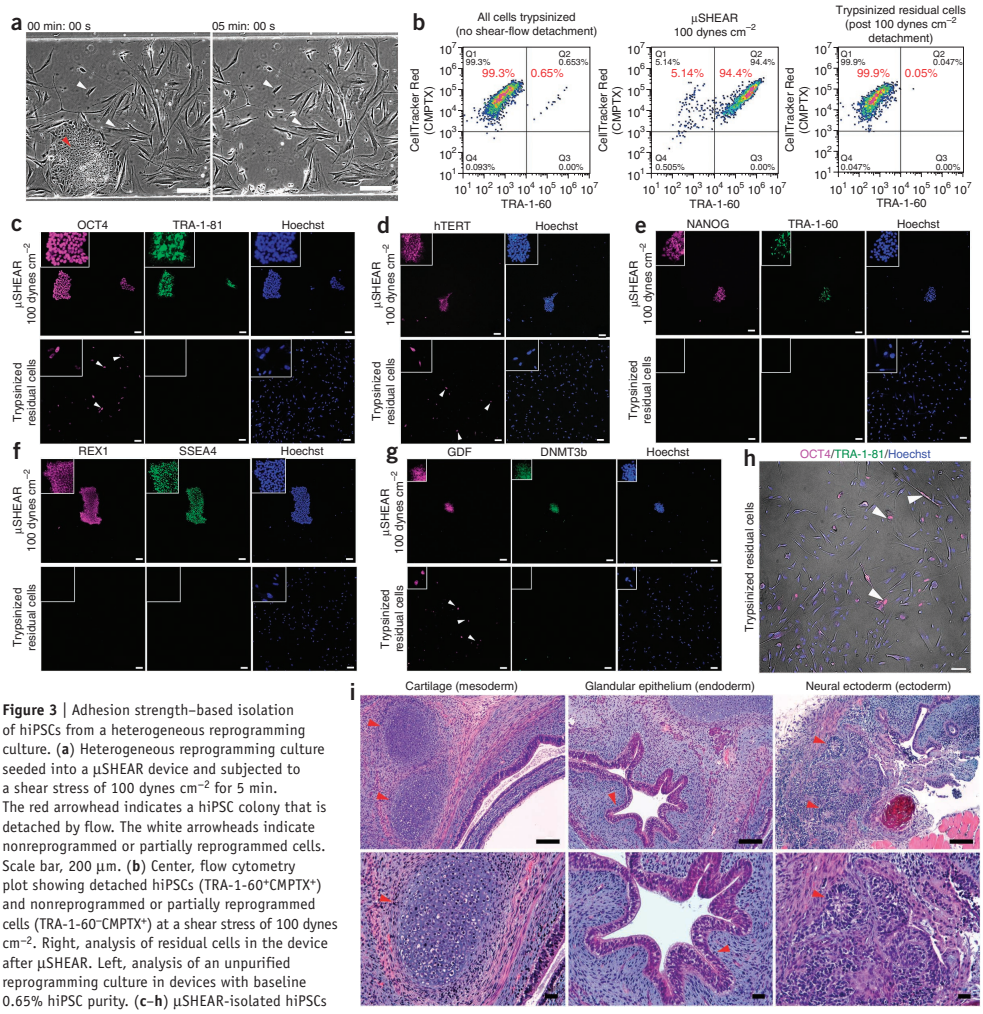

Figure 3 | Adhesion strength–based isolation of hiPSCs from a heterogeneous reprogramming culture. (**a**) Heterogeneous reprogramming culture seeded into a μSHEAR device and subjected to a shear stress of 100 dynes cm^{-2} for 5 min. The red arrowhead indicates a hiPSC colony that is detached by flow. The white arrowheads indicate nonreprogrammed or partially reprogrammed cells. Scale bar, 200 μm. (**b**) Center, flow cytometry plot showing detached hiPSCs (TRA-1-60$^+$CMPTX$^+$) and nonreprogrammed or partially reprogrammed cells (TRA-1-60$^-$CMPTX$^+$) at a shear stress of 100 dynes cm^{-2}. Right, analysis of residual cells in the device after μSHEAR. Left, analysis of an unpurified reprogramming culture in devices with baseline 0.65% hiPSC purity. (**c**–**h**) μSHEAR-isolated hiPSCs and residual cells from the devices replated on Matrigel and stained for the indicated markers. The white arrowheads indicate partially reprogrammed cells expressing pluripotency markers. Scale bars, 50 μm. (**i**) Representative hematoxylin-and-eosin–stained sections from a formalin-fixed teratoma produced from μSHEAR-isolated hiPSCs. μSHEAR-isolated cells formed differentiated tissues representing all three embryonic germ layers. Scale bars: 100 μm (top row), 25 μm (bottom row).

could also selectively enrich hiPSCs after the cells were allowed to proliferate with parental cells for 5–7 d in microfluidic devices (**Supplementary Fig. 11b,c** and **Supplementary Video 1**).

We used μSHEAR to efficiently separate hiPSCs from other parental cell types: specifically, from peripheral blood mononuclear cells (PBMCs) in blood[25]. Because PBMCs are loosely adherent (**Supplementary Fig. 12a,b**), we first exposed the reprogrammed culture to a shear stress of 10 dynes cm^{-2} to remove PBMCs, which were removed from the devices within 1 min of exposure to flow (**Supplementary Fig. 12c**). Thereafter, we collected hiPSCs as

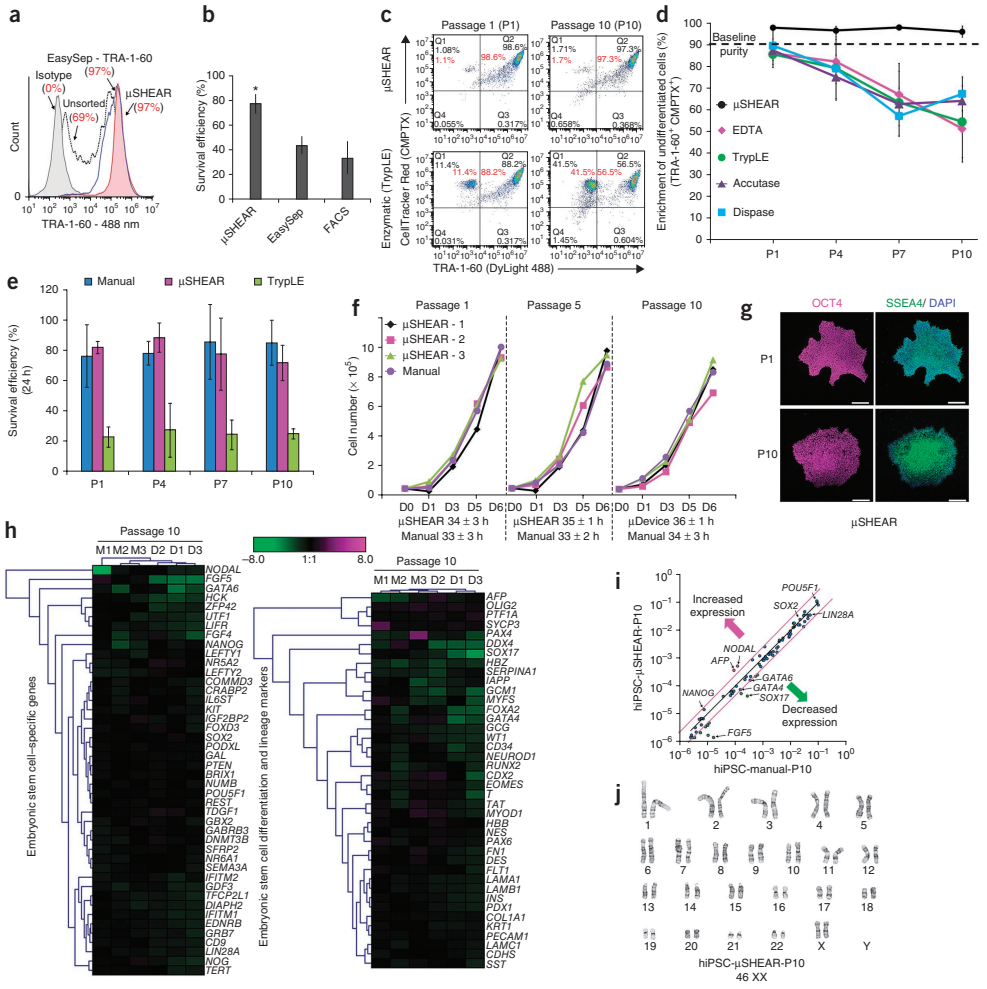

Figure 4 | Adhesion strength–based enrichment of hiPSCs from differentiating cultures. (**a**,**b**) Flow cytometry histograms (Alexa Fluor 488–TRA-1-60) showing purification (**a**) and survival efficiencies (**b**) of hiPSCs processed as indicated. (**c**) hiPSCs (TRA-1-60$^+$CMPTX$^+$) and spontaneously differentiated cells (TRA-1-60$^-$CMPTX$^+$) detached as indicated at passages 1 and 10. (**d**) Enrichment efficiency of hiPSCs upon repeated passaging with the indicated methods. P0 cells for all plots were from the same batch with 90% TRA-1-60$^+$ cells; recovered cultures were propagated for 5–6 d. (**e**,**f**) Cell survival (**e**) and growth curves (**f**) of cells on Matrigel after passaging as indicated. D, day. (**g**) Immunostaining for pluripotency markers of μSHEAR-isolated hiPSCs cultured on Matrigel across ten passages. Scale bars, 200 μm. (**h**) Fold change in expression of stem cell–related (left) and differentiation (right) genes in hiPSCs at P10 relative to at P0. D1–D3 represent triplicate runs of μSHEAR devices, and M1–M3 represent manual passaging triplicates. (**i**) Relative expression of stem cell–related genes in hiPSCs isolated manually or using μSHEAR for ten passages. Magenta lines indicate a twofold change in gene expression. (**j**) Karyotype analysis of μSHEAR-passaged hiPSCs at P10. Error bars, s.d. (*P < 0.05, n = 3).

colonies with ~99% purity by increasing the flow (**Supplementary Fig. 12d** and **Supplementary Video 2**).

hiPSCs recovered by μSHEAR initially adhered as small colonies (**Fig. 2g**) with the ability to self-renew without any signs of differentiation (**Supplementary Fig. 13**). The isolated colonies retained their pluripotent phenotype (**Fig. 2g** and **Supplementary Fig. 13**) and exhibited no chromosomal abnormalities after two rounds of purification with passages 7–8 d apart (**Fig. 2h**). μSHEAR-isolated hiPSC colonies readily generated embryoid bodies and differentiated into mesoderm, ectoderm and endoderm derivatives (**Fig. 2i**).

Isolation of hiPSCs from reprogramming cultures

We anticipated that adhesive signature differences could be exploited to selectively isolate hiPSCs from partially reprogrammed cultures. Using μSHEAR, we isolated hiPSC colonies (94% ± 3.6% purity) at 100 dynes cm^{-2} without detachment of nonreprogrammed and partially reprogrammed cells (**Fig. 3a**,**b** and **Supplementary Fig. 14a**,**b**). We observed only 0.05% residual hiPSCs, whereas non-hiPSCs constituted 99.9% of the culture remaining in the μSHEAR device (**Fig. 3b** and **Supplementary Fig. 14c**). Isolated hiPSCs expressed TRA-1-60, TRA-1-81, DNMT3B, REX1, OCT4, SSEA4, GDF3, hTERT and NANOG, indicating that they were fully reprogrammed[22]. Residual cells in the device expressed OCT4, hTERT and GDF3 but not the other markers (**Fig. 3c**–**h**). We also analyzed the methylation patterns[26,27] of endogenous *OCT4* (*POU5F1*), *NANOG* and *SOX2* genes. μSHEAR-isolated hiPSCs displayed unmethylated *OCT4*, *SOX2* and *NANOG*, similarly to hiPSCs under standard culture conditions and to unmethylated genomic DNA controls (**Supplementary Fig. 14d**). Finally, μSHEAR-isolated hiPSCs formed teratomas when implanted into immunodeficient mice (**Fig. 3i** and **Supplementary Fig. 15**). These studies demonstrate that fully reprogrammed, bona fide hiPSCs can be selectively isolated from residual parental fibroblasts and from partially reprogrammed cells using μSHEAR.

Isolation of hiPSCs from differentiated cells

We exploited the adhesive signature of undifferentiated hiPSCs to effectively separate them from differentiated progeny (**Fig. 1f**). Spontaneously differentiating hiPSC cultures with varying levels of differentiation were dissociated and cultured overnight in μSHEAR devices with hiPSCs (**Supplementary Fig. 16a**). We could isolate hiPSCs as intact epithelial colonies before detaching differentiated fibroblast-like cells with >97% purity and yield irrespective of the levels of spontaneous differentiation (6%–70% TRA-1-60$^-$), and we observed similar results with hESCs (**Supplementary Fig. 16b**–**d**). We did not achieve selective purification with commonly used enzymatic agents (**Supplementary Fig. 16b**).

hPSC isolation with TRA-1-60 antibody–based purification (EasySep (Stemcell Technologies) and FACS) requires dissociation of colonies into single cells and labeling with molecular probes. Although both EasySep and μSHEAR demonstrated 97% purification efficiency, μSHEAR achieved improved purification with less variability in TRA-1-60 expression as compared to EasySep (**Fig. 4a**). When plated, EasySep- or FACS-purified cells did not form compact epithelial colonies (**Supplementary Fig. 1**) and exhibited poor survival (<40%; **Fig. 4b**) as compared to μSHEAR (>80% survival).

We next assessed μSHEAR for culture maintenance over the course of ten passages (5–7 d apart) starting with an ~10% spontaneously differentiated population. μSHEAR-based isolation resulted in repeated high-purity populations of hPSCs (>97%), whereas passage with routinely used methods failed to selectively enrich undifferentiated cells and resulted in continuously increasing levels of spontaneous differentiation (**Fig. 4c**,**d**). Defined culture substrates, such as E-cadherin (StemAdhere (Stemcell Technologies)), which have also been used for hiPSC passaging[28], were not selective for undifferentiated hiPSCs (**Supplementary Fig. 17**). The survival efficiency of cells passaged was higher using μSHEAR than with TrypLE-based passaging (<30%; Life Technologies) and was comparable to that of cells passaged manually (**Fig. 4e**). The doubling time of μSHEAR-purified hiPSCs (~34 h) over ten passages was equivalent to that of hiPSCs passaged manually (**Fig. 4f**). hiPSC purification was selective at 85–125 dynes cm^{-2}, whereas at high shear stress, differentiated cells also detached (**Supplementary Fig. 18a**,**b**).

Recovered colonies retained pluripotency over ten passages (P1–P10) (**Fig. 4g** and **Supplementary Fig. 18c**), and the expression profiles of stem cell–related genes were similar at P10 and P0 for both μSHEAR-isolated and manually picked hiPSCs (**Fig. 4h**). Expression of differentiation and lineage-specific genes was equivalent or downregulated for both μSHEAR- and manually passaged hiPSCs as compared to starting P0 cells (**Fig. 4h**). Hierarchical clustering and scatter-plot analyses of gene expression at P10 indicated that μSHEAR-passaged hiPSCs exhibited a high degree of similarity to manually passaged cells (**Fig. 4h**,**i**). μSHEAR-passaged hiPSCs exhibited no chromosomal abnormalities at P10 (**Fig. 4j**) and showed the same methylation status of *OCT4*, *SOX2* and *NANOG* as manually passaged hiPSCs (**Supplementary Fig. 18d**).

We applied μSHEAR to isolate terminally differentiated cells. Because their adhesion strength is lower than that of hiPSCs, neurons were detached at 60 dynes cm^{-2}, whereas hiPSCs remained adherent to the substrate at this shear stress level. Isolated neurons exhibited excellent viability, neurite growth (**Supplementary Fig. 19**) and expression of MAP2 and β-III tubulin. Similarly, we successfully isolated hiPSC-derived cardiomyocytes (**Supplementary Video 3**) from hiPSCs with >95% purity (**Supplementary Fig. 20a**,**b**). Recovered hiPSC adhered as colonies, whereas the residual cardiomyocytes expressed α-smooth muscle actin and exhibited spontaneous contractile activity (**Supplementary Fig. 20c**,**d** and **Supplementary Video 4**).

DISCUSSION

High-throughput microfluidic devices are being adapted in routine cell culture[29–31] and offer advantages over conventional hydrodynamic sorting, including laminar flow with only a millionth of the buffer volume and the ability to recover detached cells[32]. We demonstrate that differences in adhesion strength can be exploited to purify undifferentiated hPSCs from other cell types in a facile, efficient and label-free manner, yielding higher hPSC survival than conventional methods provide. Our μSHEAR methodology allows the application of a wide range of shear forces with small working volumes and precise magnitudes of shear force. We also tested the high-throughput potential of μSHEAR across culture areas of 0.5–9 cm^2 and found 95%–99% enrichment efficiency of hiPSCs, demonstrating that the technology is potentially scalable.

Cells are loaded in <30 s, and no time is spent precleaning the cultures. Self-contained disposable microfluidic devices ensure sterility, and cell recovery takes ~5 min, similar to the time required for a routine centrifugation step after enzymatic dissociation. In addition, the microfluidic strategy provides for direct visualization of the detachment process of stem cell colonies; a gradient of shear forces could thus be used to serially isolate individual colonies from the same chamber, which could not be achieved with any bulk passaging methods. μSHEAR will facilitate the integration of cell isolation procedures, such as separating completely reprogrammed hiPSCs from partially reprogrammed cells, with in-line biochemical, genomic, proteomic and metabolomic analyses.

METHODS

Methods and any associated references are available in the online version of the paper.

Note: Supplementary information is available in the online version of the paper.

ACKNOWLEDGMENTS

This work was supported by an American Recovery and Reinvestment Act (ARRA) supplement to the US National Institutes of Health (NIH) grant R01 GM065918 (A.J.G.), NIH R43 NS080407 (J.M.C. and A.J.G.), the Stem Cell Engineering Center at Georgia Institute of Technology (T.C.M.), a Sloan Foundation Fellowship (H.L.), the National Science Foundation (NSF) DBI-0649833 (H.L.) and an ARRA sub-award under RC1CA144825 (H.L.), NSF CMMI-1129611 (J.F.), the Georgia Tech Emory Center for Regenerative Medicine and the Parker H. Petit Institute for Bioengineering and Bioscience at Georgia Institute of Technology. We thank J. Wu (Stanford Univ.) for providing blood cell–derived hiPSCs, C. Xu (Emory Univ.) for providing hiPSC-derived cardiomyocytes, T. Hookway for cardiomyocyte culture, A. Ortiz for teratoma studies, and A. Cheng for her help with focal adhesion assays. We thank J. Phillips, D. Dumbauld, Y. Wang and A. Bratt-Leal for insightful discussions and suggestions.

AUTHOR CONTRIBUTIONS

A.S. and S.S. conducted all adhesion and microfluidic studies, collected data and performed data analysis. S.S., A.S. and H.L. developed microfluidic methods. J.M.C. and S.L.S. established and provided the IMR90-derived hiPSC cells and neural stem cells. T.L., W.C. and J.F. developed and provided micropatterns. M.T.C. and A.S. conducted microarray and epigenetic analysis. A.J.G. and T.C.M. developed the concept, and together with A.S. contributed to the planning and design of the project. A.S., S.S., T.C.M., and A.J.G. wrote the manuscript, and all authors discussed the results and commented on the manuscript.

COMPETING FINANCIAL INTERESTS

The authors declare no competing financial interests.

1. Takahashi, K. *et al.* Induction of pluripotent stem cells from adult human fibroblasts by defined factors. *Cell* **131**, 861–872 (2007).
2. Yu, J. *et al.* Induced pluripotent stem cell lines derived from human somatic cells. *Science* **318**, 1917–1920 (2007).
3. Robinton, D.A. & Daley, G.Q. The promise of induced pluripotent stem cells in research and therapy. *Nature* **481**, 295–305 (2012).
4. Zhao, Y. *et al.* Two supporting factors greatly improve the efficiency of human iPSC generation. *Cell Stem Cell* **3**, 475–479 (2008).
5. Enver, T. *et al.* Cellular differentiation hierarchies in normal and culture-adapted human embryonic stem cells. *Hum. Mol. Genet.* **14**, 3129–3140 (2005).
6. Rodin, S. *et al.* Long-term self-renewal of human pluripotent stem cells on human recombinant laminin-511. *Nat. Biotechnol.* **28**, 611–615 (2010).
7. Boheler, K.R. *et al.* Differentiation of pluripotent embryonic stem cells into cardiomyocytes. *Circ. Res.* **91**, 189–201 (2002).
8. Burridge, P.W. *et al.* A universal system for highly efficient cardiac differentiation of human induced pluripotent stem cells that eliminates interline variability. *PLoS ONE* **6**, e18293 (2011).
9. Cho, M.S. *et al.* Highly efficient and large-scale generation of functional dopamine neurons from human embryonic stem cells. *Proc. Natl. Acad. Sci. USA* **105**, 3392–3397 (2008).
10. Lee, G. *et al.* Isolation and directed differentiation of neural crest stem cells derived from human embryonic stem cells. *Nat. Biotechnol.* **25**, 1468–1475 (2007).
11. Tang, C. *et al.* An antibody against SSEA-5 glycan on human pluripotent stem cells enables removal of teratoma-forming cells. *Nat. Biotechnol.* **29**, 829–834 (2011).
12. Ohgushi, M. *et al.* Molecular pathway and cell state responsible for dissociation-induced apoptosis in human pluripotent stem cells. *Cell Stem Cell* **7**, 225–239 (2010).
13. Nandivada, H. *et al.* Fabrication of synthetic polymer coatings and their use in feeder-free culture of human embryonic stem cells. *Nat. Protoc.* **6**, 1037–1043 (2011).
14. Baker, D.E. *et al.* Adaptation to culture of human embryonic stem cells and oncogenesis *in vivo*. *Nat. Biotechnol.* **25**, 207–215 (2007).
15. Mitalipova, M.M. *et al.* Preserving the genetic integrity of human embryonic stem cells. *Nat. Biotechnol.* **23**, 19–20 (2005).
16. Hartung, O., Huo, H., Daley, G.Q. & Schlaeger, T.M. Clump passaging and expansion of human embryonic and induced pluripotent stem cells on mouse embryonic fibroblast feeder cells. *Curr. Protoc. Stem Cell Biol.* **14**, 1C.10 (2010).
17. McCracken, K.W., Howell, J.C., Wells, J.M. & Spence, J.R. Generating human intestinal tissue from pluripotent stem cells *in vitro*. *Nat. Protoc.* **6**, 1920–1928 (2011).
18. Bajpai, R., Lesperance, J., Kim, M. & Terskikh, A.V. Efficient propagation of single cells Accutase-dissociated human embryonic stem cells. *Mol. Reprod. Dev.* **75**, 818–827 (2008).
19. Maitra, A. *et al.* Genomic alterations in cultured human embryonic stem cells. *Nat. Genet.* **37**, 1099–1103 (2005).
20. Ellerström, C., Strehl, R., Noaksson, K., Hyllner, J. & Semb, H. Facilitated expansion of human embryonic stem cells by single-cell enzymatic dissociation. *Stem Cells* **25**, 1690–1696 (2007).
21. Meng, G., Liu, S. & Rancourt, D.E. Rapid isolation of undifferentiated human pluripotent stem cells from extremely differentiated colonies. *Stem Cells Dev.* **20**, 583–591 (2011).
22. Chan, E.M. *et al.* Live cell imaging distinguishes bona fide human iPS cells from partially reprogrammed cells. *Nat. Biotechnol.* **27**, 1033–1037 (2009).
23. Gallant, N.D., Michael, K.E. & García, A.J. Cell adhesion strengthening: contributions of adhesive area, integrin binding, and focal adhesion assembly. *Mol. Biol. Cell* **16**, 4329–4340 (2005).
24. Meng, Y. *et al.* Characterization of integrin engagement during defined human embryonic stem cell culture. *FASEB J.* **24**, 1056–1065 (2010).
25. Staerk, J. *et al.* Reprogramming of human peripheral blood cells to induced pluripotent stem cells. *Cell Stem Cell* **7**, 20–24 (2010).
26. Wojdacz, T.K., Dobrovic, A. & Algar, E.M. Rapid detection of methylation change at H19 in human imprinting disorders using methylation-sensitive high-resolution melting. *Hum. Mutat.* **29**, 1255–1260 (2008).
27. Wojdacz, T.K., Dobrovic, A. & Hansen, L.L. Methylation-sensitive high-resolution melting. *Nat. Protoc.* **3**, 1903–1908 (2008).
28. Nagaoka, M., Si-Tayeb, K., Akaike, T. & Duncan, S.A. Culture of human pluripotent stem cells using completely defined conditions on a recombinant E-cadherin substratum. *BMC Dev. Biol.* **10**, 60 (2010).
29. Blagovic, K., Kim, L.Y. & Voldman, J. Microfluidic perfusion for regulating diffusible signaling in stem cells. *PLoS ONE* **6**, e22892 (2011).
30. Gómez-Sjöberg, R., Leyrat, A.A., Pirone, D.M., Chen, C.S. & Quake, S.R. Versatile, fully automated, microfluidic cell culture system. *Anal. Chem.* **79**, 8557–8563 (2007).
31. Kim, J.Y. *et al.* A cell culturing system that integrates the cell loading function on a single platform and evaluation of the pulsatile pumping effect on cells. *Biomed. Microdevices* **10**, 11–20 (2008).
32. Lu, H. *et al.* Microfluidic shear devices for quantitative analysis of cell adhesion. *Anal. Chem.* **76**, 5257–5264 (2004).

ONLINE METHODS

hiPSC reprogramming and hPSC culture. hiPSCs (IMR90) were derived and validated by ArunA Biomedical using the viPS Vector Kit (Thermo Scientific/Open Biosystems) consisting of six lentiviral vectors encoding *OCT4*, *NANOG*, *SOX2*, *LIN28*, *KLF4* and *c-MYC* (*MYC*) driven by the *EF1A* promoter. IMR90 human fetal lung fibroblasts (female, ATCC) were transduced (MOI of 10 for each vector) for reprogramming per the manufacturer's protocol. Transduced fibroblasts were seeded onto inactivated MEFs or Matrigel to form colonies, and emerging hiPSC colonies were manually passaged by mechanical dissociation on day 30. hiPSCs demonstrated well-defined borders, high nuclear-to-cytoplasmic ratio, prominent nucleoli, alkaline phosphatase activity, positive expression of cell-surface marker SSEA4, embryoid body formation and teratoma formation. To transition hiPSCs to a feeder-free culture system, we manually passaged colonies by mechanical dissociation onto Matrigel (1:100 dilution; BD Biosciences) in mTeSR1 medium (Stemcell Technologies). hiPSCs used in the study were between passages 26 and 48, routinely cultured as feeder-free undifferentiated hiPSC colonies in mTeSR1 medium on Matrigel and enzymatically passaged with dispase (1 mg mL^{-1}) and scraped. To maintain an undifferentiated state in hiPSCs, we exchanged the mTeSR1 medium daily. For μSHEAR experiments, reprogramming was performed on Matrigel, and the entire culture was introduced into the devices after 27–30 d. To obtain spontaneously differentiated cultures of hiPSCs, we exchanged mTeSR1 medium every second day and did not clean the cultures.

Human dermal fibroblast–derived hiPSCs (11b, healthy male donor) were obtained from Harvard Stem Cell Institute and cultured as above. Human peripheral blood mononuclear cell–derived hiPSCs were a gift from J. Wu (Stanford University) and were derived using Sendai virus. hESCs (H1 and H7) used in the study were at passage 35 (H1, WiCell) or passage 54 (H7, WiCell) and cultured in mTeSR1 medium on Matrigel. IMR90 human fetal lung fibroblasts (passage 15–20), human dermal fibroblasts (primary adult skin, Cell Applications) and MEFs (primary isolated, passage 2) were cultured in DMEM with 1% L-glutamine, 1% nonessential amino acids, 10% FBS and 1% penicillin/streptomycin. Immunostaining and flow cytometer measurements were performed using antibodies listed in **Supplementary Table 1**.

Neural cell and cardiomyocyte derivation. Neural rosettes and subsequent neural progenitor cells and differentiated neuronal cells were derived from feeder-free, pluripotent colonies of hiPSC (passage 40 or 52) via methods based on those previously described for hESCs[33]. Briefly, hiPSCs were enzymatically passaged 1:2 with dispase (1 mg mL^{-1}), and then cells were scraped onto BD Matrigel (diluted 1:100) in mTeSR1 medium (Stemcell Technologies). Medium was changed every other day for 4 d. On day 5, medium was switched to neural derivation medium (DMEM/F-12 supplemented with N-2), 4 ng mL^{-1} FGF2, 2 mM L-glutamine and 50 U mL^{-1}:50 μg mL^{-1} penicillin-streptomycin) and changed every other day. After 1 week in neural derivation medium, neural rosettes were manually isolated and then propagated on Matrigel (1:200) in neurobasal medium (Life Technologies) supplemented with B-27, 20 ng mL^{-1} FGF2, 10 ng mL^{-1} LIF, 2 mM L-glutamine and 50 U mL^{-1}:50 μg mL^{-1} penicillin-streptomycin, with medium changed every other day. After 4 weeks of differentiation, neural progenitor cells were manually isolated from neural rosette cultures and propagated as an adherent monolayer on Matrigel in neural proliferation medium. After several manual passages with a cell scraper, confluent cultures of hiPSC-derived neural progenitor cells on Matrigel (1:200) were differentiated for 2 weeks into mature, β-III tubulin (TUJ1)/MAP2-positive neuronal cells through removal of FGF2 from the neural proliferation medium and change of medium every 2–3 d. hiPSC (IMR90)-derived cardiomyocytes were a kind gift from C. Xu (Emory University) and were derived as previously reported[34]. Cells were cultured in RPMI/B27 medium and exhibited spontaneously contractile activity (**Supplementary Video 3**).

Design and fabrication of PDMS micropatterned arrays. Poly(dimethylsiloxane) (PDMS) micropattern arrays having islands with diameters of 10 μm, 20 μm, 56 μm and 170 μm were fabricated from silicon array masters[23,35]. Microcontact printing on glass coverslips coated with Ti (100 Å) followed by Au (100 Å) was achieved using hexadecanethiol/($HO(CH_2CH_2O)_3$-$(CH_2)_{11}SH$) chemistry[23]. Coverslips were incubated with ECM proteins (fibronectin or laminin, 50 μg mL^{-1} in PBS)[23]. After a blocking step with 1% heat-denatured bovine serum albumin (Sigma) for 30 min and protein elution for 2 h in PBS, single-cell suspensions of IMR90 cells or hiPSCs were seeded in mTeSR1 medium with ROCK inhibitors Y27362 (10 μM, Calbiochem) or thiazovivin (2 μM, Stemgent). Briefly, hiPSCs were treated with 0.05% trypsin for 1 min and scraped as intact colonies. Cells were then prepared as single cells in mTeSR1 with Y27362 ROCK inhibitor and seeded as 100,000 cells mL^{-1} on the micropatterned islands overnight. For unpatterned surfaces, glass coverslips were incubated with ECM proteins as above and single-cell suspensions were seeded as 60,000 cells mL^{-1} and cultured overnight.

Cell adhesion strength measurements. Cell adhesion strength was measured using a spinning disk system[23]. Coverslips with adherent cells cultured overnight were spun in PBS with 2 mM dextrose for 5 min at a constant speed in a custom-built device in compliance with American Society for Testing and Materials (ASTM F2664-11). The applied shear stress (τ) is given by the formula $\tau = 0.8r(\rho\mu\omega^3)^{1/2}$, where r is the radial position, ρ and μ are the fluid density and viscosity, respectively, and ω is the spinning speed. After spinning, cells were fixed in 3.7% formaldehyde, permeabilized in 0.1% Triton X-100, stained with DAPI (Life Technologies) and counted at specific radial positions using a 10× objective lens in a Nikon TE300 microscope equipped with a Ludl motorized stage, Spot-RT camera and Image Pro analysis system. Sixty-one fields were analyzed, and cell cluster counts were normalized to the number of cell cluster counts at the center of the disk, where the applied force is 0. The fraction of adherent cell clusters (f) was then fit to a sigmoid curve $f = 1/(1 + \exp(b(\tau - \tau_{50})))$, where τ_{50} is the shear stress for 50% detachment and b is the inflection slope. τ_{50} represents the mean adhesion strength for a population of cells. The adhesion-strength response was analyzed on micropatterned islands coated with fibronectin or laminin (50 μg mL^{-1}) or Matrigel (1:80).

Focal adhesion assembly. Immunofluorescence staining of focal adhesion proteins was performed as previously described[23]. Briefly, cells were prewashed with ice-cold PBS with calcium and magnesium, incubated in ice-cold cytoskeleton stabilization

buffer (50 mM NaCl, 150 mM sucrose, 3 mM $MgCl_2$, 1 μg mL^{-1} aprotinin, 1 μg mL^{-1} leupeptin, 1 μg mL^{-1} pepstatin and 1 mM phenylmethylsulfonyl fluoride) for 1 min and incubated twice (1 min each) in cytoskeleton buffer supplemented with 0.5% Triton X-100. Detergent-extracted cells were fixed in 4% paraformaldehyde in PBS, washed with PBS, incubated with a primary antibody against vinculin (Upstate) or talin (Sigma) and detected with Alexa Fluor 488–conjugated antibodies (Life Technologies).

Fabrication of microfluidic devices. PDMS (Sylgard 184, Dow Corning) microfluidic devices were fabricated as reported earlier using a negative photoresist (SU-8 2050, 50-μm thickness, MicroChem) and UV photolithography[36]. Patterned negative molds were then exposed to vapor-phase tridecafluoro-1,1,2,2-tetrahydrooctyl-1-trichlorosilane (United Chemical Technologies) in a vacuum desiccator to prevent adhesion of PDMS. A 5-mm-thick layer of degassed PDMS mixture (10:1) was cast onto the mold and cured at 70 °C for 2 h. Cast PDMS devices were peeled off and then punctured for inlet-outlet holes and bonded to glass coverslips by exposure to oxygen plasma for 20 s.

μSHEAR-based isolation. Prior to coating with ECM proteins, the microfluidic channels and tubes were cleaned with 70% ethanol and rinsed thoroughly with PBS. ECM proteins at 50 μg mL^{-1} (fibronectin or laminin) or 1:80 Matrigel were flowed through sterile devices and incubated for 1 h at room temperature. Small colonies of pluripotent stem cells and single-cell suspensions of fibroblasts were premixed and pipetted into the inlet reservoir using a 200-μL pipette tip and were cultured in the device for 24 h at 37 °C and 5% CO_2 before the detachment experiments. The device inlet was connected to a syringe pump using polyethylene tubing (BB31695-PE/4, Scientific Commodities), and outlet tubes emptied into collecting tubes. PBS was flowed at predetermined flow rates through the device to match up the desirable fluid shear stress, and cell detachment was monitored though a Nikon TE microscope. For this microfluidic flow configuration, the applied wall shear stress (τ) is defined by the formula $\tau = 12(\mu Q/wh^2)$, where w and h are the width and height of the channel, respectively, μ is the fluid viscosity and Q is the fluid flow rate[32]. Cells and colonies were plated on Matrigel-coated tissue culture plates in 10 μM ROCK inhibitor Y27362 (or 2 μM thiazovivin) containing mTeSR1 medium. For flow cytometry studies to determine purification efficiency, collected colonies or cells were immediately resuspended in a suspension of StainAlive DyLight 488 mouse anti-human TRA-1-60 antibody (Stemgent) and CMPTX CellTracker Red dye, stained for 45 min, washed and analyzed using an Accuri flow cytometer (BD Biosciences).

Pluripotent stem cell characterization. Karyotype analysis was performed on 20 metaphase spreads for each sample by CellLine Genetics. To determine population doubling time and survival, we dissociated detached colonies from μSHEAR into single cells and plated them in Matrigel-coated 12-well plates. At predetermined times, wells were washed and cells were counted. Embryoid bodies (EBs) from detached and expanded hiPSCs were formed using an ultrahigh-throughput forced aggregation method[37], and after 24 h, cell aggregates were transferred to a suspension culture on a rotary orbital shaker (65 r.p.m.) for 14 d. After differentiation, we plated EBs in cell chambers (BD Falcon), and after 21 d in chambers, differentiated cells were fixed with 4% paraformaldehyde, permeabilized with 0.05% Triton X-100 and stained with antibodies against α-fetoprotein, α-smooth muscle actin and PAX6.

Gene expression analysis. RNA was isolated from iPSCs using QIAshredder and RNeasy Mini kits (Qiagen) according to the manufacturer's protocols. We performed first-strand cDNA synthesis with the RT2 First Strand Kit (SABiosciences) followed by real-time PCR, using the Human Embryonic Stem Cells PCR array (SABiosciences) according to the manufacturer's recommended protocols and using a BioRad MyCycler and BioRad MyIQ real-time thermal cycler, respectively. Individual Ct values were first internally normalized to GAPDH and subsequently analyzed with Genesis software (Graz University of Technology), including $\log_2$ transformation and hierarchical clustering. Heat maps were generated for the expression of 84 embryonic stem cell–related genes for transcription factors, pluripotency and self-renewal, cytokines and growth factors; and embryonic stem cell differentiation/lineage marker genes extracted from gene expression microarrays. A log plot of the relative expression level of each gene ($2^{-\Delta Ct}$) between manual (x axis) and μSHEAR (y axis) was generated for analysis.

Bisulfite genomic sequencing. Bisulfite treatment of gDNA was carried out using a Cells-to-CpG Bisulfite Conversion kit (Life Technologies) according to the manufacturer's protocol and plotted as melting curves representing methylation status[26,27]. Converted gDNA was amplified by PCR using primers within the *OCT4*, *SOX2* and *NANOG* promoters. Primer sequences are as follows. *OCT4* forward: CCCTCCTCTAAAAAAC; *OCT4* reverse: GGGTTGTAGTTGTGTTTATT; *NANOG* forward: AATTACAAAAATAAACCACC; *NANOG* reverse: TAGGTGGGGAATTAGAAAAT; *SOX2* forward: CATATACAACATAATAAAAA; *SOX2* reverse: GTTTTTTTGGGTTATTTTG.

Teratoma formation. The μSHEAR-isolated cells were expanded on Matrigel and then collected as pellets resuspended in DMEM-F12 at 7 million cells per 50 μL. Cells were injected intramuscularly in the hind limb of SCID mice (Harlan). Seven weeks after injection, tumors were dissected, weighted and fixed with formalin. Paraffin-embedded tissue was sectioned and stained with hematoxylin and eosin (H/E) and imaged using a Nikon 80i microscope. All experimental and surgical procedures involving animals were approved by the Georgia Institute of Technology's Institutional Animal Care and Use Committee.

Statistics. Paired two-tailed Student's t-tests were performed to determine the significance of differences between two groups in adhesion blocking, adhesion strength and μSHEAR assays. For integrin profiling, one-way analysis of variance (ANOVA) was performed with Bonferroni correction using OriginPro 8.5.1. In all tests, $P < 0.05$ was regarded as statistically significant. All experiments were repeated in triplicate unless otherwise stated, and bar graph data represent average ± s.d.

33. Dhara, S.K. *et al.* Human neural progenitor cells derived from embryonic stem cells in feeder-free cultures. *Differentiation* **76**, 454–464 (2008).
34. Laflamme, M.A. *et al.* Cardiomyocytes derived from human embryonic stem cells in pro-survival factors enhance function of infarcted rat hearts. *Nat. Biotechnol.* **25**, 1015–1024 (2007).

doi:10.1038/nmeth.2437

35. Fu, J. *et al.* Mechanical regulation of cell function with geometrically modulated elastomeric substrates. *Nat. Methods* **7**, 733–736 (2010).
36. McDonald, J.C. *et al.* Fabrication of microfluidic systems in poly(dimethylsiloxane). *Electrophoresis* **21**, 27–40 (2000).
37. Bratt-Leal, A.M., Carpenedo, R.L., Ungrin, M.D., Zandstra, P.W. & McDevitt, T.C. Incorporation of biomaterials in multicellular aggregates modulates pluripotent stem cell differentiation. *Biomaterials* **32**, 48–56 (2011).

doi:10.1038/nmeth.2437

How vinculin regulates force transmission

David W. Dumbauld[a,b], Ted T. Lee[a,b], Ankur Singh[a,b], Jan Scrimgeour[b,c], Charles A. Gersbach[a,b], Evan A. Zamir[a,b], Jianping Fu[d], Christopher S. Chen[e], Jennifer E. Curtis[b,c], Susan W. Craig[f], and Andrés J. García[a,b,1]

[a]Woodruff School of Mechanical Engineering, [b]Petit Institute for Bioengineering and Bioscience, and [c]School of Physics, Georgia Institute of Technology, Atlanta, GA 30332; [d]Department of Mechanical Engineering, University of Michigan, Ann Arbor, MI 48109; [e]Department of Bioengineering, University of Pennsylvania, Philadelphia, PA 19104; and [f]Department of Biological Chemistry, Johns Hopkins Medical School, Baltimore, MD 21205

Edited by James A. Spudich, Stanford University School of Medicine, Stanford, CA, and approved May 1, 2013 (received for review September 18, 2012)

Focal adhesions mediate force transfer between ECM-integrin complexes and the cytoskeleton. Although vinculin has been implicated in force transmission, few direct measurements have been made, and there is little mechanistic insight. Using vinculin-null cells expressing vinculin mutants, we demonstrate that vinculin is not required for transmission of adhesive and traction forces but is necessary for myosin contractility-dependent adhesion strength and traction force and for the coupling of cell area and traction force. Adhesion strength and traction forces depend differentially on vinculin head (V_H) and tail domains. V_H enhances adhesion strength by increasing ECM-bound integrin–talin complexes, independently from interactions with vinculin tail ligands and contractility. A full-length, autoinhibition-deficient mutant (T12) increases adhesion strength compared with V_H, implying roles for both vinculin activation and the actin-binding tail. In contrast to adhesion strength, vinculin-dependent traction forces absolutely require a full-length and activated molecule; V_H has no effect. Physical linkage of the head and tail domains is required for maximal force responses. Residence times of vinculin in focal adhesions, but not T12 or V_H, correlate with applied force, supporting a mechanosensitive model for vinculin activation in which forces stabilize vinculin's active conformation to promote force transfer.

cell adhesion | fibronectin

Integrin-mediated adhesion to ECM provides mechanical anchorage and signals that direct cell migration, proliferation, and differentiation (1, 2), processes central to tissue organization, maintenance, and repair. After ligand binding, integrins cluster into focal adhesion (FA) complexes that transmit adhesive and traction forces (3–6). FAs consist of integrins and actins separated by a ∼40 nm core that includes cytoskeleton (CSK) elements, such as vinculin and talin, and signaling molecules, including focal adhesion kinase and paxillin (7). FAs mediate responses to internal and external stresses by modulating force transfer between integrins and the CSK (8–10). This function has been likened to a "mechanical clutch" between an engine and transmission (11).

On the basis of its structure and binding partners, vinculin represents an attractive candidate for orchestrator of clutch function. Vinculin consists of a globular head (V_H) linked to a tail domain (V_T) by a proline-rich strap (12). V_H contains talin, α-actinin, and α- and β-catenin binding sites; actin, paxillin, and phosphatidylinositol 4,5-bisphosphate (PIP2) binding sites are in V_T; and vasodilator-stimulated phosphoprotein (VASP), actin-related protein 2/3 (Arp2/3), and vinexin binding sites reside in the proline-rich region. Interactions with these partners are regulated by an autoinhibited conformation arising from high-affinity intramolecular head–tail binding (13, 14). Activation of vinculin can occur by simultaneous binding to talin and actin or α-catenin and actin (15, 16). Vinculin is activated when localized to FAs (17). Vinculin forms a complex with β_1 integrin and talin (18) and interacts with talin to enhance integrin activation (19). Therefore, vinculin has the required molecular properties to mechanically link integrin–ECM complexes to the actomyosin CSK in a regulated manner.

In addition to studies on vinculin's effects on muscle function (20–22), which may or may not be related to its mechanical functions, vinculin's role in force transmission has largely been inferred from studies with vinculin-deficient cells showing altered FA assembly and aberrant migration (23, 24). For instance, V_H drives FA growth via interactions with talin, whereas V_T colocalizes to actin filaments (25), but whether these interactions mediate force transfer is unknown. Vinculin-deficient cells do exhibit reduced cortical CSK stiffness and adhesive force (26, 27), and vinculin is a force-carrying component between FAs and the CSK (28). Although these studies implicate vinculin in force transmission, few such measurements have been made, and some have provided evidence against a role of vinculin in force coupling (29). Moreover, possible roles played by vinculin domains and autoinhibition in mechanotransduction are largely unexplored.

In this study we used stable lines of vinculin-null cells expressing vinculin mutants and two force-measuring platforms to directly analyze whether and how vinculin transmits force. We found that although vinculin is not essential for transmission of traction and adhesive forces, it regulates the coupling of cell area and traction force and is required for myosin contractility-dependent traction forces and adhesion strength. In addition, we found that adhesion strength and traction forces depend to different extents on V_H and V_T, but maximal force transmission requires the talin/α-actinin–binding site on V_H, physical connection of V_H and V_T, and release of the autoinhibitory head–tail interaction. Finally, we discovered a linear relationship between the traction force at an FA and the residence time for vinculin at that FA, providing evidence for a mechanosensitive model for vinculin activation in which forces applied across vinculin maintain the molecule in its active conformation to increase residence times at FAs to promote force transfer.

Results

Stable Expression of Vinculins in Vinculin-Null Cells. We expressed WT and mutant vinculins fused to enhanced green fluorescent protein (eGFP) in vinculin-null cells using a tetracycline-regulated retroviral system (Fig. 1*A* and Fig. S1*A*). This strategy has major advantages over routine approaches using transient expression in vinculin-expressing cells: (*i*) experiments are based on the same cell population, eliminating batch-to-batch variability in expression levels; (*ii*) reexpression of target vinculins in cells lacking endogenous expression avoids confounding effects of endogenous vinculin; and (*iii*) the retroviral system has high transduction efficiencies, resulting in a polyclonal population of engineered cells and avoiding issues associated with clonal lines. We applied this system to two vinculin-null mouse embryonic fibroblast lines [MEF1 (15, 30) and MEF2 (13, 23, 31)] to rule out artifacts of a particular line. After transduction, WT vinculin-eGFP positive cell populations were enriched by FACS. Western blotting confirmed expression of vinculin constructs in both lines of

Author contributions: D.W.D., S.W.C., and A.J.G. designed research; D.W.D., T.T.L., A.S., and J.S. performed research; C.A.G., E.A.Z., J.F., C.S.C., J.E.C., and S.W.C. contributed new reagents/analytic tools; D.W.D., T.T.L., A.S., J.S., and A.J.G. analyzed data; and D.W.D., A.S., J.E.C., S.W.C., and A.J.G. wrote the paper.

The authors declare no conflict of interest.

This article is a PNAS Direct Submission.

[1]To whom correspondence should be addressed. E-mail: andres.garcia@me.gatech.edu.

This article contains supporting information online at www.pnas.org/lookup/suppl/doi:10.1073/pnas.1216209110/-/DCSupplemental.

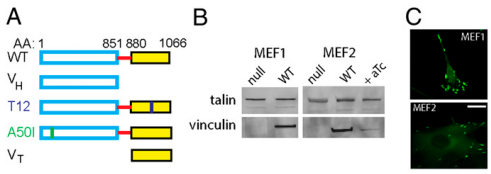

Fig. 1. Vinculin-null cells engineered to express vinculin variants. (*A*) Vinculin variants fused to eGFP: WT, head domain (V_H), auto-inhibition mutant (T12), talin-binding mutant (A50I), and tail domain (V_T). (*B*) Western blot analysis of engineered cell lines confirmed expression of vinculin constructs. Vinculin expression was repressed in presence of anhydrotetracycline (aTc, 100 ng/mL). (*C*) eGFP-vinculin localized to FAs for both MEF1- and MEF2-derived lines. (Scale bar, 10 μm.)

transduced vinculin-null MEFs (Fig. 1*B*). Expression levels for WT were comparable to levels in vinculin$^{+/+}$ cells derived from littermate controls. Culturing MEF2 cells in the presence of anhydrotetracycline significantly repressed levels of vinculin-eGFP expression. eGFP-vinculin localized to FAs, demonstrating proper function for the expressed proteins (Fig. 1*C*).

To investigate the contributions of vinculin domains to force transmission, cell lines expressing eGFP-vinculin mutants were derived from MEF1 vinculin-null cells. We first examined two mutants: (*i*) a molecule comprising only V_H (1–851) and lacking most of the proline-rich strap and actin-binding tail, and (*ii*) a full-length variant (T12) with mutations along the head–tail interface that reduce head–tail binding affinity 100-fold and render the molecule in an active conformation that can readily bind talin and actin (Fig. 1*A*). These mutants have been characterized for their binding to talin and actin and recruitment to FAs (13, 25, 31). Equivalent expression levels were observed among cell lines (Fig. S1*B*). V_H-expressing cells were more round than WT-expressing cells, and the V_H construct localized to large radial FAs (Fig. S1*C*). T12-expressing cells displayed more and larger FAs than WT-expressing cells (Fig. S1*C*). These phenotypes are consistent with observations for transiently transfected cells (13, 25).

Vinculin Activation Increases Traction Forces and Regulates Coupling Between Cell Area and Total Traction Force. We used microfabricated postarray deflection devices (mPADs) to measure traction forces. When seeded overnight onto fibronectin (FN)-coated mPADs, cells spread and developed FAs (Fig. 2*A* and Fig. S2*A*). T12-expressing cells exhibited higher spread areas compared with other lines, and V_H-expressing cells spread more than null but not WT-expressing cells (Fig. 2*B*). Treatment with blebbistatin (20 μM, 30 min), an inhibitor of myosin contractility, reduced cell area for null, WT-, and T12-expressing cells but not V_H-expressing cells. We measured post deflections for null and vinculin-expressing lines. Fig. 2*A* and Fig. S2*A* present images (*Upper*) for FN-coated posts (red) and eGFP-vinculin (green) recruited to FAs, with the cell outlined in yellow and force vectors (cyan, *Lower*) calculated from post deflections. The magnitude of traction forces varied significantly across a single cell, with the highest forces at the cell periphery (Fig. 2*A* and Fig. S2*A*). Fig. 2*C* presents box-whisker plots for the total traction force per cell, which represents the sum of the magnitudes of the force vectors for each cell and is commonly used for reporting traction forces (32). Traction forces are dynamic, and the data in Fig. 2*C* represent a "snapshot" of the traction forces in a cell population at equilibrium (overnight culture). Vinculin-null cells generate considerable traction forces (~100 nN), indicating that vinculin is not required for force transmission at FAs. WT expression increased the total traction force by 40% compared with vinculin-null controls. This result demonstrates that vinculin enhances the transmission of traction forces. In contrast, V_H expression had no effect on the total traction force compared with null cells, showing that, despite localization to FAs, V_H by itself does not influence traction forces. T12-expressing cells exhibited twofold higher total traction forces than null cells, and the total traction force was 40% higher than that generated by WT-expressing cells. This result shows that disruption of vinculin head–tail inhibition enhances the transmission of traction forces. Blebbistatin reduced traction forces by 30% in WT- and T12-expressing cells, but the total traction force in null and V_H-expressing cells was insensitive to blebbistatin. This result shows that transmission of myosin contractility-dependent traction forces at FAs requires a full-length vinculin molecule containing both V_H and V_T.

We examined the relationship between cell area and traction force because Fu et al. (32) showed tight coupling between cell area and CSK tension, suggesting that cell area–traction force coupling represents a robust metric to analyze force responses to vinculin expression. Fig. 2*D* and Fig. S2*B* plot cell area and corresponding traction force for individual cells as well as regression lines. There is a strong correlation between cell area and traction force for null, WT-, and T12-expressing cells. Vinculin-null cells displayed a linear relationship between cell area and traction force, indicating that vinculin is dispensable for cell area–traction force coupling. This result supports a role for other FA components in the transmission of traction forces, such as direct talin–actin force transfer (33). However, WT expression significantly enhances coupling between cell area and traction force, as demonstrated by the twofold increase in the regression slope compared with null cells. T12 expression results in stronger coupling between cell area and traction force compared with WT, showing that vinculin head–tail inhibition plays a critical role in regulating traction forces. V_H-expressing cells showed no coupling between cell area and traction force. This result indicates that V_H disrupts basal cell area–traction force coupling, demonstrating that both V_H and V_T are required for vinculin-enhanced coupling between cell area and total traction force. Although blebbistatin reduces cell area and traction force, it

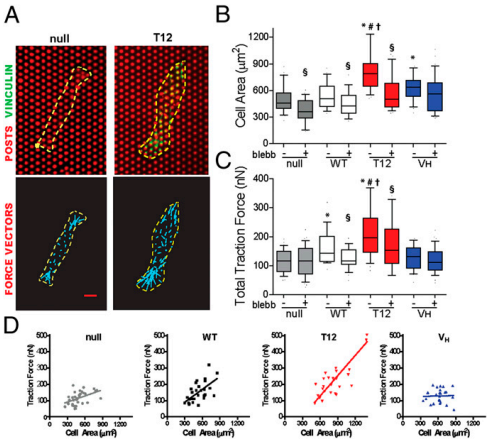

Fig. 2. Vinculin regulates traction forces. (*A*) Cells spread on mPADs (posts labeled red) showing localization of vinculin (eGFP) to FAs (*Upper*) and spreading (yellow outline) and force vectors (cyan arrows) (*Lower*). (Scale bar, 4 μm.) (*B*) Box-whisker plot (mean, 10th, 25th, 75th, and 90th percentile) for cell area (>24 cells per condition). Kruskal-Wallis $P < 0.0001$, $^{*}P < 0.05$ vs. null, $^{\#}P < 0.05$ vs. WT, $^{\dagger}P < 0.05$ vs. V_H; $^{\S}P < 0.05$ blebb vs. control. (*C*) Box-whisker plot (mean, 10th, 25th, 75th, and 90th percentile) for total traction force per cell (>24 cells). Kruskal-Wallis $P < 0.0001$, $^{*}P < 0.022$ vs. null, $^{\#}P < 0.01$ vs. WT, $^{\dagger}P < 0.01$ vs. V_H; $^{\S}P < 0.05$ blebb vs. control. (*D*) Relationship between traction force and cell area (>24 cells per condition) showing linear regression fits.

does not disrupt the relationship between cell area and traction force (Fig. S2*C*).

How Vinculin Head and Tail Domains and Autoinhibition Contribute to Adhesion Strength. We measured the steady-state (16 h after seeding) adhesion strength of cells expressing WT to FN using a spinning disk device. Whereas traction force measurements report on forces applied to the substrate arising from actomyosin contractility or actin polymerization, the adhesion strength assay measures the amount of force required to detach the cell from the ECM. The spinning disk exposes cells to a hydrodynamic shear force that increases linearly with radial position from the disk center and provides sensitive measurements of adhesion strength (Fig. S3*A*).

WT-expressing cells were cultured overnight on FN-coated micropatterned islands to eliminate differences in adhesive area and cell shape. This is an important consideration because expression of these constructs produces changes in cell area, a parameter that also regulates adhesion strength (6). Cells remained constrained to the micropatterned area as single cells. Expression of WT in vinculin-null MEF1 and MEF2 cells increased adhesion strength by 25% and 27%, respectively, over null controls (Fig. 3*A*). To test whether the increases in adhesion strength were caused by vinculin expression, we cultured WT-MEF2 cells in anhydrotetracycline to suppress expression. Under these conditions, the adhesion strength returned to the levels of null cells (Fig. 3*A*). Studies with blocking antibody demonstrated that adhesion to FN was mediated by β1 integrin (Fig. S3*B*). These results demonstrate that vinculin directly modulates adhesion strength and that this system provides direct measurements of β1 integrin–FN-mediated adhesion strength.

We next examined the adhesion strength of vinculin-null cells expressing vinculin mutants. V_H expression increased adhesion strength by 25% compared with null controls (Fig. 3*B*), indicating that recruitment of V_H to adhesive complexes increases adhesion strength independently from V_T. V_H increased adhesion strength to equivalent levels as WT. T12 expression increased adhesion strength by 50% over null cells (Fig. 3*B*), doubling the increase in adhesion strength by either WT or V_H. This result indicates that regulation of vinculin autoinhibition plays an important role in the generation of adhesion strength and that the active vinculin conformation presenting head and tail domains results in maximal adhesion strength.

We hypothesized that binding of V_H to talin or α-actinin was essential for vinculin-dependent increases in adhesion strength. We examined the effect of expressing a full-length, talin-/α-actinin-binding deficient mutant (A50I). No differences in adhesion strength were observed between A50I-expressing and null cells (Fig. S3*C*), indicating that vinculin binding to one or both of these ligands is essential for vinculin-mediated adhesion strength.

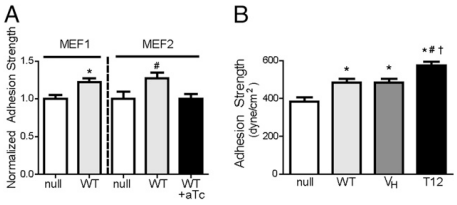

Fig. 3. Vinculin head and tail domains have distinct contributions to adhesion strength. (*A*) Expression of WT in vinculin-null cells increased adhesion strength over controls (*$P < 0.03$ vs. null, #$P < 0.05$ vs. null, +aTc). aTc-induced suppression of WT expression returned adhesion strength to null levels. (*B*) V_H expression increased adhesion strength by 25%, whereas T12 increased adhesion strength by 50% compared with null controls. ANOVA $P < 0.0001$, *$P < 0.05$ vs. null, #$P < 0.05$ vs. WT, and †$P < 0.05$ vs. V_H.

Physical Linkage Between Vinculin Head and Tail Domains Is Required for Maximal Adhesion Strength. We postulated that the increased adhesion strength for T12-expressing cells relative to V_H-expressing cells arises from differences in load transfer from the integrin–ECM complexes to the actin CSK via vinculin. We tested this model by independently expressing V_H and V_T in the same cell. We transiently transfected MEF1 cells with plasmids encoding for V_H, T12, or V_T or cotransfected plasmids for V_H and V_T. Transfected cells were enriched by flow cytometry sorting and seeded on FN islands. Image analysis demonstrated that vinculin mutants localized to FN patterns in a similar way as those in the stable lines (Fig. S4*A*). Cotransfected V_H and V_T localized to the FN island, but there was no strong colocalization because these two domains are not physically linked (Fig. S4*B*). Coexpression of separate V_H and V_T did not alter adhesion strength compared with expression of either domain, and adhesion strength was 25% lower than that for T12 expression (Fig. S4*C*). Expression of V_T resulted in similar levels of adhesion strength as V_H. This result was unexpected because V_T does not bind to the integrin–talin complex or α-actinin-rich lamellopodia protrusions (14, 34). A likely explanation for the effects of V_T is that this domain enhances adhesion strength by cross-linking actin to increase cortical CSK stiffness and load sharing among integrin bonds. Indeed, there is evidence that V_T enhances actin cross-linking and cortical CSK stiffness (29). These data show that the physical linkage between vinculin head and tail domains is required for maximal adhesion strength, indicating that force transfer from the adhesive clusters to the actin CSK via vinculin contributes to adhesion strength.

Vinculin Head–Tail Autoinhibition Regulates the Number of Integrin–FN Complexes and Recruitment of Vinculin and Talin. Because adhesion strength is regulated by the number/distribution of integrin–ECM complexes, FA assembly, and CSK interactions (6), we analyzed integrin binding and FA assembly to gain insights into possible reasons for the differences in adhesion strength. We first examined the effects of vinculin mutants on the levels and distribution of integrin–FN complexes using a cross-linking and detergent extraction method to selectively retain integrin–FN complexes. Fig. 4*A* presents images of single cells adhering to FN islands and immunostained for β1 integrin, and Fig. 4 *B* and *C* plot the fraction of the adhesive area occupied by integrin–FN complexes and the intensity of integrin staining over the micropatterned area. Vinculin-null cells assembled integrin β1–FN complexes along the periphery of the adhesive area, with minimal staining in the interior. WT expression did not change the spatial distribution or area occupied by integrin–FN complexes but resulted in a 15% increase in intensity. In contrast, V_H expression resulted in a fourfold increase in the area occupied by integrin–FN complexes, mostly localized to the periphery of the adhesive area, and a 40% increase in intensity compared with the null control. T12 expression yielded a fourfold increase in the area of integrin–FN complexes and a 50% increase in intensity compared with the null control. These results demonstrate that WT has a modest effect in regulating the number and spatial distribution of integrin–FN complexes and that presentation of V_H, either alone or in a mutant with disrupted head–tail binding, significantly increases the number and spatial distribution of integrin–FN complexes. Furthermore, the lack of differences in integrin–FN complexes between V_H and T12 indicates that V_T does not contribute significantly to the assembly or stability of integrin–FN complexes. These results indicate that vinculin head–tail inhibition to control exposure of V_H plays a major regulatory role in controlling the number and spatial distribution of ECM–integrin complexes.

We examined the role of vinculin autoinhibition on FA assembly by measuring recruitment of talin and the vinculin constructs to FAs. For all cells, talin and vinculin staining was

CELL BIOLOGY

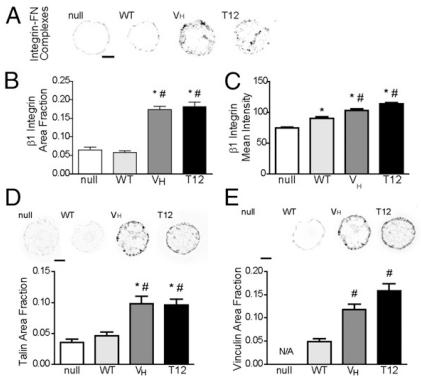

Fig. 4. Vinculin head–tail interaction regulates integrin–FN complexes and FA assembly. (*A*) Immunostaining for β1 integrin for cells adhering to FN micropatterned islands. Staining is shown as grayscale on white background to facilitate visualization. (Scale bar, 5 μm.) (*B*) Fraction of adhesive area occupied by integrin–FN complexes. ANOVA $P < 0.0001$, $^{*}P < 0.05$ vs. null, $^{\#}P < 0.05$ vs. WT. (*C*) Intensity of integrin staining over micropatterned area. ANOVA $P < 0.0001$, $^{*}P < 0.05$ vs. null, $^{\#}P < 0.05$ vs. WT (>60 cells per condition). (*D*) (*Upper*) Immunostaining for talin for cells adhering to FN islands. (Scale bar, 5 μm.) (*Lower*) Area of talin staining normalized to total adhesive area. ANOVA $P < 0.0001$, $^{*}P < 0.05$ vs. null, $^{\#}P < 0.05$ vs. WT. (*E*) (*Upper*) Immunostaining for vinculin for cells on FN islands (Scale bar, 5 μm.) (*Lower*) Area of vinculin staining normalized to total adhesive area. ANOVA $P < 0.0001$, $^{*}P < 0.05$ vs. null, $^{\#}P < 0.05$ vs. WT (>20 cells per condition).

restricted to the circumference of the micropatterned area (Fig. 4 *D* and *E*), consistent with the staining patterns for integrin–FN complexes. In addition to circumferential staining, T12- and V_H-expressing cells exhibited small vinculin and talin clusters in the interior of the adhesive area. Analysis of the adhesive area occupied by talin showed that WT expression had modest effects compared with null cells (Fig. 4*D*). In contrast, expression of V_H or T12 significantly enhanced the area occupied by talin and vinculin compared with WT and null cells (Fig. 4 *D* and *E*). These results demonstrate that WT has a modest effect in regulating FA assembly and that presentation of V_H, either alone or in a mutant with disrupted head–tail binding, significantly increases the area occupied by FAs. Furthermore, the lack of differences between V_H and T12 indicates that V_T does not contribute significantly to FA assembly. These results suggest that vinculin head–tail autoinhibition plays an important function in regulating FA assembly by controlling the exposure of V_H, resulting in an increase of both talin and vinculin recruitment to FAs.

Because there were no major differences in integrin–FN complexes and FA assembly between null and WT-expressing cells, we attribute the increased adhesion strength for WT to enhanced force distribution at the adhesive interface due to WT-mediated local cortical CSK stiffening and load transfer to the CSK. In contrast, the increased adhesion strength for V_H compared with the null control likely results from the higher number of integrin–FN complexes and enhanced FA assembly. Compared with V_H, T12 further increases adhesion strength without altering the levels of integrin–FN complexes or talin/vinculin recruitment to FAs. We attribute this additional increase in adhesion strength for T12 to V_T binding to the actin CSK to enhance load transfer.

Effect of Contractility on Adhesion Strength Is Mediated by Vinculin Autoinhibition. The increase in adhesion strength for T12 compared with V_H suggests that force transfer from FAs to the CSK via V_T is required for maximal adhesion strength. Because myosin contractility is critical to force generation (4, 5, 26, 35), we analyzed the contributions of myosin contractility to adhesion strength in the context of vinculin expression. Cells were seeded overnight on FN islands and exposed to blebbistatin (20 μM) for 30 min before measuring adhesion strength. Blebbistatin had no effect on adhesion strength for vinculin-null cells (Fig. 5). In contrast, blebbistatin reduced adhesion strength by 30% in WT-expressing cells. This result is consistent with our work demonstrating that vinculin is required for contractility-dependent adhesion strength (26). In this earlier study, we showed that the reductions in adhesion strength in response to contractility inhibition were associated with loss of vinculin and talin from FAs, in agreement with contractility-dependent FA assembly (36).

We hypothesized that the adhesion strength of V_H-expressing cells would be insensitive to blebbistatin treatment because this mutant cannot interact with the actin CSK because it lacks binding sites for Arp2/3, paxillin, and actin. Indeed, blebbistatin treatment had no effect on the adhesion strength of V_H-expressing cells (Fig. 5), indicating that the potential VASP-binding site in V_H is not capable of mediating interaction with actomyosin. Moreover, integrin–FN complex assembly and recruitment of talin and V_H to FAs were insensitive to blebbistatin (Fig. S5). This response differs from the effects of blebbistatin on WT vinculin-expressing cells and indicates that contractility-mediated changes in adhesion strength and FA assembly require a full-length, actin-binding vinculin molecule. We next analyzed the adhesion strength of T12-expressing cells with blebbistatin treatment. Surprisingly, blebbistatin enhanced adhesion strength for T12-expressing cells by 25% compared with untreated controls, in stark contrast to the effects of blebbistatin on WT-expressing cells (Fig. 5). Blebbistatin did not alter integrin–FN complex formation or vinculin and talin recruitment to FAs for T12-expressing cells (Fig. S5), so this enhancement in adhesion strength cannot be attributed to changes in integrin–FN bonds or FA assembly. These results indicate that vinculin autoinhibitory regulation is critical to contractility-mediated changes in adhesion strength, demonstrating a role for activated vinculin in force transfer. Furthermore, these data suggest that T12 promotes adhesion strength better than V_H through the ability of V_T to interact with the actin CSK and by the inability of T12 to substantially regain the autoinhibited conformation.

Vinculin Residence Times in FAs Correlate with Applied Force and Require Autoinhibitory Head–Tail Interactions. The striking difference in the effects of blebbistatin on the adhesion strength of WT- vs. T12-expressing cells implicates head–tail interactions in the regulation of contractility-mediated enhancements in adhesive force. We hypothesized that forces applied across vinculin maintain the molecule in its active conformation and counterbalance the high-affinity head–tail inhibition. For WT, inhibition of contractility unloads the vinculin molecule and promotes rebinding between V_H and V_T, resulting in vinculin inactivation and FA disassembly. For the T12 mutant, the head–tail interaction is reduced 100-fold, resulting in a molecule that, although not constitutively open (13), is much easier to open and harder to reclose. This mutant retains the WT affinity of V_H for talin and V_T for actin. Because of the ~100-fold reduced head–tail autoinhibition,

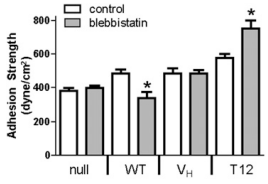

Fig. 5. Effect of contractility on adhesion strength is mediated by vinculin autoinhibition. $^{*}P < 0.05$ vs. control.

the T12 mutant would not reclose significantly when unloaded, and it would therefore transmit adhesive forces even during blebbistatin-mediated inhibition of contractility.

To test this model, we examined the relationship between vinculin residence times at FAs and applied force by performing fluorescence recovery after photobleaching (FRAP) experiments on cells on mPADs. We examined recovery times after photobleaching for eGFP-vinculin–containing FAs associated with posts with known deflections. In this fashion we could monitor vinculin dynamics at FAs under force. FRAP movies for WT-vinculin FAs under different traction forces are provided (Movies S1–S4), and Fig. S6*A* presents images of WT-containing FAs on mPADs before and after photobleaching. Fig. 6*A* displays FRAP recovery curves for WT in FAs transmitting different forces. The applied force remained constant over the 3-min FRAP experiment (Fig. S6 *B* and *C*). The half-life recovery time ($t_{1/2}$) vs. traction force for individual FAs in WT-expressing cells is plotted in Fig. 6*B*. Strikingly, we observed a linear relationship between applied force and recovery time for WT. A simple explanation for the strong correlation between vinculin residence time in FAs and applied force is that tension applied across the vinculin molecule maintains vinculin in the active conformation to increase its residence time in FAs. Blebbistatin (20 μM) eliminates the linear relationship between recovery time and force (Fig. 6*C*), consistent with our model. We also examined the recovery time vs. force relationship for cells expressing T12 and V_H (Fig. 6*D*). Both V_H and T12 exhibited twofold slower recovery times compared with WT, consistent with previous data (25, 31). However, in stark contrast to WT, recovery times for T12 and V_H did not correlate with applied forces at FAs. These results demonstrate that the vinculin head–tail interaction is critical to the coupling of vinculin residence time at FAs and applied force. Importantly, the lack of correlation of recovery times with force for V_H demonstrates that V_T is required for FA residence time–force coupling. Additionally, this result rules out the explanation that this phenomenon arises from force-mediated exposure of vinculin binding sites on talin (37). These findings support a mechanosensitive model for vinculin activation in which forces applied across vinculin maintain the molecule in its active conformation to increase residence times at FAs to transfer force.

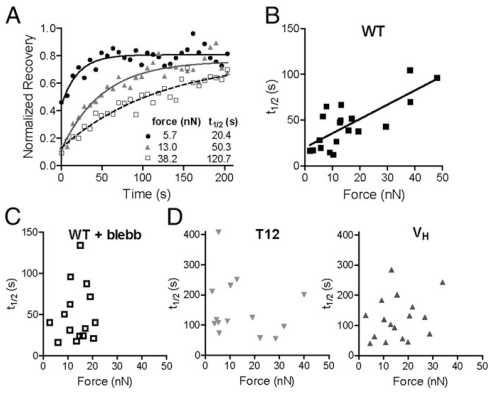

Fig. 6. Vinculin residence times in FAs correlate with applied force and require head–tail interactions. FRAP was performed on FAs on mPAD posts with known applied forces. (*A*) FRAP recovery curves for WT localized to FAs transmitting different forces. (*B*) Correlation between recovery time ($t_{1/2}$) and applied force (>15 cells analyzed per condition) for WT. Linear regression: $t_{1/2} = 1.56 \times \text{force} + 20.0$, $P < 0.0001$. (*C*) Blebbistatin treatment (20 μM) eliminates linear relationship between recovery time and force (no linear dependence, $P = 0.75$). (*D*) No correlation between $t_{1/2}$ and applied force was observed for T12 ($P = 0.45$) or V_H ($P = 0.35$). Different *y* axis scales were used between WT and V_H, T12 for ease of visualization.

Discussion

How vinculin and its interactions with binding partners transmit force remains poorly understood. Here we clearly demonstrate that vinculin regulates both traction forces and adhesion strength to ECM and dissect the contributions of different vinculin domains to these force outputs. The vinculin-dependent enhancements in traction force and adhesion strength quantify vinculin's contributions in force transmission and provide a mechanical basis to explain the effects of vinculin deletion on impaired cell spreading, migration, and muscle contraction. We show that vinculin regulates the coupling between cell area and traction force. The coupling between cell area and traction force reflects an integrated feedback response regulating cell shape and has been implicated in rigidity sensing (32). Our finding that full-length vinculin enhances cell area–traction force coupling but V_H completely disrupts this coupling indicates that vinculin is a key regulator of these mechanical responses and identifies a unique function for vinculin in mechanosensing.

Although V_H drives FA growth and V_T localizes to actin filaments (25), we demonstrate distinct contributions to force transmission for each domain. Vinculin transmits force by increasing ECM-bound integrin–talin complexes via V_H, whereas V_T transfers force to the actin CSK (Fig. S7). These mechanical functions require the talin/α-actinin-binding site on V_H. We note that vinculin-dependent changes in force transmission do not scale proportionally with changes in integrin-FN binding and FA assembly owing to biomechanical considerations, including spatial location of integrin–FN complexes and cortical CSK stiffness that result in nonlinear bond loading (6, 38). We also discovered an important role for vinculin's head–tail autoinhibitory interaction in regulating traction forces, adhesion strength, and the coupling between cell area and traction force. Finally, maximal adhesion strength requires V_H and V_T to be physically coupled, indicating that force transfer occurs through the vinculin molecule rather than independent contributions from each domain.

Although myosin contractility is critical to traction forces and adhesion strength, the contribution of vinculin to myosin contractility-dependent adhesive forces is unknown. We demonstrate that a full-length vinculin molecule containing both V_H and V_T is required for myosin contractility-dependent effects on traction force and adhesion strength, suggesting that force transfer occurs through the vinculin molecule. For WT-expressing cells, blebbistatin treatment reduced adhesion strength to vinculin-null levels, whereas blebbistatin did not alter adhesion strength in vinculin-null cells. Surprisingly, blebbistatin enhanced adhesion strength for T12-expressing cells, indicating that head–tail autoinhibition regulates the vinculin-dependent effects of myosin contractility on adhesion strength. One explanation for the blebbistatin-dependent increases in adhesion strength for T12 is that inhibition of contractility reduces the internal force applied to FAs, thereby increasing the force that can be supported by the external ECM–integrin linkage at FAs (39). The requirement for vinculin in myosin contractility-dependent adhesive forces establishes a unique function for vinculin in mechanotransduction beyond regulation of FA assembly (25, 28).

By applying FRAP to an FA under force, we discovered that vinculin residence time at an FA correlates linearly with the force applied to that FA. Vinculin residence time–force coupling requires a full-length molecule, head–tail autoinhibition, and myosin contractility. These results directly relate vinculin dynamics to force and complement studies showing that contractility influences FA dynamics (40). Our data support a model for vinculin stabilization in which forces applied across vinculin maintain the molecule in its active conformation to increase residence times at FAs to promote force transfer (Fig. S7). Direct measurements of the forces experienced by vinculin in the context of adhesion strength and traction forces are still needed to fully validate this model. Vinculin's binding partners and

phosphorylation sites could provide indirect mechanisms for its force-regulated recruitment and activity.

Our findings support a mechanosensitive model for vinculin activation. Structural and biochemical data support a role for talin and actin binding in vinculin activation (13, 15, 41, 42). Given the requirements for the talin-binding site on V_H and the actin-binding V_T for force transmission, it is likely that coordinated activation by talin and actin provides a major mechanism driving vinculin activation and that force transmission across vinculin stabilizes its active conformation. This mechanism provides an explanation for the observation that vinculin recruitment to FAs is separable from mechanical loading (28). Force-dependent vinculin activation identifies another mechanism that complements mechanosensitive pathways at FAs, such as integrin–FN binding (43, 44) and talin stretching to expose binding sites (37).

The improved understanding of vinculin's contributions to force transmission provided by this work has several implications. First, vinculin regulates the transmission of adhesive forces by modulating ECM–integrin complexes via V_H and transmitting forces from these complexes to the actin CSK via V_T. Second, vinculin regulates cell area–traction force coupling and myosin contractility-dependent adhesion strength and traction forces. As such, vinculin likely provides "fine tuning" control required for coordinated processes like migration and contraction. Finally, force-based regulation of vinculin activation provides a mechanism to generate local mechanosensitive responses at FAs such as force-dependent FA growth (8, 36). Mechano-regulation of vinculin residence times at FAs represents a pathway for coordinated assembly of FAs at the leading edge and disassembly of FAs at the rear of the cell. In fact, experiments with a force sensor revealed high forces across vinculin at the leading edge and low forces at the trailing edge (28), consistent with our model. Collectively, this work provides these important insights into how vinculin's structure and binding partners interact with contractility to regulate force transmission.

Methods

Vinculin lines were generated by retroviral transduction of vinculin-null cells and FACS selection. Cell adhesion strength and traction forces were measured with a spinning disk device and mPADs, respectively. FRAP was performed on cells on mPADs. Detailed methods are presented in *SI Methods*.

ACKNOWLEDGMENTS. Funding was provided by National Institutes of Health Grants R01-GM065918 (to A.J.G.), R01-EB00262, R01-GM74048 (both to C.S.C.), and R01-GM41605 (to S.W.C.), RESBIO Technology Resource for Polymeric Biomaterials, Human Frontier Science Program Grant RGP0013 (to J.F.C.), and National Science Foundation Career Award DMR-0955811 (to J.E.C.) and CMMI-1129611 (to J.F.).

1. Hynes RO (2002) Integrins: Bidirectional, allosteric signaling machines. *Cell* 110(6): 673–687.
2. Wickström SA, Radovanac K, Fässler R (2011) Genetic analyses of integrin signaling. *Cold Spring Harb Perspect Biol* 3(2):a005116.
3. Beningo KA, Dembo M, Kaverina I, Small JV, Wang YL (2001) Nascent focal adhesions are responsible for the generation of strong propulsive forces in migrating fibroblasts. *J Cell Biol* 153(4):881–888.
4. Balaban NQ, et al. (2001) Force and focal adhesion assembly: A close relationship studied using elastic micropatterned substrates. *Nat Cell Biol* 3(5):466–472.
5. Tan JL, et al. (2003) Cells lying on a bed of microneedles: An approach to isolate mechanical force. *Proc Natl Acad Sci USA* 100(4):1484–1489.
6. Gallant ND, Michael KE, García AJ (2005) Cell adhesion strengthening: Contributions of adhesive area, integrin binding, and focal adhesion assembly. *Mol Biol Cell* 16(9): 4329–4340.
7. Kanchanawong P, et al. (2010) Nanoscale architecture of integrin-based cell adhesions. *Nature* 468(7323):580–584.
8. Riveline D, et al. (2001) Focal contacts as mechanosensors: externally applied local mechanical force induces growth of focal contacts by an mDia1-dependent and ROCK-independent mechanism. *J Cell Biol* 153(6):1175–1186.
9. Galbraith CG, Yamada KM, Sheetz MP (2002) The relationship between force and focal complex development. *J Cell Biol* 159(4):695–705.
10. Choquet D, Felsenfeld DP, Sheetz MP (1997) Extracellular matrix rigidity causes strengthening of integrin-cytoskeleton linkages. *Cell* 88(1):39–48.
11. Smilenov LB, Mikhailov A, Pelham RJ, Marcantonio EE, Gundersen GG (1999) Focal adhesion motility revealed in stationary fibroblasts. *Science* 286(5442):1172–1174.
12. Ziegler WH, Liddington RC, Critchley DR (2006) The structure and regulation of vinculin. *Trends Cell Biol* 16(9):453–460.
13. Cohen DM, Chen H, Johnson RP, Choudhury B, Craig SW (2005) Two distinct head-tail interfaces cooperate to suppress activation of vinculin by talin. *J Biol Chem* 280(17): 17109–17117.
14. Johnson RP, Craig SW (1995) F-actin binding site masked by the intramolecular association of vinculin head and tail domains. *Nature* 373(6511):261–264.
15. Chen H, Choudhury DM, Craig SW (2006) Coincidence of actin filaments and talin is required to activate vinculin. *J Biol Chem* 281(52):40389–40398.
16. Peng X, Maiers JL, Choudhury D, Craig SW, DeMali KA (2012) α-Catenin uses a novel mechanism to activate vinculin. *J Biol Chem* 287(10):7728–7737.
17. Chen H, Cohen DM, Choudhury DM, Kioka N, Craig SW (2005) Spatial distribution and functional significance of activated vinculin in living cells. *J Cell Biol* 169(3):459–470.
18. Horwitz AF, Duggan K, Buck CA, Beckerle MC, Burridge K (1986) Interaction of plasma membrane fibronectin receptor with talin—a transmembrane linkage. *Nature* 320(6062):531–533.
19. Ohmori T, et al. (2010) Vinculin activates inside-out signaling of integrin αIIbβ3 in Chinese hamster ovary cells. *Biochem Biophys Res Commun* 400(3):323–328.
20. Zemljic-Harpf AE, et al. (2007) Cardiac-myocyte-specific excision of the vinculin gene disrupts cellular junctions, causing sudden death or dilated cardiomyopathy. *Mol Cell Biol* 27(21):7522–7537.
21. Huang Y, Zhang W, Gunst SJ (2011) Activation of vinculin induced by cholinergic stimulation regulates contraction of tracheal smooth muscle tissue. *J Biol Chem* 286(5):3630–3644.
22. Barstead RJ, Waterston RH (1991) Vinculin is essential for muscle function in the nematode. *J Cell Biol* 114(4):715–724.
23. Xu W, Baribault H, Adamson ED (1998) Vinculin knockout results in heart and brain defects during embryonic development. *Development* 125(2):327–337.
24. Xu W, Coll JL, Adamson ED (1998) Rescue of the mutant phenotype by reexpression of full-length vinculin in null F9 cells; effects on cell locomotion by domain deleted vinculin. *J Cell Sci* 111(Pt 11):1535–1544.
25. Humphries JD, et al. (2007) Vinculin controls focal adhesion formation by direct interactions with talin and actin. *J Cell Biol* 179(5):1043–1057.
26. Dumbauld DW, et al. (2010) Contractility modulates cell adhesion strengthening through focal adhesion kinase and assembly of vinculin-containing focal adhesions. *J Cell Physiol* 223(3):746–756.
27. Diez G, Auernheimer V, Fabry B, Goldmann WH (2011) Head/tail interaction of vinculin influences cell mechanical behavior. *Biochem Biophys Res Commun* 406(1): 85–88.
28. Grashoff C, et al. (2010) Measuring mechanical tension across vinculin reveals regulation of focal adhesion dynamics. *Nature* 466(7303):263–266.
29. Mierke CT, et al. (2008) Mechano-coupling and regulation of contractility by the vinculin tail domain. *Biophys J* 94(2):661–670.
30. DeMali KA, Barlow CA, Burridge K (2002) Recruitment of the Arp2/3 complex to vinculin: Coupling membrane protrusion to matrix adhesion. *J Cell Biol* 159(5): 881–891.
31. Cohen DM, Kutscher B, Chen H, Murphy DB, Craig SW (2006) A conformational switch in vinculin drives formation and dynamics of a talin-vinculin complex at focal adhesions. *J Biol Chem* 281(23):16006–16015.
32. Fu J, et al. (2010) Mechanical regulation of cell function with geometrically modulated elastomeric substrates. *Nat Methods* 7(9):733–736.
33. Jiang G, Giannone G, Critchley DR, Fukumoto E, Sheetz MP (2003) Two-piconewton slip bond between fibronectin and the cytoskeleton depends on talin. *Nature* 424(6946): 334–337.
34. Menkel AR, et al. (1994) Characterization of an F-actin-binding domain in the cytoskeletal protein vinculin. *J Cell Biol* 126(5):1231–1240.
35. Gardel ML, et al. (2008) Traction stress in focal adhesions correlates biphasically with actin retrograde flow speed. *J Cell Biol* 183(6):999–1005.
36. Chrzanowska-Wodnicka M, Burridge K (1996) Rho-stimulated contractility drives the formation of stress fibers and focal adhesions. *J Cell Biol* 133(6):1403–1415.
37. del Rio A, et al. (2009) Stretching single talin rod molecules activates vinculin binding. *Science* 323(5914):638–641.
38. Evans EA (1985) Detailed mechanics of membrane-membrane adhesion and separation. II. Discrete kinetically trapped molecular cross-bridges. *Biophys J* 48(1): 185–192.
39. Coyer SR, et al. (2012) Nanopatterning reveals an ECM area threshold for focal adhesion assembly and force transmission that is regulated by integrin activation and cytoskeleton tension. *J Cell Sci* 125(Pt 21):5110–5123.
40. Wolfenson H, Bershadsky A, Henis YI, Geiger B (2011) Actomyosin-generated tension controls the molecular kinetics of focal adhesions. *J Cell Sci* 124(9):1425–1432.
41. Izard T, et al. (2004) Vinculin activation by talin through helical bundle conversion. *Nature* 427(6970):171–175.
42. Bakolitsa C, et al. (2004) Structural basis for vinculin activation at sites of cell adhesion. *Nature* 430(6999):583–586.
43. Friedland JC, Lee MH, Boettiger D (2009) Mechanically activated integrin switch controls alpha5beta1 function. *Science* 323(5914):642–644.
44. Kong F, García AJ, Mould AP, Humphries MJ, Zhu C (2009) Demonstration of catch bonds between an integrin and its ligand. *J Cell Biol* 185(7):1275–1284.

A1.5 *Dynamic cell-adhesive microenvironments and their effect on myogenic differentiation.* Acta Biomaterialia.

Acta Biomaterialia 9 (2013) 8059–8066

Contents lists available at SciVerse ScienceDirect

Acta Biomaterialia

journal homepage: www.elsevier.com/locate/actabiomat

Dynamic cell-adhesive microenvironments and their effect on myogenic differentiation

Simone Weis [a], Ted T. Lee [b], Aránzazu del Campo [a,*], Andrés J. García [b,*]

[a] Max-Planck-Institut für Polymerforschung, Ackermannweg 10, 55128 Mainz, Germany
[b] Woodruff School of Mechanical Engineering, Petit Institute for Bioengineering and Bioscience, Georgia Institute of Technology, 315 Ferst Drive, Atlanta, GA 30332–0363, USA

ARTICLE INFO

Article history:
Received 12 April 2013
Received in revised form 7 June 2013
Accepted 12 June 2013
Available online 19 June 2013

Keywords:
Integrin
RGD
Biomaterial
Fibronectin
Cell adhesion

ABSTRACT

Integrin-mediated cell adhesion plays a central role in cell behavior on biomaterial surfaces and influences various cell functions. Photoactivatable RGD adhesive peptides were used to investigate the effect of the density and time point of bioadhesive ligand presentation on cell adhesion, proliferation and differentiation. PEGylated self-assembled monolayers were functionalized with RGD and caged RGD ligands and seeded with C2C12 myoblasts. The cultures were irradiated at various time points between 1 and 48 h after cell seeding in order to increase RGD surface concentration at defined time points. Attachment, spreading and myogenic differentiation of C2C12 myoblasts strongly varied with the density of RGD at the surface. Proliferation and myogenesis were further regulated by the time point at which RGD was presented to the cell, reaching highest levels when RGD exposure occurred ≤6 h after cell seeding. These results provide fundamental insights in cell–biomaterial interactions of C2C12 myoblasts in terms of temporal integrin-mediated cell responses.

1. Introduction

A promising strategy for successful integration of implanted substrates in living organisms is the engineering of application-specific biointerfaces that mimic characteristics of the extracellular matrix (ECM) [1–5]. Such substrates should allow on-demand regulation of the properties of the cellular microenvironment over time and space and, consequently, of the cell–biomaterial interactions and concomitant cell responses. Although the relevance of the temporal presentation of signaling factors at the cellular microenvironment has now been recognized by the biomaterials community, experimental studies in this context are still scarce [6,7]. At first sight, this fact appears surprising, since attempts to control the pharmacokinetic profile of soluble factors have a long history in therapeutics, and gradients of chemotactic factors have been widely applied for studies of directed migration. However, the complexity and interplay of biochemical and physical signaling factors involved in cell–ECM interactions (i.e. different matrix-anchored ligands or the mechanical properties and morphology of the matrix) involved in cell–ECM regulation, as well as the different spatial and temporal scales at which they occur, cannot easily be addressed with encapsulation strategies developed for soluble factors and require design and development of new and specific materials.

The presence of cell-adhesive ligands at the biomaterial surface is crucial for the regulation of cell–material communication and therefore cellular function, well beyond initial cell attachment and survival [8–13]. Cell attachment is mainly mediated by integrin receptors at the cell membrane and their interactions with components of the ECM [14]. The study of this interaction and the related signaling cascades can be performed using biointerfaces containing synthetic peptides mimicking the active domains of the ECM matrix components [15–17]. RGD-modified substrates have been used for this purpose and the role of a static RGD concentration in adhesion [18,19], migration [20], proliferation [21] and differentiation [22,23] processes has been demonstrated. Although relevant information has been gained from these studies on "static" surfaces, more sophisticated synthetic biointerfaces are required for mimicking the "dynamic" presence of adhesive factors in the ECM and its role in guiding cellular function.

Photoremovable protecting groups ("cages") are light-triggers that allow accurate spatiotemporal control and in situ regulation of molecular factors involved in signalling pathways. The "cage" can be attached to the active site of a biomolecule in order to inhibit its activity (latent state). Function is restored at a later time point by light exposure and photocleavage of the cage. Caged RGD derivatives (Scheme 1A) were developed by our groups for the controlled activation and deactivation of integrin-associated regulatory signals and concomitant modulation of cell response [24–28]. Caged cyclo[RGD(DMNPB)fK] peptide, where the 3-(4,5-dimethoxy-2-nitrophenyl)-2-butyl (DMNPB) chromophore is attached to the carboxylic side group of the

* Corresponding authors. Tel.: +49 6131 379563; fax: +49 06131 379271 (A. del Campo), tel.: +1 404 894 9384 (A.J. García).
E-mail addresses: delcampo@mpip-mainz.mpg.de (A. del Campo), andres.garcia@me.gatech.edu (A.J. García).

1742-7061/$ - see front matter © 2013 Acta Materialia Inc. Published by Elsevier Ltd. All rights reserved.
http://dx.doi.org/10.1016/j.actbio.2013.06.019

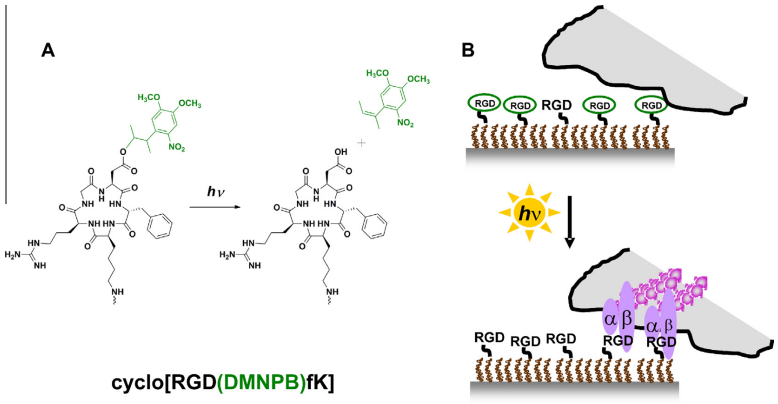

Scheme 1. (A) Chemical structure of cyclo[RGD(DMNPB)fK] before and after irradiation, including photolytic byproducts. (B) SAM functionalized with a mixture of caged RGD and RGD allows photomodulation of RGD surface density by light exposure at defined time points.

aspartic acid to inhibit biological activity, has allowed phototriggering of cell attachment [24,25] and migration [29] events over surfaces with light-dose-controlled RGD density. Light-triggered cell detachment from cultured cells was also realized using RGD-modified surface linkers with an intercalated photocleavable group that allowed release of the surface-anchored RGD functionality by light exposure [30]. A similar strategy has been extended to 3-D cell cultures, and joint influence of the decrease in the concentration of bioadhesive ligand and in the matrix stiffness in chondrogenic differentiation while photodegrading the hydrogel matrix was demonstrated [6].

The latent functionality of caged RGD can be activated at different time points using sequential illumination steps of controlled dose. This represents a unique strategy for the dynamic regulation of the RGD presentation at the surface and the generation of tunable bioadhesive states with temporal and spatial resolution (Scheme 1B). In this work we apply this strategy to study, for the first time, the influence of the temporal presentation and concentration of RGD ligands on the proliferation and differentiation of C2C12 myoblasts.

2. Materials and methods

2.1. Reagents and antibodies

All reagents and chemicals were used as received unless stated otherwise. Cell culture reagents, fetal bovine serum (FBS), goat serum (GS), insulin-transferrin-selenium-X (ITS) and Dulbecco's phosphate-buffered saline (DPBS) were obtained from Invitrogen (Carlsbad, CA). Cyclic RGD peptide (cyclo[RGDfK]) was purchased from Peptides International Inc. (Louisville, KY), GRDGSPC from Aapptec (Louisville, KY) and caged cyclic RGD peptide (cyclo[RGD(DMNPB)fK]) was synthesized and characterized as previously reported [24,25]. Tri(ethylene glycol)-terminated thiols ($HS\text{-}(CH_2)_{11}\text{-}(OCH_2CH_2)_3\text{-}OH$; EG_3 and $HS\text{-}(CH_2)_{11}\text{-}(OCH_2CH_2)_6\text{-}OCH_2COOH$; EG_6) for the preparation of self-assembled monolayers were purchased from ProChimia Surfaces (Sopot, Poland). Peptide tethering reagents, *N*-(3-dimethylaminopropyl)-*N*′-ethylcarbodiimide hydrochloride (EDC) and *N*-hydroxysuccinimide (NHS), as well as additives for cytoskeleton buffer, 1,4-piperazinediethanesulfonic acid (PIPES) and phenylmethanesulfonyl fluoride (PMSF), were obtained from Sigma-Aldrich (St Louis, MO). Triton X-100 was acquired from EMC Chemicals (Elkhorn, WI). Monoclonal MF 20 IgG2b anti-mouse sarcomeric myosin antibody was purchased from the Developmental Studies Hybridoma Bank (Iowa City, IA). Monoclonal anti-vinculin antibody, bovine serum albumin (BSA) and the protease inhibitors leupeptin, aprotinin and pepstatin A were obtained from Sigma-Aldrich (St Louis, MO). Alexa Fluor 555-conjugated phalloidin, 4′,6-diamidino-2-phenylindole dihydrochloride (DAPI), Alexa Fluor 488-conjugated goat anti-mouse IgG antibody and a Click-it® Alexa Fluor 488-conjugated EdU Imaging Kit (including Hoechst 33342 dye) for evaluation of cell proliferation were acquired from Invitrogen (Carlsbad, CA). Fluoromount G was obtained from Electron Microscopy Sciences (Hatfield, PA).

2.2. Model biomaterial surfaces/RGD functionalized self-assembled monolayers

Self-assembled monolayers (SAMs) of alkanethiols on gold were used as well-defined, ordered surfaces presenting anchoring groups within a non-fouling background. Gold-coated substrates were prepared by successive deposition of titanium (100 Å) and gold (200 Å) films on glass coverslips using an electron beam evaporator (Thermionics Laboratories, Hayward, CA, 2×10^{-6} torr) at a deposition rate of 2 Å s^{-1}. Mixed SAMs were prepared by immersing the gold-coated coverslips in a 1.2 mM mixed solution of EG_6/EG_3 = 1/49 in ethanol overnight. The solution was aspirated, and following rinsing with ethanol and ultrapure water, the substrates were equilibrated in ultrapure water for 1 h. Peptides were tethered to the carboxylic acid groups of the SAMs using standard peptide chemistry [31]. For this purpose, substrates were immersed in 0.2 M EDC and 0.1 M NHS in 0.1 M 2-(*N*-morpho)-ethanesulfonic acid. After 20 min, substrates were rinsed with ultrapure water and then incubated in an 0.12 mM peptide solution: either cyclo[RGDfK], or cyclo[RGD(DMNPB)fK], or GRDGSPC, or a mixed solution of cyclo[RGDfK]/cyclo[RGD(DMNPB)fK] in 1:5 molar ratio. Substrates with different surface densities of cyclo[RGDfK] were prepared by incubation in 1, 5, 20, 50, 72 μg ml^{-1} (= 1.7, 8.3, 33, 83, 120 μM) solutions of cyclo[RGDfK]. After coupling for 1 h the substrates were rinsed with ultrapure water.

For cell-adhesion experiments, surfaces were immersed in 2 ml Dulbecco's Modified Eagle's Medium (DMEM) in a 35 mm culture dish, and irradiated using an X-Cite 120 fluorescence illumination system equipped with a bandpass filter (center wavelength

355 nm, full width half maximum 53 nm). Irradiation conditions were 3 min and 3.5 mW cm^{-2}. Finally, to reduce non-specific protein adsorption, surfaces were blocked in 1.0 wt.% bovine serum albumin (BSA) in DPBS for 30 min at room temperature, and rinsed with DPBS prior to immediate cell seeding [32].

2.3. Cell culture

Murine C2C12 myoblasts (ATCC, CRL-1772) were used for all experiments to study the effects of surface modifications on cell adhesion, proliferation and differentiation. Cells were maintained in DMEM supplemented with 20% fetal bovine serum and 1% penicillin–streptomycin at 37 °C in a humidified atmosphere and 5% CO_2. Cells were subcultured prior to reaching confluence (approximately every 1–2 days). Cells were seeded at a density of 5,000 cells cm^{-2} on peptide-presenting SAMs for all experiments. For myogenic differentiation experiments, C2C12 cells were seeded in DMEM supplemented with 1% penicillin–streptomycin and 1% ITS and for cell-adhesion assays in DMEM supplemented with 10% fetal bovine serum and 1% penicillin–streptomycin.

2.4. Myogenic differentiation assay

C2C12 cells were seeded on peptide-modified SAMs and cultured for 3 days at 37 °C under differentiation conditions followed by immunostaining for sarcomeric myosin. For experiments investigating a temporal threshold of the RGD surface density on myogenic differentiation, surfaces modified with both peptides cyclo[RGDfK] and cyclo[RGD(DMNPB)fK] (tethering ratio: 1/5) were irradiated for 3 min at 1, 6, 24 or 48 h after cell seeding (X-Cite 120 fluorescence illumination system, bandpass filter with center wavelength: 355 nm, full width half maximum: 53 nm, 3.5 mW cm^{-2}) to uncage the caged peptide at the prescribed time point. Cultures were fixed in 70% ethanol/37% formaldehyde/glacial acetic acid (20:2:1) and then blocked in 5% goat serum in DPBS for 1 h. Substrates were successively incubated in MF 20 anti-mouse sarcomeric myosin antibody (1:500 in 5% goat serum), and Alexa Fluor 488-conjugated goat anti-mouse IgG antibody (1:200 in 5% goat serum) for 1 h each. Cell nuclei were counterstained with DAPI (1 μg ml^{-1} in 5% goat serum) for 10 min, and samples were mounted on slides (Fluoromount G, Electron Microscopy Sciences, Hatfield, PA). Cultures were scored for differentiation as the percentage of cells stained positive for sarcomeric myosin determined as the number of sarcomeric myosin-positive cells divided by the total number of nuclei, and the percentage of multinucleated/fused cells determined as the number of sarcomeric myosin-positive cells having two or more nuclei divided by the total number of nuclei, using fluorescence microscopy and an in-house image-analysis routine.

2.5. Cell adhesion and immunofluorescence staining for focal adhesion components

C2C12 cells were seeded on SAMs modified with either cyclo[RGDfK], or cyclo[RGD(DMNPB)fK], or GRDGSPC (non-irradiated and irradiated) and cultured for 2.5 h at 37 °C in DMEM supplemented with 1% penicillin–streptomycin and 5% fetal bovine serum followed by immunostaining for F-actin and the focal adhesion component vinculin. Cultures were gently washed with ice-cold DPBS, followed by permeabilization in ice-cold cytoskeleton buffer (10 mM PIPES, 50 mM NaCl, 150 mM sucrose, 3 mM $MgCl_2 \cdot 6H_2O$, pH 6.8) and twice in ice-cold supplemented cytoskeleton buffer (10 mM PIPES, 50 mM NaCl, 150 mM sucrose, 3 mM $MgCl_2 \cdot 6H_2O$, 0.5% Triton X-100, 1 μg ml^{-1} leupeptin, 1 μg ml^{-1} aprotinin, 1 μg ml^{-1} pepstatin, 1 mM PMSF, pH 6.8) for 1 min each. Cells were then fixed in 3.7% formaldehyde in DPBS for 10 min. Surfaces were blocked in 5% goat serum in DPBS for 1 h, and sequentially incubated in anti-vinculin antibody (1:200 in 5% goat serum) for 1 h and combined Alexa Fluor 488-conjugated goat anti-mouse IgG antibody (1:200 in 5% goat serum) and Alexa Fluor 555-conjugated phalloidin (1:50 in 5% goat serum) for 1 h. Cell nuclei were counterstained with DAPI (1 mg ml^{-1} in 5% goat serum) for 10 min, and samples were mounted on slides (Fluoromount G). Samples were scored for the total number of cells per given area using fluorescence microscopy.

2.6. Proliferation assay and EdU incorporation

C2C12 cells were seeded on peptide-modified SAMs (tethering ratio cyclo[RGDfK]/cyclo[RGD(DMNPB)fK] = 1:5) and cultured for 3 days at 37 °C under differentiation conditions. Surfaces were irradiated for 3 min at 1, 6, 24 or 48 h after cell seeding to uncage the caged peptide at the prescribed time point. EdU (10 μM final concentration) was added to cultures 54 h post cell-seeding and incubated for 14 h at 37 °C. Cultures were gently washed with DPBS and fixed in 3.7% formaldehyde in DPBS for 15 min followed by permeabilization in 0.5% Triton X-100 for 20 min and washing with 3% BSA. Proliferated cells were stained with a Click-it® Alexa Fluor 488-conjugated EdU Imaging Kit (Invitrogen, Carlsbad, CA). Surfaces were incubated with Alexa Fluor 488-conjugated azide in Click-it® reaction buffer supplemented with $CuSO_4$ and reaction buffer additive for 30 min. After washing with 3% bovine serum albumin and DPBS cell nuclei were counterstained with Hoechst 33342 (5 μg ml^{-1} in DPBS) for 30 min. After washing, samples were mounted on slides (Fluoromount G). Cultures were scored by fluorescence microscopy for proliferation as the percentage of cells positive for EdU incorporation relative to the total number of cell nuclei using an in-house image-analysis routine.

2.7. Statistical analysis

Data represent characteristic results from a particular experimental run with at least three independent runs performed. Data are represented as mean ± standard error. Results were analyzed by Wilcoxon test using JMP Pro 9. A 95% confidence level was considered significant.

3. Results

SAMs of mixed alkanethiols on gold with oligo(ethylene glycol) groups (EG_6-COOH and EG_3) were used as model non-fouling surfaces presenting moieties for peptide tethering [31]. RGD peptides (cyclic and caged RGD) were tethered to the COOH groups of the SAM using EDC/NHS coupling chemistry [31]. The density of anchoring groups is an important parameter to optimize in order to balance between sufficient ligand densities for cells to attach while preventing non-specific protein adsorption and cell adhesion. Based on our previous results [31], a solution ratio of EG_6-COOH/EG_3 of 0.02 generates SAMs with functional surface densities of single adhesive ligands, while maintaining low background levels of non-specific adsorption. This ratio was also used in the present experiments.

3.1. Density of tethered RGD regulates myogenic differentiation

RGD-functionalized SAMs with different surface densities of the cell-adhesive ligand were prepared following the strategy of Petrie et al. [31] who controlled the tethered peptide densities by varying the coating concentrations of a linear RGD peptide [31] SAMs were incubated with solutions of cyclo[RGDfK] of different concentrations (0, 1, 5, 20, 50 and 72 μg ml^{-1}) to generate different tethered

densities. Pilot experiments demonstrated similar tethering behavior for the cyclic RGDfK and the linear RGD peptide (GRGDSPC). The effect of the density of c[RGDfK] on the extent of myogenic differentiation of C2C12 cells was evaluated by quantification of the percentage of cells stained positive for sarcomeric myosin after 3 days in culture. Because the available spreading area and the number of cell–cell contacts influence cell behavior [33], a seeding cell density of 5,000 cells cm^{-2} was chosen to minimize cell–cell interactions. The absence of adherent cells on non-modified and surfaces modified with 1 μg ml^{-1} cyclic RGD at 3 days after cell seeding indicates that there is a minimum RGD concentration required for cells to attach to the non-adhesive SAM. Cells spread on SAMs modified with higher RGD concentrations. On SAMs modified with RGD concentrations above 20 μg ml^{-1}, cells showed distinct markers of myogenesis, including expression of sarcomeric myosin and fusion into myotubes at 3 days in culture (Fig. 1A). Myogenic differentiation increased up to 80% with increasing concentrations of RGD and could be described by a hyperbolic profile (Fig. 1B). This result demonstrates that myogenic differentiation is regulated by the surface density of bioadhesive RGD ligand. The value obtained with 72 μg ml^{-1} (120 μM) was considered as a convenient ligand density to maximize the degree of differentiation for the engineered surfaces and was used for subsequent experiments. According to previous experiments with the linear RGD peptide [31], this coating concentration corresponds to a surface density of cyclic RGD of ~3.0 pmol cm^{-2}.

3.2. Light-controlled changes in RGD density using a photoactivatable caged RGD

SAMs were modified with the photoactivatable caged cyclic RGD peptide c[RGD(DMNPB)fK] (“caged RGD”) [24] to generate surfaces with phototunable densities of tethered cell adhesive peptide (Scheme 1B). Initially, control surfaces modified with a 72 μg ml^{-1} (120 μM) solution of either c[RGDfK], photoactivatable c[RGD(DMNPB)fK] or the negative control peptide GRDGSPC were prepared and incubated with cells for 2.5 h. A surface concentration of peptide of ~3.0 pmol cm^{-2} is expected under these coupling conditions [31]. SAMs modified with GRDGSPC and non-modified SAMs without tethered peptides did not show cell attachment, whereas RGD-modified SAMs showed effective cell spreading (Fig. 2). This result indicates that cell attachment to the RGD-modified SAMs is specific and mediated by integrin–RGD interactions. Few cells attached to SAMs modified with caged RGD that were not exposed to light. After light exposure, a 6-fold increase in cell density was observed. Comparable cell densities and cell spreading were obtained for irradiated caged cyclic RGD and cyclic RGD, demonstrating effective light-mediated restoration of the functionality of the caged RGD. No differences in cell density and spreading were observed between irradiated and non-irradiated cyclic RGD-modified substrates, demonstrating that the irradiation conditions did not cause photodamage of the surface layer to influence adhesion. In contrast to cells spreading on irradiated caged RGD, the few cells that attached to caged RGD were rounded but some showed an outstretched, polarized morphology. Nevertheless, these results show significant differences in the number and spreading of cells on irradiated caged RGD compared to control caged RGD.

The assembly and distribution of focal adhesions of adherent cells on modified SAMs were examined after staining for F-actin and the focal adhesion component vinculin (Fig. 2A). Cells on caged RGD showed poor organization of the cytoskeleton and diffuse distribution of vinculin, and thus no assembly of focal adhesions, which is consistent with the overall low number of adherent cells and poor spreading. Cells on surfaces modified with cyclic RGD (irradiated and non-irradiated) showed comparably high organization of F-actin stress fibers terminating at vinculin clusters at the cell edges, indicating distinct assembly and organization of focal adhesion complexes. Similar findings were observed for surfaces presenting irradiated caged RGD, which further demonstrates that irradiation of caged RGD provides restoration of functional bioadhesive RGD units to support integrin-mediated cell adhesion.

3.3. Temporal presentation of tethered RGD influences cell proliferation

We next determined whether an increase of the RGD surface density, i.e. adhesion promotion, at defined time points during cell culture modulates the proliferation of C2C12 myoblasts. For this purpose, SAMs were reacted with a 120 μM mixture of cyclic RGD and caged cyclic RGD in a 1:5 ratio. In this way, surfaces presenting a basal level of RGD and a light-tunable density of RGD were obtained. The density of basal cyclic RGD to obtain sufficient cell-adhesive surface properties is required to ensure initial cell adhesion. The optimum basal density was investigated in pilot experiments during which cells were cultured on surfaces presenting various ratios of cyclic RGD and caged cyclic RGD under differentiation conditions (data not shown). The optimum basal density was selected to allow sufficient cell adhesion levels for cells to attach, remain adherent and spread throughout the entire culture time in order to examine the effects of temporal RGD presentation in cell functions (e.g. proliferation, differentiation) rather than simply controlling gross levels of number of adherent cells. C2C12 cells were seeded on mixed RGD-modified SAMs and cultured under differentiation conditions. At selected time points after cell seeding

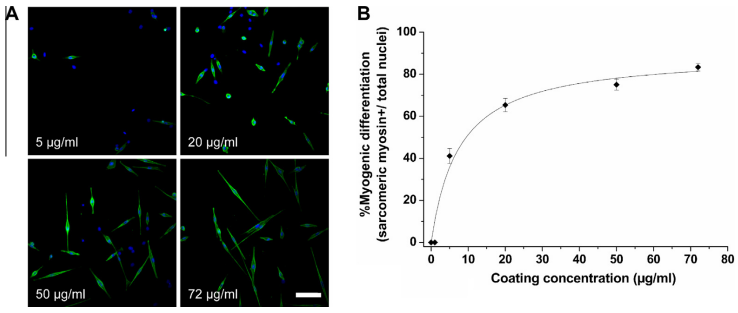

Fig. 1. (A) Fluorescence images of myoblasts on modified SAMs showing sarcomeric myosin (green) and nuclei (blue) (bar 100 μm). (B) Myogenic differentiation of myoblasts as a function of the coating concentration of cyclo[RGDfK] tethered to 2% EG6-COOH:EG3-OH SAM surfaces (hyberbolic curve fit, $R^2 = 0.98$).

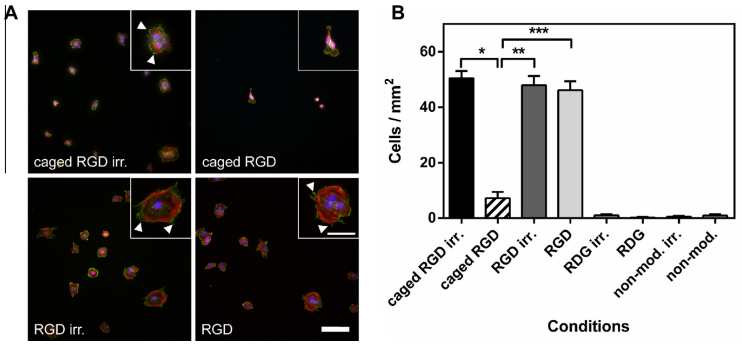

Fig. 2. Ligand tethering and irradiation of 2% EG6-COOH:EG3-OH SAM surfaces affects the extent of cell adhesion of C2C12 myoblasts. (A) Fluorescence images of myoblasts on modified SAMs showing actin (red), vinculin (green) and nuclei (blue) (bar 100 μm, 50 μm in inset images). (B) Cultures were incubated for 2.5 h and analyzed for cell density by immunostaining. Wilcoxon test revealed surface-dependent differences: *caged RGD irr. vs. caged RGD ($P < 0.0001$); **caged RGD vs. RGD irr. ($P < 0.0001$); ***caged RGD vs. RGD ($P < 0.0001$).

(1, 6, 24 and 48 h), substrates were irradiated in order to increase the surface density of RGD from initially ~17% to the maximum available surface density (referred to as 100%). The proliferation rate of the cells after 3 days culture on the different substrates and corresponding controls was quantified by EdU incorporation and staining (Fig. 3A). EdU is an analogue of thymidine used to determine cell proliferation, as it is incorporated into DNA during the synthesis phase of the cell cycle and can easily be visualized via immunostaining. After 1 day in culture, cells became round on the non-modified SAMs (no RGD), while they remained well spread on different RGD-modified surfaces. Higher levels of proliferation were observed for cells cultured on surfaces that presented the maximum level of active RGD at early stages of cell culture (i.e. irradiation after 1 or 6 h) (Fig. 3B). Lower levels of cell proliferation were found for surfaces presenting the basal level of cyclic RGD throughout the whole culture time (DARK substrates). Similarly, low proliferation levels were observed for cells cultured on low densities of RGD until 24 and 48 h after cell seeding. These results demonstrate a significant impact of the density and the time scale of the availability of the cell-adhesive ligand at the surface on the proliferation of C2C12 myoblasts.

3.4. Temporal RGD presentation regulates the extent of myogenic differentiation

We next evaluated the impact of temporal RGD presentation on myogenic differentiation by evaluating the expression of sarcomeric myosin and fusion into myotubes. Cells were cultured on

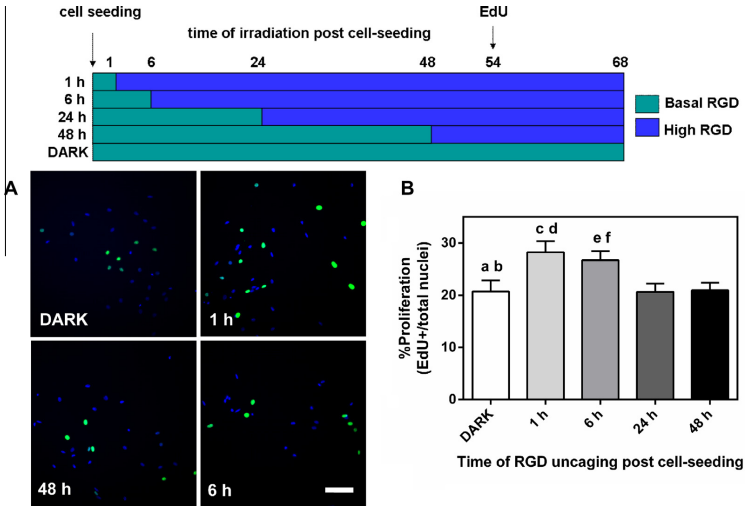

Fig. 3. Presentation of uncaged cell-adhesive RGD peptide at different time points modulates proliferation after 3 days in culture. (A) Fluorescence images showing nuclei with incorporated EdU (green) and all nuclei (blue) of myoblasts on modified SAMs (bar 100 μm). (B) Cells were incubated in EdU for 14 h and analyzed for EdU incorporation by immunostaining. Statistical significance: a vs. 1 h ($P < 0.013$); b vs. 6 h ($P < 0.021$); c vs. 24 h ($P < 0.019$); d vs. 48 h ($P < 0.015$); e vs. 24 h ($P < 0.027$); f vs. 48 h ($P < 0.011$), as determined using the Wilcoxon test.

surfaces under the same conditions described in the proliferation assay. At day 3 cells were immunostained for sarcomeric myosin. Fig. 4A shows representative microscopy images for myogenic differentiation (sarcomeric myosin-positive cells, green) and cell nuclei (blue) as a function of temporal presentation of high levels of RGD ligand. Quantification of the percentage of sarcomeric myosin-positive cells is shown in Fig. 4B. Myogenic differentiation was low on surfaces with only basal levels of RGD throughout the entire duration of culture (DARK). Surfaces irradiated at late time points of culture (24, 48 h) also demonstrated low levels of differentiation, reaching a minimum for 48 h, which showed similar differentiation levels as the DARK substrates. Differentiation significantly increased on substrates with high levels of active RGD presented at 1 and 6 h after cell seeding, with 74% differentiated cells on substrates irradiated at 6 h after cell seeding. As a second marker for myogenic differentiation, cell fusion into myotubes was characterized by scoring cell nuclei for multinucleated (fused, two or more nuclei) and mononucleated (non-fused) sarcomeric myosin-positive cells (Fig. 5). The results for cell fusion follow the same trend as sarcomeric myosin expression with a significantly stronger impact of the time points of ligand density increase on the fusion of cells. This demonstrates the necessity of a sufficient density of bioadhesive ligand in early stages of cell culture for cells to differentiate and fuse into myotubes. This data indicates that the RGD density and the time point of RGD presentation influence myogenic differentiation in terms of expression of sarcomeric myosin and cell fusion to myotubes. These results indicate an important role for integrin-mediated cell adhesion at early stages of cell attachment on the cell's differentiation potential.

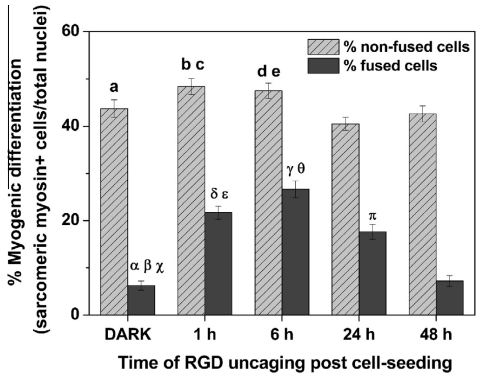

Fig. 5. Myogenic differentiation of myoblasts depending on time point of peptide presentation as determined by the percentage of multinucleated and mononucleated sarcomeric myosin-positive cells after 3 days in culture. Statistical significance of myogenic differentiation (non-fused cells): a vs. 6 h ($P < 0.021$); b vs. 24 h ($P < 0.0006$); c vs. 48 h ($P < 0.05$); d vs. 24 h ($P < 0.0003$); e vs. 48 h ($P < 0.005$). Statistical significance of myogenic differentiation (fused cells): α vs. 1 h ($P < 0.0001$); β vs. 6 h ($P < 0.0001$); χ vs. 24 h ($P < 0.0001$); δ vs. 6 h ($P < 0.035$); ε vs. 48 h ($P < 0.0001$), γ vs. 24 h ($P < 0.0006$); θ vs. 48 h ($P < 0.0001$); π vs. 48 h ($P < 0.0001$), as determined using the Wilcoxon test.

4. Discussion

Gaining a better fundamental understanding of cell–surface interactions and hence substrate-controlled cell behavior is a critical prerequisite to improving designs of biomaterials for biotechnological applications and biomedical devices. Although modifications of biomedical surfaces with biologically active factors have improved cell–surface interactions, previous studies lack insights into the influence of the temporal control over bioactive ligand presentation on cell adhesion and modulation of cell function as desired in the integration process of implants. The application of a photoactivatable bioadhesive derivative (caged cyclic

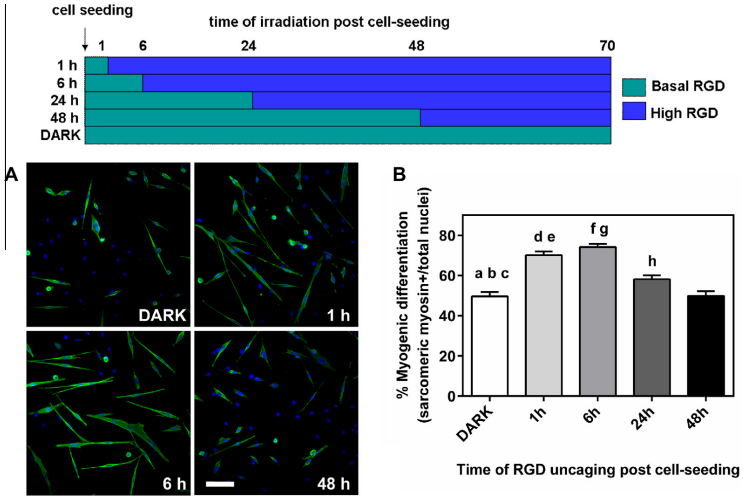

Fig. 4. Temporal activation and resulting RGD density-dependent differences in myogenic differentiation after 3 days. (A) Fluorescence images showing sarcomeric myosin-positive cells (green) and cell nuclei (blue) on modified SAMs (bar 100 μm). (B) Myogenic differentiation of myoblasts depending on time point of peptide presentation as determined by the percentage of sarcomeric myosin-positive cells after 3 days in culture. Statistical significance of myogenic differentiation: a vs. 1 h ($P < 0.0001$); b vs. 6 h ($P < 0.0001$); c vs. 24 h ($P < 0.003$); d vs. 24 h ($P < 0.0001$); e vs. 48 h ($P < 0.0001$); f vs. 24 h ($P < 0.0001$), g vs. 48 h ($P < 0.001$); h vs. 48 h ($P < 0.005$), as determined using the Wilcoxon test.

RGD) allows precise light-triggered control of the density and the time point of ligand presentation on surfaces, and thus modulation of integrin-mediated cell–surface interactions. In this work, we engineered biointerfaces with coexisting active and temporarily inactivated concentrations of cyclic RGD. These substrates allow in situ modulation of surface-tethered RGD concentration via a one-step light exposure. This strategy allowed us to evaluate the response of myoblasts to a temporally defined increase in RGD density at the surface. In particular, the impact of RGD exposure to the attachment, proliferation and differentiation of myoblasts was studied.

We applied two strategies to change the concentration of cyclic RGD at the surface. The total surface RGD density was defined by the RGD solution concentration during the tethering reaction, as has been previously reported for linear RGD peptide [31]. The time-regulated RGD surface density was achieved by surface co-modification with the non-adhesive caged cyclic RGD. Light exposure at cell-compatible UV doses uncages the RGD and activates its biological activity [24]. Non-cell adhesive caged RGD surfaces become cell adhesive after irradiation. Similar cell densities and cell spreading were obtained for uncaged RGD and cyclic RGD, indicating that the caging group effectively inhibits RGD–integrin interactions, while the uncaging reaction successfully restores bioactivity. Amongst available strategies for modulated RGD exposure, caged RGD has been demonstrated to enable precise spatial control of cell adhesion (i.e. cell patterns) and direct control of the RGD–integrin molecular interaction [25]. In this work, we further demonstrate the flexibility of this approach and its applicability to study time- and concentration-dependent RGD–integrin interactions and their effects on cell behavior.

Our results demonstrate that changes in the temporal presentation and concentration of surface-tethered RGD modulate cell behavior beyond cell attachment and spreading. Myogenic differentiation of C2C12 cells has been used in previous studies to evaluate the influence of surface properties on cell behavior [34–37]. We observed a clear increase in myogenic differentiation of C2C12 cells with increasing densities of surface-tethered RGD. This result demonstrates a strong correlation between integrin-mediated cell adhesion and myogenic differentiation, in agreement with studies using surface-tethered linear RGD [22]. Moreover, both proliferation and myogenic differentiation were promoted when a high density of RGD was available at the surface at early stages of cell attachment (<6 h incubation). Proliferation levels showed a similar trend as myogenic differentiation in relation to timed ligand presentation. These findings are in contrast to reported molecular mechanisms controlling myogenic differentiation of this cell type, which suggest a down-regulation of proliferation (cell cycle withdrawal) during myogenesis [37,38]. Taken together, our results demonstrate an integrin-mediated mechanism for the regulation of C2C12 proliferation and myogenic differentiation by using biointerfaces which allow a timed onset of integrin-binding using a photoactivatable cell-adhesive RGD peptide.

5. Conclusions

SAMs of alkanethiols and tethered cyclic RGD and caged cyclic RGD were used to present defined densities of RGD in a temporally controlled manner to cell cultures after light exposure. Attachment, spreading and myogenic differentiation of C2C12 myoblasts strongly depended on the density and timed presentation of cyclic RGD available to the cells at the surface. Proliferation and myogenesis were further regulated by the time point at which RGD was presented to the cell, reaching highest levels when RGD exposure occurred $\leq$6 h after cell seeding. Beyond basic studies of interactions between cells and RGD-modified supports, this work provides new insights into the influence of a kinetic profile of ligand presentation and identifies a possible strategy applicable to improve the in vivo performance of biomedical devices in terms of time-controlled cell–surface interactions.

Acknowledgements

The authors thank M. Wirkner and T.A. Petrie for assistance with pilot experiments on peptide modified SAMs. The authors thank the Materials World Network (DFG AOBJ 569628, NSF DMR-0909002) for financial support. S.W. thanks the Max-Planck-Graduate Center for financial support.

Appendix A. Figures with essential colour discrimination

Certain figures in this article, particularly Figs. 1–4, are difficult to interpret in black and white. The full colour images can be found in the on-line version, at doi:http://dx.doi.org/10.1016/j.actbio.2013.06.019.

References

[1] Kim J, Hayward RC. Mimicking dynamic in vivo environments with stimuli-responsive materials for cell culture. Trends Biotechnol 2012;30:426–39.
[2] Kshitiz, Kim DH, Beebe DJ, Levchenko A. Micro- and nanoengineering for stem cell biology: the promise with a caution. Trends Biotechnol 2011;29:399–408.
[3] Seliktar D. Designing cell-compatible hydrogels for biomedical applications. Science 2012;336:1124–8.
[4] Stuart MAC, Huck WTS, Genzer J, Muller M, Ober C, Stamm M, et al. Emerging applications of stimuli-responsive polymer materials. Nat Mater 2010;9:101–13.
[5] Sun YB, Chen CS, Fu JP. Forcing stem cells to behave: a biophysical perspective of the cellular microenvironment. Annu Rev Biophys 2012;41:519–42.
[6] Kloxin AM, Kasko AM, Salinas CN, Anseth KS. Photodegradable hydrogels for dynamic tuning of physical and chemical properties. Science 2009;324:59–63.
[7] Silva EA, Mooney DJ. Effects of VEGF temporal and spatial presentation on angiogenesis. Biomaterials 2010;31:1235–41.
[8] García AJ. Get a grip: integrins in cell–biomaterial interactions. Biomaterials 2005;26:7525–9.
[9] Johansson S, Svineng G, Wennerberg K, Armulik A, Lohikangas L. Fibronectin–integrin interactions. Front Biosci (online) 1997;2:D126–46.
[10] Danen EHJ, Sonnenberg A. Erratum: integrins in regulation of tissue development and function. J Pathol 2003;201:632–41.
[11] Giancotti FG, Ruoslahti E. Integrin signaling. Science 1999;285:1028–32.
[12] Wade RJ, Burdick JA. Engineering ECM signals into biomaterials. Mater Today 2012;15:454–9.
[13] Robertus J, Browne WR, Feringa BL. Dynamic control over cell adhesive properties using molecular-based surface engineering strategies. Chem Soc Rev 2010;39:354–78.
[14] De Arcangelis A, Georges-Labouesse E. Integrin and ECM functions: roles in vertebrate development. Trends Genet 2000;16:389–95.
[15] Hersel U, Dahmen C, Kessler H. RGD modified polymers: biomaterials for stimulated cell adhesion and beyond. Biomaterials 2003;24:4385–415.
[16] Raynor JE, Petrie TA, Garcia AJ, Collard DM. Controlling cell adhesion to titanium: functionalization of poly[oligo(ethylene glycol)methacrylate] brushes with cell-adhesive peptides. Adv Mater 2007;19:1724–8.
[17] Kustra S, Bettinger CJ. Smart polymers and interfaces for dynamic cell-biomaterials interactions. MRS Bull 2012;37:836–46.
[18] Eisenberg JL, Piper JL, Mrksich M. Using self-assembled monolayers to model cell adhesion to the 9th and 10th type III domains of fibronectin. Langmuir 2009;25:13942–51.
[19] Altrock E, Muth CA, Klein G, Spatz JP, Lee-Thedieck C. The significance of integrin ligand nanopatterning on lipid raft clustering in hematopoietic stem cells. Biomaterials 2012;33:3107–18.
[20] Guarnieri D, De Capua A, Ventre M, Borzacchiello A, Pedone C, Marasco D, et al. Covalent immobilized RGD gradient on PEG hydrogel scaffold influences cell migration parameters. Acta Biomater 2010;6:2532–9.
[21] Wohlrab S, Mueller S, Schmidt A, Neubauer S, Kessler H, Leal-Egana A, et al. Cell adhesion and proliferation on RGD-modified recombinant spider silk proteins. Biomaterials 2012;33:6650–9.
[22] Rowley JA, Mooney DJ. Alginate type and RGD density control myoblast phenotype. J Biomed Mater Res 2002;60:217–23.
[23] Kilian KA, Mrksich M. Directing stem cell fate by controlling the affinity and density of ligand–receptor interactions at the biomaterials interface. Angew Chem Int Ed 2012;51:4891–5.
[24] Wirkner M, Weis S, Álvarez V, Álvarez S, Gropeanu RA, Salierno M, et al. Photoactivatable caged cyclic RGD peptide for triggering integrin binding and cell adhesion to surfaces. ChemBioChem 2011;12:2623–9.

[25] Petersen S, Alonso JM, Specht A, Duodu P, Goeldner M, del Campo A. Phototriggering of cell adhesion by caged cyclic RGD peptides13. Angew Chem Int Ed 2008;47:3192–5.
[26] Goubko CA, Basak A, Majumdar S, Jarrell H, Huan Khieu N, Cao X. Comparative analysis of photocaged RGDS peptides for cell patterning. J Biomed Mater Res A 2013;101A:787–96.
[27] Goubko C, Majumdar S, Basak A, Cao X. Hydrogel cell patterning incorporating photocaged RGDS peptides. Biomed Microdevices 2010;12:555–68.
[28] Ohmuro-Matsuyama Y, Tatsu Y. Photocontrolled cell adhesion on a surface functionalized with a caged arginine-glycine-aspartate peptide. Angew Chem Int Ed 2008;47:7527–9.
[29] Salierno M, Garcia AJ, Del Campo A. Photo-activatable surfaces for cell migration assays. Adv Funct Mater, http://dx.doi.org/10.1002/adfm.201300902.
[30] Wirkner M, Alonso JM, Maus V, Salierno M, Lee TT, García AJ, et al. Triggered cell release from materials using bioadhesive photocleavable linkers. Adv Mater 2011;23:3907–10.
[31] Petrie TA, Capadona JR, Reyes CD, García AJ. Integrin specificity and enhanced cellular activities associated with surfaces presenting a recombinant fibronectin fragment compared to RGD supports. Biomaterials 2006;27:5459–70.
[32] Capadona JR, Collard DM, García AJ. Fibronectin adsorption and cell adhesion to mixed monolayers of tri(ethylene glycol)- and methyl-terminated alkanethiols. Langmuir 2002;19:1847–52.
[33] Tanaka K, Sato K, Yoshida T, Fukuda T, Hanamura K, Kojima N, et al. Evidence for cell density affecting C2C12 myogenesis: possible regulation of myogenesis by cell–cell communication. Muscle Nerve 2011;44:968–77.
[34] Charest JL, García AJ, King WP. Myoblast alignment and differentiation on cell culture substrates with microscale topography and model chemistries. Biomaterials 2007;28:2202–10.
[35] Garcia AJ, Vega MaD, Boettiger D. Modulation of cell proliferation and differentiation through substrate-dependent changes in fibronectin conformation. Mol Biol Cell 1999;10:785–98.
[36] Lan MA, Gersbach CA, Michael KE, Keselowsky BG, García AJ. Myoblast proliferation and differentiation on fibronectin-coated self assembled monolayers presenting different surface chemistries. Biomaterials 2005;26:4523–31.
[37] Sabourin LA, Rudnicki MA. The molecular regulation of myogenesis. Clin Genet 2000;57:16–25.
[38] Andrés V, Walsh K. Myogenin expression, cell cycle withdrawal, and phenotypic differentiation are temporally separable events that precede cell fusion upon myogenesis. J Cell Biol 1996;132:657–66.

REFERENCES

1. Alberts, B., *Molecular biology of the cell*. 2008: Garland Science.

2. Reichardt, L.F., T. Kreis, and R. Vale, *Introduction: Extracellular matrix molecules*, in *Guidebook to the Extracellular Matrix, Anchor, and Adhesion Proteins*. 1999, Oxford University Press: New York, NY. p. 335-344.

3. Berg, J.M., J.L. Tymoczko, and L. Stryer, *Biochemistry*. 2007: W. H. Freeman.

4. Andrade, J., et al., *Proteins at interfaces: principles, multivariate aspects, protein resistant surfaces, and direct imaging and manipulation of adsorbed proteins.* Clinical materials, 1992. **11**(1-4): p. 67-84.

5. Horbett, T.A. and J.L. Brash. *Proteins at interfaces: current issues and future prospects*. 1987. ACS Publications.

6. Hynes, R.O., *Integrins:: Bidirectional, Allosteric Signaling Machines.* Cell, 2002. **110**(6): p. 673-687.

7. Garcia, A.J., *Get a grip: integrins in cell-biomaterial interactions.* Biomaterials, 2005. **26**(36): p. 7525-9.

8. De Arcangelis, A. and E. Georges-Labouesse, *Integrin and ECM functions: roles in vertebrate development.* Trends Genet, 2000. **16**(9): p. 389-95.

9. Danen, E.H. and A. Sonnenberg, *Integrins in regulation of tissue development and function.* J Pathol, 2003. **201**(4): p. 632-41.

10. George, E.L., et al., *Defects in mesoderm, neural tube and vascular development in mouse embryos lacking fibronectin.* Development, 1993. **119**(4): p. 1079-91.

11. Stephens, L.E., et al., *Deletion of beta 1 integrins in mice results in inner cell mass failure and peri-implantation lethality.* Genes Dev, 1995. **9**(15): p. 1883-95.

12. Furuta, Y., et al., *Mesodermal defect in late phase of gastrulation by a targeted mutation of focal adhesion kinase, FAK.* Oncogene, 1995. **11**(10): p. 1989-95.

13. Xu, W., H. Baribault, and E.D. Adamson, *Vinculin knockout results in heart and brain defects during embryonic development.* Development, 1998. **125**(2): p. 327-37.

14. Wehrle-Haller, B. and B.A. Imhof, *Integrin-dependent pathologies.* J Pathol, 2003. **200**(4): p. 481-7.

15. Jin, H. and J. Varner, *Integrins: roles in cancer development and as treatment targets.* Br.J Cancer, 2004. **90**(3): p. 561-565.

16. Chen, C.S., *Mechanotransduction–a field pulling together?* Journal of Cell Science, 2008. **121**(20): p. 3285.

17. Wozniak, M.A., et al., *ROCK-generated contractility regulates breast epithelial cell differentiation in response to the physical properties of a three-dimensional collagen matrix.* Journal of Cell Biology, 2003. **163**(3): p. 583-95.

18. McBeath, R., et al., *Cell shape, cytoskeletal tension, and RhoA regulate stem cell lineage commitment.* Dev Cell, 2004. **6**(4): p. 483-95.

19. Mammoto, A., et al., *Role of RhoA, mDia, and ROCK in cell shape-dependent control of the Skp2-p27kip1 pathway and the G1/S transition.* Journal of Biological Chemistry, 2004. **279**(25): p. 26323-30.

20. Polte, T.R., et al., *Extracellular matrix controls myosin light chain phosphorylation and cell contractility through modulation of cell shape and cytoskeletal prestress.* Am J Physiol Cell Physiol, 2004. **286**(3): p. C518-28.

21. Engler, A.J., et al., *Myotubes differentiate optimally on substrates with tissue-like stiffness: pathological implications for soft or stiff microenvironments.* Journal of Cell Biology, 2004. **166**(6): p. 877-87.

22. Paszek, M.J., et al., *Tensional homeostasis and the malignant phenotype.* Cancer Cell, 2005. **8**(3): p. 241-54.

23. Hynes, R.O., *Integrins: Bidirectional, allosteric signaling machines.* Cell, 2002. **110**(6): p. 673-687.

24. Faull, R.J., et al., *Affinity modulation of integrin alpha 5 beta 1: regulation of the functional response by soluble fibronectin.* Journal of Cell Biology, 1993. **121**(1): p. 155-62.

25. Choquet, D., D.P. Felsenfeld, and M.P. Sheetz, *Extracellular matrix rigidity causes strengthening of integrin-cytoskeleton linkages.* Cell, 1997. **88**(1): p. 39-48.

26. Garcia, A.J., F. Huber, and D. Boettiger, *Force required to break alpha5beta1 integrin-fibronectin bonds in intact adherent cells is sensitive to integrin activation state.* Journal of Biological Chemistry, 1998. **273**(18): p. 10988-93.

27. Ginsberg, M.H., A. Partridge, and S.J. Shattil, *Integrin regulation.* Current Opinion in Cell Biology, 2005. **17**(5): p. 509-516.

28. Geiger, B. and A. Bershadsky, *Assembly and mechanosensory function of focal contacts.* Current Opinion in Cell Biology, 2001. **13**(5): p. 584-592.

29. Gupton, S.L. and C.M. Waterman-Storer, *Spatiotemporal feedback between actomyosin and focal-adhesion systems optimizes rapid cell migration.* Cell, 2006. **125**(7): p. 1361-1374.

30. Ridley, A.J., et al., *Cell migration: Integrating signals from front to back.* Science, 2003. **302**(5651): p. 1704-1709.

31. Ridley, A.J. and A. Hall, *The Small Gtp-Binding Protein Rho Regulates the Assembly of Focal Adhesions and Actin Stress Fibers in Response to Growth-Factors.* Cell, 1992. **70**(3): p. 389-399.

32. Greenwood, J.A., et al., *Restructuring of focal adhesion plaques by PI 3-kinase: Regulation by PtdIns (3,4,5)-P-3 binding to alpha-actinin.* Journal of Cell Biology, 2000. **150**(3): p. 627-641.

33. Riveline, D., et al., *Focal contacts as mechanosensors: Externally applied local mechanical force induces growth of focal contacts by an mDia1-dependent and ROCK-independent mechanism.* Journal of Cell Biology, 2001. **153**(6): p. 1175-1185.

34. Amano, M., et al., *Formation of actin stress fibers and focal adhesions enhanced by Rho-kinase.* Science, 1997. **275**(5304): p. 1308-1311.

35. Kimura, K., et al., *Regulation of myosin phosphatase by Rho and Rho-associated kinase (Rho-kinase).* Science, 1996. **273**(5272): p. 245-248.

36. Chrzanowska-Wodnicka, M. and K. Burridge, *Rho-stimulated contractility drives the formation of stress fibers and focal adhesions.* Journal of Cell Biology, 1996. **133**(6): p. 1403-15.

37. Amano, M., et al., *Myosin II activation promotes neurite retraction during the action of Rho and Rho-kinase.* Genes Cells, 1998. **3**(3): p. 177-88.

38. Munevar, S., Y.L. Wang, and M. Dembo, *Distinct roles of frontal and rear cell-substrate adhesions in fibroblast migration.* Molecular Biology of the Cell, 2001. **12**(12): p. 3947-54.

39. Palecek, S.P., et al., *Integrin-ligand binding properties govern cell migration speed through cell-substratum adhesiveness.* Nature, 1997. **385**(6616): p. 537-40.

40. de Rooij, J., et al., *Integrin-dependent actomyosin contraction regulates epithelial cell scattering.* Journal of Cell Biology, 2005. **171**(1): p. 153-64.

41. Lotz, M.M., et al., *Cell adhesion to fibronectin and tenascin: quantitative measurements of initial binding and subsequent strengthening response.* Journal of Cell Biology, 1989. **109**(4 Pt 1): p. 1795-805.

42. LaFlamme, S.E., S.K. Akiyama, and K.M. Yamada, *Regulation of fibronectin receptor distribution.* Journal of Cell Biology, 1992. **117**(2): p. 437-47.

43. Miyamoto, S., S.K. Akiyama, and K.M. Yamada, *Synergistic roles for receptor occupancy and aggregation in integrin transmembrane function.* Science, 1995. **267**(5199): p. 883-5.

44. Miyamoto, S., et al., *Integrin function: molecular hierarchies of cytoskeletal and signaling molecules.* Journal of Cell Biology, 1995. **131**(3): p. 791-805.

45. Broberg, M., C. Eriksson, and H. Nygren, *GpIIb/IIIa is the main receptor for initial platelet adhesion to glass and titanium surfaces in contact with whole blood* 1.* Journal of Laboratory and Clinical Medicine, 2002. **139**(3): p. 163-172.

46. Gorbet, M.B. and M.V. Sefton, *Material-induced tissue factor expression but not CD11b upregulation depends on the presence of platelets.* Journal of biomedical materials research. Part A, 2003. **67**(3): p. 792-800.

47. Tang, L., et al., *Molecular determinants of acute inflammatory responses to biomaterials.* Journal of Clinical Investigation, 1996. **97**(5): p. 1329.

48. Flick, M.J., et al., *Leukocyte engagement of fibrin (ogen) via the integrin receptor alpha~ Mbeta~ 2/Mac-1 is critical for host inflammatory response in vivo.* Journal of Clinical Investigation, 2004. **113**(11): p. 1596-1606.

49. Hu, W.J., et al., *Molecular basis of biomaterial-mediated foreign body reactions.* Blood, 2001. **98**(4): p. 1231-1238.

50. Tang, L. and J.W. Eaton, *Fibrin (ogen) mediates acute inflammatory responses to biomaterials.* The Journal of experimental medicine, 1993. **178**(6): p. 2147.

51. Howlett, C.R., et al., *Mechanism of initial attachment of cells derived from human bone to commonly used prosthetic materials during cell culture.* Biomaterials, 1994. **15**(3): p. 213-222.

52. MERRILL, E.W., *Poly (ethylene oxide) and blood contact*. 1992: Plenum Press, New York.

53. Hoffman, A.S., *Non-fouling surface technologies.* Journal of biomaterials science. Polymer edition, 1999. **10**(10): p. 1011.

54. Prime, K.L. and G.M. Whitesides, *Self-assembled organic monolayers: model systems for studying adsorption of proteins at surfaces.* Science (New York, NY), 1991. **252**(5010): p. 1164.

55. Prime, K.L. and G.M. Whitesides, *Adsorption of proteins onto surfaces containing end-attached oligo (ethylene oxide): a model system using self-assembled monolayers.* Journal of the American Chemical Society, 1993. **115**(23): p. 10714-10721.

56. Mrksich, M., G.B. Sigal, and G.M. Whitesides, *Surface plasmon resonance permits in situ measurement of protein adsorption on self-assembled monolayers of alkanethiolates on gold.* Langmuir, 1995. **11**(11): p. 4383-4385.

57. Mrksich, M., *A surface chemistry approach to studying cell adhesion.* Chemical Society Reviews, 2000. **29**(4): p. 267-273.

58. Houseman, B.T. and M. Mrksich, *Efficient solid-phase synthesis of peptide-substituted alkanethiols for the preparation of substrates that support the adhesion of cells.* J.Org.Chem., 1998. **63**: p. 7552-7555.

59. Flynn, N.T., et al., *Long-term stability of self-assembled monolayers in biological media.* Langmuir, 2003. **19**(26): p. 10909-10915.

60. Nelson, C.M., et al., *Degradation of micropatterned surfaces by cell-dependent and-independent processes.* Langmuir, 2003. **19**(5): p. 1493-1499.

61. Mrksich, M., et al., *Using microcontact printing to pattern the attachment of mammalian cells to self-assembled monolayers of alkanethiolates on transparent films of gold and silver.* Experimental Cell Research, 1997. **235**(2): p. 305-313.

62. Yang, Y., et al., *Electrical switching and bistability in organic/polymeric thin films and memory devices.* Advanced Functional Materials, 2006. **16**(8): p. 1001-1014.

63. Fan, X., et al., *Biomimetic anchor for surface-initiated polymerization from metal substrates.* Journal of the American Chemical Society, 2005. **127**(45): p. 15843-15847.

64. Petrie, T.A., et al., *The effect of integrin-specific bioactive coatings on tissue healing and implant osseointegration.* Biomaterials, 2008. **29**(19): p. 2849-57.

65. Raynor, J.E., et al. *Polymer brushes and self-assembled monolayers: Versatile platforms to control cell adhesion to biomaterials (Review)*. 2009. AVS.

66. Lutolf, M. and J. Hubbell, *Synthetic biomaterials as instructive extracellular microenvironments for morphogenesis in tissue engineering.* Nature biotechnology, 2005. **23**(1): p. 47-55.

67. Ruoslahti, E. and M.D. Pierschbacher, *New perspectives in cell adhesion: RGD and integrins.* Science, 1987. **238**: p. 491-497.

68. Graf, J., et al., *A pentapeptide from the laminin B1 chain mediates cell adhesion and binds the 67,000 laminin receptor.* Biochemistry, 1987. **26**(22): p. 6896-6900.

69. Hubbell, J.A., *Bioactive biomaterials.* Curr Opin Biotechnol, 1999. **10**(2): p. 123-129.

70. Hubbell, J.A., *Materials as morphogenetic guides in tissue engineering.* Curr.Opin.Biotechnol, 2003. **14**(5): p. 551-558.

71. Shakesheff, K., S. Cannizzaro, and R. Langer, *Creating biomimetic micro-environments with synthetic polymer-peptide hybrid molecules.* J Biomater Sci Polym Ed, 1998. **9**(5): p. 507-518.

72. Hersel, U., C. Dahmen, and H. Kessler, *RGD modified polymers: biomaterials for stimulated cell adhesion and beyond.* Biomaterials, 2003. **24**(24): p. 4385-4415.

73. Massia, S.P. and J.A. Hubbell, *An RGD spacing of 440 nm is sufficient for integrin alpha v beta 3-mediated fibroblast spreading and 140 nm for focal contact and stress fiber formation.* Journal of Cell Biology, 1991. **114**: p. 1089-1100.

74. Maheshwari, G., et al., *Cell adhesion and motility depend on nanoscale RGD clustering.* J Cell Sci, 2000. **113 (Pt 10)**: p. 1677-86.

75. Shin, H., S. Jo, and A.G. Mikos, *Modulation of marrow stromal osteoblast adhesion on biomimetic oligo[poly(ethylene glycol) fumarate] hydrogels modified with Arg-Gly-Asp peptides and a poly(ethyleneglycol) spacer.* J Biomed Mater Res, 2002. **61**(2): p. 169-179.

76. Sagnella, S.M., et al., *Human microvascular endothelial cell growth and migration on biomimetic surfactant polymers.* Biomaterials, 2004. **25**(7-8): p. 1249-1259.

77. Schense, J.C. and J.A. Hubbell, *Three-dimensional migration of neurites is mediated by adhesion site density and affinity.* J Biol Chem, 2000. **275**(10): p. 6813-6818.

78. Silva, G.A., et al., *Selective differentiation of neural progenitor cells by high-epitope density nanofibers.* Science, 2004. **303**(5662): p. 1352-1355.

79. Mann, B.K. and J.L. West, *Cell adhesion peptides alter smooth muscle cell adhesion, proliferation, migration, and matrix protein synthesis on modified surfaces and in polymer scaffolds.* J Biomed Mater Res, 2002. **60**(1): p. 86-93.

80. Petrie, T.A., et al., *Integrin specificity and enhanced cellular activities associated with surfaces presenting a recombinant fibronectin fragment compared to RGD supports.* Biomaterials, 2006. **27**(31): p. 5459-5470.

81. Rowley, J.A. and D.J. Mooney, *Alginate type and RGD density control myoblast phenotype.* J Biomed Mater Res, 2002. **60**(2): p. 217-223.

82. Rezania, A. and K.E. Healy, *The effect of peptide surface density on mineralization of a matrix deposited by osteogenic cells.* J Biomed Mater Res, 2000. **52**(4): p. 595-600.

83. Alsberg, E., et al., *Engineering growing tissues.* Proc.Natl.Acad.Sci.U.S.A, 2002. **99**(19): p. 12025-12030.

84. Schense, J.C., et al., *Enzymatic incorporation of bioactive peptides into fibrin matrices enhances neurite extension.* Nat.Biotechnol, 2000. **18**(4): p. 415-419.

85. Yu, X. and R.V. Bellamkonda, *Tissue-engineered scaffolds are effective alternatives to autografts for bridging peripheral nerve gaps.* Tissue Eng, 2003. **9**(3): p. 421-430.

86. Li, F., et al., *Cellular and nerve regeneration within a biosynthetic extracellular matrix for corneal transplantation.* Proc.Natl.Acad.Sci.U.S.A, 2003. **100**(26): p. 15346-15351.

87. Cutler, S.M. and A.J. Garc¡a, *Engineering cell adhesive surfaces that direct integrin alpha5beta1 binding using a recombinant fragment of fibronectin.* Biomaterials, 2003. **24**(10): p. 1759-1770.

88. Nomizu, M., et al., *Identification of cell binding sites in the laminin 1 chain carboxyl-terminal globular domain by systematic screening of synthetic peptides.* Journal of Biological Chemistry, 1995. **270**(35): p. 20583.

89. Humphries, J.D., et al., *Molecular basis of ligand recognition by integrin alpha5beta 1. II. Specificity of arg-gly-Asp binding is determined by Trp157 OF THE alpha subunit.* J Biol Chem, 2000. **275**(27): p. 20337-20345.

90. Kao, W.J., et al., *Fibronectin modulates macrophage adhesion and FBGC formation: the role of RGD, PHSRN, and PRRARV domains.* J Biomed Mater Res, 2001. **55**(1): p. 79-88.

91. Ochsenhirt, S.E., et al., *Effect of RGD secondary structure and the synergy site PHSRN on cell adhesion, spreading and specific integrin engagement.* Biomaterials, 2006. **27**(20): p. 3863-74.

92. Rezania, A. and K.E. Healy, *Biomimetic peptide surfaces that regulate adhesion, spreading, cytoskeletal organization, and mineralization of the matrix deposited by osteoblast-like cells.* Biotechnol Prog, 1999. **15**(1): p. 19-32.

93. Dee, K.C., T.T. Andersen, and R. Bizios, *Design and function of novel osteoblast-adhesive peptides for chemical modification of biomaterials.* Journal of Biomedical Materials Research, 1998. **40**(3): p. 371-377.

94. Reyes, C.D. and A.J. Garcia, *Engineering integrin-specific surfaces with a triple-helical collagen-mimetic peptide* J Biomed Mater Res, 2003. **65A**: p. 511-523.

95. Reyes, C.D. and A.J. Garcia, *Alpha2beta1 integrin-specific collagen-mimetic surfaces supporting osteoblastic differentiation.* J Biomed Mater Res, 2004. **69A**(4): p. 591-600.

96. Reyes, C.D., et al., *Biomolecular surface coating to enhance orthopaedic tissue healing and integration* Biomaterials, 2007. **28**(21): p. 3228-3235.

97. Jiang, X., et al., *Electrochemical desorption of self-assembled monolayers noninvasively releases patterned cells from geometrical confinements.* Journal of the American Chemical Society, 2003. **125**(9): p. 2366-7.

98. Zhao, C., I. Witte, and G. Wittstock, *Switching on cell adhesion with microelectrodes.* Angewandte Chemie International Edition, 2006. **45**(33): p. 5469-5471.

99. Wittstock, G., et al., *Scanning electrochemical microscopy for direct imaging of reaction rates.* Angewandte Chemie International Edition, 2007. **46**(10): p. 1584-1617.

100. Kaji, H., et al., *Microelectrochemical approach to induce local cell adhesion and growth on substrates.* Langmuir, 2004. **20**(1): p. 16-19.

101. Yamaguchi, K., et al., *Novel silane coupling agents containing a photolabile 2-nitrobenzyl ester for introduction of a carboxy group on the surface of silica gel.* Chemistry Letters, 2000. **29**(3): p. 228-229.

102. Nakanishi, J., et al., *Spatiotemporal control of migration of single cells on a photoactivatable cell microarray.* J Am Chem Soc, 2007. **129**(21): p. 6694-5.

103. Dillmore, W.S., M.N. Yousaf, and M. Mrksich, *A photochemical method for patterning the immobilization of ligands and cells to self-assembled monolayers.* Langmuir, 2004. **20**(17): p. 7223-7231.

104. Petersen, S., et al., *Phototriggering of cell adhesion by caged cyclic RGD peptides.* Angew Chem Int Ed Engl, 2008. **47**(17): p. 3192-5.

105. Yeo, W.S., C.D. Hodneland, and M. Mrksich, *Electroactive monolayer substrates that selectively release adherent cells.* ChemBioChem, 2001. **2**(7 8): p. 590-593.

106. Yeo, W.S. and M. Mrksich, *Electroactive self-assembled monolayers that permit orthogonal control over the adhesion of cells to patterned substrates.* Langmuir, 2006. **22**(25): p. 10816-10820.

107. Wirkner, M., et al., *Triggered Cell Release from Materials Using Bioadhesive Photocleavable Linkers.* Advanced Materials, 2011: p. n/a-n/a.

108. Liu, D., et al., *Using Azobenzene Embedded Self Assembled Monolayers To Photochemically Control Cell Adhesion Reversibly.* Angewandte Chemie International Edition, 2009. **48**(24): p. 4406-4408.

109. Auernheimer, J., et al., *Photoswitched cell adhesion on surfaces with RGD peptides.* Journal of the American Chemical Society, 2005. **127**(46): p. 16107-10.

110. Robertus, J., W.R. Browne, and B.L. Feringa, *Dynamic control over cell adhesive properties using molecular-based surface engineering strategies.* Chemical Society Reviews, 2010. **39**(1): p. 354-378.

111. Okano, T., et al., *Mechanism of cell detachment from temperature-modulated, hydrophilic-hydrophobic polymer surfaces.* Biomaterials, 1995. **16**(4): p. 297-303.

112. Yang, J., et al., *Reconstruction of functional tissues with cell sheet engineering.* Biomaterials, 2007. **28**(34): p. 5033-5043.

113. Shimizu, T., et al., *Cell sheet engineering for myocardial tissue reconstruction.* Biomaterials, 2003. **24**(13): p. 2309-2316.

114. Chen, C.S., J. Tan, and J. Tien, *Mechanotransduction at cell-matrix and cell-cell contacts.* Annual Review of Biomedical Engineering, 2004. **6**: p. 275-302.

115. Harris, A.K., P. Wild, and D. Stopak, *Silicone rubber substrata: a new wrinkle in the study of cell locomotion.* Science, 1980. **208**(4440): p. 177.

116. Balaban, N.Q., et al., *Force and focal adhesion assembly: a close relationship studied using elastic micropatterned substrates.* Nature Cell Biology, 2001. **3**(5): p. 466-472.

117. Galbraith, C.G. and M.P. Sheetz, *A micromachined device provides a new bend on fibroblast traction forces.* Proceedings of the National Academy of Sciences, 1997. **94**(17): p. 9114.

118. Tan, J.L., et al., *Cells lying on a bed of microneedles: an approach to isolate mechanical force.* Proc Natl Acad Sci U S A, 2003. **100**(4): p. 1484-9.

119. Yang, M.T., et al., *Assaying stem cell mechanobiology on microfabricated elastomeric substrates with geometrically modulated rigidity.* Nature protocols, 2011. **6**(2): p. 187-213.

120. Anderson, J.M., A. Rodriguez, and D.T. Chang. *Foreign body reaction to biomaterials*. in *Seminars in immunology*. 2008. NIH Public Access.

121. Sutherland, K. and J. Mahoney, *Degradation of biomaterials by phagocyte-derived oxidants.* Journal of Clinical Investigation, 1993. **92**(5): p. 2360.

122. Zhao, Q., et al., *Foreign-body giant cells and polyurethane biostability: In vivo correlation of cell adhesion and surface cracking.* Journal of Biomedical Materials Research, 2004. **25**(2): p. 177-183.

123. Wojtecki, R.J., M.A. Meador, and S.J. Rowan, *Using the dynamic bond to access macroscopically responsive structurally dynamic polymers.* Nature materials, 2011. **10**(1): p. 14-27.

124. Gupta, P., K. Vermani, and S. Garg, *Hydrogels: from controlled release to pH-responsive drug delivery.* Drug discovery today, 2002. **7**(10): p. 569-579.

125. Murdan, S., *Electro-responsive drug delivery from hydrogels.* Journal of controlled release, 2003. **92**(1): p. 1-17.

126. Kao, W.J. and D. Lee, *In vivo modulation of host response and macrophage behavior by polymer networks grafted with fibronectin-derived biomimetic oligopeptides: the role of RGD and PHSRN domains.* Biomaterials, 2001. **22**(21): p. 2901-2909.

127. Phelps, E.A., et al., *Maleimide Cross-Linked Bioactive PEG Hydrogel Exhibits Improved Reaction Kinetics and Cross-Linking for Cell Encapsulation and In situ Delivery.* Advanced Materials, 2012. **24**(1): p. 64-70.

128. Phelps, E.A., et al., *Bioartificial matrices for therapeutic vascularization.* Proceedings of the National Academy of Sciences, 2010. **107**(8): p. 3323-3328.

129. Legate, K.R., S.A. Wickström, and R. Fässler, *Genetic and cell biological analysis of integrin outside-in signaling.* Genes & development, 2009. **23**(4): p. 397-418.

130. Beningo, K.A., et al., *Nascent focal adhesions are responsible for the generation of strong propulsive forces in migrating fibroblasts.* Journal of Cell Biology, 2001. **153**(4): p. 881-8.

131. Balaban, N.Q., et al., *Force and focal adhesion assembly: a close relationship studied using elastic micropatterned substrates.* Nature Cell Biology, 2001. **3**(5): p. 466-72.

132. Gallant, N.D., K.E. Michael, and A.J. Garcia, *Cell adhesion strengthening: contributions of adhesive area, integrin binding, and focal adhesion assembly.* Molecular Biology of the Cell, 2005. **16**(9): p. 4329-40.

133. Kanchanawong, P., et al., *Nanoscale architecture of integrin-based cell adhesions.* Nature, 2010. **468**(7323): p. 580-584.

134. Tan, J.L., et al., *Cells lying on a bed of microneedles: an approach to isolate mechanical force.* Proceedings of the National Academy of Sciences of the United States of America, 2003. **100**(4): p. 1484.

135. Smilenov, L.B., et al., *Focal adhesion motility revealed in stationary fibroblasts.* Science, 1999. **286**(5442): p. 1172-1174.

136. Ziegler, W.H., R.C. Liddington, and D.R. Critchley, *The structure and regulation of vinculin.* Trends in cell biology, 2006. **16**(9): p. 453-460.

137. Cohen, D.M., et al., *A conformational switch in vinculin drives formation and dynamics of a talin-vinculin complex at focal adhesions.* Journal of Biological Chemistry, 2006. **281**(23): p. 16006-16015.

138. Horwitz, A.F., et al., *Interaction of plasma membrane fibronectin receptor with talin-a transmembrane linkage.* Nature, 1986. **320**: p. 531-533.

139. Chen, H., et al., *Spatial distribution and functional significance of activated vinculin in living cells.* The Journal of cell biology, 2005. **169**(3): p. 459-470.

140. Zemljic-Harpf, A.E., et al., *Cardiac-myocyte-specific excision of the vinculin gene disrupts cellular junctions, causing sudden death or dilated cardiomyopathy.* Molecular and cellular biology, 2007. **27**(21): p. 7522-7537.

141. Borghi, N., et al., *Regulation of cell motile behavior by crosstalk between cadherin-and integrin-mediated adhesions.* Proceedings of the National Academy of Sciences, 2010. **107**(30): p. 13324-13329.

142. le Duc, Q., et al., *Vinculin potentiates E-cadherin mechanosensing and is recruited to actin-anchored sites within adherens junctions in a myosin II–dependent manner.* The Journal of cell biology, 2010. **189**(7): p. 1107-1115.

143. Peng, X., et al., *Vinculin regulates cell-surface E-cadherin expression by binding to β-catenin.* Journal of cell science, 2010. **123**(4): p. 567-577.

144. Grashoff, C., et al., *Measuring mechanical tension across vinculin reveals regulation of focal adhesion dynamics.* Nature, 2010. **466**(7303): p. 263-266.

145. Dumbauld, D.W., et al., *How vinculin regulates force transmission.* Proceedings of the National Academy of Sciences, 2013.

146. Yu, C.-h., et al., *Early integrin binding to Arg-Gly-Asp peptide activates actin polymerization and contractile movement that stimulates outward translocation.* Proceedings of the National Academy of Sciences, 2011. **108**(51): p. 20585-20590.

147. Pasapera, A.M., et al., *Myosin II activity regulates vinculin recruitment to focal adhesions through FAK-mediated paxillin phosphorylation.* The Journal of cell biology, 2010. **188**(6): p. 877-890.

148. Hagel, M., et al., *The adaptor protein paxillin is essential for normal development in the mouse and is a critical transducer of fibronectin signaling.* Molecular and cellular biology, 2002. **22**(3): p. 901-915.

149. Fu, J., et al., *Mechanical regulation of cell function with geometrically modulated elastomeric substrates.* Nature methods, 2010. **7**(9): p. 733-736.